

Historic Thermal Calibration of Landsat 5 TM through an
Improved Physics Based Approach

by

Francis P. Padula

Bachelor of Science, Meteorology
State University of New York at Brockport, 2005

A thesis submitted in partial fulfillment of the
requirements for the degree of Master of Science
in the Chester F. Carlson Center for Imaging Science
Rochester Institute of Technology

October, 2008

Signature of the Author _____

Accepted by _____
Coordinator, M.S. Degree Program Date

CHESTER F. CARLSON CENTER FOR IMAGING SCIENCE
ROCHESTER INSTITUTE OF TECHNOLOGY
ROCHESTER, NEW YORK

CERTIFICATE OF APPROVAL

M.S. DEGREE THESIS

The M.S. Degree Thesis of Francis P. Padula
has been examined and approved by the
thesis committee as satisfactory for the
thesis required for the
M.S. degree in Imaging Science

Dr. John R. Schott, Thesis Advisor

Dr. Carl Salvaggio

Dr. Anthony Vodacek

Date

Thesis/Dissertation Author Permission Statement

Title of thesis or dissertation: _____

Name of author: _____

Degree: _____

Program: _____

College: _____

I understand that I must submit a print copy of my thesis or dissertation to the RIT Archives, per current RIT guidelines for the completion of my degree. I hereby grant to the Rochester Institute of Technology and its agents the non-exclusive license to archive and make accessible my thesis or dissertation in whole or in part in all forms of media in perpetuity. I retain all other ownership rights to the copyright of the thesis or dissertation. I also retain the right to use in future works (such as articles or books) all or part of this thesis or dissertation.

Print Reproduction Permission Granted:

I, _____, hereby **grant permission** to the Rochester Institute of Technology to reproduce my print thesis or dissertation in whole or in part. Any reproduction will not be for commercial use or profit.

Signature of Author: _____ Date: _____

Print Reproduction Permission Denied:

I, _____, hereby **deny permission** to the RIT Library of the Rochester Institute of Technology to reproduce my print thesis or dissertation in whole or in part.

Signature of Author: _____ Date: _____

Inclusion in the RIT Digital Media Library Electronic Thesis & Dissertation (ETD) Archive

I, _____, additionally grant to the Rochester Institute of Technology Digital Media Library (RIT DML) the non-exclusive license to archive and provide electronic access to my thesis or dissertation in whole or in part in all forms of media in perpetuity.

I understand that my work, in addition to its bibliographic record and abstract, will be available to the world-wide community of scholars and researchers through the RIT DML. I retain all other ownership rights to the copyright of the thesis or dissertation. I also retain the right to use in future works (such as articles or books) all or part of this thesis or dissertation. I am aware that the Rochester Institute of Technology does not require registration of copyright for ETDs.

I hereby certify that, if appropriate, I have obtained and attached written permission statements from the owners of each third party copyrighted matter to be included in my thesis or dissertation. I certify that the version I submitted is the same as that approved by my committee.

Signature of Author: _____ Date: _____

Acknowledgments

My Advisor: Dr. Schott

Thank you for your great mentorship and of course thank you for giving me a chance. I hope you don't regret it. I really can't thank you enough for the positive impact you have made on my life.

My committee: Dr. Salvaggio & Dr. Vodacek

It has been a pleasure working with you both, thanks for everything.

DIRS group - Thanks for all of your support. Keep up the good work!

My undergraduate advisors: Dr. Maliekal & Dr. Rochette

Thank you so much for everything.

Special thanks to:

Raqueno's (Rolo and Nina): you guys are so great! Thank you for everything.

Julia Barsi, NASA - Thanks for everything, especially for getting me well.... "a few images... :) thanks again."

Scott Brown - I just want to say I really look up to you, thanks again for all of your help.

Mike Richardson - Thanks for your continual advice and guidance, I really appreciate it.

Cindy Schultz - what can I say, "THANK YOU!!!"

Dr. LaLonde & Dr. Bajorski - thank you for your statistical guidance.

I want to personally thank Matt Montanaro, Aaron Gerace and Stefania Matteoli for all of your support. I truly hope we will all be lifelong friends. I really look up to you guys both as colleagues and as friends.

Lastly I want to thank my family for always being there for me. You are my true inspiration, and I know that I am so fortunate to have such a great family. In particular I want to thank my parents for all of the sacrifices they have made for me and my family. I can only hope to be as great of parents as the both of you. And mom I will never forget, "keep on climbing..."! You are the best.... Love you Mom ;)

A quote from Elbert Hubbard,

"The greatest mistake you can make in life is to continually be afraid you will make one."

Historic Thermal Calibration of Landsat 5 TM through an Improved Physics Based Approach

by

Francis P. Padula

Submitted to the

Chester F. Carlson Center for Imaging Science
in partial fulfillment of the requirements
for the Master of Science Degree
at the Rochester Institute of Technology

Abstract

This investigation is motivated by the current need for a detailed post launch calibration of the Thematic Mapper (TM) thermal band (Band 6), aboard NASA's Landsat 5 spacecraft. The historical calibration spans the period from 1984 to 2007. It is through fusion of environmental data sources (i.e. buoy observations, surface observations, and radiosonde observations) that a vicarious calibration approach will be implemented to construct the complete calibration record of the Landsat 5 TM thermal band. The vicarious calibration process takes advantage of the long standing National Data Buoy Center (NDBC) moored buoy fleet to acquire historic ground truth measurements needed over the lifetime of Landsat 5. These measurements are propagated to the sensor through the use of physics based models to establish a predicted at sensor radiance. Through comparison of the predicted at sensor radiance and the actual sensor observed radiance, a calibration metric is established.

Results indicate the Landsat 5 TM thermal band, originally planned for a 3 year mission, has fluctuated only slightly (~ 1 K) over the 24+ years in orbit. The calibration curve developed in this study is consistent with previous results from campaigns performed in 1985 and post 1999. The data indicated that the sensor exhibited a clear gain issue (i.e. over estimates low radiance targets and under estimates high radiance targets) found to be approximately consistent over time. Additionally, an event occurring either prior to or during 1999, caused a discernible fluctuation in sensor performance (i.e. dominant cold bias) for all data post 1999. It is the recommendation of this vicarious calibration

II

campaign that a linear (Dual: slope & intercept) correction be applied to the Landsat 5 data archive. As a result of the correction, the Landsat 5 TM Band 6 is radiometrically calibrated to within ± 0.488 K, in reference to a 300 K blackbody. This result was verified through an extensive error propagation analysis, which found the proposed methodology to have an expected error of 0.454 K. The proposed methodology was also verified by a comparison study to the traditional approach (i.e. non buoy derived ground truth) using the closely monitored and trusted Landsat 7 data calibrated using the traditional approach. The comparison found the two methods were not statistically different, which offered the confidence that this methodology could be applied successfully over the domain of this study. This comparison not only validates the calibration record of Landsat 5, but also demonstrates the utility of the method in future efforts.

This work has demonstrated that a successful historical vicarious calibration campaign can be conducted using exclusively free and easily accessible data. It has been established that the proposed methodology can be implemented to achieve a high level of radiometric integrity, which includes both historic and future efforts, in the calibration of remote thermal infrared systems.

Contents

Abstract	I
List of Figures	VII
List of Tables	XIV
1 Introduction	1
2 Background	3
2.1 Calibration History of Landsat 5 Band 6	3
2.2 Vicarious Calibration: Sites & Thermal Targets	4
2.3 Vicarious Thermal Calibration for Satellite Radiometers	8
2.3.1 Single Channel Methods	9
2.3.2 Profile (Multiple Altitude) Method:	9
2.3.3 Multiple Angle Method:	10
2.3.4 Atmospheric Propagation Modeling used with Ground Truth Observations:	10
2.4 Satellite Temperature Retrieval Biases	12
2.5 Radiance to Temperature Conversions	17
2.6 Bulk to Skin Water Temperature Models	18
2.7 Error Propagation	27
2.8 Summary	28
3 Theory	31
3.1 Landsat Program Overview	31

3.1.1	Landsat 5	33
3.1.2	Landsat 7	37
3.2	Radiation Propagation	39
3.2.1	Thermal Energy Paths	39
3.2.2	Blackbody Radiance & the Planckian Equation	40
3.2.3	Kirchoff's law	41
3.3	Governing Radiometry	42
3.3.1	Effective Radiance	43
3.4	Atmosphere	44
3.4.1	Atmospheric Boundary Layer	44
3.4.1.1	Internal Boundary Layer	48
3.4.2	Troposphere	51
3.4.3	Stratosphere	51
3.4.4	Upper Atmosphere	53
3.5	Atmospheric Effects on Sensor Reaching Radiance	53
3.5.1	Atmospheric Transmission	54
3.5.1.1	Atmospheric Absorption	54
3.5.1.2	Atmospheric Scattering	54
3.5.2	Atmospheric Self-Emission: Upwelled Radiance and Downwelled Radiance	56
3.5.3	Computation of Atmospheric Affects through Physical Modeling . .	56
3.6	Sampling of Environmental Parameters	61
3.6.1	Upper-air Data	61
3.6.2	Buoy data	63
3.7	Surface Phenomenology of Large Water Bodies	66
3.8	Summary	68
4	Approach	71
4.1	Proposed Calibration Sites	72
4.1.0.1	Lake Huron (Site #1)	73
4.1.1	Lake Superior (Site #2)	78

4.1.2	Lake Ontario (Site #3)	79
4.1.3	Delmarva Peninsula (Site #4)	80
4.2	Environmental Data Sources	82
4.3	Scene Selection - Ranking Structure	83
4.4	Process Overview	85
4.5	Computation of T_b to T_s	85
4.6	Recreation of the Atmospheric Column	88
4.6.1	Surface Correction	92
4.6.2	Upper-Air Interpolation & Processing	96
4.7	Alternative Atmospheric Data Sources	100
4.8	Extracting Atmospheric Terms	103
4.9	Obtain Image Derived Radiance	104
4.10	Landsat 7 Process Validation Study	105
4.11	Error Propagation: Process Error	106
4.11.1	Bulk to Skin Temperature Error Propagation Methodology	107
4.11.2	Atmospheric Error Propagation Methodology	108
4.12	Determination of Process Error	115
4.12.1	Ground Truth Process Error (T_b to T_s)	115
4.12.2	Atmospheric Process Error	120
4.12.3	Overall Process Error	123
4.13	Validation of Approach	131
4.13.1	Landsat 7 Comparison Study	131
4.13.2	Landsat 5 Comparison Study	132
4.13.3	Proposed Methodology vs. Traditional Methodology	135
5	Results	139
5.1	Preprocessing of the Calibration Data	139
5.2	Calibration Results: Proposed Corrections	150
5.2.1	Linear (Global: Slope & Intercept) Correction	150
5.2.2	Linear (Dual: Slope & Intercept) Correction	154
5.2.3	Linear (Global Slope & Dual Intercept) Correction	159

5.2.4	Global Bias Correction	162
5.2.5	Time Dependent Bias Correction	166
5.2.6	Dual: Linear (Global: Slope & Intercept) & Global Bias Correction	169
5.2.7	Dual: Time Dependent Bias & Linear (Global: Slope & Intercept) Correction	173
5.2.8	Conclusions: Summary of the Proposed Corrections	175
5.2.9	Recommendation	178
5.2.10	Reverse Engineering Case	179
5.2.11	Summary	181
5.3	Summary Statistics	182
5.4	Recommendations and Summary	188
A	Landsat Program Overview	193
B	Volcanic Contamination Correction Study	195
C	Internal Boundary Layer Study	197
D	Surface Correction Study	203
E	Upper Air Study	211
F	MODTRAN Standard Atmosphere's	219
G	Buoy Hull Type and Location History	223
H	User Workflow	227
I	MODTRAN Formatting	229
J	Error Propagation: Atmospheric Profiles	231
	Bibliography	239

List of Figures

2.1	Schematic of Ideal Ground Truth Collection	7
2.2	RIT Ground Truth Schematic: Thermistor Float & Buoy	7
2.3	Spectral Emissivity of Water	13
2.4	CO_2 , O_3 and Water Vapor Ground-to-Space Transmission	15
2.5	Near Surface Temperature Variation at Depth	19
2.6	Oversimplified T_s to T_b Model	22
2.7	Schematic of the Computation of T_b to T_s	24
3.1	Landsat Program Overview	32
3.2	Cutaway of the TM	34
3.3	Landsat TM Optical Layout	35
3.4	Landsat TM Ground Track	36
3.5	Landsat 5 Band 6 Response & Thermal Specs	36
3.6	Landsat 7 Band 6 Response & Thermal Specs	38
3.7	Thermal Energy Paths	39
3.8	Thermal Energy Paths for Radiance Reaching an Orbiting Satellite	43
3.9	Standard Atmospheric Temperature Profile	45
3.10	Atmospheric Diurnal Variation Example	46
3.11	Diurnal Variation Over Land (Fair Weather)	46
3.12	Surface Inversion Example	47
3.13	Stably Stratified IBL Schematic	49
3.14	Tropopause Height Analysis Example	52
3.15	Atmospheric Scattering	55

3.16 Atmospheric Approximations - Development of Homogeneous Layers . . .	57
3.17 MODTRAN Computation of τ	59
3.18 MODTRAN Computation of L_u	60
3.19 MODTRAN Computation of L_d	60
3.20 North American Radiosonde Locations	61
3.21 Radiosonde predicted Trajectory Example	62
3.22 NDBC Moored Buoy Program Platforms	63
3.23 Moored Buoy Locations within the Great Lakes	64
3.24 NDBC 3m Discus Moored Buoy	65
3.25 Thermal Bar Schematic	67
3.26 Two Examples of Lake Huron's Thermodynamic Structure	68
4.1 Vicarious Calibration Overview	72
4.2 Great Lakes Study Domain	73
4.3 Calibration Site 1	74
4.4 Lake Huron Buoy Location History	75
4.5 Calibration Site 2	76
4.6 Lake Huron Thermal Bar Evolution	77
4.7 Filter Example: Spatial Variation in Surface Temperature	77
4.8 Calibration Site 2	78
4.9 Lake Superior Buoy Location History	79
4.10 Calibration Site 3	80
4.11 Calibration Site 4	80
4.12 Delmarva Peninsula Buoy Location History	82
4.13 Example of Ranked Scenes	84
4.14 Process Overview	85
4.15 Buoy Method Comparison	87
4.16 Buoy Method Comparison vs Wind Speed	88
4.17 Atmospheric Column Generation Points	89
4.18 Radiosonde 12 UTC & 00 UTC Visualizer Ex. 1	90
4.19 Radiosonde 12 UTC & 00 UTC Visualizer Ex. 2	91

4.20 Atmospheric Surface Correction: Boundary Layer	93
4.21 Atmospheric Surface Correction: Internal Boundary Layer	94
4.22 Atmospheric Surface Correction	95
4.23 MODTRAN: Mid-Latitude Summer	96
4.24 Appending the Upper-Air Model to Radiosonde Observations	97
4.25 Atmospheric Upper-Air Dew Point Interpolations	99
4.26 Bufrkit Data Availability	102
4.27 Computation of an Effective Radiance	103
4.28 Image Derived Radiance	104
4.29 Schematic of Atmospheric Error Propagation Methodology	112
4.30 Proposed Error in Atmospheric Processing	114
4.31 Error Propagation: Buoy Process Input Values	116
4.32 Sensitivity of T_b to T_s : 3m and 12m Buoy	119
4.33 Scatter Plots of Atmospheric Terms	122
4.34 Sensitivity Analysis on the Governing Equation: Spring Atmosphere 1 a . .	126
4.35 Sensitivity Analysis on the Governing Equation: Spring Atmosphere 1 b . .	127
4.36 Sensitivity Analysis on the Governing Equation: Summer Atmosphere 1 a .	128
4.37 Sensitivity Analysis on the Governing Equation: Summer Atmosphere 1 b .	129
4.38 Landsat 7 Comparison Study: Predicted At-Sensor Radiance vs. Image Derived Radiance	132
4.39 Landsat 5 Comparison Study: Temperature Bias vs Tme	134
4.40 Landsat 5 Comparison Study: Predicted At-Sensor Radiance vs. Image Derived Radiance	134
5.1 Temperature Bias vs Time (All Data)	139
5.2 Temperature Bias vs Time (DD and Highly Variant Surface Temperature Filtered)	141
5.3 Temperature Bias vs Time (DD and Highly Variant Surface Temperature Filtered and Volcanic Correction)	141
5.4 Data Coverage: Filtered Data	142
5.5 Temperature Bias vs Time (Filtered Data)	143

5.6	Predicted At-Sensor Radiance vs. Image Derived Radiance (All Data) . . .	144
5.7	Predicted At-Sensor Radiance vs. Image Derived Radiance (Filtered Data)	145
5.8	Predicted At-Sensor Radiance vs. Image Derived Radiance (Filtered and 1999 Plus Uncorrected Data)	146
5.9	Temperature Bias vs Time (Filtered and Uncorrected Data)	147
5.10	Predicted At-Sensor Radiance vs. Image Derived Radiance (Filtered and 1999 Plus Uncorrected Data): 1999 Plus Investigation)	148
5.11	Temperature Bias vs Time 6 Month Moving Average (Filtered and Uncor- rected Data)	149
5.12	Predicted At-Sensor Radiance vs. Image Derived Radiance: Linear (Global: Slope & Intercept) Correction	151
5.13	Temperature Bias vs Time (Linear (Global: Slope & Intercept) Correction)	152
5.14	Predicted At-Sensor Radiance vs. Image Derived Radiance: Linear (Dual: Slope & Intercept) Correction	154
5.15	Predicted At-Sensor Radiance vs. Image Derived Radiance: Linear (Dual: Slope & Intercept) Correction compared to Linear (Global: Slope & Inter- cept) Correction	155
5.16	Temperature Bias vs Time (Linear (Dual: Slope & Intercept) Correction)	156
5.17	Linear (Dual: Slope & Intercept) Correction: 6 Month Moving Average . .	156
5.18	Linear (Dual: Slope & Intercept) Correction: 6 Month and 2 Year Running Average	157
5.19	Predicted At-Sensor Radiance vs. Image Derived Radiance: Linear (Global Slope & Dual Intercept) Correction	160
5.20	Temperature Bias vs Time (Linear (Global Slope & Dual Intercept) Cor- rection)	160
5.21	Radiance Bias vs Time (Filtered & Uncorrected Data)	162
5.22	Temperature Bias vs Time (Global Bias Correction)	163
5.23	Predicted At-Sensor Radiance vs. Image Derived Radiance: Global Bias Correction	164
5.24	Bias Radiance vs. Time: Filtered & Uncorrected Data (Segmented into 2 Classes)	167

5.25	Temperature Bias vs. Time (Time Dependent Bias Correction)	167
5.26	Predicted At-Sensor Radiance vs. Image Derived Radiance: Time Dependent Bias Correction	168
5.27	Temperature Bias vs Time (Linear (Global: Slope & Intercept) Correction)	169
5.28	Radiance Bias vs Time (Linear (Global: Slope & Intercept) Correction) . .	170
5.29	Predicted At-Sensor Radiance vs. Image Derived Radiance: Linear (Global: Slope & Intercept) & Global Bias Correction	171
5.30	Temperature Bias vs Time (Linear (Global: Slope & Intercept) & Global Bias Correction)	171
5.31	Predicted At-Sensor Radiance vs. Image Derived Radiance: Dual: Time Dependent Bias & Linear (Global: Slope & Intercept) Correction	173
5.32	Temperature Bias vs Time (Dual: Time Dependent Bias & Linear (Global: Slope & Intercept) Correction)	174
5.33	Histogram: Bias Temperature from the Linear (Dual: Slope & Intercept) .	177
5.34	Error Propagation: Reverse Engineering Case	181
5.35	Histogram: Ground Truth Temperatures	182
5.36	Histogram: Ground Truth Temperature Applied T_b to T_s Corrections . . .	184
5.37	Calibration Site Ground Truth Contribution	185
5.38	Histogram: Site 1 & 2 Specific Ground Truth Temperatures	186
5.39	Histogram: Site 3 & 4 Specific Ground Truth Temperatures	187
5.40	Potential Calibration Sites for Future Work	190
B.1	Volcanic Correction Study	195
C.1	IBL Study: 27 May 90	198
C.2	IBL Study: 10 Jun 84	199
C.3	IBL Study: 16 Aug 85	199
C.4	IBL Study: 24 Aug 05	200
C.5	IBL Study: 26 Jun 01	200
C.6	IBL Study: 17 Jun 86	201
D.1	Surface Correction: Data	204
D.2	Surface Correction: Box Plot of Abs. Difference Between Methods	205

D.3	Surface Correction: 03 May 87	206
D.4	Surface Correction: 14 Jun 91	207
D.5	Surface Correction: 14 Feb 06	207
D.6	Surface Correction: 16 Jun 87	208
D.7	Surface Correction: 10 Jul 89	208
D.8	Surface Correction: 21 Sep 84	209
D.9	Surface Correction: 06 Jul 99	209
D.10	Surface Correction: 28 Mar 86	210
E.1	Upper-Air Study: 26 Jan 02	213
E.2	Upper-Air Study: 28 Apr 03	214
E.3	Upper-Air Study: 27 May 90	214
E.4	Upper-Air Study: 24 Jun 90	215
E.5	Upper-Air Study: 24 Oct 98	215
E.6	Upper-Air Study: 06 Jul 99	216
E.7	Upper-Air Study: 16 Aug 85	216
E.8	Upper-Air Study: Data	217
F.1	MODTRAN Standard Atmosphere: Mid-Latitude Summer	220
F.2	MODTRAN Standard Atmosphere: Mid-Latitude Winter	221
F.3	MODTRAN Standard Atmosphere: Tropical	222
G.1	Buoy Location and Payload History: 45003	224
G.2	Buoy Location and Payload History: 45008	224
G.3	Buoy Location and Payload History: 45001	225
G.4	Buoy Location and Payload History: 45004	225
G.5	Buoy Location and Payload History: 44009 & 44012	226
I.1	MODTRAN Inputs	229
J.1	Atmospheric Profile Error Propagation Profile 1	232
J.2	Atmospheric Profile Error Propagation Profile 2	233
J.3	Atmospheric Profile Error Propagation Profile 3	234
J.4	Atmospheric Profile Error Propagation Profile 4	235

J.5	Atmospheric Profile Error Propagation Profile 5	236
J.6	Atmospheric Profile Error Propagation Profile 6	237
J.7	Atmospheric Profile Error Propagation Profile 7	238

List of Tables

2.1	Oversimplified T_s to T_b Model	21
2.2	Extracted values from Fairall et al. (1996) Table 3	26
2.3	Simplified Fairall et al. (1996) treatment	26
3.1	Multispectral Scanner (MSS) & Thematic Mapper (TM), USGS.	33
3.2	Landsat 5 orbital characteristics, USGS.	34
3.3	ETM+ Band Specs, USGS.	37
3.4	Eq. 3.10 description; all variables, except F , have a spectral dependence . .	42
3.5	IBL Height Model Variable Description	49
3.6	Variables of Atmospheric Transmission [Eq. 3.18].	55
3.7	Moored Buoy Sensor Heights, NBDC.	65
3.8	Buoy Specifications of Interest, NBDC.	66
4.1	Results from the comparison study of the two bulk to skin approaches. . . .	86
4.2	Listing and declaration of error terms in Eq. 4.4.	106
4.3	Listing and declaration of error terms in Eq. 4.6.	108
4.4	Declaration of specifications for atmospheric observations.	109
4.5	Listing and declaration of error terms in Eq. 4.12.	117
4.6	Atmospheric Error Propagation Results	120
4.7	Correlation values of τ , L_u and L_d derived from 114 unique atmospheric profiles.	121

4.8	Error in the effective radiance (L_{eff}) at the sensor due to uncertainties in the entire proposed methodology. Note error is expressed in apparent temperature [K] and all other radiance values are in units of $[W/m^2 sr \mu m]$. Note all atmospheric error values used to populate this table are found in [Table 4.6], while all remaining error estimates are shown in [Table 4.2].	124
4.9	Absolute average bias temperature difference for 1999+ data from: proposed methodology (RIT buoy), RIT traditional approach, & JPL.	133
4.10	Listing and declaration of error terms in Eq. 4.4.	136
4.11	Data from the comparison error propagation study, comparing the proposed method to the traditional method. Reported is the error in the effective radiance (L_{eff}) at the sensor and the error in temperature at the sensor provided a unit change in target temperature due to uncertainties in the entire proposed methodology. Note error is expressed in apparent temperature [K].	137
4.12	Error comparison: proposed method vs. traditional method	137
5.1	Volcanic Correction Summary	140
5.2	Summary of Proposed Calibration Corrections	175
5.3	Proposed Calibration Corrections	179
5.4	Listing and declaration of error terms in Eq. 5.3.	180
5.5	Ground Truth Data Summary Statistics	183
A.1	Landsat program overview: Landsat 1 to Landsat 7 Lillesand et al. (2004) .	194
C.1	Results from the IBL surface correction study.	198

Chapter 1

Introduction

This work is motivated by the current need for a detailed post launch calibration of the Thematic Mapper (TM) thermal band (Band 6), aboard the National Aeronautics and Space Administration (NASA) Landsat 5 spacecraft. The historical calibration effort spans the lifetime of the satellite, with specific interest on the period from 1985 to 1999 where no information regarding the state of the instruments calibration is known. It is through fusion of environmental data sources (i.e. buoy observations, surface observations, radiosonde observations) a vicarious calibration approach will be implemented to construct the complete historical calibration of the Landsat 5 TM thermal band. The vicarious calibration process has two main thrusts: 1) convert buoy derived water temperature at depth z (T_b) to skin temperature (T_s) (for correlation with remotely sensed radiometric temperature); 2) capture the state of the atmosphere at the time of image acquisition.

The novelty in such an approach is realized when considering the simplicity of the entire process. To date elaborate ground truth collection campaigns are conducted for calibration efforts which exhaust both resources and time potentially involving numerous personnel. This approach relies on ground truth measurements which have been acquiring target temperature measurements roughly every hour for the last roughly 28 years, obtained via National Data Buoy Center (NDBC) moored buoy fleet. This data is freely available, quality controlled and easily accessible. In long practice, the Advanced Very High Resolution Radiometer (AVHRR) instrument has relied on buoy derived measurements to both develop and validate temperature retrieval algorithms, as well as, calibrate the thermal bands of the instrument, which has been used as part of the National Ocean

and Atmospheric Administrations (NOAA) polar orbiting satellite program since 1979 [c.f. Emery et al. (2001), Li et al. (2001) and Walton et al. (1998)].

The proposed vicarious calibration effort will take advantage of the NDBC's long-standing moored buoy program to acquire the necessary ground truth measurements needed throughout the lifetime of Landsat 5. Using this data in conjunction with various meteorological data sources and Radiative Transfer Modeling (RTM), a predicted at-sensor radiance will be computed. By predicting the radiance that the sensor should detect, and defining it as truth, a comparison can be made with the actual observed satellite radiance to investigate the state of the instrument.

This work will also focus on the validation of the proposed methodology and final calibration curve. Validation will be conducted using both error propagation analysis, as well as comparison studies to the traditional approaches. At the conclusion of this work a recommendation will be presented to NASA regarding the lifetime state of the TM thermal band; if corrections are need to the calibration record; and if corrections are needed, how they should be addressed.

Chapter 2

Background

This chapter provides an overview of the process of thermal infrared (IR) vicarious calibration. Discussion will span the process from selecting a calibration site to the generation of a calibration curve, in addition the characterization and reduction of associated errors in the process will be addressed.

2.1 Calibration History of Landsat 5 Band 6

Calibration of the TM is unknown over much of the instruments lifetime. Specifically, the state of the TM's thermal band between the period of 1985 and 1999 is unknown Barsi et al. (2007). While under U.S. Government control in 1985 NASA had funded the Rochester Institute of Technology (RIT) to conduct a post launch thermal calibration effort. Results from the campaign suggested the TM's Band 6 was calibrated to within ± 0.9 K Barsi et al. (2003). A potentially more representative conclusion may be drawn from this campaign by taking a weighted average of the results listed in [Schott et al. (1986); Table 3.A-1], which revealed the TM Band 6 exhibited a warm bias of $+0.56$ K. Thus, as of 1985, vicarious calibration efforts revealed the sensor had a small warm bias.

Due to a commercialization effort in late 1985, the government turned control of Landsat 5 to a private company. Over the course of the following 14 years emphasis on calibration was let go or was for the most part undocumented. In July 2001, control of the satellite was brought back to the US government. Since then, NASA and the United States Geological Survey (USGS) have placed a strong effort in the calibration and validation of

the staggering 24+ year global TM data archive Barsi et al. (2007).

In 2001 two independent teams from RIT and NASA's Jet Propulsion Laboratory (JPL) began monitoring the calibration of the TM thermal band. The two teams used primarily water targets from Lake Tahoe (JPL) and Lakes Erie and Ontario (RIT) in their vicarious calibration campaigns. Using historic Lake Tahoe buoy data, the JPL team was able to extend their calibration study back to the extent of their buoy data archive (1999). The two independent teams concluded a cold bias existed of $-0.092 [W/m^2 sr \mu m]$ or about -0.68 K at 300 K Barsi et al. (2007). This result, different from the findings of Schott and Volchok (1985) illustrated that the state of the instrument may have changed throughout its history. Note, the internal calibrator has behaved as expected over time. Given these results NASA implemented a correction to the calibration of the TM instrument for all data after April 01, 1999. Currently NASA is funding JPL and RIT to perform on-going thermal calibration efforts of both Landsat 5 and Landsat 7.

In summary the current calibration record suggests that the instrument had a warm bias shortly after launch (i.e. mid 1980's), validated by Schott et al. (1986), and a cold bias in the modern era (1999 plus), validated by both RIT and JPL Barsi et al. (2003). The need for such a historical study is particularly important because this effort is aimed at evaluating whether a similar correction is needed for data during the period 1985 - 1999 when no vicarious calibration data are available.

2.2 Vicarious Calibration: Sites & Thermal Targets

From a review of the literature the optimal requirements for thermal calibration sites are discussed below; consistent with [Slater et al. (1996), Wan et al. (1999) and Tonooka et al. (2005)]. Calibration sites should encompass targets, which are homogenous in both surface temperature and emissivity. Sites should be free of any obstructions which could cast shadows, potentially introducing temperature contrasts across the surface (i.e. need uniform illumination). Strongly favored locations are: water bodies, dry lake beds and/or large snow covered areas. Ideal atmospheric conditions for calibration sites are: dry, cloud-free (clear) and fair weather (stable). In particular dry atmospheric conditions are desired, for example, Tonooka et al. (2005) state that the total water vapor column over

the calibration site should be small, as the accuracy in the radiative transfer computation is directly related to knowledge of the total water vapor column over the calibration site. Thus, the state of the atmosphere must be known. Ample consideration must also be placed on how such atmospheric observations can be obtained. If possible it is ideal to select sites that are located at high elevations, which essentially aids in reducing the effects of the atmosphere, by literal exclusion. For example, Tonooka et al. (2005) discusses how JPL utilizes a water site at Lake Tahoe in the Sierra Nevada Mountains. This location features a water surface which is approximately 2 km above sea level, thus excluding the most dense and typically most problematic region of the atmosphere. In addition, due to the geographic location, the overlaid atmosphere is typically dry and can be used year round for calibration purposes as the lake does not freeze over due to its extreme water depth of about 500 m.

Ideal thermal targets are large (would encompass numerous pixels), uniform, spatially and spectrally homogeneous, thermally stable (high heat capacity/ high thermal inertia) and have a well known spectral emissivity. Villa-Aleman et al. investigated a number of targets with known temperatures to validate the calibration of the Multispectral Thermal Imager (MTI) satellite. The targets included natural water bodies, power plant heated lakes, volcano lava vents, desert playas and aluminized Mylar tarps. Most of these target types are impractical in regards to a historical calibration effort, with the exception of water targets. Water is used as a primary target in thermal calibration efforts because it has a high and well known emissivity, uniform composition and often exhibits low spatial variation (less than or equal to 1°C) over large areas due to its high thermal inertia, (Barsi et al. (2003) and Tonooka et al. (2005)). Water bodies are often most practical because an in situ contact measurement of water's temperature can be easily obtained, in addition, unique emissivity measurements are not typically required.

It is important to understand that the site location and thermal target selected are critical to the final results of the calibration effort; as the type of target determines the valid temperature range for the calibration. For example, water targets can be used to validate temperatures from roughly 0°C to 30°C , where a temperature range in excess of 50°C can be achieved in desert lake beds Tonooka et al. (2005). Although, realize that each site location carries with it its own challenges regarding how accurate and reliable

target measurements can be obtained given the restrictions of the chosen site.

Given an ideal calibration site and target, strong consideration must be placed on the most appropriate ground truth collection method available. Ground truth is a phrase adopted by the remote sensing community, which refers to surface target observations measured by trusted and well-calibrated sensors at the time (or as close as possible) to satellite over-flight. Accurate ground truth measurements provide information regarding the target temperature or target radiance only. Measurements are typically made using contact thermistors and emissivity values (ϵ) determined by either field or laboratory measurements. Note that for solid targets it is difficult to provide an accurate contact measurement. Thus, it may be more appropriate and is ideal to acquire ground truth with a well calibrated radiometer (ideally with the same spectral bandpass as the orbiting sensor) Schott (2007). This method may reduce errors in ground truth measurements. For example, the orbiting LWIR sensor captures radiance about the surface, therefore, if ground truth data are obtained in radiance, there is no need for a conversion process from radiance to temperature. Conversely, if collected ground truth are measured in temperature one needs to convert temperature to radiance. Due to a variety of logistical problems it is quite difficult to acquire quality ground truth measurements, as well as, realizing that campaigns can often be very costly and time consuming Schott (2007).

Lets consider collecting ground truth measurements from a water target. Radiance emitted from a water body originates from the top tens of microns of the water surface, known as the skin temperature (T_s). To obtain accurate ground truth from such a target one must obtain the T_s . Again, ideally the use of a well-calibrated sensor (with the same bandpass as the observing satellite) is the best option, however, this method is often expensive, cumbersome and not applicable in regards to available historic data [Figure 2.1]; thus alternatives are discussed. Used in real-time, a cost-effective approach employed by RIT is through use of a contact thermistor attached to a block of styrofoam [Figure 2.2 (a)]. This approach is somewhat laborious and measures the near surface bulk temperature, thus corrections are needed to acquire the desired skin temperature (as will be discussed in Section 2.6). Similarly, buoy and ship derived water temperatures are of the bulk water temperature, thus larger corrections are typically needed to obtain reliable ground truth [Figure 2.2 (b)] from these sources. Ryan et al. note that differences between skin and

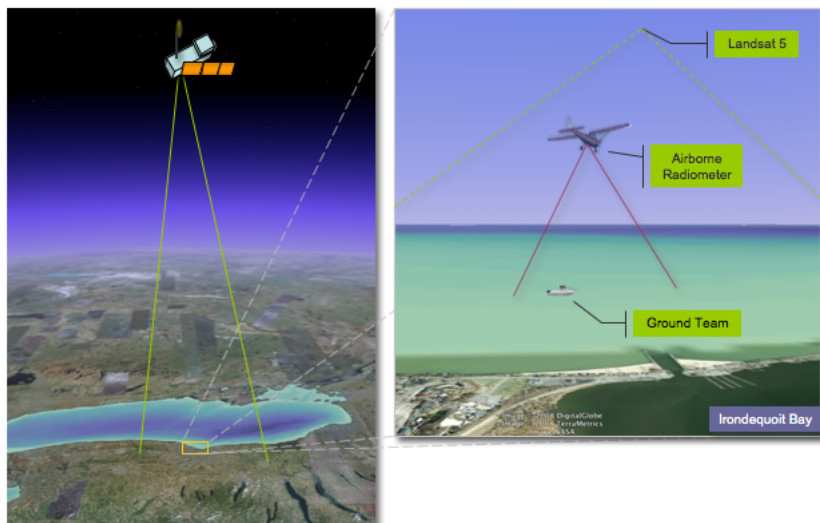


Figure 2.1: Schematic of ideal ground truth collection.

buoy derived bulk temperatures can be 1 °C or more. Aside from the added complexity due to the bulk to skin correction, buoy measurements are free, easily accessible and historically available, which make them a very practical and attractive source of ground truth.

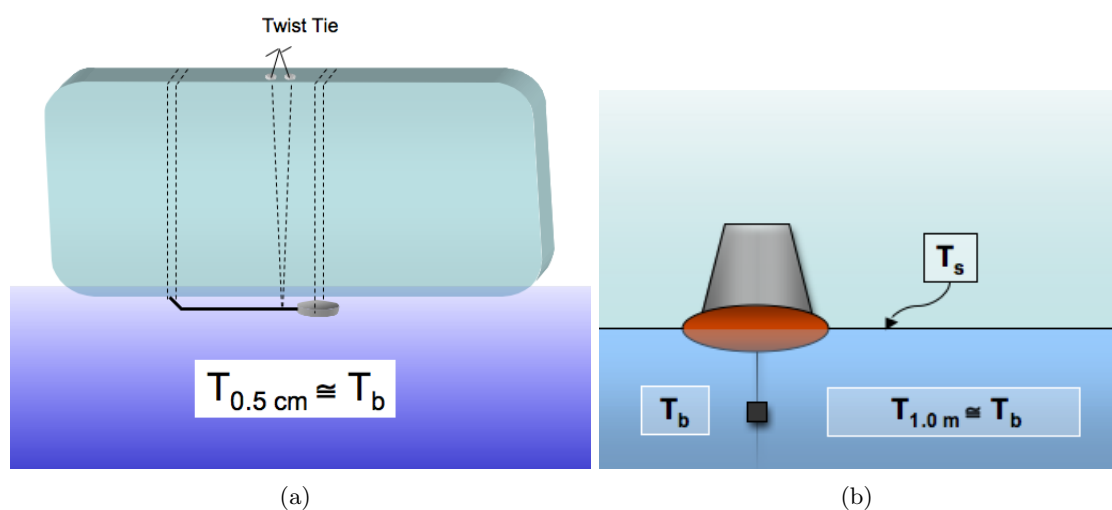


Figure 2.2: Schematic of a thermistor float (a) and a buoy (b) used to collect near surface temperatures. (Note (a) adopted from Schott and Raqueno (2006))

The determination of a calibration site requires the consideration of happily marrying all physical factors such as the site location, site specific target(s), target size(s), class of thermal target (i.e. warm/cold source), and site specific prevailing weather conditions.

In addition, logistical matters such as the most appropriate and cost effective manner to collect quality ground truth measurements simultaneously with satellite overpass must also be considered.

2.3 Vicarious Thermal Calibration for Satellite Radiometers

Vicarious calibration is an on-orbit technique in which deployed well calibrated ground based or airborne sensors simultaneously observe a thermal target at the time of satellite overpass (Barsi (2000)). The purpose of the simultaneous airborne or ground-based sensors allow for the prediction of radiance reaching the space-based sensor, so that a comparison to the observed satellite radiance can be performed, known as forward-engineering Schott (2007). The result yields a point on a calibration curve, thus, through repetition the calibration of the sensor can be evaluated.

After a review of the literature, it is apparent that the challenges in vicarious calibration efforts are essentially two fold. The first is how the target surface is characterized (i.e. ground truth methods: airborne sensors, field radiometers, thermistor, and/or bulk temperature measurements, as previously explained). The second is how the approach accounts for atmospheric effects on sensor reaching radiance.

Considering only the second objective, we can simplify the vicarious calibration process to that of satellite temperature retrieval. There are numerous approaches of satellite temperature retrieval that can be found through even a brief survey of the literature, most of which developed concerning a given sensor type and application. An overview provided by Gupta (2003) offers the simplified statement that thermal spectral radiance observed at the sensor can be characterized into two main components: thermal emission from the target and the atmospheric contribution. Revealing the fact that arguably the major concern in all thermal IR missions is how to account for the atmospheric effects on observed sensor radiance.

There are three major atmospheric effects: upward atmospheric emission, downward atmospheric irradiance reflected off the target surface and atmospheric scattering and absorption. In any temperature retrieval mission the goal is to back out or account for

these atmospheric affects. Multitudes of approaches exist, although all can be generally subdivided into four unique atmospheric correction techniques: the single channel method, the split-window method, the multi-angle method and combinations of the split-window and multi-angle method Dash et al. (2002). For the sake of brevity, this work will focus on methods which concern the single channel method only, due to the physical constraints of the TM instrument (one thermal IR channel). Although realize, split window techniques are quite popular and take advantage of the differential effect of the atmosphere on the observed spectral radiance between given sensor bands. These methods demonstrate an accuracy of ± 0.3 K to ± 1.0 K depending upon amount of atmospheric moisture present Czajkowski et al. (1998), although other studies have shown more significant errors. Most importantly these methods allow atmospheric correction without any further knowledge of the atmosphere, however, if sufficient data is provided about the state of the atmosphere, single-channel methods can be more accurate Dash et al. (2002).

2.3.1 Single Channel Methods

Single channel methods correct for atmospheric effects by use of radiance measurements in one IR channel. Approaches include in-scene methods: Profile (Multiple Altitude) approach & Multiple view angle approach, as well as, ground truth methods in conjunction with atmospheric propagation modeling. Note, in-scene techniques utilize multiple images of a common scene, thus are not adequate for this historical calibration effort. However, these methods will be briefly discussed as previous TM thermal calibration efforts used such approaches. The following summary of methods focuses on the forward engineering process mentioned above.

2.3.2 Profile (Multiple Altitude) Method:

Due to the uncertainties or lack of confidence in Radiative Transfer Models (RTM) at the time, Schott (1979) developed an empirical method which derives atmospheric transmission and upwelled radiance by flying an infrared radiometer at a series of altitudes over the same surface target. Accuracies in water surface temperature using this technique result in a standard error of 0.4 K, derived from a comparison to simultaneously acquired ground truth observations. This method has the advantage that it excludes the depen-

dence of ground truth campaigns (i.e. is an in-scene approach) Schott (2007). In an effort to calibrate NASA’s Heat Capacity Mapping Mission (HCMM) longwave infrared (LWIR) satellite, Schott and Schimminger (1981) utilized this approach. Provided the well documented accuracy of the aerial calibration method, in-conjunction with, a simultaneous satellite overpass, the HCMM was reported to be accurately calibrated to approximately 1.1 K given this approach [Schott et al. (1986) and Schott (2007)]. As mentioned above, to investigate the post launch thermal calibration of Landsat 5 Band 6 Schott and Volchok (1985) used this approach. The approach has also been used more recently by Barsi (2000) to calibrate the thermal band of Landsat 7. The study demonstrated an accuracy of 1.3 K, using 3-5 layers for each of the 5 profiles collected. Although proven accurate, the approach has the disadvantage of being expensive and very difficult (logistically speaking) to use in satellite calibration studies, as the data must be acquired simultaneously with satellite overpasses, which depending on various factors can become impractical Schott (2007).

2.3.3 Multiple Angle Method:

All multi-angle methods rely on the assumption that the atmospheric column is spatially uniform and exploits the differential absorption due to various slant paths when a common object is observed at various view angles [Dash et al. (2002) and Schott (2007)]. In general, the use of this method is often restricted to certain altitudes and atmospheric conditions or types, however, this approach does not require ground truth data or low-altitude flying aircraft. Schott (2007) also reports that various authors found potential errors of several degrees Kelvin, but considerable improvements can be made using better assumptions. Similar to the Profile method this approach is not applicable to this study due to the instrument under consideration.

2.3.4 Atmospheric Propagation Modeling used with Ground Truth Observations:

The most generally accepted method for processing surface radiance to a predicted observed satellite radiance is by use of RTMs, such as MODTRAN (Berk et al. (1999)). With knowledge of the lower atmosphere via radiosonde observations for example, the at-

atmospheric effects on sensor reaching radiance can be computed using MODTRAN (Schott et al. (1986)). The quality of atmospheric modeling has greatly improved over the lifetime of Landsat 5. For example, Schott et al. (1986) discussed concerns about the uncertainties and observed discrepancies existing in the then LOWTRAN model. Since then, numerous improvements have been incorporated into various RTMs, however, realize the models were developed to provide solutions regardless of accuracy. Not to mention the fact that even assuming a perfect RTM, the output is still dependent and limited to the input provided, which exposes the current lack of ability to perfectly capture the state of the atmosphere at the time of interest.

As Cracknell (1997) states, "it would be a mistake to place uncritical faith in the use of physically based RTMs, as their use relies on having a complete theoretical model which accurately describes all possible factors relating to top-of-the-atmosphere (TOA) radiance to the skin temperature at the surface."

According to Dash et al. (2002), methods relying on modeling require:

- The vertical and horizontal distribution of atmospheric temperature and water vapor to be accurately known.
- Upper-air observations are discrete in both space and time, therefore spatial and temporal interpolations are necessary to capture the state of the atmosphere over the ROI.
- RTM - to simulate atmospheric effects for a given atmosphere.
- Surface spectral emissivity must be known.

Sources for atmospheric profiles of both temperature and water vapor include radiosonde observations, numerical weather prediction models, satellite atmospheric sounder observations, and aircraft profile observations (when available). Radiosonde data provide the most accurate information regarding temperature and water vapor in the troposphere, however, if unavailable numerical weather prediction models may be the most readily accessible option to consider. The intent of obtaining atmospheric profile data is to capture the state of the atmosphere over the target (i.e. the entire atmospheric column) at the time of satellite overpass. Highlighted above, both spatial and temporal interpolations are needed to account for the desired location in reference to its proximity to upper-air data. Specific interpolations vary depending on the desired modeling effort and based on the

availability of data.

These methods rely on surface ground truth [Section 2.2], as RTMs define the atmospheric effects which modify the surface leaving radiance. Regardless of the form of ground truth provided, a surface leaving radiance need be obtained. The atmospheric profile data is used as input to MODTRAN. MODTRAN's output is used in-conjunction with the obtained surface leaving radiance and sensor band effective response file to compute the desired predicted at-sensor radiance.

2.4 Satellite Temperature Retrieval Biases

Assuming a calibrated sensor, temperature retrieval from a spacecraft is complicated by three main factors: atmospheric, angular, and emissivity effects Dash et al. (2002). Collectively, these errors can lead to a range of 1-2°C, Gupta (2003); or potentially higher to over 10°C Merchant et al. (1999). Atmospheric effects are inescapable, however, angular effects can be neglected when imaging at near nadir views, while emissivity effects can be greatly reduced if the target domain is restricted and its emissivity is well known. According to Dash et al. (2002) temperature retrieval is simplified and more precise when large homogeneous targets, in thermodynamic equilibrium are considered. Large water bodies offer such characteristics. Water has a widely known emissivity spectrum which is both high (i.e. close to 1) and spectrally flat,[Figure 2.4] when viewed from nadir Schott (2007). Harris et al. (1994) report wind speed has a significant effect on waters emissivity at view angles above approximately 50°, while negligible around normal incidence (i.e. nadir). Thus, thermal IR surface temperature retrieval is greatly simplified when focus is limited to sea surface temperature (SST) retrieval compared to that of land-surface temperature retrieval. Land surfaces are typically composed of various materials (i.e. varying emissivity ϵ) and geometries, which consequently effect the overlying atmospheric conditions making surface temperature retrieval over land an increasingly more complex process. Especially when an accurate knowledge of the surface spectral emissivity ϵ is needed for an accurate surface temperature extraction Becker (1987). Atmospheric profiles over land are subject to increased variations due to topographic changes. Aerosol source regions are more prevalent and varying over land surfaces (i.e. pollen, dust, combustion products,

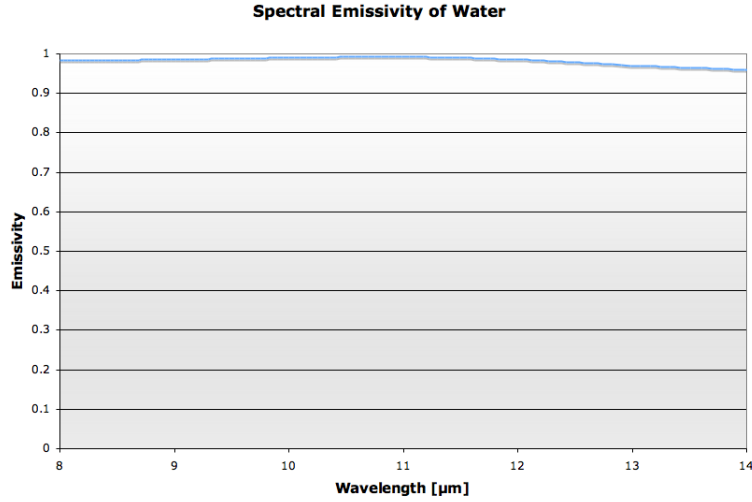


Figure 2.3: Spectral emissivity of water. Water has an emissivity that is both high and flat across the 8 to 14 μm window (average emissivity of 0.986), courtesy RIT - DIRS 2008.

etc.) than that over water bodies Wan and Dozier (1989).

Bartolucci et al. (1988) conducted an experiment investigating the atmospheric effects on TM thermal data. Standard profiles in MODTRAN were used to study a scene over Lake Michigan. A competing effect between atmospheric path radiance and atmospheric transmission was noted. Specifically, a relative inverse relationship was found between the amount of path radiance and the attenuated target radiance (due to absorption), over the nominal TM ($10.4 - 12.5\mu\text{m}$) wavelength band. Results also showed the accuracy of remotely sensed temperatures to be a function of the contrast between the target temperature and the air temperature. For example, when target temperatures are much lower than the overlaid air temperature, an overestimation of the target temperature would result, due to the compensating effect of path radiance. The authors, however, did conclude that special cases can occur where the amount of transmission loss is compensated for by path radiance, resulting in acceptable temperature errors (with no performed atmospheric correction) better than 1 K.

In a similar study Montanaro et al. (2008) also demonstrated results that illustrated the competing atmospheric effects of additive path radiance and transmission loss. The work investigated various surface water vapor conditions and its impact on remotely sensed

temperature. Three major findings were shown: 1) Temperature errors are higher for warm moist surface layers. 2) The apparent temperature error is a function of the targets temperature (i.e. higher target temperatures resulted in higher temperature errors). 3) The target temperature in comparison to the overlaid atmosphere will determine the weighting between the competing atmospheric factors. Note, these results were derived in a low altitude study (vertical extent 100 m).

In the 8-14 μ m region it is widely documented that CO_2 , O_3 and water vapor are principally responsible for the atmospheric effects on sensor reaching radiance. Water vapor predominately resides in the troposphere (nominally, 0-10 km) and has a maximum concentration near the surface and generally decreases exponentially with height in the troposphere [Houghton (1985)]. Houghton (1985) further notes that although much of the stratosphere (nominally, 10 - 50 km) is relatively dry, it still contains a radiationally important amount of water vapor. CO_2 and O_3 unlike water vapor vary slowly and have relatively known spatial characteristics throughout the atmosphere. CO_2 is a uniformly mixed gas up to at least several tens of kilometers, where O_3 is a relatively minor constituent in the troposphere, but significant in the stratosphere reaching a maximum concentration at a height of about 20-25 km, Houghton (1985) and Dash et al. (2002). Thus, thermal IR satellites are typically designed with bandpasses which avoid such influences [Figure 2.4: (a) & (b)].

Through visual inspection [Figure 2.4 (c)] it is evident that water vapor in the atmosphere is the primary deterrent to sensor reaching radiance in the LWIR, consistent with [Dash et al. (2002), Wan and Dozier (1989), Barnes and Price (1980), Merchant et al. (1999) and Donlon et al. (2002)]. Specifically, dominant absorption in the 10 to 13 μ m window is due to water vapor continuum absorption, which is an effect of the far wings of spectral lines broadened by both water-water and water-air collisions Merchant et al. (1999). Merchant et al. (1999) also report on their work concerning SST retrievals accuracies for the satellite-borne Along-Track Scanning Radiometer (ATSR), where cold biases of up to 0.4 K were associated with regions of high water vapor loading.

Studies have shown that volcanic aerosols can introduce negative bias errors in SST retrievals. The studies of Reynolds (1993), Merchant et al. (1999), Stowe et al. (1992) and Walton et al. (1998) all have noted this bias due to the fact that major volcanic

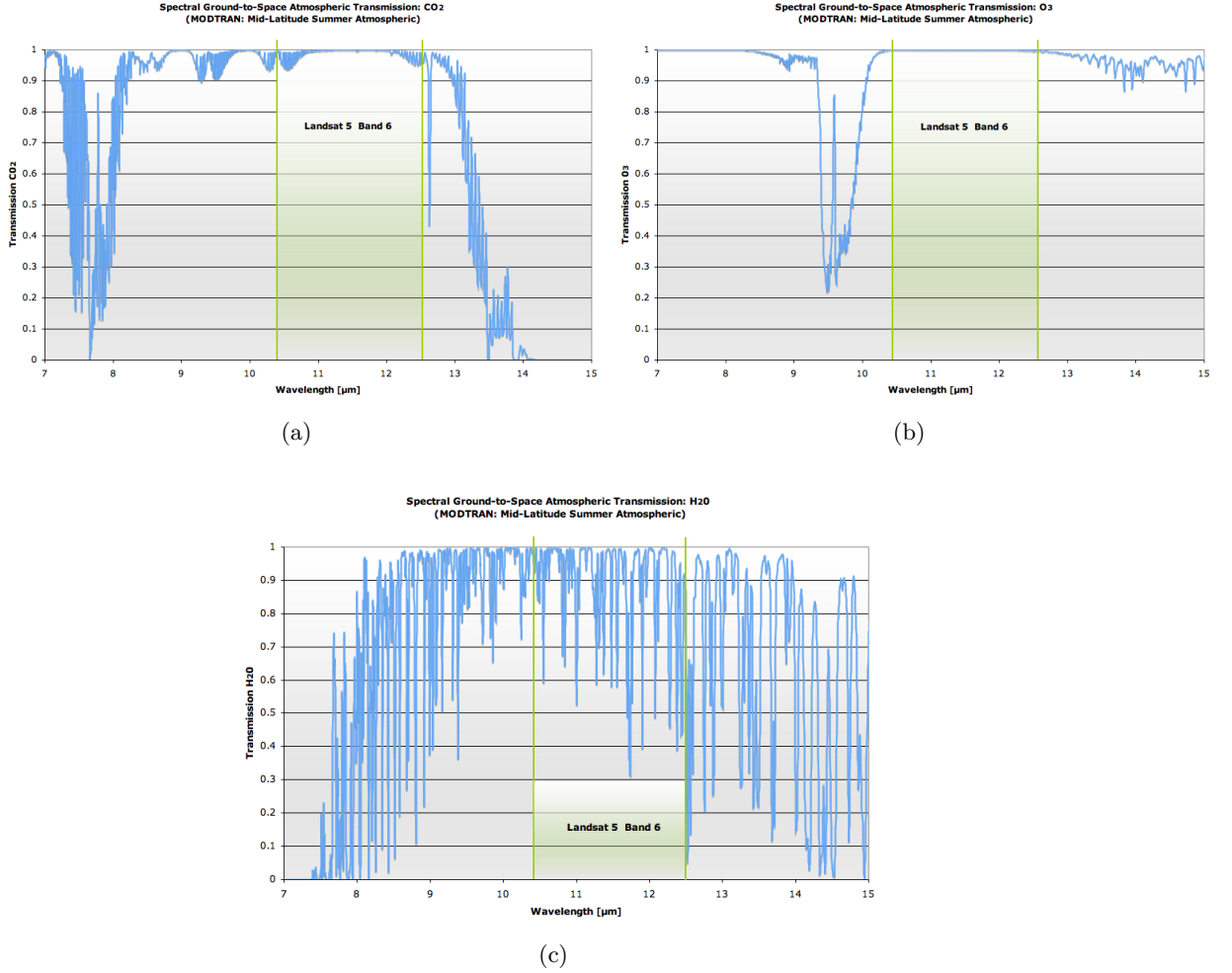


Figure 2.4: MODTRAN mid-latitude summer derived transmission: CO_2 (a), O_3 (b) and water vapor (c). Note that CO_2 and O_3 have almost negligible affects on TM Band 6 and that water vapor is almost principally responsible for atmospheric effects in the LWIR over the TM Band 6 bandpass.

eruptions introduce massive amounts of aerosols into the stratosphere, which is typically assumed to be aerosol free. The evolution of volcanic debris in the stratosphere is complex following an eruption. Merchant et al. (1999) notes after injection into the stratosphere, the volcanic matter is dispersed zonally and meridionally, chemically evolves, and undergoes sedimentation. For example, after the eruption of Mt. Pinatubo in June 1991, in the Philippines (15°S, 120°E), the volcanic plume had encircled the earth within 3 weeks between 10°S and 30°N at heights of 20 to 25 km [Merchant et al. (1999)]. Watanabe et al. (2004) mentions that studies found Pinatubo aerosols had already arrived in the

Arctic polar vortex by the winter of 1991-1992 (~ 6 months after eruption).

The following discusses the general evolution of major volcanic plumes, consistent with reports in Walton et al. (1998), Merchant et al. (1999) and Watanabe et al. (2004). Shortly after a major eruption (~ 1 month) the volcanic plume is typically characterized by fresh volcanic aerosols, which have a relatively localized distribution and consists of dust, silicate, and gas (SO_2). On the order of 1 year after an eruption, aerosols may disperse globally while larger dust and silicate particles drop out, due to gravitational sedimentation leaving: aged volcanic aerosols. The final class of volcanic aerosol is the background aerosol. This class is typically composed of 75% sulfuric acid (H_2SO_4) and may persist many years after a major eruption. Background aerosols reside globally in the lower stratosphere in what is called the stratospheric sulfate aerosol (SSA) layer. The SSA has two major sources: carbonyl sulfide (OCS) and sulfur dioxide due to volcanic injections. In reference to the Mt. Pinatubo eruption, Watanabe et al. (2004) stated that a number of studies have suggested that Pinatubo aerosols were completely removed from the stratosphere by 1996-1997, however, other studies claim residual aerosols persisted into the late 1990s.

Merchant et al. (1999) found that volcanic aerosols introduce cold biases in SST retrievals of up to ~ 1.5 K in the tropics, regarding SST retrieval from ATSR. Similarly, Reynolds (1993) found negative bias SST retrieval errors with magnitudes of greater than 1 K. Depending upon geographic location and time after eruption, the magnitude of potential errors will fluctuate; [Appendix B]. It should be emphasized that the highest errors found were in the tropics close to the time of eruption, thus, errors of reduced magnitude should be expected outside of the tropics, especially as time past eruption increases.

The previously mentioned phenomenology is representative of major volcanic eruptions (i.e. large enough to inject matter into the stratosphere, nominally 10-15 km). This does not imply that smaller eruptions will not introduce biases in temperature retrieval, only that these situations be identified on a more localized basis. The three most recent major volcanic eruptions are: Agung in 1963, El Chichon in 1982, and Pinatubo in 1991 [Merchant et al. (1999)].

In summary the most important points from this section are listed:

- The principle atmospheric absorbers in the LWIR are: CO_2 , O_3 & water vapor.
- Largest deterrent in LWIR (or most significant contributor towards retrieval error): water vapor.
- Target emissivity must be known.
- Major Volcanic eruptions can introduce temperature retrieval errors many years following an eruption.

2.5 Radiance to Temperature Conversions

Temperature is defined as the average kinetic energy of an object. Traditional methods of measuring temperature typically place the sensor in contact with the medium at which is under consideration. For remote sensing applications the introduction of an apparent temperature (also referred to as brightness temperature) is needed. Apparent temperature is the blackbody equivalent temperature observed by a radiometer.

Thermal measurements observed by spacecraft obtain an effective radiance value in radiometric units (i.e. $[W/m^{-2}sr\mu m]$), however, the desired parameter is surface temperature. Thus, the need for a conversion method from radiance to temperature is realized. For a given temperature and defined responsivity locations over a sensors finite bandwidth, the Planck Equation [Eq. 3.1] can be used to obtain a blackbody equivalent radiance. Thus, it is intuitive to think that this equation can be solved for temperature. However, it should become apparent that because the sensor provides an integrated radiance over some finite bandwidth, an easy conversion between observed sensor radiance and temperature is not as intuitive as one may suspect. Two approaches which convert radiance to apparent temperature are discussed: 1) conversion by inverting the Planck Equation [Eq. 3.1] and 2) conversion by a Look-Up-Table (LUT).

Inverting the Planck equation [Eq. 3.1] to yield an apparent temperature (T_{app}) [K] follows the form:

$$T_{app} = \frac{hc}{\lambda k} \left[\ln \left(\frac{2h^2}{L\lambda^5} + 1 \right) \right]^{-1} \quad (2.1)$$

Sospedra et al. (1986) shows how several authors simplify the conversion following the general form:

$$T_{app} = \frac{K_2}{\ln \left(\frac{K_1}{L+1} \right)} \quad (2.2)$$

where L ($mWcm^{-2}sr^{-1}\mu m^{-1}$) is the blackbody radiance for a temperature T integrated over the TM band 6. Schott and Volchok (1985) report the free parameters values of K_1 and K_2 vary among instruments, for example:

$$K_1 = 67.162 mWcm^{-2}sr^{-1}\mu m^{-1}) \quad K_2 = 1284.3K$$

for the TM onboard Landsat 4

$$K_1 = 60.776 mWcm^{-2}sr^{-1}\mu m^{-1}) \quad K_2 = 1260.56K$$

for the TM onboard Landsat 5

The overall approach has been used by numerous authors [Sospedra et al. (1986), Barnes and Price (1980), Tonooka et al. (2005), Schott and Volchok (1985) among others]. This method is preferred when computational power is limited. If high accuracy is needed inverting the Planck Equation [Eq. 3.1] may introduce errors because some information about the shape of the blackbody curve may be lost. Also, this approach is not constant among varying applications (i.e. SST retrieval and land-surface retrieval).

Sospedra et al. (1986) declare the most accurate way to convert radiance L to temperature T is by use of a LUT with L and T pairs. The LUT is generated by determining a valid range of finely spaced temperatures (i.e. spacing of 0.001 K) to each be individually evaluated by the Planck Equation [Eq. 3.1] using the responsivity locations defined for a given sensor. The result yields a radiance value at each temperature (L and T pairs). Thus, to determine the desired apparent temperature from a given radiance value, the minimum Euclidean distance is found among the radiance values and the subsequent apparent temperature is reported [Eq. 2.3].

$$T_{app} = LUT(L_{sensor}) \quad [K] \quad (2.3)$$

2.6 Bulk to Skin Water Temperature Models

Skin temperature (T_s) is a temperature measured by a radiometer which originates from the top tens of microns $\sim 50\mu m$ [Merchant et al. (1999)] of the water surface and is a function of time, wind speed, and sky condition. Typically, in situ derived water temperature measurements are of bulk temperature (T_b). Donlon et al. (2002) define bulk temperature as any temperature within the water column beneath an approximate depth of a little

over 1 mm, where turbulent heat transfer processes dominate. T_b has a time scale on the order of hours, varies with depth, and is susceptible to be significantly influenced by local solar heating.

For correlation with remotely sensed radiometric temperature, in situ buoy measurements of bulk water temperature at depth must be extrapolated to the water surface to yield a skin temperature. Accounting for such phenomenology allows for potentially higher radiometric precision in terms of the final calibration results, as Ryan et al. noted that differences between skin and buoy derived bulk temperatures can exceed 1 °C. We will first develop an understanding of the near surface water phenomenology, then investigate two approaches developed to derive the skin temperature from the bulk water temperature.

On a diurnal scale, the near surface temperatures of water bodies undergo a significant variation in temperature as a function of both depth and time Fairall et al. (1996).

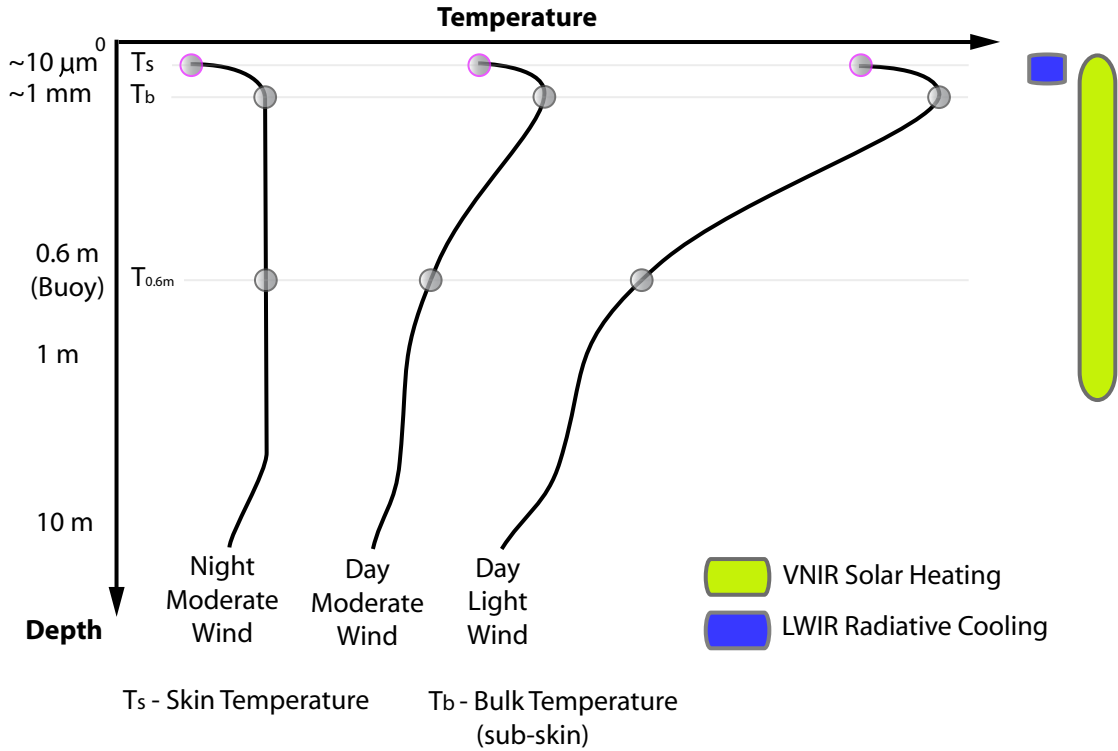


Figure 2.5: Idealized temperature profiles demonstrating the variation in temperature with depth under three prevailing wind conditions.

We will define the bulk of these variations to be within the warm layer ($\sim 1\text{mm}$ to the depth at which heating has occurred). The warm layer is a diurnal phenomena, which occurs during the day when temperature stratification caused by the absorption of solar flux is strong enough to surpass shear-induced mixing Fairall et al. (1996). At first pass [Figure 2.5], two important observations can be identified: the diurnal nature of the warm layer and the importance of the knowledge of the reference depth or (mean depth) of the T_b measurement. Typically, the shallower the sensor, the smaller the warm layer correction Fairall et al. (1996). The characteristic thermal structure during the day or night under moderate to strong winds demonstrates a tendency to homogenize the near surface layers due to turbulent mixing processes [Donlon et al. (2002); Figure 2.5]. At night the T_b to T_s relationship is often simplified under moderate wind conditions due to the absence of solar heating (induced by absorption of visible and shortwave infrared radiation) allowing the near surface waters to become thermally well-mixed and at a nominally constant temperature. However, notice that in all cases, the very near surface layer will be cooled due to a net radiation loss to a cold sky [Schott and Raqueno (2006) (cool skin effect)]. During the day the cool skin effect is likely to persist as the water surface is still significantly warmer than the sky (about 240 K) in the LWIR from a net radiation standpoint. Donlon et al. (2002) show for a large data set that the cool skin effect [$T_{b-s} = T_b - T_s$] is approximately 0.17 K for wind speeds greater than 6 m/sec; consistent with [Fairall et al. (1996), Horrocks et al. (2003), and Schluessel et al. (1990)]. Fairall et al. (1996) explain that the net cooling effect at the air-water interface can be exceeded, near Noon, under wind speeds below about 1 [m/s], due to absorption of solar flux in the top tens of microns of the water surface. This scenario may not only lead to no net cool skin, near Noon, but also a potential warm skin. With that said, situations regarding weak to absent wind speeds must be evaluated and characterized appropriately, given the application and will be avoided in this study.

Near surface thermal stratification is most apparent for the characteristic situation from late morning to early afternoon, following a period of calm or light winds (below approximately 2 m/sec) with solar insolation Donlon et al. (2002). Fairall et al. (1996) reports the region of significant warming begins near the surface and propagates downward as it intensifies with increasing solar intensity, reaching depths of measurable warming as

deep as 20 m. The authors also state that under light winds it is possible that the near surface warming can peak before noon, as warming can be quite abrupt in the morning when the atmosphere is still relatively stable (i.e. weak winds). In summary, it is apparent that wind speed plays a dominant role in shaping the near surface water column. Specifically, strong to moderate persistent winds produces a more well mixed near surface layer, in contrast to light or calm winds (during the day) which tend to create large thermal gradients resulting in a more complex system.

Remember the desired parameter in this modeling effort is skin temperature. Consistent with the results of Fairall et al. (1996) and Zeng et al. (1999), an oversimplified description of day time surface gradients can be expressed mathematically as (Figure 2.6):

$$T_s = T_z - az - d \quad [K] \quad (2.4)$$

T_s	desired skin temperature [K]
T_z	temperature at some depth shallower than Z_m [K]
Z_m	depth to which heating has occurred [m]
a	warm surface thermal gradient [K/m]
d	cool skin effect ($T_b - T_s$) [K]

Table 2.1: Oversimplified bulk to surface temperature model.

The description illustrated in [Figure 2.6] is an oversimplified treatment of the system, however, it provides a good fundamental overview of the modeling effort. Models accounting for parameters such as wind speed, time of day, and to a lesser extent other environmental parameters (i.e. sky conditions) need be investigated to yield a more appropriate representation of the near surface water column Schott and Raqueno (2006).

Within the literature there are numerous methods available to model T_s to T_b . This study investigated two T_b to T_s models of the general form of [Eq. 2.4]: 1) Zeng et al. (1999) use an empirically derived approach that attempts to capture T_s from near-surface wind speed and the diurnal variation of T_b , 2) a simplified treatment derived from Fairall et al. (1996). This approach modeled the thermal response to surface heating generating tabulated results for peak increase in temperature and depth as a function of wind speed and clear sky conditions. The second modeling effort Fairall et al. (1996) has been proposed to examine the validity of the preferred Zeng et al. (1999) approach.

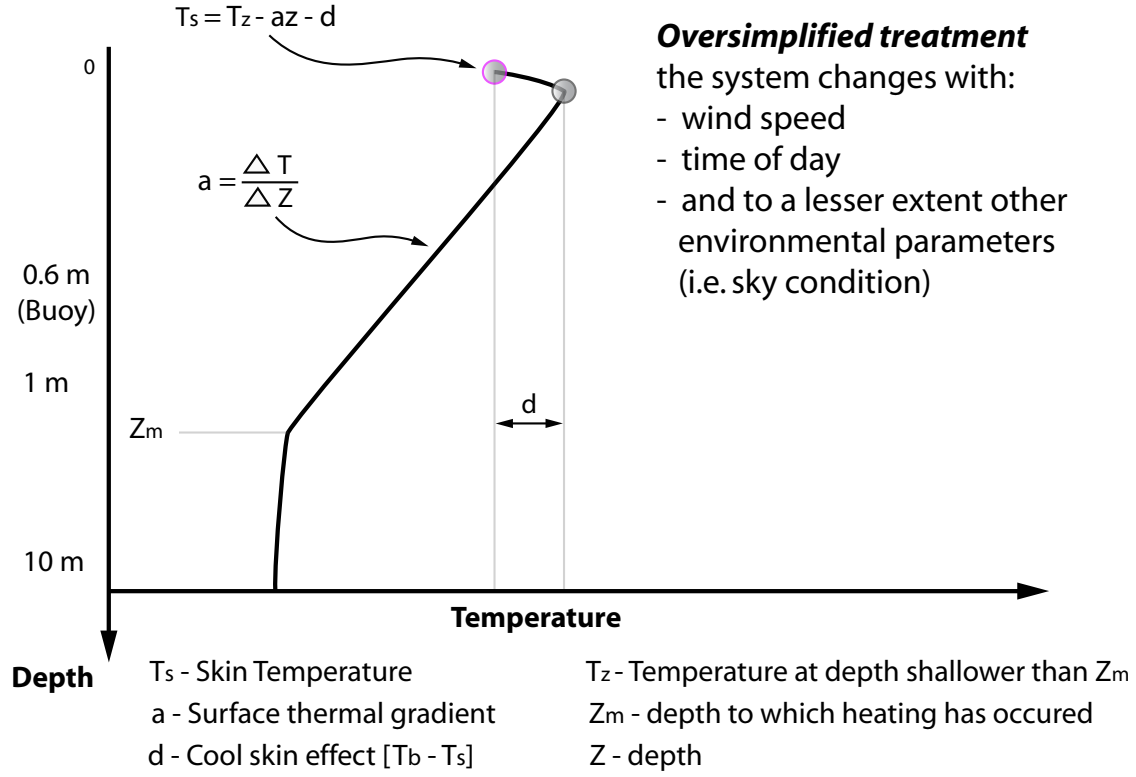


Figure 2.6: Oversimplified bulk to skin temperature model.

Zeng et al. (1999) report that previous modeling studies have shown that surface layer mixing, net surface heat flux and wind speed determine the temporal variation of skin temperature, and largely the temporal variation of bulk temperature. The derived model uses 24 hour bulk temperature and wind speed observations in an effort to capture the diurnal variation of T_b to compute the desired skin temperature. The following development of this model follows the discussion presented in Schott and Raqueno (2006). The Zeng et al. (1999) model is essentially a 24 hour expected value version of Eq. 2.4:

$$\langle T_0 \rangle = \langle T_z \rangle - az - d \quad (2.5)$$

where $\langle T_0 \rangle$ is the 24 hour average skin temperature [K], $\langle T_z \rangle$ is the 24 hour average temperature at depth (z [m]) [K], d is the surface cool skin effect for winds greater than 4.5 m/sec [K], where the authors propose a value of $d = 0.2K$. The thermal gradient (a)

is expressed as:

$$a = 0.05 - \frac{0.6}{u_m} + 0.03 \ln(u_m) \quad (2.6)$$

where u_m is the average 24 hour wind speed at 10 m [m/s]. Wind speeds observed at heights different from 10 m, can be converted to a 10 m wind speed by solving the following two equations iteratively:

$$z_o = \frac{0.011 u^2}{9.8} + \frac{1.65 \times 10^{-6}}{u} \quad (2.7)$$

and

$$u = \frac{0.4 u}{\ln\left(\frac{z}{z_o}\right)} \quad (2.8)$$

where Eq. 2.7 yields the roughness length for momentum and Eq. 2.8 provides the wind stress under neutral conditions Zeng et al. (1999). Schott and Raqueno (2006) notes that simplified methods for the correction of wind speed altitude exist. For example, the Iowa Energy Center Wind Energy Manual (<http://www.energy.iastate.edu/renewable/wind>) make use of the following equation:

$$U_2 = U_1 \times \left(\frac{H_2}{H_1}\right)^n \quad (2.9)$$

where U_2 [m/sec] is the wind speed at height H_2 [m], given a wind speed U_1 at height H_1 . The variable n is a function of the upwind terrain ($n = 0.1$ for a long ocean fetch & $n = 0.2$ for crops and low woods) Schott and Raqueno (2006).

Using Eq. 2.10, Zeng et al. (1999) solve empirically for the magnitude of the diurnal surface variation at a time t .

$$f(t - cz) = \frac{T(z, t) - \langle T_z \rangle}{e^{-bz}} \quad (2.10)$$

where f is the variation of temperature around $\langle T_o \rangle$, cz is a phase term, e^{-bz} is the diurnal amplitude, $T(z, t)$ is the temperature at depth z and time t . Note that $f(t)$ is solved for by interpolation from the values of $f(t - cz)$ at the hour t of interest. Zeng et al. (1999)

empirically derive the phase constant (c) in [hr/m] as:

$$c = 1.32 - 0.64 \ln(u_m) \quad (2.11)$$

and the damping constant (b) with depth in [m] as:

$$b = 0.35 + 0.018 e^{0.4 u_m} \quad (2.12)$$

This process can be shown graphically [Figure 2.7] which aids to a better understanding of the process.

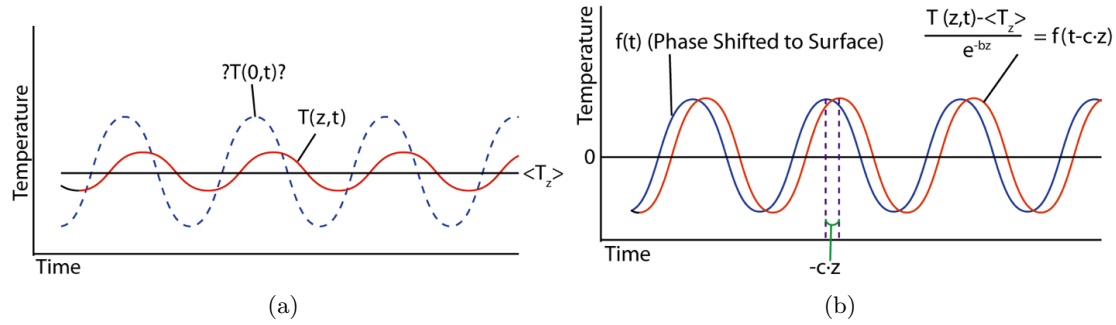


Figure 2.7: Schematic illustration of the diurnal variation of T_b and T_s : (a) diurnal amplitude: T_b (known, red), T_s (unknown, blue), (b) amplitude corrected and phase shifted bulk variation to predict T_s , adopted from Schott and Raqueno (2006).

The desired skin temperature can be solved, at a given time t , using $\langle T_0 \rangle$ and $f(t)$ solved for above, with the following expression:

$$T_s = T(0, t) = \langle T_0 \rangle + f(t) \quad (2.13)$$

The coefficients a , b , c and d were empirically derived using observational data from the R/V Franklin during the Tropical Ocean-Global Atmosphere (TOGA) Coupled Ocean-Atmosphere Response Experiment (COARE). The experiment captured bulk and skin temperatures from a maritime vessel utilizing infrared radiometers to capture T_s and submerged thermistors (at a depth of 2.4 m) to capture T_b . The coefficients a , b and c are all a function of wind speed, since all were empirically fit with wind speed, to yield Eq.'s (2.6, 2.12 2.11) for a large data set, respectively. The physical meaning of these terms

as implied in Eq. 2.10 & 2.5 is consistent with the previously developed understanding that a stronger wind, increases surface mixing, deepening the surface warm layer, and thus homogenizing the layer. Note that this situation also is consistent with a more rapid decrease of diurnal temperature amplitude with depth, in addition to a reduced temperature phase lag with depth Zeng et al. (1999).

The coefficients were derived under clear sky conditions and are valid but not limited to the wind speed range of 1.5 - 7.6 m/s provided the following restrictions are met: $-1.1 < az < 0$, $1 < e^{bz} < 6$ and $0 < cz < 4$. Realize, that under light to absent wind conditions, as previously mentioned, the system tends to become more complex. Specifically, the derived values of cool skin effect (d) may potentially become in question. Realize for the general case, the rigorously derived value of $d = 0.17$ K by Donlon et al. (2002) may be more appropriate.

The procedure above can be summarized to a four step process, where Zeng et al. (1999) explain that skin temperature can be obtained from bulk temperature at depth z by: 1) obtaining $\langle T_0 \rangle$ from Eq. 2.5, 2) obtaining $f(t - cz)$ from Eq. 2.10, 3) linearly interpolating $f(t - cz)$ to $f(t)$ at each hour, and 4) computing the skin temperature from Eq. 2.13.

In contrast to other methods this approach is appealing because knowledge of the surface flux is not exclusively required; as it is implied through the temporal variation of the bulk temperature. From a theoretical standpoint, skin temperature is determined by bulk temperature at a given depth, near surface wind speed, and net surface heat flux Price et al. (1998). With that said, this model appears physically adequate to use outside of the tropical Pacific region (i.e. mid-latitudes). Although, Zeng et al. (1999) note the method has limitations: bulk temperatures should be measured from nearly a fixed location within the upper 2.5 m of the water surface; requires 24 hour observations of both bulk temperature and wind speed; and model derived skin temperatures only show effects of heat fluxes, wind and precipitation that significantly affect the bulk temperature at depth. From this explanation, it is clear that moored buoy derived observations, measuring bulk temperature typically around a depth of 1 m and wind speed at or within 10 m, are well suited for such an approach.

The second proposed approach is now considered. Following a simplified treatment

derived from the results of Fairall et al. (1996), Schott and Raqueno (2006) proposed a simplified approach to convert T_b to T_s using the methodology developed in Eq. 2.4 [Figure 2.6]. The Fairall et al. (1996) approach modeled the thermal response to surface heating generating tabulated results for peak increase in temperature and depth as a function of wind speed and clear sky conditions. Applying the simplified thermal profile [Eq. 2.4; Figure 2.6], Schott and Raqueno (2006) were able to generate warm layer ΔT , values corresponding to

$$\Delta T_{b-zm} = T_b - T_{zm} \quad (2.14)$$

derived from data in Fairall et al. (1996), shown in Table 2.6. Recall T_{zm} is the depth to which heating has occurred.

U [m/s]	D_T [m]	ΔT_w [K]
1	0.7	3.8
2	2.1	1.6
3	4.2	0.9
4	6.0	0.6
5	10.0	0.4
6	14.0	0.25
7	19.0	0.15

Table 2.2: Variables from Fairall et al. (1996) Table 3: U denotes wind speed, D_T denotes depth of the warm layer and ΔT_w denotes model-computed solar heating peak (using Fairall et al. (1996) Eq. (25)).

U [m/s]*	ΔT_{b-1m} [K]	ΔT_{b-2m} [K]	ΔT_{s-b} [K]	ΔT_{s-1m} [K]	ΔT_{s-2m} [K]
1	3.8	3.8	-0.17	3.63	3.63
2	0.76	1.52	-0.17	0.59	1.35
3	0.21	0.43	-0.17	0.04	0.26
4	0.10	0.20	-0.17	-0.07	0.03
5	0.04	0.08	-0.17	-0.13	-0.09
6	0.02	0.04	-0.17	-0.15	-0.13
7	0.01	0.02	-0.17	-0.16	-0.15

* 10 m wind speed

Table 2.3: Warm layer ΔT vs. wind speed for one meter and two meter layers, as well as, the correction for cool skin effect. ΔT_{b-z} derived from Schott and Raqueno (2006).

The results illustrated in Table 2.3 provide a means of converting a bulk temperature at depth to a skin temperature. The first two columns represent the warm layer values (i.e. implicit thermal gradient (a) [Eq. 2.4]) at depth. The third column is the cool skin effect using the value developed by Donlon et al. (2002). Combining the warm layer values with the cool skin effect yields a first order correction for the subsurface measurements taken at depth, near Noon Local Standard Time (LST). Note the results (columns 5 & 6) vary only with measurement depth and wind speed, and should be added to kinetic measurements at depth to yield the desired skin temperature Schott and Raqueno (2006). Investigation of these results make physical sense, for example the correction for a sensor a 1 m depth is 3.63 K for a wind speed at 2 m/s, where a smaller correction of -0.15 is needed at a wind speed of 6 m/s.

This section introduced to methods for predicting a skin temperature provided a bulk water temperature at depth (i.e. buoy derived water temperature). The two models will be tested and analyzed to determine the most appropriate model for this study. Our last topic of discussion offers methodology to account for errors in a given process, such as revealing the error involved in the above mentioned T_b to T_s models.

2.7 Error Propagation

The discussion of the Beers method of error propagation analysis presented here will follow that described in Schott (2007); Section 4.6.2. As Schott (2007) declares the root sum square error value is often used to describe how closely any individual measurement comes to truth, expressed as:

$$S_m = (S_p^2 + S_i^2)^{\frac{1}{2}} \quad (2.15)$$

where S_p is the precision of the measurement, S_i is the accuracy of the instrument or approach and S_m is the total error (i.e. error associated with the individual measurement). Simply stated, precision denotes the repeatability of a measurement, where accuracy denotes how closely an instrument or procedure can match some standardized value (i.e. truth).

In general, the total error regarding a measurement approach are the consequence of errors with the procedure or values that go into that measurement. For situations

where a parameter of interest can be characterized by a governing equation, a relatively simple expression can be contrived to explain the relationship between errors. Consider the general expression of a dependent variable Y in terms of one or more independent variables X_i .

$$Y = f(X_1, X_2, \dots, X_N) \quad (2.16)$$

Using the Beers method of error propagation, the errors in $Y(S_Y)$ can be expressed as:

$$S_Y = \left[\left(\frac{\partial Y}{\partial X_1} S_{X_1} \right)^2 + \left(\frac{\partial Y}{\partial X_2} S_{X_2} \right)^2 + \dots + \left(\frac{\partial Y}{\partial X_N} S_{X_N} \right)^2 + \sum 2 \rho_{ij} \frac{\partial Y}{\partial X_i} \frac{\partial Y}{\partial X_j} S_{X_i} S_{X_j} \right]^{\frac{1}{2}} \quad (2.17)$$

where S_{X_i} is the error in the individual input variables and ρ_{ij} is the standard correlation coefficient between variables X_i and X_j and the sum is over all combinations of correlated variables. The partials of the dependent variable Y with respect to the input variables characterizes the sensitivity of Y against small changes in X . The error in $Y_{S_{Y_i}}$ associated with an error in X_i is found by multiplying the partial derivative by the error on the input variable X_i . Due to the fact that independent errors tend to add in quadrature, the total error can be found by the square root of the sum of squared values. The merit in such an approach allows one to assess the overall error by inspecting the individual error terms S_{Y_i} , revealing which parameters have the greatest contribution to error. Thus, a successful error propagation or sensitivity analysis will yield the most appropriate focus regarding efforts to reduce and quantify errors.

2.8 Summary

In this chapter the requirements for the determination of ideal calibration sites and thermal targets was addressed. In addition, methods of collecting ground truth and issues relating to ground truth were discussed. This includes the methodology to allow for the use of buoy derived bulk water temperatures to be used as ground truth to achieve a high level radiometric accuracy. Provided the above, various approaches towards atmospheric correction were discussed, as well as, the most probable sources of error in temperature retrieval methods [i.e. water vapor, O_3 , CO_2 and volcanic contamination]. The last topic within this section developed the methodology to quantify the total error within a given

process, as well as the unique ability to discern the most contributing factors to error within a given process. The next chapter provides the fundamental and/or physical ground work need to encompass the above mentioned methodology.

Chapter 3

Theory

This chapter provides an overview of the fundamental phenomenology needed for this study. We will restrict our focus to the 8 to 14 micron spectral region sampled by Landsat's thermal band.

3.1 Landsat Program Overview

The Landsat program is NASA's longest operating earth imaging program Barsi (2000). Initiated in 1967, NASA with cooperation of the U.S. Department of the Interior, developed a program planned for a sequence of six satellites originally named the Earth Resources Technology Satellites (ERTS). ERTS-1 (renamed later to Landsat 1) launched by a Thor-Delta rocket on July 23, 1972 was the first unmanned satellite designed specifically to capture earth resources on a systematic, repetitive, medium resolution, and multispectral basis. This program was also unique because the data collected was in accordance with an "open skies" principle, meaning that anyone in the world was granted access to the data collected. The ERTS program, on January 22, 1975, was officially changed by NASA to the "Landsat" program to differentiate it from the planned oceanographic Seasat satellite program. As of 2008, there have been six successful Landsat satellites launched, Landsat 1-5 and Landsat 7 (Landsat 6 failed to reach orbit) [Appendix A]. Five different sensors have been used in the Landsat program: the Return Beam Vidicon (RBV), the Multispectral Scanner (MSS), the Thematic Mapper (TM), the Enhanced Thematic Mapper (ETM), and the Enhanced Thematic Mapper Plus (ETM+). An interesting point to

note [Appendix A] is that Landsat 4, 5 and 7 orbits were lowered from 900 to 705 km so that the spacecrafts could potentially be retrievable by the space shuttle, as well as, to aid in the improvement of the ground resolution of the onboard sensors Lillesand et al. (2004).

The Landsat data set is unprecedented in regards to the available temporal and spatial coverage, in addition to the available spatial resolution, as it provides over three decades worth of global multispectral imagery [Figure 3.1]. Researchers using this data set can now investigate global temporal data cubes and search for clues linking global climate change, domestic growth, water resource management, etc. It becomes obvious that the study of such data is crucial in the understanding of our earth, thus the need for an accurate calibration of such data is pivotal. As Schott (2007) proclaims, "... Landsat data represents the backbone for a large number of Earth remote sensing studies, particularly where temporal issues or high spatial detail over large areas are required."

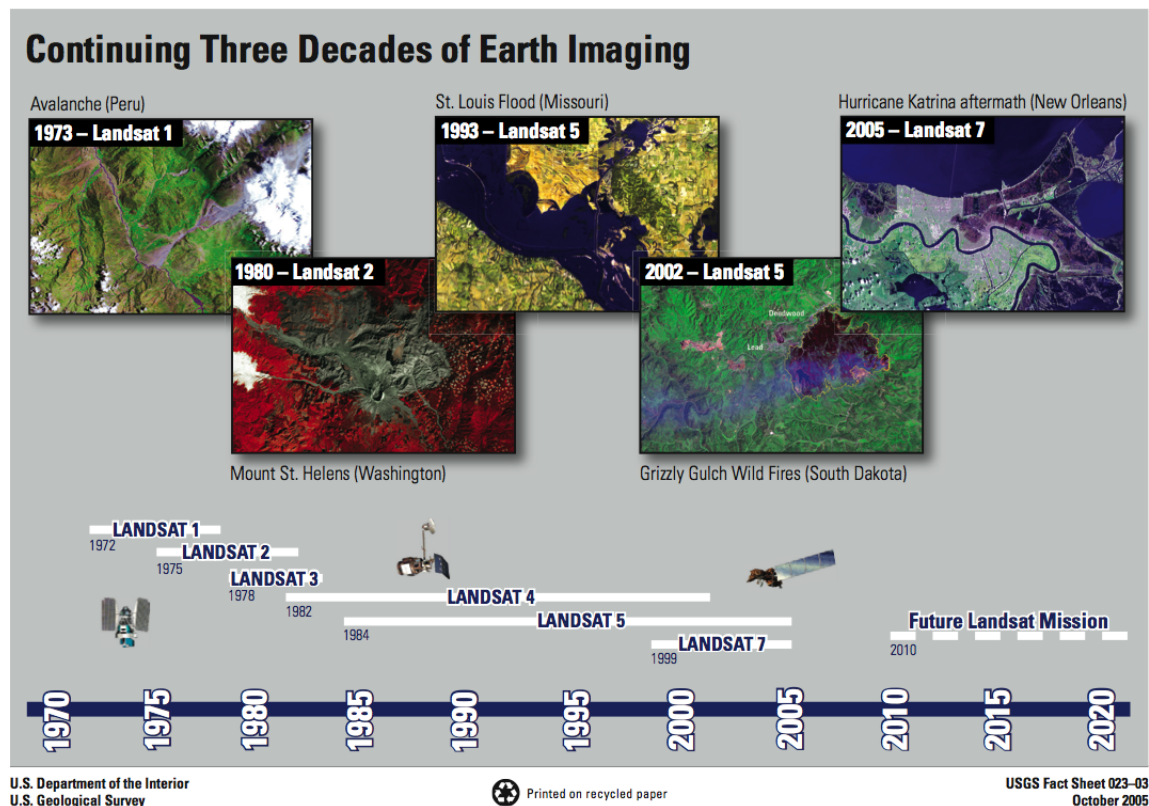


Figure 3.1: Landsat program overview, courtesy USGS.

3.1.1 Landsat 5

Landsat 5 was launched by NASA on March 1, 1984 aboard a Delta 3920 launch vehicle from Vandenberg Air Force Base, CA. The spacecraft has an approximate weight of 4,800 lbs carrying the Multispectral Scanner (MSS) and the Thematic Mapper (TM) instrument [Table 3.1]. The spacecraft has been in orbit over 24 years, well surpassing its life expectancy of only 3 years. The satellites orbit offers an image acquisition time at approximately the same LST, for a given point on the earth, every 16 days [Table 3.2]. Landsat 5 uses the Worldwide Reference System-2 (WRS-2) to catalog each image location. The WRS-2 has been designed so that each orbit within a cycle is designated a path, along the paths, rows can be designated by the nominal sensor frame centers. Therefore, any scene can be uniquely defined by its path, row and date Lillesand et al. (2004).

Landsat 5 was operated by the U.S. Government for the first 18 months of operation. Due to a commercialization effort in late 1985, satellite operations were turned-over to a private company (Earth Observation Satellite Company (EOSAT), now Space Imaging). The satellite along with its entire data archive was returned to the control of the U.S. Government, specifically the U.S. Geological Survey (USGS) Center for Earth Resources Observation and Science (EROS), in July 2001 Barsi et al. (2007).

Table 3.1: Multispectral Scanner (MSS) & Thematic Mapper (TM), USGS.

MSS	Bandwidth [μm]	TM	Bandwidth [μm]	Resolution
—	—	Band 1	Visible (0.45 - 0.52)	30m
—	—	Band 2	Visible (0.52 - 0.60)	30m
—	—	Band 3	Visible (0.63 - 0.69)	30m
Band 4	Visible green (0.5 - 0.6)	Band 4	NIR (0.76 - 0.90)	30m
Band 5	Visible red (0.6 - 0.7)	Band 5	NIR (1.55 - 1.75)	30m
Band 6	Near Infrared (NIR) (0.7 - 0.8)	Band 6	Thermal (10.40 - 12.50)	120m
Band 7	NIR (0.8 - 1.1)	Band 7	Mid IR (2.08 - 2.35)	30m

MSS - Ground Sampling Interval (pixel size): 57 x 79 m

Landsat 5 uses X-band and S-band antennas to transmit directly to ground receiving stations. If ground stations are not available, the satellite's high gain antenna can be used to transmit data to the Tracking and Data Relay Satellite System (TDRSS), although it has an onboard recorder. The TM has a data transfer rate of 85 Mbps and an 8 bit quantization (providing 256 levels) Lillesand et al. (2004).

Table 3.2: Landsat 5 orbital characteristics, USGS.

Orbit	Circular, sun-synchronous, near-polar
Time/Orbit	approximately 99 min
Altitude	705 km (438 mi)
Inclination Angle	98.2°
Repeat Cycle	16 days
Swath Width	185 km (115 mi)
Equatorial Crossing	9:45 a.m. \pm 15 minutes
Cataloged	WRS-2 path/row system

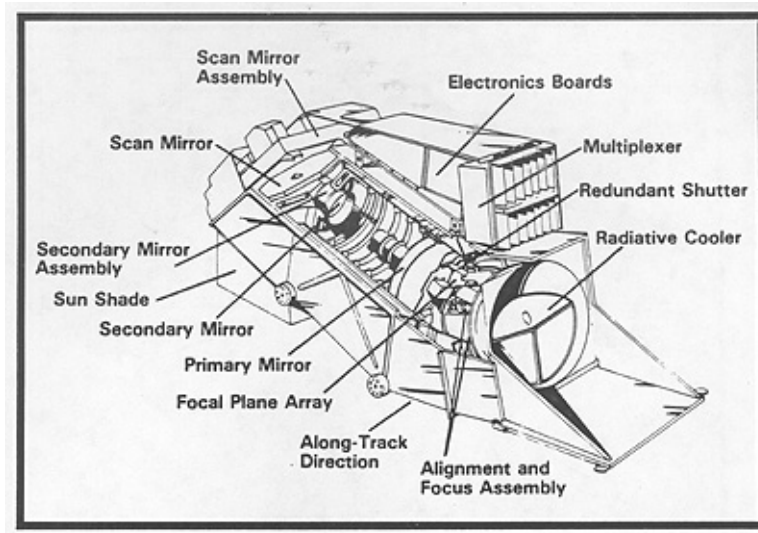


Figure 3.2: Cutaway of the TM illustrating its major components (Image courtesy NASA).

Our focus is devoted to the TM instrument [Figure 3.2 & Figure 3.3]. The TM employs an oscillating mirror that scans in both directions and relies on a scan line corrector to ensure complete ground coverage [Figure 3.3]. The system design is referred to as a whisk-broom sensor. Detectors are located on the focal plane using a staggered array. By use of relay optics a portion of the image is focused onto the cooled focal plane of the short-wave infrared (SWIR) InSb and long-wave infrared (LWIR) HgCdTe detectors Schott (2007).

On-board calibration of the thermal band is achieved by waving a calibration wand across the focal plane each scan [Figure 3.3]. It provides the necessary means to convert digital counts to radiance (i.e. calibrates the HgCdTe detectors), however, realize that such a measure is not sufficient regarding the instrument's calibration overtime, as the wand lies behind the primary optics. To rely on the calibration wand in regards to the

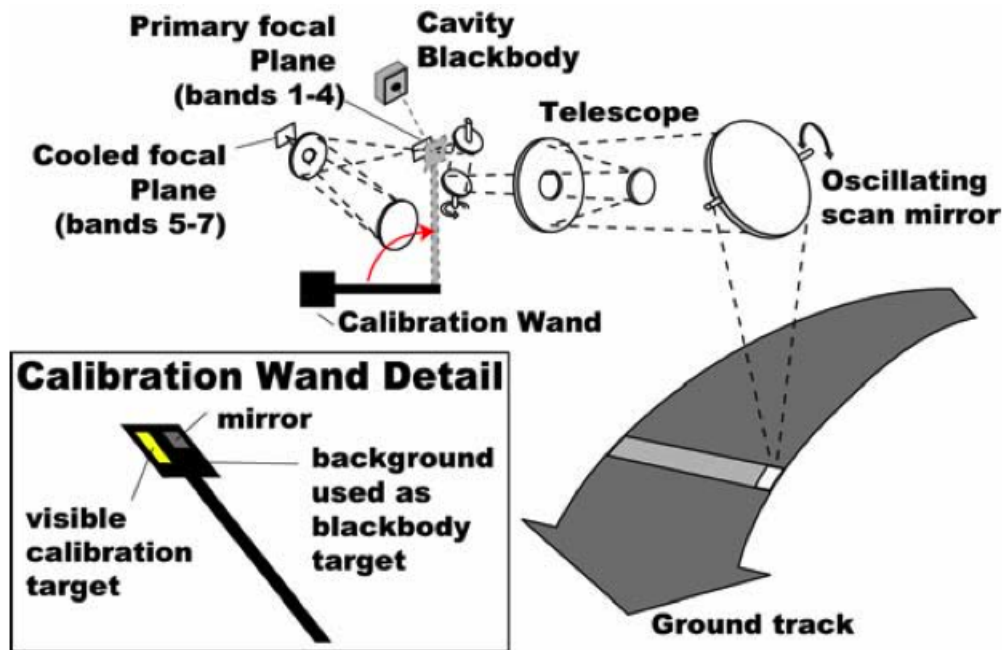


Figure 3.3: Landsat TM optical path. REPORT A.

instruments calibration as a whole, accurate knowledge of the fore-optics must be known. Therefore, the overall calibration of the system must be investigated through vicarious calibration efforts to determine if any trends in the instrument behavior can be realized overtime.

Band 6 of Landsat 5 is located in the LWIR and has a spectral bandwidth of 10.4 to 12.5 μm . A spatial resolution of 120 m (four times that of the others bands on the TM (Table 3.1) was required to achieve adequate signal to noise Schott (2007). The spectral responsivity of the TM Band 6 is shown in Figure 3.5. Gupta (2003) states that Band 6 is nominally sensitive to temperatures from sub-zero to 68 °C. Note for typical thermal phenomena on the earths surface a normal temperature range is 3-50°C.

3.1.2 Landsat 7

Introduction of the Landsat 7 satellite is necessary for this study because it will be used to validate the proposed methodology and allow for the confidence to propagate back in time; more detail on this methodology is presented in Section 4.10. Landsat 7 has a known and trusted calibration record, as it has been monitored closely since launch by both JPL and RIT [Barsi et al. (2003)].

Landsat 7 was launched on April 15, 1999 from Vandenberg Air Force Base aboard a Delta II launch vehicle. Like its predecessor, Landsat 7 flies at a nominal height of 705 km in a sun synchronous LEO with a 16-day repeat cycle. At launch the satellite weighted approximately 4,800 lbs equal to that of Landsat 5, although Landsat 7 carries only a single nadir-pointing instrument, the Enhanced Thematic Mapper (ETM+). With the exception of an additional panchromatic band, the ETM+ relies on the same optical design as the TM, however, the ETM+ provides both low and high gain thermal resolution of 60 m; a (2x) improvement in thermal spatial resolution [Table 3.3], USGS.

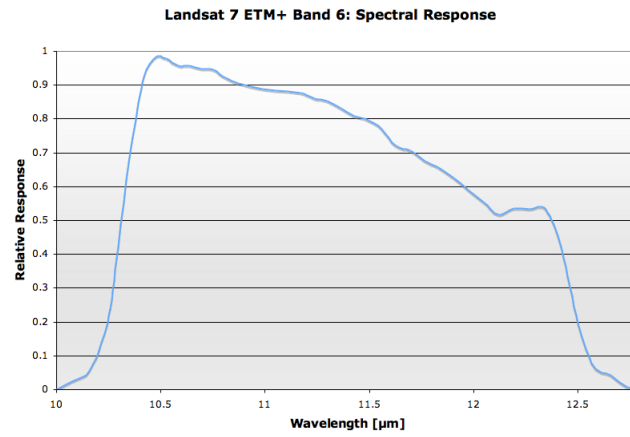
Table 3.3: ETM+ Band Specs, USGS.

ETM+	Bandwidth [μm]	Resolution
Band 1	Visible (0.45 - 0.52)	30m
Band 2	Visible (0.52 - 0.60)	30m
Band 3	Visible (0.63 - 0.69)	30m
Band 4	Near Infrared (NIR)(0.77 - 0.90)	30m
Band 5	NIR (1.55 - 1.75)	30m
Band 6	Thermal (10.40 - 12.50)	60m
Band 7	SW (2.08 - 2.35)	30m
Band 8	Panchromatic (0.52 - 0.90)	15m

In summary the Landsat 7 satellite's known and trusted thermal calibration record will be used to leverage confidence in the proposed methodology via a comparison study. Meaning if the proposed methodology provides statistically significant results against the previous calibration efforts of RIT and JPL for Landsat 7 thermal data, the proposed method can be applied confidently throughout the history of Landsat 5.

NE Δ T	
[K at 280 K]	H 0.22; L 0.28
Radiometric Scalling	
Range [$\frac{W}{m^2 sr \mu m}$]	L 0.00-17.04
Useful Temperature	
Range [K]	H 240-320 L 130-350

(a)



(b)

Figure 3.6: (a) ETM+ thermal specifications (b) Landsat 7 Enhanced Thematic Mapper plus spectral response, band 6.

3.2 Radiation Propagation

3.2.1 Thermal Energy Paths

Any matter which is above absolute zero will radiate energy, known as self-emission. How much energy an object radiates is a function of two parameters: its surface temperature and emissivity; which vary spatially and temporally Gupta (2003). Remote sensing missions operating in the thermal IR must consider the self emissive contributions from sources not only from the desired target, but from the atmosphere and surrounding objects as well. Figure 3.7 illustrates all thermal energy paths of interest. In the thermal

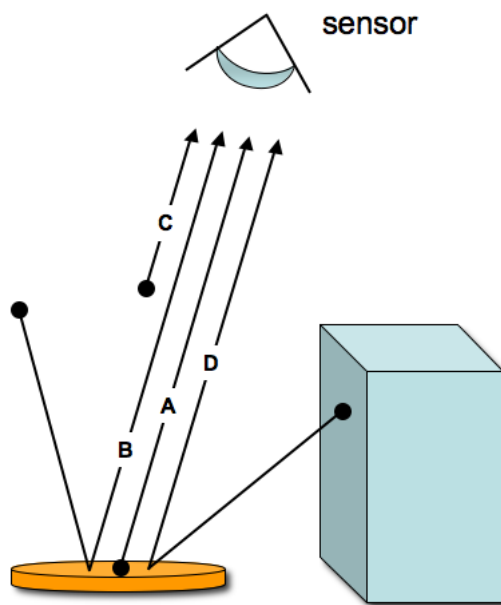


Figure 3.7: Self-emitted thermal energy paths, adopted from Schott (2007).

IR photons originating from the target to the sensor (path A in Figure 3.7) are of highest importance as they are the only path carrying information about the targets temperature. Again, the atmosphere has some non-zero temperature above the target. Some of that energy is radiated upward towards the sensor as well as downward towards the earths surface. Energy emitted and scattered down onto the target, considered over the entire sky dome, reflecting off of the target towards the sensor (path B in Figure 3.7) is collectively referred to as downwelled radiance. Path C photons [Figure 3.7], referred to as upwelled radiance, are caused by line-of-sight path emission and scatter of self-emitted photons directly to the

sensor, independent of the surface. The last energy path to be considered is that of path D [Figure 3.7]. These photons originate off background objects obstructing the sky above the target, radiate energy based on its own temperature, reflect off of the target and are propagated up to the sensor. It is important to point out that path D photons [Figure 3.7] are negligible for most natural surfaces without large background objects Schott (2007).

3.2.2 Blackbody Radiance & the Planckian Equation

A blackbody is a hypothetical body in-which all incident radiation is completely absorbed (absorptivity $\alpha = 1$) and then completely reradiated; having the unique property of zero reflectivity. In reference to Wallace and Hobbs (1977), the amount of emitted radiation from a blackbody is uniquely determined by its temperature, as expressed by Planck's law:

$$L_{BB}(T, \lambda) = \frac{2hc^2}{\lambda^5 [e^{hc/\lambda kT} - 1]} \left[\frac{W}{m^2 sr \mu m} \right] \quad (3.1)$$

where T is the temperature [K], k is the Boltzmann gas constant ($k = 1.3806503 \cdot 10^{-23} JK^{-1}$), h is Planck's constant ($h = 6.6260755 \cdot 10^{-34} Js$) and c is the speed of light ($c = 299792458.0 m/s$). Realize that Eq. 3.1 is both a function of temperature and wavelength, as well as, isotropic, that is to say, the radiance is independent of direction Wallace and Hobbs (1977).

As stated previously, only photons emitted from the target itself carry information regarding the temperature of the target [Figure 3.8, path A]. In reality, blackbody radiation can only be approximated by imperfect absorbers, thus the introduction of emissivity is needed. Emissivity ($\epsilon(\lambda)$) is a unit-less value with a range from 0 to 1, and is defined as the ratio of spectral radiance $L_\lambda(T)$ from an object at temperature T to the radiance from a blackbody at the same temperature $L_{\lambda BB}(T, \lambda)$:

$$\epsilon(T) = \frac{L_\lambda(T)}{L_{\lambda BB}(T)} \quad (3.2)$$

Emissivity is a measure of how well an object radiates energy compared to a perfect blackbody radiator and depends on two main factors: composition and surface geometry Gupta (2003). Objects whose emissivity is approximately constant with wavelength are referred to as gray bodies, where objects whose emissivities vary with wavelength are

referred to as selective radiators, Schott (2007).

3.2.3 Kirchoff's law

This discussion will begin with a brief development of transmission τ_λ , reflectivity r_λ , and absorptivity α_λ and was developed from Schott (2007). Transmission is defined as the ability of the material to allow flux to propagate through it. Mathematically, it can be expressed as the unitless ratio of the exitance from the back of a sample (M_τ) to the irradiance on the front of the sample (E_i):

$$\tau_\lambda = \frac{M_\tau}{E_i} \quad (3.3)$$

The reflectivity of a material is its ability to turn incident flux back into the hemisphere above the material. Reflectivity is a unitless parameter, expressed as:

$$r_\lambda = \frac{M_r}{E_i} \quad (3.4)$$

where M_r is the exitance from the front of a sample. Lastly, absorptivity of a material is its ability to remove energy from the system by converting incident flux to an alternate form of energy (i.e. thermal energy). Absorptivity can be expressed mathematically as:

$$\alpha_\lambda = \frac{M_\alpha}{E_i} \quad (3.5)$$

where M_α is the exitance of the alternate energy; absorptivity is unitless.

From the theory of conservation of energy, which states all incident energy must be transmitted, reflected, or absorbed the following expression is developed:

$$\tau_\lambda + r_\lambda + a_\lambda = 1 \quad (3.6)$$

According to Wallace and Hobbs (1977), Kirchoff's law states, in qualitative terms, that materials which are strong absorbers at a given wavelength will also be strong emitters at that wavelength; likewise, weak absorbers are weak emitters, through the relationship:

$$a_\lambda = \epsilon_\lambda \quad (3.7)$$

The authors also state that this condition is satisfied within the earth's atmosphere to approximately 60 km, above which the atmosphere is not sufficiently dense, for the condition to hold true. Lets now consider opaque materials, where $\tau = 0$, reducing Eq. 3.6 to:

$$r_\lambda + a_\lambda = 1 \quad (3.8)$$

Using Kirchoff's law, Eq. 3.7, emissivity (ϵ_λ) can be substituted into Eq. 3.9 and rearranged to form the relationship:

$$r_\lambda = 1 - \epsilon_\lambda \quad (3.9)$$

3.3 Governing Radiometry

Schott (2007) discussed radiance propagating to a sensor due to the targets temperature will be a function of the Planck Equation, Eq. 3.1, and the spectral emissivity of the target. As well as an attenuation due to transmission; biased by upwelled radiance along the target sensor path; and further biased by the downwelled and background radiance due to the sky-dome and relevant background objects. By combining the above mentioned phenomenology, the governing equation for sensor reaching radiance in the thermal IR is expressed mathematically as:

$$L_\lambda = (\epsilon L_{BB} + F(1 - \epsilon)L_d + (1 - F)(1 - \epsilon)L_b)\tau + L_u \quad (3.10)$$

Table 3.4: Eq. 3.10 description; all variables, except F , have a spectral dependence

ϵ	target emissivity
L_{BB}	blackbody radiance at temperature $T[W/m^{-2}sr\mu m]$
$1 - \epsilon$	reflectivity of the target as developed in Section 3.2.3
τ	atmospheric transmission from the sensor to the target
F	fraction of the hemisphere seen by the target
L_d	downwelled self emitted radiance from the sky onto the target $[W/m^{-2}sr\mu m]$
L_b	self emitted background radiance incident on target $[W/m^{-2}sr\mu m]$
L_u	self emitted upwelled radiance $[W/m^{-2}sr\mu m]$

In terms of vicarious satellite calibration efforts radiance reaching an orbiting satellite system operating in the thermal IR is shown in Figure 3.8.

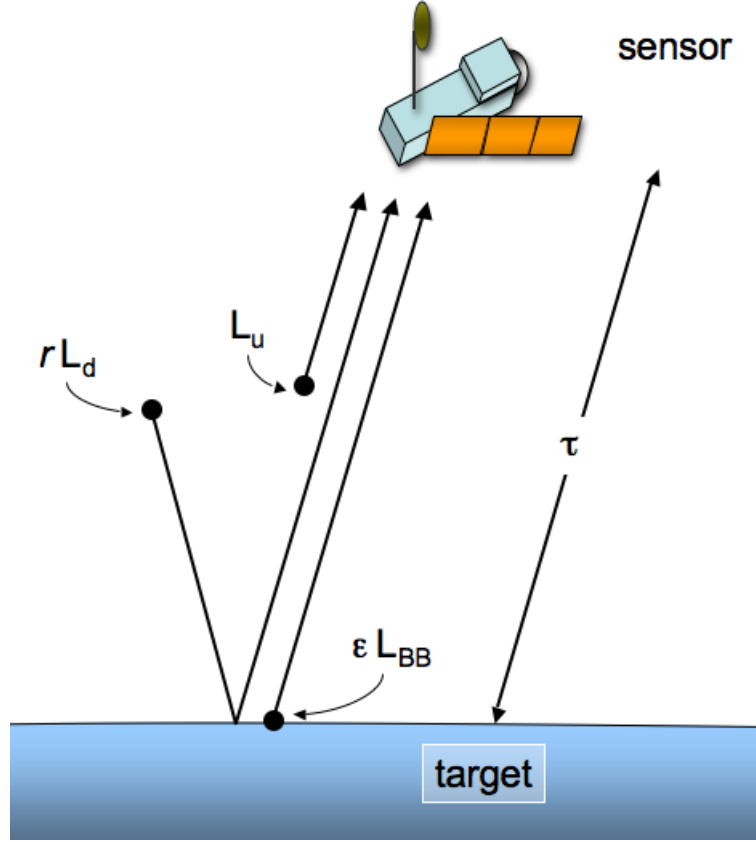


Figure 3.8: Self-emitted thermal energy paths for radiance reaching an orbiting satellite sensor.

As mentioned in Section 3.2.1, the background radiance term (L_b) can often be neglected for most natural surfaces without large background objects, reducing the governing equation to:

$$L_\lambda = (\epsilon L_{BB} + (1 - \epsilon)L_d)\tau + L_u \quad (3.11)$$

3.3.1 Effective Radiance

The sensor reaching radiance encompasses a spectral dependence, as does the responsivity of the detectors. Defined by Schott (2007) responsivity, at each wavelength, is defined as the signal out (S) per unit flux incident (Φ) on the detector at the wavelength of interest and thus, the spectral response function is expressed as:

$$R_\lambda = \frac{dS}{d\Phi_\lambda} \quad (3.12)$$

with units of $[amps\ W^{-1}]$ or $[volts\ W^{-1}]$. Of particular interest is the unitless peak normalized spectral response function:

$$R'_\lambda = \frac{R_\lambda}{R_{\lambda_{max}}} \quad (3.13)$$

where $R(\lambda)_{max}$ is the maximum value of [Eq. 3.12]. The sensor response is due to a combined effect of the optical lens transmission as well as the spectral sensitivity of the physical detector. By weighting the sensor reaching radiance [Eq. 3.14] a normalized effective spectral radiance value is obtained over the detector bandpass. For example, taking [Eq. 3.14] and cascading it with [Eq. 3.13] yields the output signal from the sensor, which will be referred to as an effective radiance L_{eff} in units of $[W/m^{-2}sr\mu m]$:

$$L_{eff} = \frac{\int_{\lambda_1}^{\lambda_2} ((\epsilon L_{BB} + (1 - \epsilon)L_d)\tau + L_u) R'_\lambda d\lambda}{\int_{\lambda_1}^{\lambda_2} R'_\lambda d\lambda} \quad (3.14)$$

Equation 3.14 illustrates the governing equation for a satellite radiometer in regards to the restrictions of this study. This equation is crucial to this study as it is the definition of "truth" and provides the mechanism for comparison to the image derived radiance for each scene to populate the calibration curve of the instrument.

3.4 Atmosphere

The atmosphere can be assumed to be divided into four general layers: troposphere, stratosphere, mesosphere and thermosphere. Each of these layers is divided by well known layers marked as transition layers: tropopause, stratopause and mesopause [Figure 3.9]. This section discusses each of these layers focusing on there significance to this study.

3.4.1 Atmospheric Boundary Layer

The atmospheric boundary layer or boundary layer (BL) is the lowest portion of the troposphere and is directly influenced by the earths surface as it extends nominally to 1-2 km above ground. The discussion of the boundary layer here was derived from Stull (1988). The thickness of the BL is quite variable and largely a function of time of day, surface material type (Ex. land or water), and prevailing weather conditions. Surface forcing

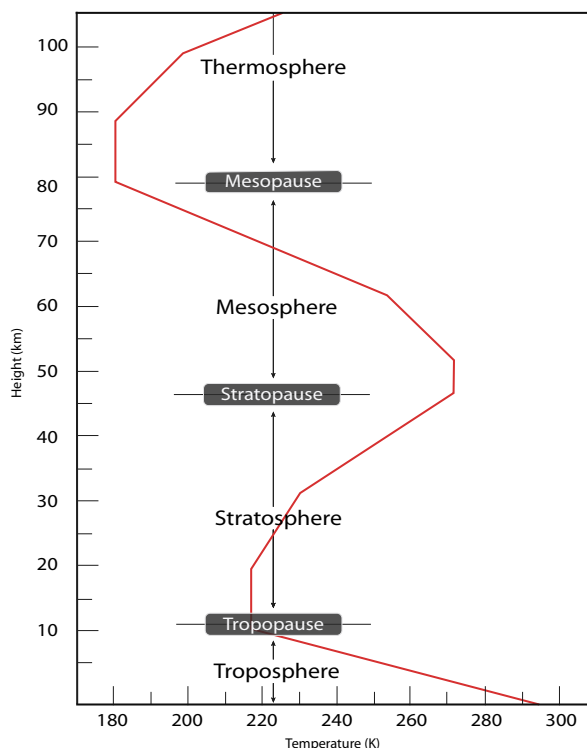


Figure 3.9: Diagram of the atmospheric layers temperature distribution.

mechanisms in the BL respond on an approximate time-scale of an hour or less, which include frictional drag, evaporation and transpiration, heat transfer, pollutant emission among others.

Temperature in the BL varies on a known diurnal cycle [Figure 3.10]. Stull (1988) investigated the BL temperature variation, of four contiguous fair weather days, by launching rawinsonde soundings every couple of hours over a common ground site. Results showed that the near surface temperature variation demonstrated a clear diurnal variation, which is not evident at greater altitudes. The diurnal temperature variation near the surface is due primarily to solar absorption on the ground (typically on the order of 90 percent), therefore, little solar radiation is absorbed in the BL (i.e. most is transmitted). The importance of this discussion is the understanding that the BL will change as the earth's surface warms and cools in response to incident solar radiation. In contrast this example shows that in fair weather conditions above the BL the atmosphere is much less variant, Stull (1988).

The BL can be subdivided into three primary layers based on heat transfer: the molec-

Fig. 1.2
Evolution of
temperatures
measured near
the ground
(97.5 kPa) and
at a height of
roughly 1100 m
above ground
(85 kPa).
Based on
rawinsonde
lauches from
Ft. Sill, OK.

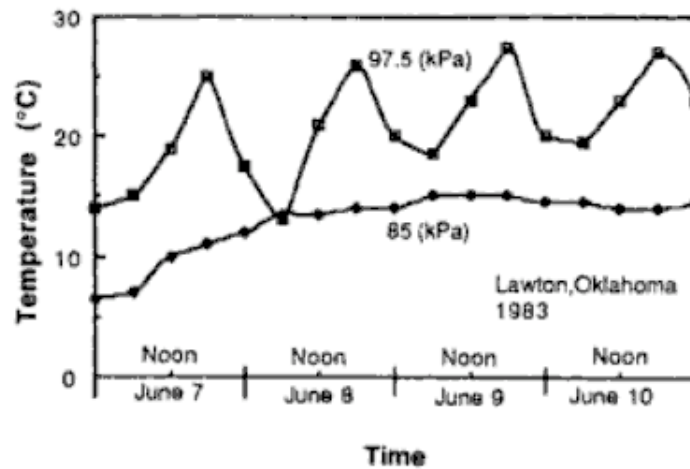


Figure 3.10: Temperature evolution measured near surface (97.5 kPa) and ~ 1 km above ground (85 kPa) by rawinsonde, Stull (1988).

ular layer, the surface layer and the mixed layer. The molecular layer has a vertical extent of less than 1 mm where molecular conduction and diffusion are the principle mechanisms for the vertical transport of sensible heat and water vapor. Immediately above the molecular BL is the surface layer. This layer has a vertical extent within the lowest few tens of meters from the earth's surface where micro-scale turbulence provides the transfer of sensible heat and water vapor. The mixed layer makes up the bulk of the BL during the day, with large transport mechanisms such as thermals and convective rolls.

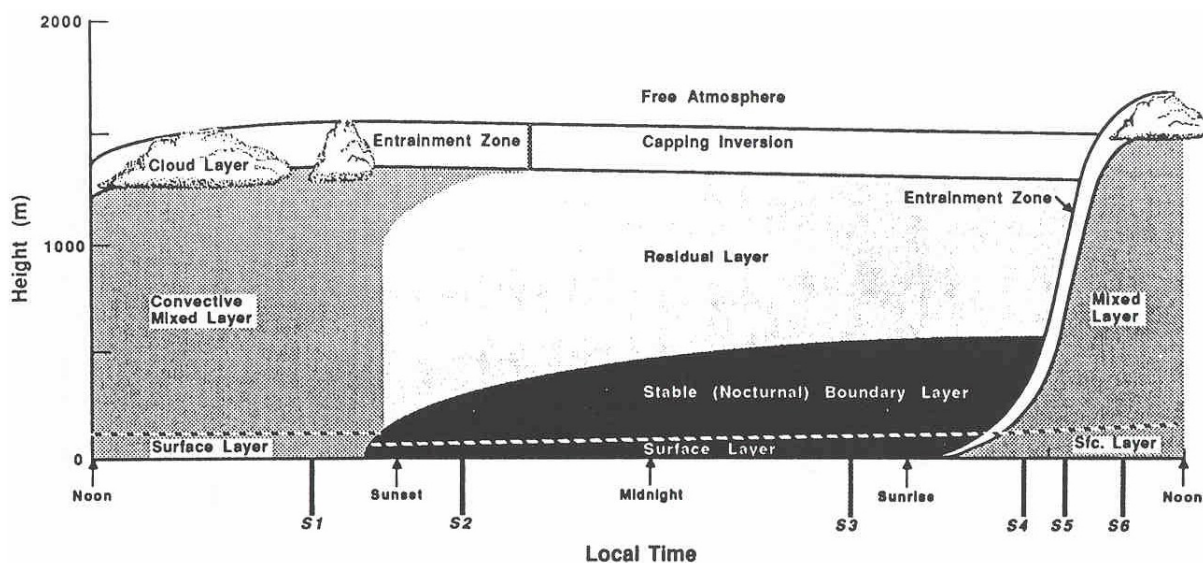


Figure 3.11: Diurnal variation over land, under fair weather conditions Stull (1988)

The diurnal evolution and structure of the BL over land during fair weather conditions

is shown in Figure 3.11. During the day solar radiation is absorbed by the earth's surface and emitted back to a cold sky. This emitted radiation (i.e. thermals) allows the mixed layer to grow in depth and is typically capped by a statically stable layer of air known as the entrainment zone or temperature inversion. Temperature inversions (also referred to as capping inversions) are layers where temperature increases with height and are marked as statically stable layers (meaning there is little turbulent exchange within the layer). Thus, the height of the BL is constrained to the height of the capping inversion. During sunset, turbulence in the BL decays, allowing the residual layer to take the place of the once turbulent mixed layer. Throughout the night due to radiative cooling at the surface, a statically stable BL develops in the lowest portions of the residual layer. Thus, the vertical extent of the BL is much closer to the surface at night than during the day. In practice one can typically determine the height of the boundary layer from radiosonde profiles of temperature by observing the near surface temperature inversion (most easily discernible in the morning sounding) [Figure 3.12].

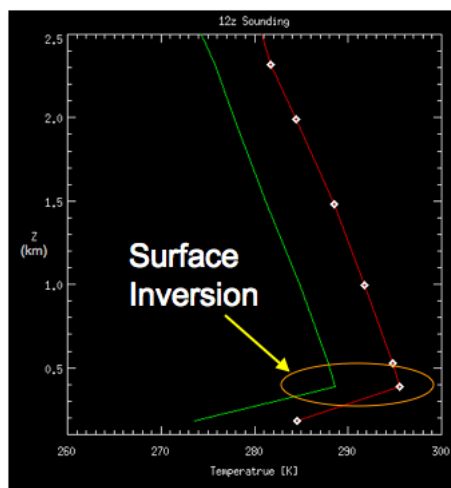


Figure 3.12: Illustration of a morning temperature inversion, found by visually inspecting a temperature (red) and dew point (green) profile. Note the height of the boundary layer in this case is quite shallow (roughly 400 m).

Over large water bodies the BL varies relatively slowly in both space and time, due to the small change of sea surface temperature over a diurnal cycle; due to the active mixing of near surface waters. Water has a larger heat capacity (than land, for example), meaning that large amounts of solar radiation can be absorbed with relatively little temperature

change. As previously discussed, the BL will change in accordance with the fluctuation of surface fluxes, thus, it makes sense that the marine BL is a slowly varying entity with slowly varying forcing into the lower portions of the BL Stull (1988). It is important to realize that the height of the marine BL will be shallower than the BL over land. The marine BL is still an area of active research today.

3.4.1.1 Internal Boundary Layer

The atmospheric boundary layer above any semi-enclosed (or enclosed) body of water (lake, sea, etc.) will almost always feel the presence of the surrounding land mass by means of advection. For the sake of example, consider a coastal region along the eastern sea-board of the United States, where warm air is flowing offshore over a cold ocean. Note there is a large discontinuity in surface material at the land to water interface, which introduces a discontinuity in surface heat flux. This situation lends itself to the development of the Internal Boundary Layer (IBL). The American Meteorological Society (AMS) defines the IBL as a layer associated with the horizontal advection of air across a discontinuity in some property of the surface (i.e. surface heat flux) and can be viewed as layers in which the atmosphere is adjusting to new surface properties.

Our discussion focuses on the horizontal advection of warm (continental) air flowing over a cooler water surface [Figure 3.13] leading towards the development of a stably stratified layer. This schematic illustrates how the mixed layer temperature profile (within 1-2 km) is typically modified as it is advected across a cooler water surface. Note the mixed layer temperature profile [Figure 3.13 (left)] will be primarily modified below the vertical extent of the IBL. In a study over the Gulf of Maine Angevine et al. (2006) found that the formation of the IBL (or stable layer), involves cooling a layer roughly 50 to 100 m thick by 5-15 K, which occurs in the first 10 km from the coast, on a time scale of roughly a half hour. Garratt and Ryan (1989) and Smedman et al. (1997) show the IBL is initially stably stratified (meaning the temperature profile slopes upward from left to right, resembling [Figure 3.12]), however, as the advection distance increases, stability decreases and a well-mixed slightly stable layer capped by an inversion develops. Simply meaning that the strong inversion decays with distance from the shoreline, which makes intuitive sense because as the fetch increases the IBL will eventually adjust to the underlying surface.

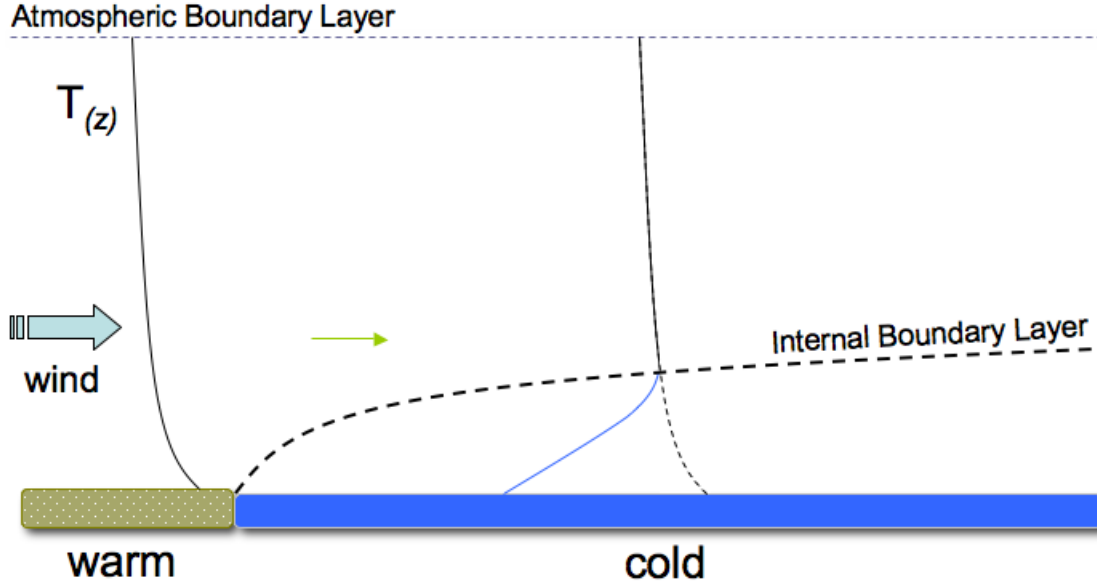


Figure 3.13: Illustrates the development of a stably stratified IBL as the warm (continental) air is advected over a cooler sea surface under fair weather conditions. Note the mixed layer temperature profile (left) is primarily modified below the limiting height of that of the vertical extent of the IBL.

Csanady (1974) observed these conditions quite frequently over Lake Ontario.

Garratt and Ryan (1989) developed an empirically derived model for the prediction of IBL height [Eq. 3.15] given knowledge of the upstream mixed layer over land and the sea surface at distance x from the shoreline [Table 3.5].

$$h = \alpha U x^{1/2} \left(\frac{g(T_{\theta_{land}} - T_{\theta_{sea}})}{T_{\theta_{land}}} \right)^{-1/2} \quad (3.15)$$

Table 3.5: Description of variables used in Eq. 3.15.

h	internal boundary layer height [m]
α	constant .02
U	upstream (normal to shoreline) mean mixed layer wind speed [m/s]
g	gravitational acceleration $0.98 [m/s^2]$
x	distance from the shoreline (fetch) [m]
$T_{\theta_{land}}$	mean mixed layer potential temperature [K]
$T_{\theta_{sea}}$	mean sea surface potential temperature [K]

Note: the (AMS) defines potential temperature (T_{θ}) as the temperature that an unsaturated parcel of dry air would have if brought adiabatically and reversibly from its initial

state to a standard pressure, p_0 , typically 1000 mb, expressed as:

$$T_\theta = T \left(\frac{p_0}{p} \right)^K \quad (3.16)$$

where T is temperature, p is pressure, and K is the poisson constant ($K = 0.2854$).

Consistent with [Eq. 3.15], Garratt and Ryan (1989) and Smedman et al. (1997) found that smaller differences between continental air and the sea surface lead to a deeper (increased height) IBL. Conversely, the IBL was found to be shallower and more stably stratified as the land sea difference increased. This makes physical sense because as warmer air over runs a colder sea surface a steep temperature inversion (stably stratified) develops, limiting the amount of mixing among layers, thus resulting in a shallow IBL. Additionally, the mixed layer wind speed is a critical parameter in the prediction of IBL height, as it drives the advection process. The authors also found consistent with Eq. 3.15 the IBL height increases with increasing wind speed (and vice versa), primarily due to the fact that as wind speed increases so does the amount of mixing, resulting in an increased IBL height.

Through field studies [Garratt and Ryan (1989), Smedman et al. (1997) and Angevine et al. (2006)] found that the predicted IBL heights h , using [Eq. 3.15], were found to be considerably less than the observed IBL heights. The cause likely being the difficulty in adequately initializing the model with the true environmental state variables, as well as, the realization that Eq. 3.15 may not account for all processes influencing the IBL height. Studies have developed differing values of α (i.e. Hsu (1983) $\alpha = 0.015$ for x values < 50 km) to better predict h for their site, however, Garratt and Ryan (1989) believe that an α value of 0.02 should be used to predict the IBL height to within 25-50% for x values of at least 5 - 300 km. The significance of the IBL in terms of the overall temperature error are examined in a sensitivity study [Appendix C]. In short, the study concluded that the IBL generally introduced errors of ~ 0.1 K when compared to profiles using the height of the boundary layer, thus it will be introduced into our processing and generation of the atmospheric column.

3.4.2 Troposphere

The troposphere is the lowest of the four major layers in the atmosphere extending from the ground to roughly 10-12 km. More than 80% of the earth's atmospheric mass and nearly all of the earth's atmospheric water vapor, clouds, and precipitation can be attributed to the troposphere. Kumar et al. (2003) explains the mean distribution of atmospheric water vapor shows a seasonal migration in the summer hemisphere, with a maximum in the equatorial region, and a decrease towards polar latitudes. The authors go on to note that more than 90% of the atmosphere's water vapor is confined to the layer below 500 hPa (about 5-6 km), and the steepest gradients and most distinct temporal variability of water vapor occurs in the subtropics (i.e. mid-latitudes). The troposphere is characterized by strong vertical mixing, which can be easily realized by observing daily weather patterns. Over the course of a few days, in clear air, it is not uncommon for an air molecule to traverse the entire depth of the troposphere. In fact, tropospheric aerosols have a relatively short mean residence time, ranging from a few days to a few weeks, Wallace and Hobbs (1977). Temperature in the troposphere decreases with height and is generally capped by a temperature inversion known as the tropopause. The tropopause is the immediate layer between the troposphere and the stratosphere. The height of this layer is not constant and varies in both space and time, Barry and Chorley (1977). The dynamic height of the troposphere can typically be found by observing temperature and dew point profiles of radiosonde observations, by searching for a pronounced inversion at roughly 10 - 15 km [Figure 3.14]. The transition from the troposphere to the stratosphere is typically marked by an abrupt change in concentration of water vapor and ozone constituents. For example, water vapor concentrations sharply decrease as ozone concentrations typically increase by an order of magnitude, only a few kilometers above the tropopause. Essentially, there is relatively little mixing between relatively moist, ozone-poor tropospheric air and dry, ozone-rich stratospheric air, Wallace and Hobbs (1977).

3.4.3 Stratosphere

The stratosphere is the second major layer of the atmosphere as it extends from the tropopause to approximately 50 km. As alluded to earlier, the stratosphere (predominantly the lower stratosphere) contains a radiationally important amount of water vapor

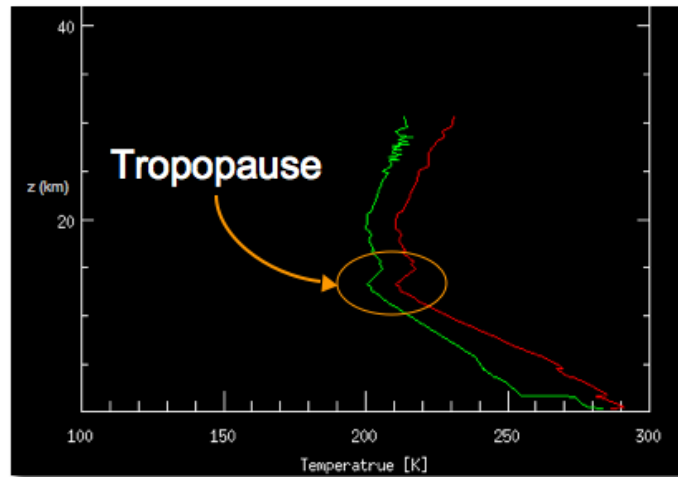


Figure 3.14: Use of radiosonde observations in the determination of the height of the tropopause. Note tropopause is roughly 14 km in this example radiosonde 12z sounding: 17 May 1998 Alpena, MI.

Houghton (1985). Although, the largest concern in the LWIR regarding temperature retrieval in the stratosphere is the constituent O_3 . Much of the atmosphere's total ozone O_3 concentration is found within the stratosphere, reaching a peak density at approximately 22 km [Figure 3.9], Barry and Chorley (1977). This ozone rich layer is crucial to life on earth due to its part in absorbing much of the harmful ultraviolet solar radiation. Realize however, that both the total amount of ozone and its vertical distribution are subject to latitudinal and seasonal variations, in addition to fluctuations at finer spatial and temporal scales, Houghton (1985). Recall that absorption of ozone is strong within the 8 to 14 μm window [Figure 2.4], therefore thermal satellite bandpasses in the LWIR typically exclude the strong O_3 absorption feature.

One of the most important concepts to stress in this section, is that the stratosphere is characterized by very little mixing, as Figure 3.9 shows the temperature throughout the layer increases with height (i.e. thermodynamically stable). As a result of the relatively weak mixing processes, stratospheric aerosols are observed to persist for long periods of time (1 year or longer). For instance, events such as past nuclear explosions and dust from large volcanic eruptions can be sources of lingering stratospheric particulate potentially many years after an event. Thus, the stratosphere behaves somewhat like a reservoir for certain atmospheric pollutants, Wallace and Hobbs (1977).

3.4.4 Upper Atmosphere

Our discussion of the atmosphere's structure will conclude with a brief discussion on the mesosphere and the thermosphere, which will be referred to here as the upper atmosphere. The mesosphere extends to about 80 km and is a region, similar to the troposphere, where temperature decreases with height to the mesopause. Immediately following the mesopause lies the thermosphere which extends upward to an altitude of several hundred kilometers to the thermopause. At such distances from the earth's surface the atmosphere is quite thin, however, there still resides a sufficient amount of atmosphere to induce drag on low earth orbiting spacecraft, so that orbital corrections are necessary over time. Depending upon the amount of solar activity, temperatures in the thermosphere range from 500 [K] to 2000 [K]. Realize that molecular collisions are quite infrequent at such altitudes, so that traditional means of temperature are difficult to define. Beyond the thermopause, there is the exosphere. This layer is extremely thin and relatively isothermal, as it is made up of neutral particles and charged particles. The vertical extent of the exosphere ranges from the thermopause to approximately 750 km. Wallace and Hobbs (1977).

In summary, the upper atmosphere is a static and relatively non-important portion of the atmosphere in terms of this study. As proof to this claim Appendix E illustrates a brief sensitivity study regarding the upper atmosphere. The study sequentially removed layers from the top of the atmosphere towards the surface, in an effort to determine at which height do acceptable temperature errors become significant (i.e. $\sim 0.1K$). Results found that dry atmospheric profiles resulted in critical heights of ~ 2 km, although for typical conditions critical heights of 4 - 7 km were observed. The range in critical height is dependent upon the amount of moisture present in the atmospheric profile (note as moisture increases the critical height increases as well).

3.5 Atmospheric Effects on Sensor Reaching Radiance

With an understanding of the pertinent atmospheric effects contributing to the observed satellite radiance and an understanding of the structure of the atmosphere, our discussion will now shift to the physical nature of the three dominant atmospheric effects, as well as, their numerical computation.

3.5.1 Atmospheric Transmission

3.5.1.1 Atmospheric Absorption

Fundamental characteristics of atmospheric transmission can be defined in two main categories: atmospheric absorption and atmospheric scattering. Absorption is a process which converts electromagnetic energy to another form of energy (typically thermal), resulting in a removal of energy from the beam Schott (2007). Transmission in terms of concentration-depth absorption can be expressed as:

$$\tau = e^{-C_{\alpha} m z} \quad (3.17)$$

where C_{α} is the absorption cross section (effective size of a molecule to the photon flux at that wavelength); m is the number density (number of molecules per unit volume); z is the path length.

Simply stated by Schott (2007), to determine atmospheric transmission along a beam three variables need be identified: 1) the number density of each constituent molecule along the path, 2) the absorption cross section as a function of wavelength for each constituent and 3) how the cross section varies with the environmental parameters Temperature (T) and Pressure (P) along the path.

3.5.1.2 Atmospheric Scattering

In general atmospheric scattering is theoretically approximated to generally follow one of three explanations: Rayleigh scattering, Mie scattering, and Nonselective scattering. For spherical size particles, Rayleigh scattering occurs when the wavelength of the incident flux is much larger than the particles it is interacting with (i.e. visible light incident upon air molecules). Mie scattering occurs when the particle sizes are approximately equal in size to the wavelength of incident flux (i.e. visible light incident upon aerosols and small dust). Finally, nonselective scattering occurs when the wavelength of incident flux is much smaller than the particle size (i.e. visible incident upon water droplets and ice crystals), Schott (2007). Clearly, the differences in scattering type are primarily a function of wavelength and particle size distribution [Figure 3.15].

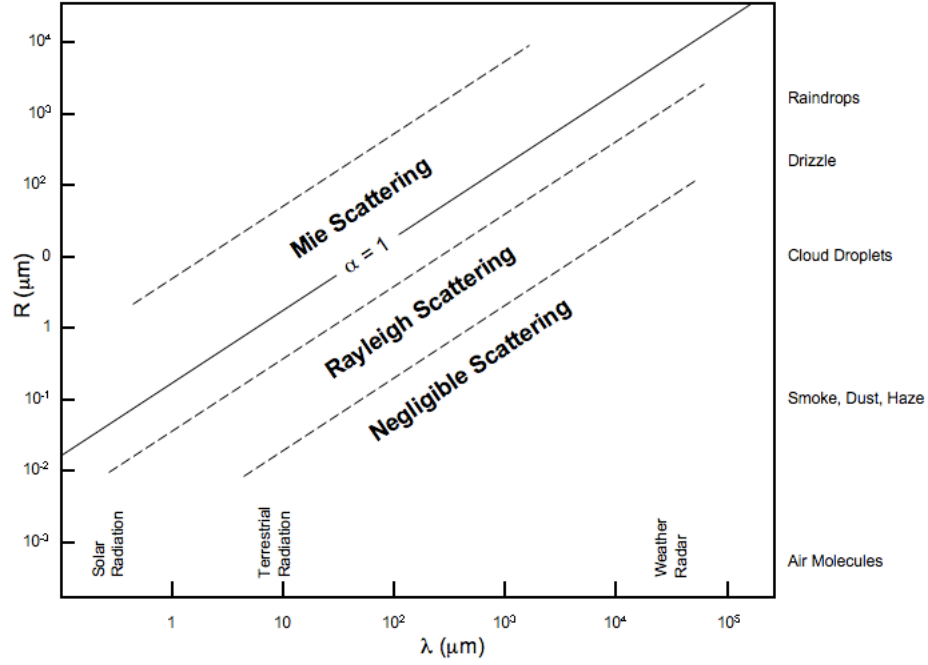


Figure 3.15: Size parameter α as a function of wavelength of the incident radiation and particle radius, taken from Wallace and Hobbs (1977).

Collectively transmission can be expressed mathematically as:

$$\tau = e^{-(\beta_\alpha + \beta_r + \beta_a + \beta_{ns})z} = e^{-\beta_{ext}z} \quad (3.18)$$

Table 3.6: Variables of Atmospheric Transmission [Eq. 3.18].

β_α	fractional amount of flux lost to absorption per unit length
β_r	fractional amount of flux lost to rayleigh scattering per unit length
β_a	fractional amount of flux lost to aerosol scattering "Mie scattering" per unit length
β_{ns}	fractional amount of flux lost to nonselective scattering per unit length
β_{ext}	sum of absorption and scattering coefficients
z	transit path length of a propagating beam

Through visual inspection of [Figure 3.15] it is apparent that within the region of 8 - 14 μm (terrestrial radiation) atmospheric scattering can be assumed to be negligible, when clear sky conditions are considered. Therefore, [Eq. 3.18] can be simplified to:

$$\tau = e^{-(\beta_\alpha)z} \quad (3.19)$$

stating total atmospheric transmission in the LWIR is dependent solely on atmospheric absorption, under clear sky conditions. Understand that haze, aerosols, etc. can invalidate this statement, but MODTRAN will include scatter even though it is a small term.

3.5.2 Atmospheric Self-Emission: Upwelled Radiance and Downwelled Radiance

Consideration must also be placed on the contribution of upwelled and downwelled radiance. These terms unlike transmission account for an additive bias in sensor reaching radiance. The atmosphere's temperature is above absolute zero, thus all resident molecules within the sensors path will have a self-emitted contribution to the sensor reaching radiance [recall, Figure 3.8]. These two terms vary strongly with the vertical structure of the atmosphere, specifically, warm-moist layers increase the contribution to sensor reaching radiance Dash et al. (2002). Note that as altitude increases in the troposphere, temperatures decrease and tend to be less moist, thus the significance of these terms at higher altitudes decreases. Additionally, understand that for high emissivity targets (i.e. $\epsilon \approx 1$) the amount of downwelled radiance reaching the sensor becomes almost negligible.

3.5.3 Computation of Atmospheric Effects through Physical Modeling

This section was developed through the discussion presented in [Schott (2007), Section 7.3.3]. Accounting for the atmospheric effects discussed above is quite a challenging effort and still a very active topic of research. At any one time, the atmosphere encompasses a multitude of governing variables making the effort of capturing and characterizing the true state of atmosphere a daunting task. Physical modeling efforts, referred to as RTM or atmospheric propagation code, have been developed to take on such a characterization task. Let's consider probably the most widely used and readily available RTM to date; MODTRAN, Berk et al. (1999). MODTRAN is an acronym, which stands for MODerate spectral resolution atmospheric TRANsmittance algorithm and computer model; developed by the Air Force Research Labs (AFRL) in collaboration with Spectral Sciences, Inc (SSI).

In a general statement, MODTRAN is used, but not limited, to yield solutions regarding the atmospheric effects to at-sensor radiance. RTMs are convenient because they can

be applied to any image with relative ease, to obtain solutions for atmospheric correction. However, these models provide solutions regardless of accuracies. Knowing this, the responsibility lies within the user to appropriately recreate the state of the atmosphere for the desired simulation to be adequate.

At the heart of RTM efforts are defining the appropriate input parameters which make up the atmospheric column (i.e. profile). Input atmospheric profiles can be characterized by observed profiles (via radiosonde, aircraft, model data, etc.) or can utilize standard atmospheric profiles stored in the MODTRAN model, (Appendix F illustrates three MODTRAN standard atmospheric profiles: Mid Latitude Summer, Mid Latitude Winter and Tropical).

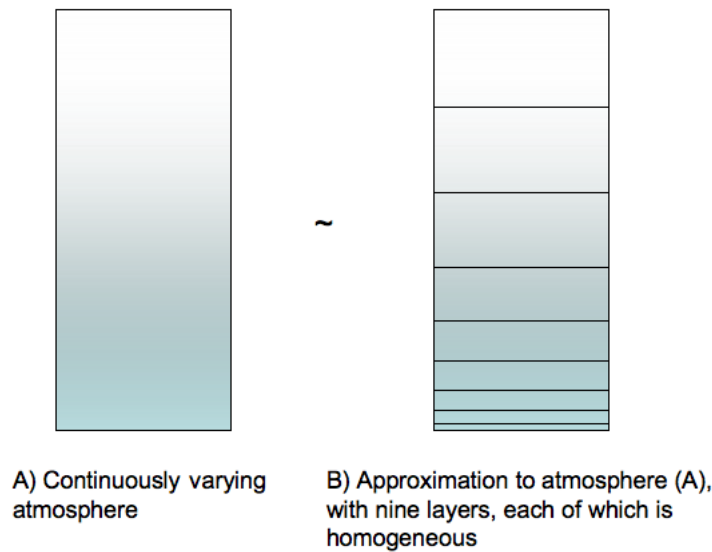


Figure 3.16: Schematic illustration of how RTMs characterize the atmosphere into homogenous layers, adopted from Schott (2007).

Generally RTMs assume the atmosphere can be divided into homogenous layers [Figure 3.16]. Recognize that if a user defined profile is provided, MODTRAN will define its layers based on the specified layers within the profile. As a function of height, atmospheric pressure and moisture variables (i.e. dew point or relative humidity) can be used to estimate the concentration of permanent gases and water vapor present. Similarly, based on user-supplied surface observations (or stored values) of visibility, season, and air mass type, estimates of aerosol number densities and size distributions can be approximated Schott (2007). In MODTRAN, if needed parameters are not explicitly defined by the

user, the model will use default values to yield its solution.

The numerical computation of atmospheric transmission, upwelled radiance and downwelled radiance will be discussed below:

Provided the general form of atmospheric transmission [Eq. 3.17], a numerical approximation can be made to solve for transmission through the i^{th} layer of the atmosphere at any wavelength as:

$$\tau_{ik} = e^{-m_{ik}C_k z_i} \quad (3.20)$$

where m_{ik} is the number density of the k^{th} atmospheric constituent in the i^{th} layer, C_k is the spectral extinction cross section of that constituent, and z_i is the path length for propagation through the i^{th} layer.

Calculation of atmospheric transmission in MODTRAN [Figure 3.17], uses an empirical approximation to Eq. 3.20 and solves for the total transmission using database and/or user supplied values Schott (2007). A unique solution is found for each layer, and the product of each solution is found to determine the total transmission throughout the entire column Eq. 3.21, Barsi (2000); note this is the transmission term [Eq. 3.14].

$$\tau_{i\lambda} = \prod_k \tau_{ik} \quad (3.21)$$

Similarly the upwelled or path radiance is computed in MODTRAN as:

$$L_{u\lambda} = \sum_{i=1}^N \left[(1 - \tau_{ik}) L_{BBi} \prod_{k=1}^{i-1} \tau_i \right] \left[\frac{W}{m^2 sr \mu m} \right] \quad (3.22)$$

where the spectral dependence on each term has been omitted for clarity, note this is the upwelled radiance term in Eq. 3.14. The indexing scheme in reference to the atmospheric layers begins at the sensor and ends with the layer just above the ground. Recall from Section 3.2.3, that for a homogeneous layer i , the conservation of energy requires that:

$$\Delta\tau_i + \Delta r_i + \Delta\alpha_i = 1 \quad (3.23)$$

where Δr_i is the reflection and $\Delta\alpha_i$ is the absorption in the the i^{th} layer along the beam. As discussed in Section 3.5.1.2, scattering in the LWIR is generally negligible (i.e. $\Delta r_i = 0$)

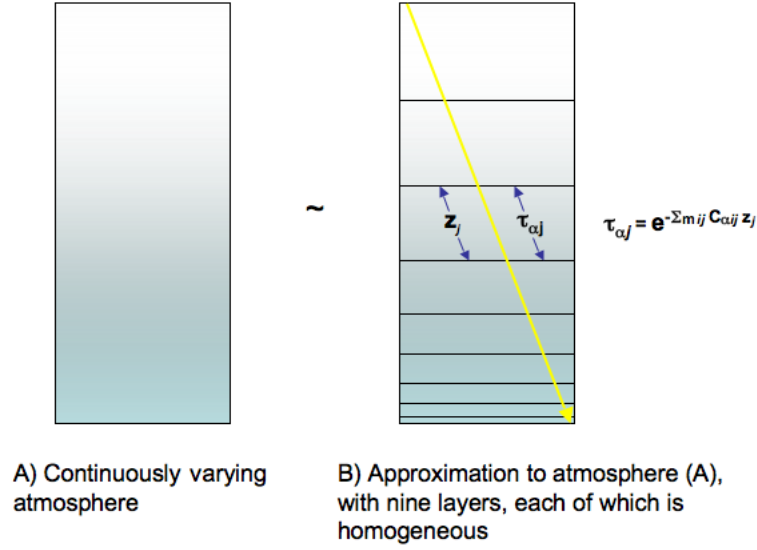


Figure 3.17: Transmission calculations using homogeneous layers to approximate a stratified atmosphere. Each constituent designated by the subscript i has an absorption cross section $C_{\alpha ij}$ and a number density m_{ij} where subscript j designates the layer Schott (2007).

reducing Eq. 3.23 to:

$$\Delta\tau_i + \Delta\alpha_i = 1 \quad (3.24)$$

where making use of Kirchoff's Law Eq. 3.7 and rearranging, the effective emissivity of the layer i^{th} is expressed as:

$$\Delta\epsilon_i = 1 - \Delta\tau_i \quad (3.25)$$

In a similar fashion the downwelled radiance can be solved by reversing the atmospheric layer indexing to start just above the ground and end at the top of the atmosphere. The downwelled radiance is computed over the hemisphere above the target which is sky. For our discussion we will consider a lambertian target completely exposed to the above sky dome. In order to perform the hemispherical integration one could either force MODTRAN to iteratively account for the sky dome or one could also take advantage of the Digital Imaging and Remote Sensing Image Generation model (DIRSIG) [Schott et al. (1999)] used in conjunction with MODTRAN which computes the downwelled radiance as:

$$L_{d\lambda} = \int_0^{2\pi} \sum_{i=1}^N \left[(1 - \Delta\tau_i) L_{BBi} \prod_{j=1}^{i-1} \Delta\tau_j \right] \cos \sigma \frac{r(\lambda)}{\pi} d\Omega \quad \left[\frac{W}{m^2 sr \mu m} \right] \quad (3.26)$$

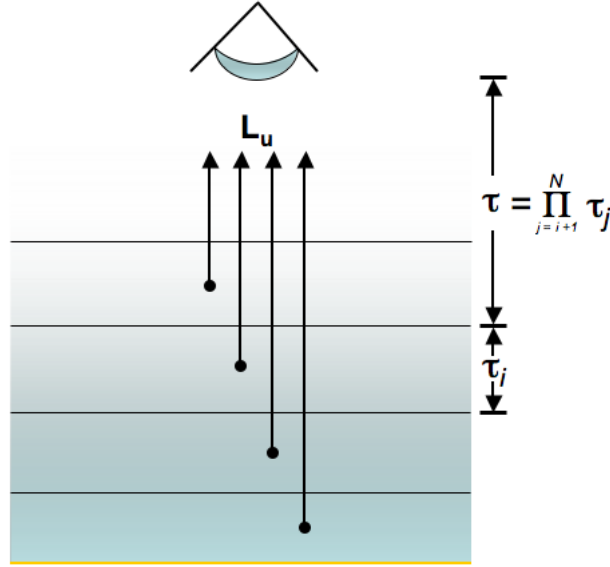


Figure 3.18: Summation of the contributions from each layer in the atmosphere to obtain the cumulative path radiance reaching the sensor, adopted from Schott (2007).

where $\frac{r(\lambda)}{\pi}$ is the target reflectance and $d\Omega$ is the differential element of solid angle. The total atmospheric downwelled contribution from the sky dome is then multiplied by the target reflectance to yield the reflected downwelled term [Eq. 3.14].

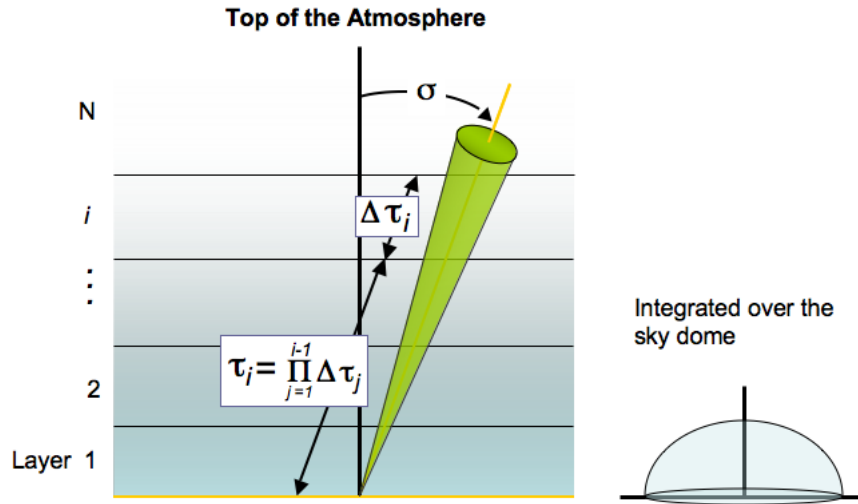


Figure 3.19: Downwelled radiance due to self emission, adopted from Schott (2007).

In summary this section has discussed the physical modeling required to account for the atmospheric effects on sensor reaching radiance (i.e transmission, upwelled and downwelled radiance). In the following section a discussion of the available environmental in-situ observational network will be addressed along with its limitations.

3.6 Sampling of Environmental Parameters

3.6.1 Upper-air Data

Radiosonde observations measure atmospheric profiles of temperature, pressure, relative humidity (RH) and wind speed. Since the late 1930s, the National Weather Service (NWS) under NOAA have observations times compliant with the World Meteorological Organization (WMO), daily at 1200 UTC & 0000 UTC (coordinated universal time (UTC); formally Greenwich mean time (GMT)). Figure 3.20 illustrates the available radiosonde locations about North America (as of September, 2008), realize the network has both spatial and temporal limitations.



Figure 3.20: North American radiosonde locations (Image: courtesy the University of Wyoming).

Radiosondes can ascend to over 35 km and drift over 200 km from there release point. Figure 3.21 illustrates a simulated balloon launch at 12z July 22, 2008 from Atlantic City International Airport, NJ (ACY) visualized in Google Earth and based on atmospheric state parameters from the Global Forecast System (GFS) model. This example is shown to emphasize that radiosondes do not sample a perfect vertical column and that the sampling is dictated by the upper level dynamics over the duration of flight. The vertical extent of the balloons are generally limited to its elastic material as the balloons burst and parachute back towards earth at a diameter of about 6 m (20'). Note if a radiosondes does not reach a

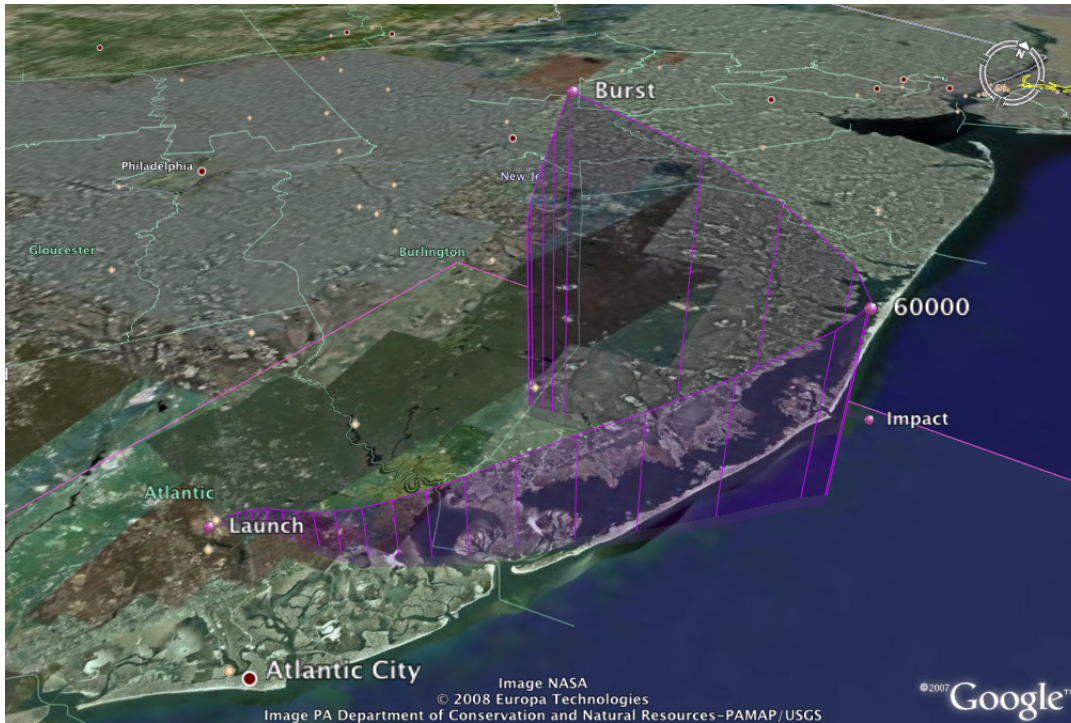


Figure 3.21: Simulated launch trajectory for a balloon launched at 12z July 22, 2008 at the Atlantic City International Airport, NJ (ACY) (Visualization: courtesy the University of Wyoming at <http://weather.uwyo.edu/polar/>).

nominal altitude of 7 km (considered minimally acceptable for NWS operations) a second launch may be deemed necessary, NWS.

Miloshevich et al. (2001) report that relative humidity measurements are known to be unreliable at cold temperatures. In fact, the NWS prior to 1993 did not even report RH measurements below -40°C (this correlates to approximately the mid to upper troposphere $\sim 7\text{-}9$ km) because of the measurements known unreliability Ross and Elliott (1996). Miloshevich et al. (2001) reports that stratospheric radiosonde RH measurements are considered to be essentially useless, due to the uncertainty in measurements typically exceeding stratospheric humidities by a few percent. Although humidity sensors continue to improve, problems still exist, specifically under very cold conditions Ross and Elliott (1996). Post 1993 numerous studies and low cost instruments have been proposed to account for these uncertainties. For a detailed discussion regarding radiosonde humidity measurements consult Miloshevich et al. (2001).

In addition to radiosonde data, as of 2001 NOAA's Forecast Systems Laboratory (FSL) has made available to researchers and NWS forecasters, automated weather reports via

commercial aircraft(ACARS). This data provides temperature profiles of the atmosphere during both ascending and descending aircraft flights. A database can be accessed, containing all cooperating airlines, updated every 10 minutes, however, note that this data set is limited to locations which are in relatively close proximity to existing airports. However, when available this data can aid in overcoming the spatial and temporal limitations in NWS radiosonde network.

3.6.2 Buoy data

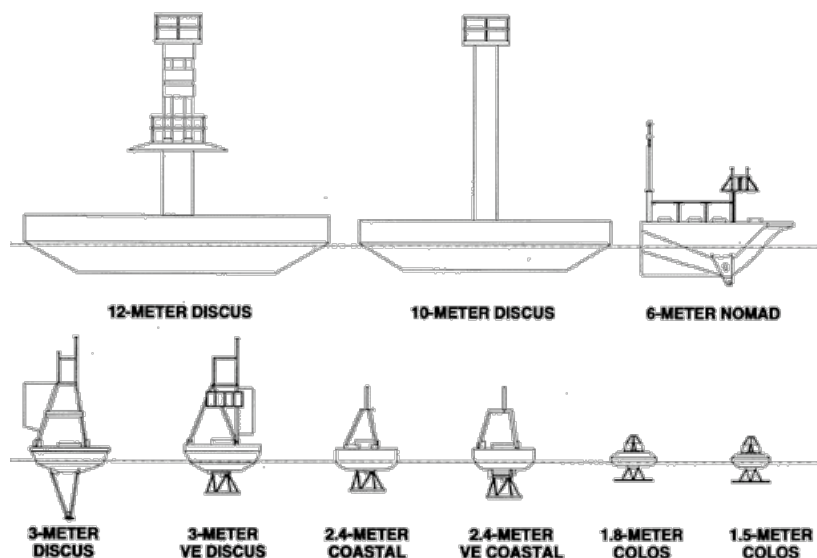


Figure 3.22: NDBC moored buoy program platforms. (Image: courtesy NDBC).

The NOAA National Data Buoy Center (NDBC) operates a fleet of moored buoys [Figure 3.22]. The fleet includes six buoy types: 3-m, 10-m, and 12-m discus hulls; 6-m boat-shaped (NOMAD) hulls; and the most recent addition, the Coastal Buoy and the Coastal Oceanographic Line-of-Sight (COLOS) buoy, NDBC. The decision of which hull type is used operationally is determined by the intended deployment location and measurement requirements.

The NDBC has operated a series of satellite-reporting weather buoys in the Great Lakes since 1979 [Figure 3.23]. Historical and current observations are available during the ice-free season, where the buoys are generally calibrated and deployed each year, typically in early spring (late March to early April) and recovered in late fall (mid to

late November), Schwab et al. (1999). In contrast moored buoys deployed in the ocean remain operational year round. These buoys are serviced at least every two years by the NDBC (or when critical fixes are needed). When serviced newly calibrated instruments are deployed and the replaced sensors are taken and back calibrated (i.e. all NDBC data is quality controlled (*c.f.* www.ndbc.noaa.gov/)).

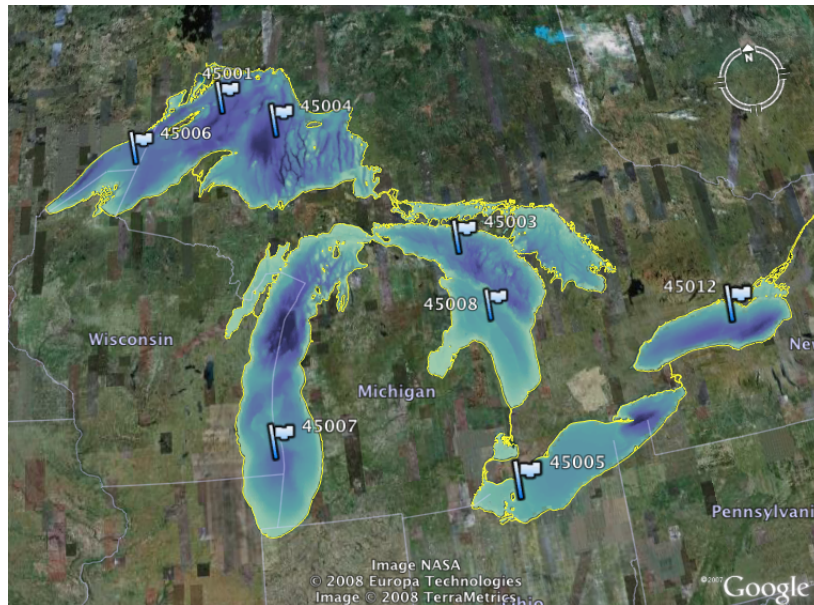


Figure 3.23: Moored buoy locations shown over bathymetry maps of the Great Lakes; darker blue refers to deeper water; image: courtesy Google Earth.

The identified Great Lakes buoy locations [Figure 3.23] are illustrated as constant over time, however, this is misleading. Each year to every few years the buoy location is slightly changed, due to concerns of an aging mooring. When new moorings are deployed, effort is placed on restricting the new mooring location to within a quarter mile of the previous buoy locale, phone correspondent NDBC, Steve Cucullu. Information regarding the historical record of the NDBC's moored buoy locations can be found at <http://www.nodc.noaa.gov/BUOY/buoy.html>. Currently deployed in the Great Lakes are the NDBC's aluminum-hulled, 3-meter discus moored buoy's [Figure 3.24], however, throughout history 12 m, 6 m, and 2.4 m hull buoys have been deployed. These buoys measure and transmit barometric pressure; wind direction, speed, and gust speed; air temperature and water temperature at depth; along with various water surface wave characteristic measurements. Recognize that surface atmospheric dew point and visibility

measurements are not typically reported.

It is important to understand that each platform or hull type offers differing measurement heights [Table 3.7]. For example, the thermistor is mated with the keel and hull

Table 3.7: Moored Buoy Sensor Heights, NBDC.

Hull Type	Anemometer Height	Thermistor Depth
10m & 12m	10.0 m	1.5 m
3m & 6m	5.0 m	1.0 m to 0.6 m

of the buoy, thus the depth of the sensor will be dependent upon the hull type, please correspondence NBDC Steve Cucullu. For a detailed description of the specific payload used aboard each buoy type (*c.f.* <http://www.ndbc.noaa.gov/rsa.shtml>). The payload specifications, in the interest to this study, are constant throughout all NBDC moored buoys [Table 3.8]. Regardless of platform, the specifications regarding wind speed, air temperature, and water temperature are constant. Thus, the only difference between various buoy hull type observations are the height and depths at which the measurements are obtained. Realize that the platforms used about each location has varied throughout history, for each moored buoy location. Also note, the observed data are not instantaneous values, but that of 8 minute averages for water temperature, air temperature and wind speed reported once an hour.

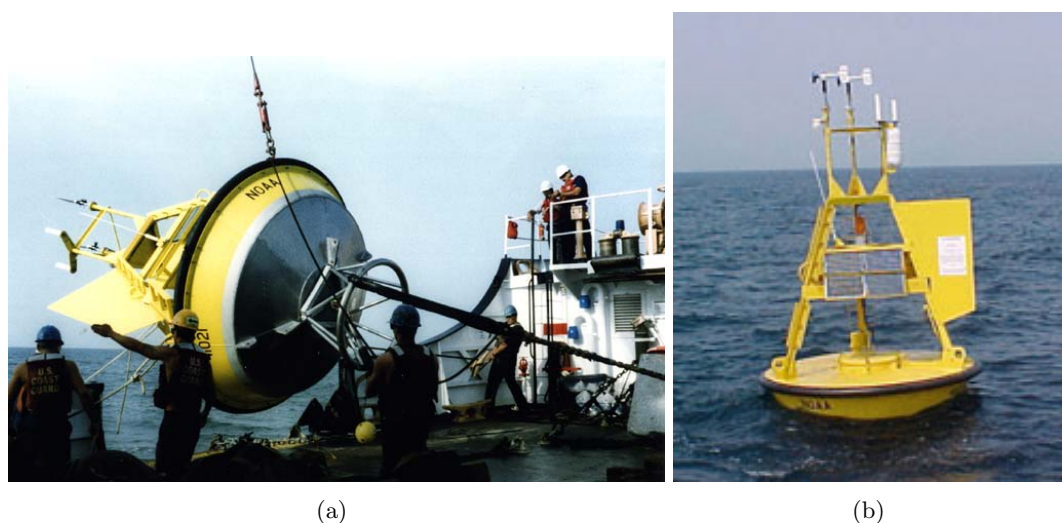


Figure 3.24: NBDC 3m discus moored buoy used in the Great Lakes: (a) deployment of buoy in early spring (note the relative size of the buoy) (b) successfully deployed moored buoy. (Images: courtesy NBDC)

In summary it is important to take away from this discussion: 1) various moored buoy

Table 3.8: Buoy Specifications of Interest, NBDC.

Parameter	Range	Resolution
Water Temp.	-5 to 40 °C	± 0.1 °C
Air Temp.	-40 to 50°C	± 0.1 °C
Wind Speed	0 to 62 m/s	0.1 m/s
Pressure	800 to 1100 hPa	0.1 hPa
NBDC payloads: VEEP, GSBP and DACT		

hull types are used depending upon geographic location, which is also a function of the data availability (i.e. larger buoy types (i.e. more permanent) are used in the open ocean, while smaller and more temporary buoys are deployed in the Great Lakes; 2) the buoy hull type must be known, because it determines the depth of the submerged thermistor (note: buoy hull type not consistent in time for most of the buoy locations); 3) the payload specifications are consistent throughout the entire NBDC moored buoy fleet; 4) the exact location of each buoy has changed over time. Collectively these factors must be accounted for in all processing.

3.7 Surface Phenomenology of Large Water Bodies

As described in Section 2.6, the near surface of water bodies undergo significant variations on a diurnal cycle. Lets now consider a synoptic view of large water bodies, for example, the North American Great Lakes which are complex, highly dynamic systems which encompass multiple subsystems varying seasonally and on longer cycles, EPA.

A phenomenon known as the thermal bar has been widely studied and characterized since the late 1960's [Rodgers (1971)] and is a result of seasonal variations. As winter begins to give way to spring the temperature in large temperate lakes (Ex. the Great Lakes) is relatively constant and typically $< 4^{\circ}C$ ($4^{\circ}C$ is the maximum density of water). As spring progresses, the near shore waters increase in temperature at a much faster rate when compared to the deeper open waters. This is primarily due to convective heating in the shallower waters, but also largely because of spring rain and snow melt. Due to this warming, when the water temperature reaches $4^{\circ}C$ it will tend to sink, causing a partition between warm near shore waters and cool open waters [Figure 3.25 (a)]. A warm stable stratification layer near shore results, while the deeper water remains at some temperature

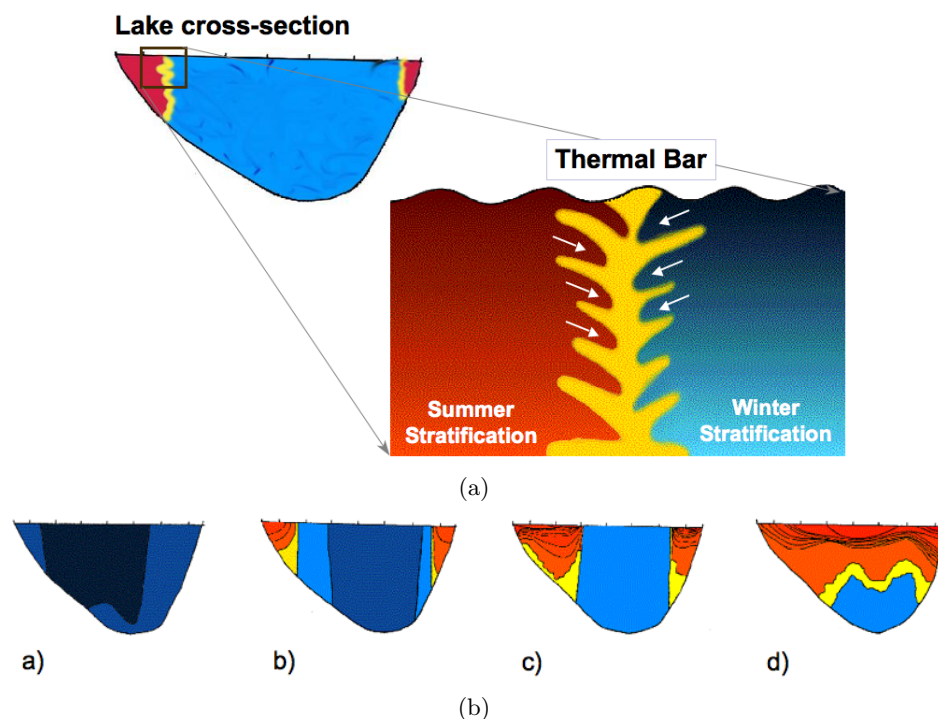


Figure 3.25: (a) Phenomenology of the thermal bar acting as the dominant barrier between warm and cool water. (b) Illustrates a cross-sectional view of the evolution of the thermal structure of Lake Ontario: late April, mid May, early June, and Late June (a,b,c and d respectively) DIRS at RIT.

below 4°C . Note it is the zone of sinking water in the vicinity to a water temperature corresponding to water's maximum density that is referred to as the thermal bar Rao et al. (2004). This phenomena is significant because of its role in inhibiting the horizontal exchange of water between near shore and offshore regions [Gbah et al. (1998); Rao et al. (2004)]. Lasting approximately 1-2 months the thermal bar will progressively migrate to the deepest region of the lake, eventually giving way to summer stratification [Figure 3.25 (b)].

Figure 3.26 (a) illustrates a defined thermal bar in Lake Huron on May 4, 1999. From this image it can clearly be shown that buoy measurements (especially in the deepest regions of the lake) provide ideal thermal targets (i.e. large and spatially invariant). Therefore, in this study the known thermodynamic and dynamic structure offered by the thermal bar will be taken advantage (when applicable) to ensure a high level of confidence in the collected ground truth data and extracted image ROIs. In contrast, Figure 3.26 (b)

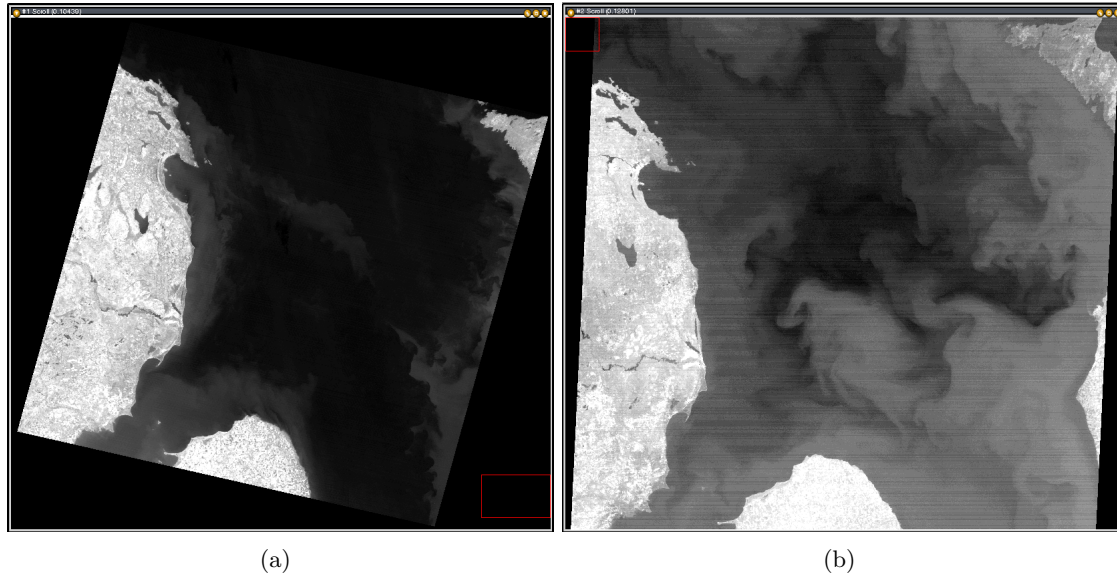


Figure 3.26: (a) Illustrates an example of a defined thermal bar structure in Lake Huron on May 4, 1999. (b) Illustrates a highly dynamic water body: Lake Huron on October 5, 1998 (i.e. the thermal bar has given way to summer stratification).

illustrates Lake Huron experiencing deep summer stratification. This scenario is clearly much more complex from a thermodynamic standpoint and raises uncertainty in the confidence levels specifically in the image extracted ROIs (i.e. if the buoy lies above an edge of a sharp temperature gradient). In conclusion, the thermal bar provides an ideal scenario for capturing low temperature targets at a high level of confidence. Note however, that due to the spatial limitations of this study (i.e. fixed buoy locations) the temperature contrast within the thermal bar cannot be taken advantage of.

3.8 Summary

This chapter has alluded to the depth and breadth of the Landsat program, while also addressing the necessary physical phenomenology for this vicarious calibration campaign. Factors such as the atmospheric structure, distribution of water vapor, atmospheric scattering, and boundary layer processes were developed, as all are significant elements in this study. In addition, the investigation's governing radiometry was developed along with the proposed governing equation. Bridging from the theoretical phenomenology, environmen-

tal sampling was discussed, as well as methods to numerically compute the atmospheric terms of τ , Lu and L_d . The following chapter will discuss the proposed methodology to construct the historical calibration record of the Landsat 5 TM thermal band.

Chapter 4

Approach

The proposed vicarious calibration effort can be summarized with the following explanation [Figure 4.1]: Imagine a satellite passing over a scene collecting thermal data about the earth. The resulting image can be investigated and regions of interest extracted (about the buoy location(s)), to obtain an observed sensor radiance. About the same image region of interest location(s), taking a known temperature and propagating it through the same atmosphere, a predicted at-sensor radiance is obtained. The result being two answers for a common scene location. The intent is to define the predicted at-sensor radiance as truth, so that a comparison can be drawn against the observed satellite radiance. Differencing the two solutions yields a point along a calibration curve. Thus, repetition of such a process is needed, to evaluate the calibration of the instrument over time.

It is the thrust of this work to recreate the entire state of the environment over each defined calibration site for a given scene at the time of image capture (i.e. re-construct the atmospheric column). Successful completion of such a task is imperative to the success of this work, because our ability to recreate the scene phenomenology is what primarily drives our definition of truth. Before further discussion, recall accuracy in a measurement process describes how well an instrument or procedure can match some standardized value or intuitively, what we have defined as truth, Schott (2007). Therefore, emphasis must be placed on solidifying the undertaking involved in this vicarious calibration process, so that errors and especially fluctuations in processing can be minimized, so that our value of "Truth" is accurate for each day, as well as, consistent throughout. This section develops the complete end-to-end proposed process from the selection of calibration sites,

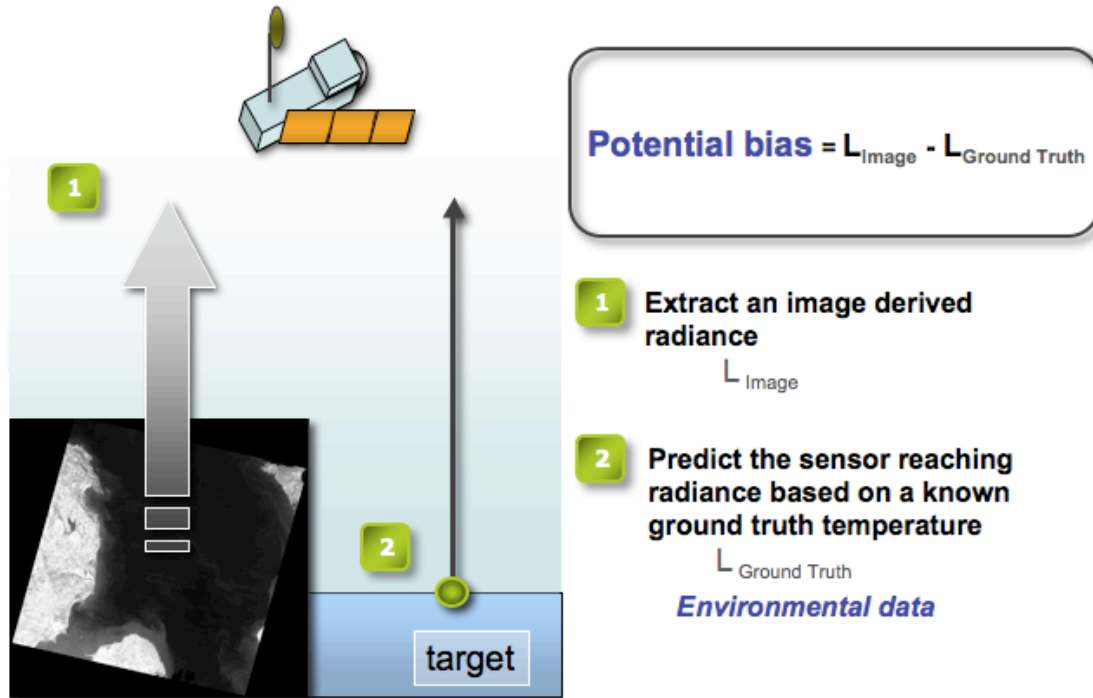


Figure 4.1: Overview of the proposed vicarious calibration process. Differencing the two solutions yields the potential bias of the sensor as a point on the TM’s Band 6 calibration curve.

assimilation of data sources, the generation of the calibration curve, and the methodology to quantify the error associated in the proposed approach.

4.1 Proposed Calibration Sites

For the reasons explained in Section 2.2 the Great Lakes offer a very practical domain to conduct such a historical study. The lakes provide large thermally stable targets, especially throughout the developing and mature stages of the thermal bar cycle [Section 3.7]; bulk temperatures (target temperatures) have been observed historically by NDBC moored buoys [Section 3.6.2] over the entire calibration period; and finally meteorological parameters (i.e. surface and upper-air observations) are also historically available about this domain. All potential Great Lake calibration sites were first surveyed based on the visual interpretation of Figure 4.2. Note, this set of criteria is valid in alternative regions, so long as each data source is simultaneously and historically available.

Three Great Lake locations and one coastal Atlantic Ocean location have been deemed

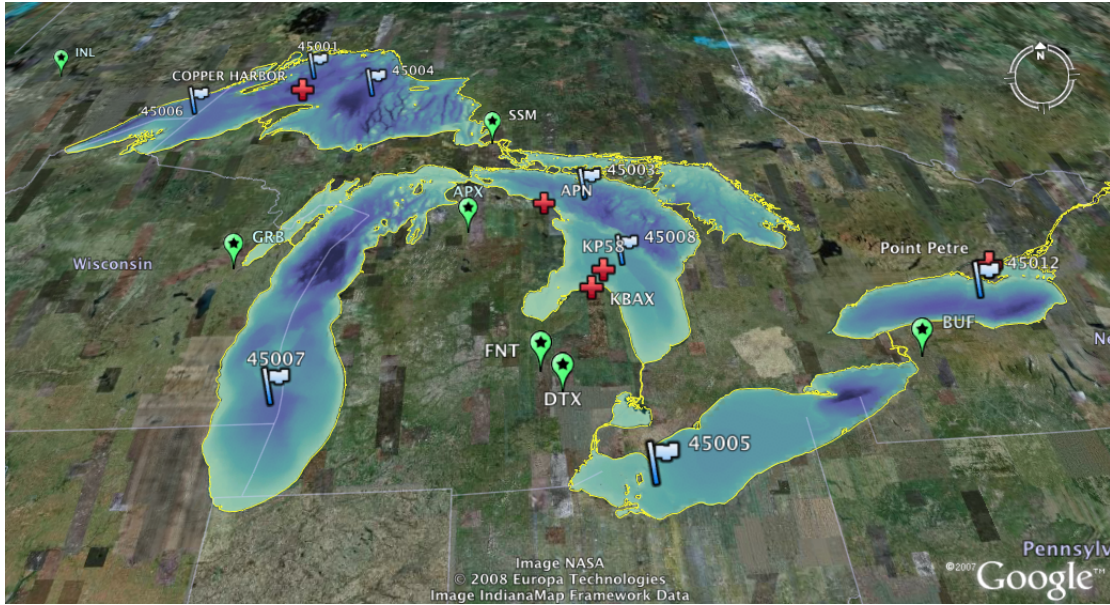


Figure 4.2: Great Lakes study domain. Historical environmental data: radiosonde locations (green *), surface observations (red +) and buoy locations (flags). (Image courtesy Google Earth).

adequate calibration sites for this study. Each site was determined using the hierarchical structure: 1) availability of buoy data; 2) its proximity to upper-air data (i.e. radiosonde data); and 3) available atmospheric surface dew point (T_d) data. Clearly the buoy data is of greatest importance, as it provides the needed ground truth bulk water temperature, as well as surface air temperature, pressure, and wind speed. Radiosonde data is equally important as it accounts for the majority of the environmental data needed. Each selected calibration site is summarized below. Recall, our efforts are focused on re-creating the atmospheric column over each defined calibration site.

4.1.0.1 Lake Huron (Site #1)

Landsat WRS-2 path/row: 20/29 was determined to be the best spatial scenario in regards to both image location ("constant") and available historic environmental data [Figure 4.3]. Each scene contains two NDBC moored buoys (north: 45003 & south: 45008); offering potentially two calibration points for each scene. Data archives for each buoy cover the years: 1980 - present and 1981-present, for buoys 45003 & 45008 respectively. Buoy 45003 is over a water depth of about 142.0 m, where buoy 45008 is over a water depth of about 58.2 m, thus both buoys are in sufficiently deep water. Figure 4.4 illustrates the location



Figure 4.3: Lake Huron Calibration Site (Site #1). Image location (pink rectangle), buoy location (flag), surface observation (red +) and upper-air data (*). Note bathymetry maps have been overlaid about the Lake regions.

history of these moored buoys used, realize that the locations vary over time.

The proximity to upper-air stations gave this site a clear advantage compared to other locations within the Great Lakes. Radiosonde data from Sault Saint Marie, Michigan (SSM) is available prior to 1995, where radiosonde data from Gaylord/Aplena (APX) will be used for dates including and post 1995 for this calibration site. Although the upper-air locations are roughly 90 to 130 miles from the scene center, remember that the predominate flow in the mid-latitudes is westerly. Also, consider that Michigan is in the heart of the Great Lakes, and is essentially a large peninsula, with water bodies surrounding each of its borders except for the south. Therefore, the chosen radiosonde locations should be quite representative of the atmosphere of that over the buoy locations. To further justify these locations as adequate, consider Figure 4.5, which illustrates radiosonde trajectory forecasts based on the Global Forecast System (GFS) model for 23 random samples over a 5 month period (July 2007 - November 2007). Notice that for SSM the overlaying column, originates from the flow typically over Lake Superior and that of APX originates typically from the flow off of Lake Michigan and/or Lake Superior. In either case the

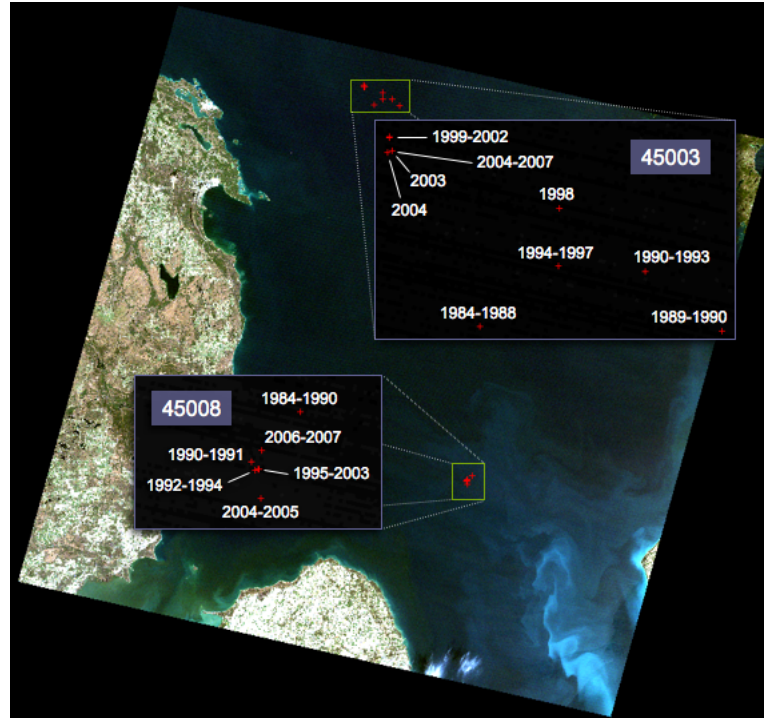


Figure 4.4: Time history of the geographic locations of buoys 45003 and 45008. Refer to Appendix G for a detailed listing of the buoy locations and deployed payloads for each year.

atmospheric columns should demonstrate characteristics of the atmospheric columns over these lakes. The APX site clearly demonstrates good spatial coverage, which makes it a highly considered site for not only historical studies, but future calibration efforts.

Surface observation locations were investigated using visualization tools provided by the National Climate Data Center (NCDC). Surface stations from Alpena, MI County Airport (APN), Bad Axe, MI (KBAX) and Port Harbor, MI (KP58) were chosen considering factors of proximity to buoy locations and data availability [Figure 4.3].

Figure 4.6 depicts the clear distinction between situations where the thermal bar is well defined in April and May and virtually non-existent from roughly July through the remainder of the warm season. Realize, as summer stratifications becomes more prevalent the surface temperature structure becomes more dynamic (i.e. variant) [recall, Figure 3.26 (b); Section 3.7]. These situations must be investigated thoroughly as any errors regarding the geometric integrity of the imagery may potentially have a strong influence on errors in the overall process. However, when the thermal bar is well defined and the core of the lake resides at roughly a constant temperature, these types of errors are

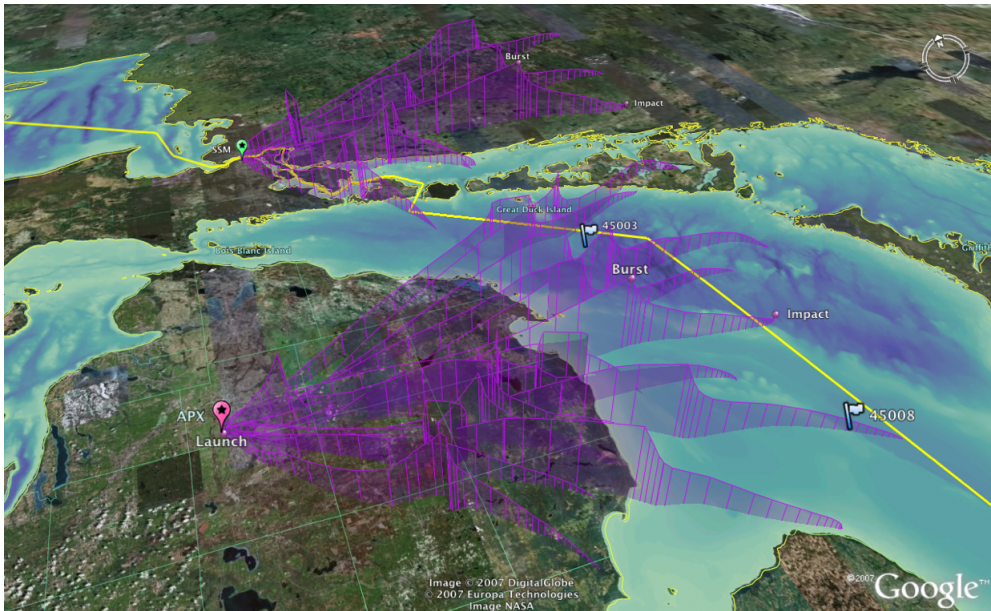


Figure 4.5: Global Forecast System model (GFS) balloon trajectory forecasts from 23 random samples over a 5 month period (July 2007 - November 2007) for the locations SSM & APX. The forecast trajectories are made available courtesy of a web-based tool developed by the University of Wyoming.

greatly reduced [recall, Figure 3.26 (a); Section 3.7]. The criteria formulated to account for the decision whether to accept or reject a potential calibration point based on spatial variation in surface temperature is rather subjective. A general rule of thumb for rejection on the basis of thermal surface variation is if the digital count (DC) values vary by more than 2 or 3 DC levels (which is approximately 0.84 K and 1.25 K, respectively) in close proximity to the buoy location of interest; note this is a rare occurrence. As discussed in Section 2.2 the ideal target surface is uniform in temperature (recall, water targets often exhibit low spatial variation (less than or equal to 1°C) over large areas), thus highly variant temperature surfaces will be discarded to reduce potential errors in the calibration results. Figure 4.7 illustrates a simulated scenario of a highly variant temperature surface on Lake Huron, offered to provide the reader of an exaggerated case which would have been discarded.

Note that buoy 45003 is over much deeper water (depth 142.0 m) than buoy 45008 (depth 58.2 m), consequently water in the shallower southern regions of the lake warm faster than the deeper northern half of the Lake. Thus, during the mid to later stages of the warm season, the Lake Huron moored buoys provide a temperature range in each scene; typically around $\Delta 3\text{-}5$ K, but differences can approach 10 K.

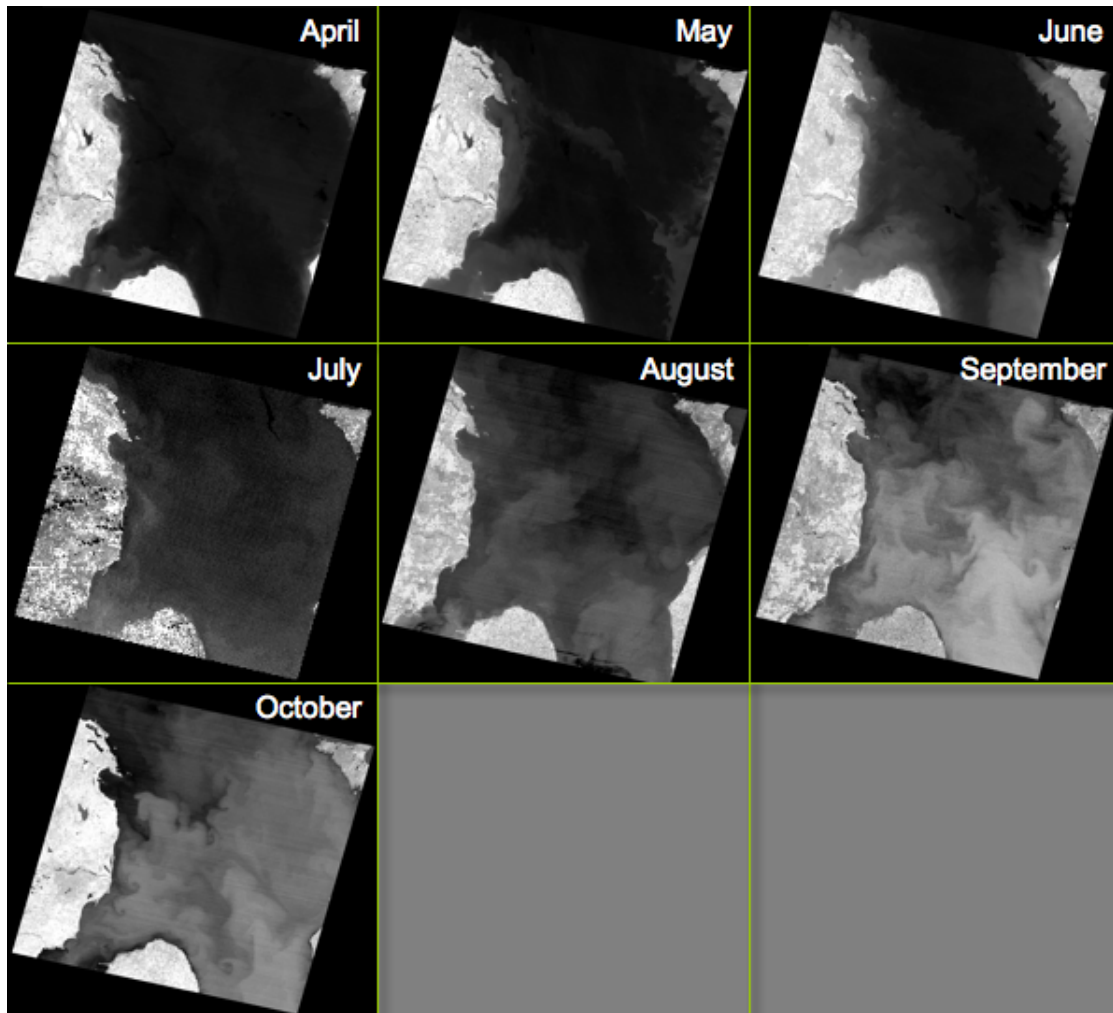


Figure 4.6: Illustration of the Lake Huron thermal bar evolution via Landsat 5 TM Band 6 imagery. Images depict typical surface properties for each of the labeled months. Notice that surface thermal variation increases towards the end of the warm season.

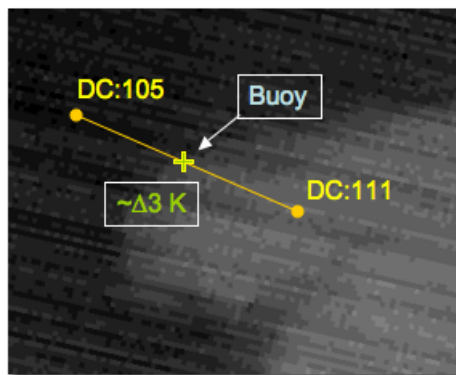


Figure 4.7: Illustrates a calibration point that would be filtered (rejected) from further processing based on high spatial variation in surface temperature.

4.1.1 Lake Superior (Site #2)



Figure 4.8: Lake Superior Calibration Site (Site #2). Image location (pink rectangle), buoy location (flag), surface observation (red +) and upper-air data (*). Note bathymetry maps have been overlaid about the Lake regions.

Landsat WRS-2 path/row 27/24 was determined to be the second consider calibration site. The site contains potentially two buoy locations (Buoy ID's: 45001 & 45004). Due to the near edge image location of Buoy 45004, any fluctuations in the satellites orbit will have the potential to make the buoy susceptible to reside outside of the image. Figure 4.9 depicts the location history of the Lake Superior moored buoys of interest. The buoys are both located in extremely deep water 45001 is located over a depth of about 261.6 m and 45004 is located over a depth of roughly 300.0 m. Lake Superior is the largest and most northerly of the Great Lakes, demonstrating a later and generally prolonged thermal bar cycle. Due to extended winter conditions the lakes moored buoys are typically deployed later in spring. Note especially in the early 1980s observations were reported in the harshest of winter months (January and February), however, these buoys were often retrieved and then later redeployed in the ensuing spring.

Another advantage of this scene is the surface observation station located at Copper Harbor at the northern limits of the Keweenaw Peninsula, MI [Figure 4.8]. The peninsula

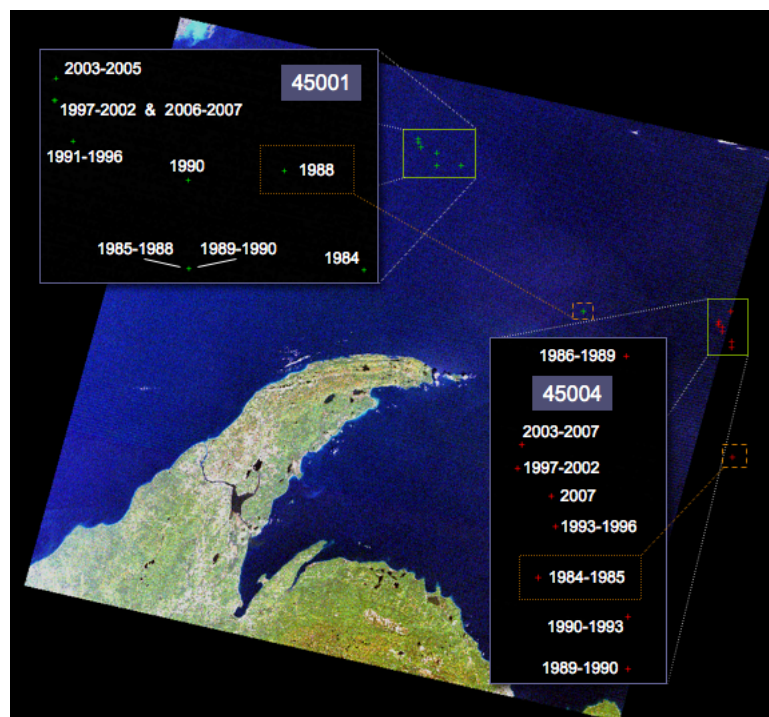


Figure 4.9: Time history of the geographic locations of buoys 45001 and 45004. Refer to Appendix G for a detailed listing of the buoy locations and deployed payloads for each year.

is located roughly within the center of the scene, thus surface observations of dew point should be quite representative of that over the buoy locations. A limiting factor to this location is its proximity to upper-air data. For the time period prior to 1995, which comprises a large window of our calibration effort, this site can utilize the observations from SSM. SSM observations, as described in Section 4.1.0.1, should provide an accurate characterization of the atmospheric column over Lake Superior. Post 1995 the upper-air locations of APX and International Falls, MN (INL) will be investigated, in that order.

4.1.2 Lake Ontario (Site #3)

This location offers overlapping image coverage of Landsat WRS-2 path/row: 17/30 and 16/30 making imagery available every 8 days. The site consists of one moored buoy location (Buoy ID: 45012) which is a relatively new member of the Great Lakes moored buoy fleet with data ranging from 2002 to present. Surface observations are used from a Canadian station at Point Petre, which is roughly 20 miles from buoy 45012 and the Rochester International Airport (ROC). Lake Ontario is also a very deep lake which does



Figure 4.10: Lake Ontario Calibration Site (Site #3). Image location (pink rectangle), buoy location (flag), surface observation (red +) and upper-air data (*). Note bathymetry maps have been overlaid about the Lake regions.

not freeze-over and experiences a thermal bar cycle similar to that of Lake Huron, if not a bit more prolonged. The rationale to investigate this site was to validate the current buoy derived effort against previous calibration studies performed by RIT on Lake Ontario.

4.1.3 Delmarva Peninsula (Site #4)



Figure 4.11: Delmarva Peninsula Calibration Site (Site #4)

To prove that this methodology is applicable outside of the Great Lakes, the final calibration site was to be chosen at an alternative location, over the domain of the NDBC North American moored buoy fleet. Using the same selection criteria as each of the previous sites, the fourth and final calibration site was determined to be in the Atlantic Ocean, south east of Delaware Bay. Similar to the Ontario site, this location offers overlapping image regions of Landsat WRS-2 path/row 13/33 and 14/33 providing imagery every 8 days. The Delaware Bay is bound by the state of Delaware and the state of New Jersey where its surroundings comprises of one of the most developed, industrialized and populated areas in the United States, Keiner and Yan (1997). The bay is part of the Delaware River Estuary.

The scene locations comprise of two buoy locations, buoy 44012 and buoy 44009. Buoy 44012 is available from 1984 to 1992 where buoy 44009 is available from 1984 to present. The buoys are located above a water depth of approximately 30 m. Note unlike the moored buoys in the Great Lakes, the ocean buoys are deployed year round offering greater potential for clear calibration quality atmospheres to be investigated.

From the beginning of our calibration window to mid 1994, radiosonde observations are available from Atlantic City International Airport, NJ (ACY) located within the scene. This is a highly desirable scenario, as the upper-air data should be quite representative (at least spatially) over the calibration site, though temporal interpolations are still necessary. For dates following 1994 radiosonde data will be used from launches released at Wallops Island, VI (WAL) roughly 30 miles from the scene location. Note upper-air data is available from WAL throughout the entire calibration period. Also note surface data is available from numerous nearby locations, however, observations from Cape May, NJ (KWWD), Millville Municipal Airport, NJ (KMIV) and Salisbury (KSBY) will be used.

Disclaimer: Potential calibration sites were investigated in all regions along the eastern seaboard, Gulf of Mexico, and the west coast of the United States. Considering all factors, the determined site was easily chosen. Its most appealing quality was that it demonstrated optimal environmental data characteristics, over all other considered sites, in addition to encompassing two buoy locations for a large portion of the study.



Figure 4.12: Time history of the geographic locations of buoys 44012 and 44009. Refer to Appendix G for a detailed listing of the buoy locations and deployed payloads for each year.

4.2 Environmental Data Sources

Moored buoy data was obtained via the worldwide-web from the NDBC at:

- <http://www.ndbc.noaa.gov/hmd.shtml>

Moored buoy locations were obtained via the worldwide-web from the National Oceanographic Data Center (NODC) at:

- <http://www.nodc.noaa.gov/BUOY/buoy.html>

Radiosonde data was obtained through NOAA's Forecast Systems Laboratory (FSL) via multiple methods. Data observed prior to 1994 was obtained from in-house NOAA North America radiosonde database CDs. Data including and after 1994 was obtained via the worldwide-web:

- <http://raob.fsl.noaa.gov>

Surface hourly observations were obtained using a global surface data visualization tool, which provides all available observations (geographically displayed) within a given region, developed by the National Climatic Data Center (NCDC) at:

- <http://gis.ncdc.noaa.gov/website/ims-cdo/ish/viewer.htm>

Landsat 5 TM Band 6 data was obtained through correspondents with NASA Goddard's Julia Barsi, however, the USGS Global Visualization Viewer was used to survey the Landsat 5 TM data archive at:

- <http://glovis.usgs.gov>

4.3 Scene Selection - Ranking Structure

All archived scenes for each calibration site were considered. To assess the quality of a given scene, a ranking structure was developed. Each scene was ranked on a scale of 1 to 5 (highest to lowest quality, respectively) based on sky condition and data availability (i.e. ground truth buoy data and atmospheric data). As described in Section 2.2, clear sky conditions are desired (i.e. cloud free). Under clear sky conditions, the atmosphere is both well behaved and well known, making the assumption that the atmosphere is non-varying throughout the scene a valid assumption. Therefore, scenes which satisfy these criteria, provided the appropriate ground truth data is available, were ranked with the highest quality (1). However, if the scene is cloud filled or has missing data (i.e. no buoy data, no upper-air data, etc.) the scene would be ranked poorly (5). On days where the atmosphere over a scene has few clouds, but over the ground truth location is clear, will be ranked (2).

This process will be performed over each calibration site. Only scenes of ranking 1 and 2 will be considered for processing [Figure 4.13]. It is particularly important that one is stern at this stage because allowing the processing of poor quality days may lead to less confidence when drawing conclusive results.

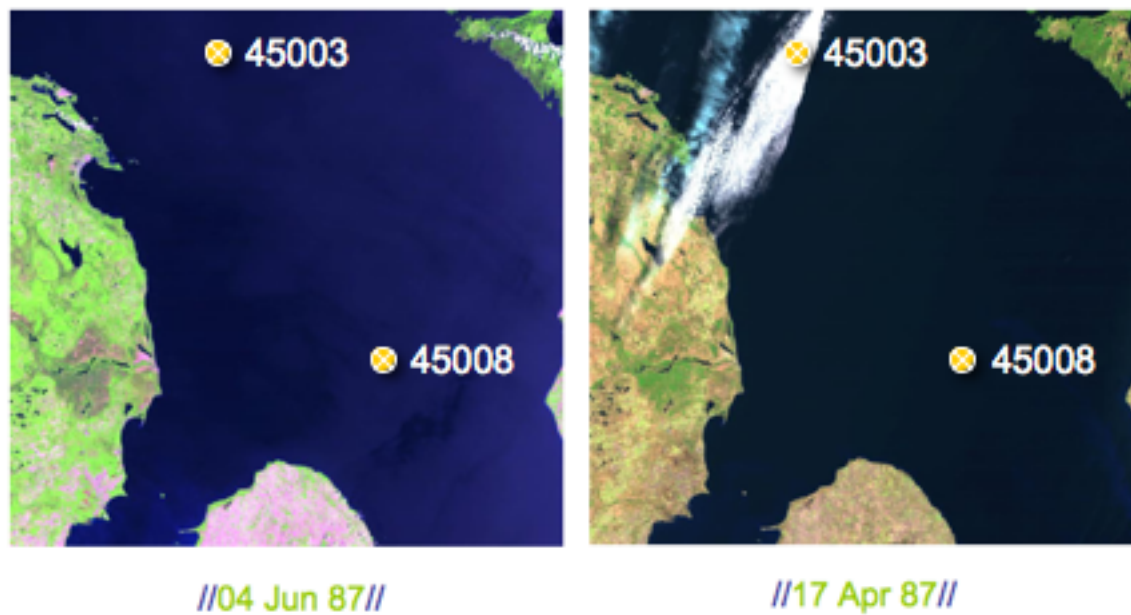


Figure 4.13: Example of ranking structure (Site #1). The scene (left) was ranked with highest quality 1 where scene (right) was ranked as a 2. Note the orange circles illustrate the Lake Huron moored buoy locations.

4.4 Process Overview

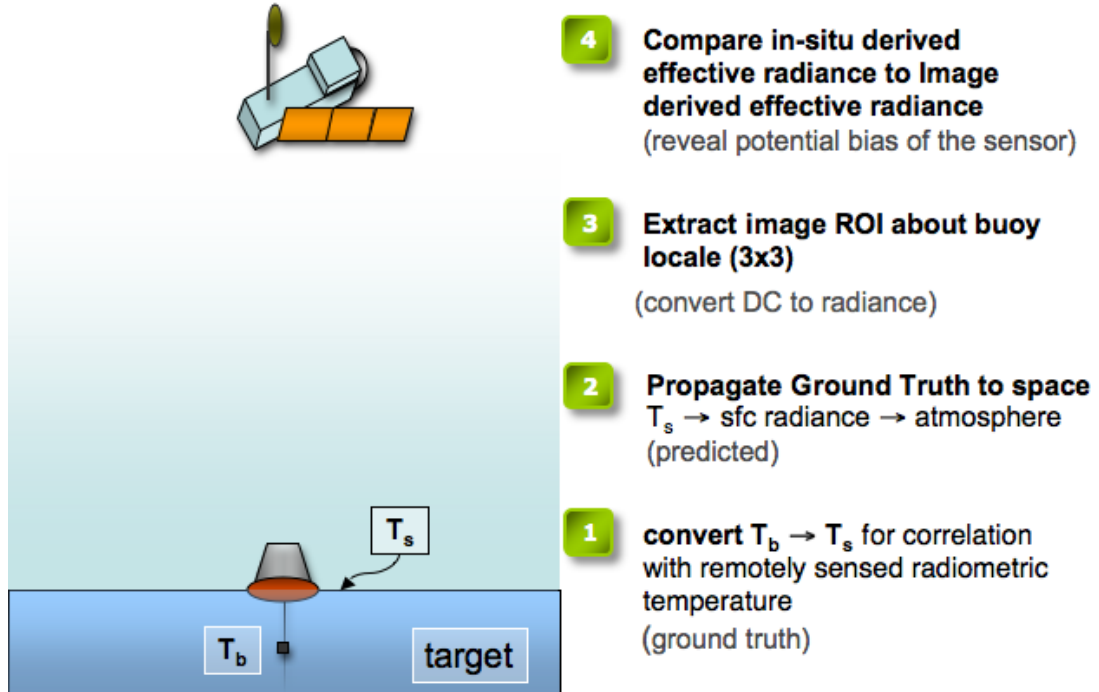


Figure 4.14: Schematic of the process overview.

The proposed process is illustrated in Figure 4.14. For correlation with remotely sensed radiometric temperature a surface skin temperature is predicted from buoy derived bulk water temperature observations. Using the predicted T_s , TM Band 6 responsivity locations, the known emissivity of water ($\epsilon = 0.986$) and the Planck Equation [Eq. 3.1] a surface leaving radiance is found. This radiance is then modified by the atmospheric terms derived from MODTRAN in an effort to compute the predicted at-sensor radiance (or effective radiance [Eq. 3.14]). Next, image ROI(s) are extracted to acquire an observed sensor radiance or image derived radiance. Lastly the image derived radiance is differenced with the predicted at-sensor radiance, which yields a point on a calibration curve.

4.5 Computation of T_b to T_s

A study comparing the skin temperature correction of [(Zeng et al. (1999) and the simplified Fairall et al. (1996) approaches, Section 2.6] was conducted, using buoy observations for 28 days. The effort here was to determine if the simplified Fairall et al. (1996) tech-

nique would be sufficient enough to use compared to the more rigorous Zeng et al. (1999) method; but also as a measure of pure comparison. Results from the study are presented in Figure 4.15 and Table 4.1. Notice [Table 4.1] the Zeng et al. (1999) correction on average is approximately 0 K, which makes physical sense because depending upon the characteristics of a given day the correction can vary in sign. Also notice [Table 4.1] the mean absolute value of the difference between the corrections from the two approaches is roughly 0.2 K. Again it is emphasized that the Zeng et al. (1999) approach is much more stringent, although both approaches for the most part yield similar results. Figure 4.15 demonstrates that overall both methods are in relatively good agreement with a few exceptions.

Table 4.1: Results from the comparison study of the two bulk to skin approaches.

Correction Statistic	Fairall et al. (1996) Approach	Zeng et al. (1999) Approach	Absolute Difference
Mean	0.123 K	-0.000485 K	0.123 K
Mean of absolute value	0.139 K	0.192 K	0.0532 K
Mean of absolute value of the difference between approaches			0.181 K

For days with weak wind speeds ($\sim \leq 3$ m/s) the Zeng correction demonstrates larger corrections than that of the simplified Fairall approach. For example, consider the days (coded [YearMonthDay]) 20060510, 20060821 and 20050601 from Figure 4.15. Each of these days demonstrated low mean wind speeds. Figure 4.16 illustrates that the difference between the two methods is greatest at low winds speeds. Recall from our previous discussion [Section 2.6] the system is more complex at lower wind speeds, thus resulting in less confidence in the proposed modeling effort. Through this study it was determined that the Zeng et al. (1999) approach will be the method of choice, therefore, will be used for all processing.

Due to our uncertainties in modeling low wind speed scenarios, bulk-to-surface corrections larger than 1°C will be flagged and investigated on the basis of its validity. Although, over periods where the 12 m hull type buoys were deployed, larger corrections are anticipated, as the thermistor depth is located 1.5 m below the surface. Conversely, at high mean wind speeds, if the discussed restrictions are not met ($-1.1 < az < 0, 1 < e^{bz} < 6$

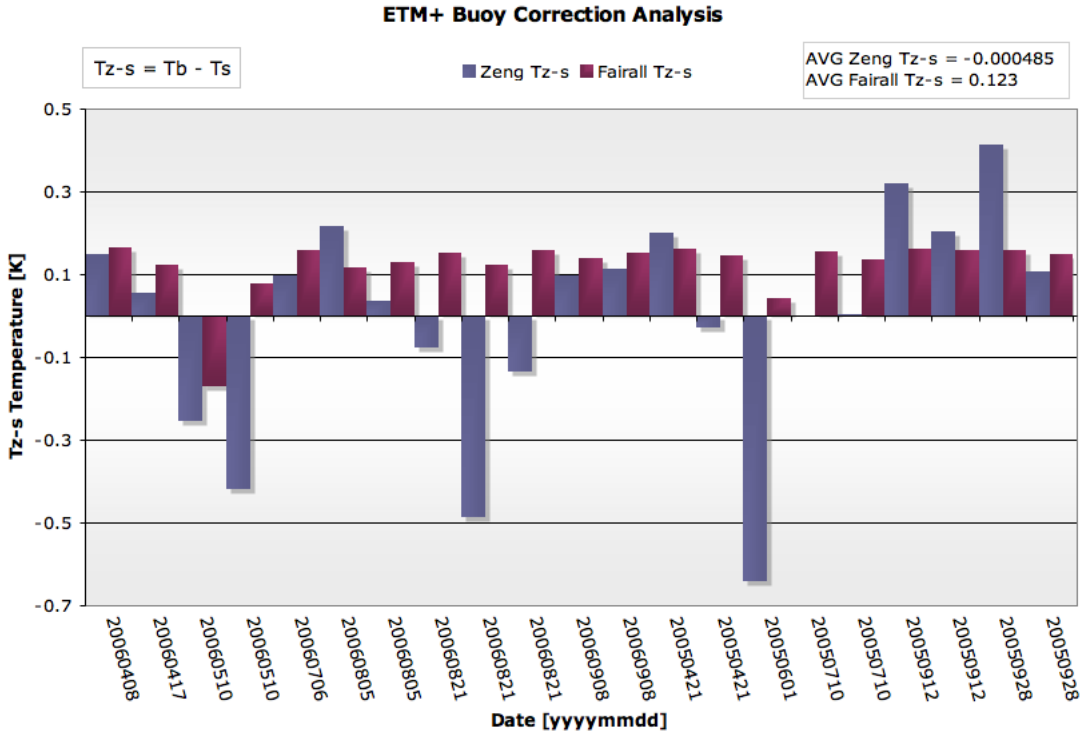


Figure 4.15: Comparison of the Zeng et al. (1999) and Fairall et al. (1996) approaches for days specified for the calibration of ETM+. Note each day with an extreme negative skin-correction were days with light winds.

and $0 < cz < 4$) the Donlon et al. (2002) cool skin value ($d = 0.17$) will be assumed the only correction needed. The rationale being at high wind speeds the warm layer will be sufficiently mixed, so that the only correction to the observed bulk temperature is for the cool skin effect. Note all corrections will be interpolated to the image acquisition time (from the image header file) to the nearest minute.

As mentioned in Section 3.6.2 the NDBC has deployed moored buoys with various payloads, hull types and locations (given the same buoy ID) over the history of each calibration site. Again, important to this study is that regardless of the payload all specifications of interest remained constant (i.e. water temperature and wind speed measurements, [c.f. Section 3.6.2, Table 3.8]). The same cannot be said for the hull types. Each hull type is associated with varying instrument heights [c.f. Section 3.6.2, Table 3.7], thus our efforts must account for these changes. Lastly, as discussed in Section 3.6.2 the exact location of each identified buoy ID fluctuates over time. Appendix G provides a detailed account of all such issues, for each identified buoy.

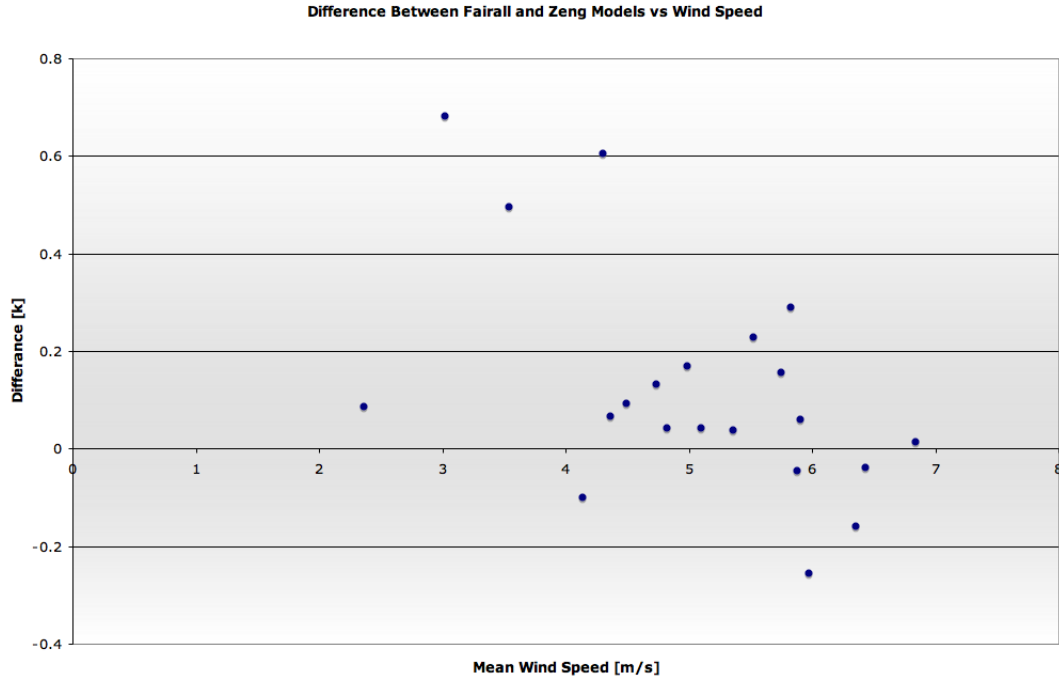


Figure 4.16: Difference between methods vs averaged wind speed. Note that larger differences occur at lower mean wind speeds.

4.6 Recreation of the Atmospheric Column

As discussed in Section 2.3.4, an accurate recreation of the state of the atmosphere (i.e. atmospheric column) at the time of image acquisition is needed as input into MODTRAN to obtain the appropriate atmospheric variables in the formulation of a predicted at-sensor radiance. The goal of this effort is to create a representative atmospheric column, from the water surface to 100 km, over each of the specified buoy locations, given the available data. Provided the limitations of available data, we are restricted to processing at three atmospheric levels [Figure 4.17]: 1) the surface (using surface observations (buoy, Automated Surface Observing System (ASOS)), 2) lowest 15-35 km (radiosonde profiles) and 3) from the vertical extent of the radiosonde sounding to 100 km, where an upper-air model is appended to the radiosonde profile.

As discussed in Sections 3.4 and 3.5.2, the lower atmosphere (essentially the troposphere) is the most important layer in regards to this study. As shown in Figure 4.17, information regarding the troposphere and the lower stratosphere are provided by radiosonde observations, thus accounting for the bulk of necessary data. Surface data is used to further refine the assimilated column with data taken by observations surround-

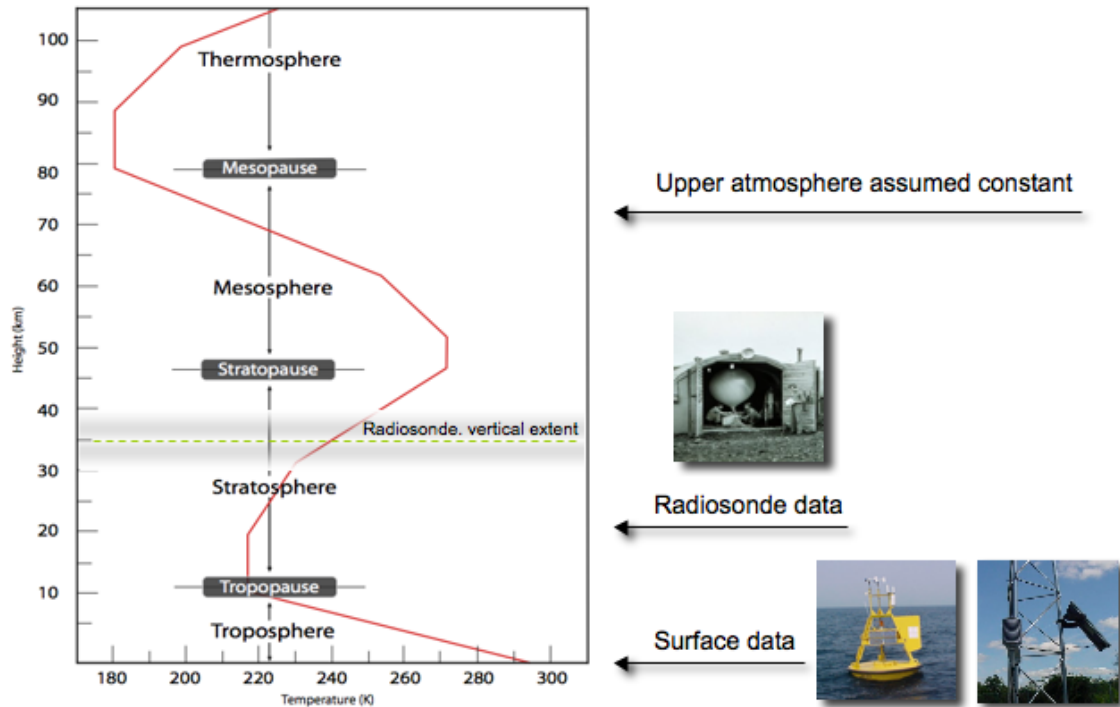


Figure 4.17: Illustrates that the atmospheric column is generated using all available data sources: surface, radiosonde, and upper-air model.

ing the hour of image acquisition. This correction is necessary due to the spatial and temporal characteristics of NOAA's radiosonde network. Each considered calibration site has an associated near Noon image acquisition time. As mentioned above, the WMO has standard upper-air observation locations and times (12 UTC and 00 UTC), thus spatial and temporal interpolations are necessary to recreate the state of the atmosphere over the specified buoy locations. Again, processing is performed at both the surface and aloft.

Processing on a given day begins by plotting both the 12 UTC and 00 UTC soundings in an effort to identify the most relevant sounding, as described in Sections 4.1.0.1 - 4.1.3. Consistent with the methodology [Section 2.2], each sounding will be investigated based upon a subjective measure of the total water vapor column present in each profile. The apparent moisture content within each column can be determined subjectively by a measure of dew point depression (DD). DD is the difference between the temperature and dew point temperature. As a general rule of thumb, a $DD \leq 3^{\circ}\text{C}$ can be considered as a saturated layer (i.e. in radiosonde profile: visible cloud). Thus, when observing radiosonde

profiles, moist layers and cloud layers can be identified by simply observing the DD. For clarity an example of the proposed atmospheric column generation is provided. Figure

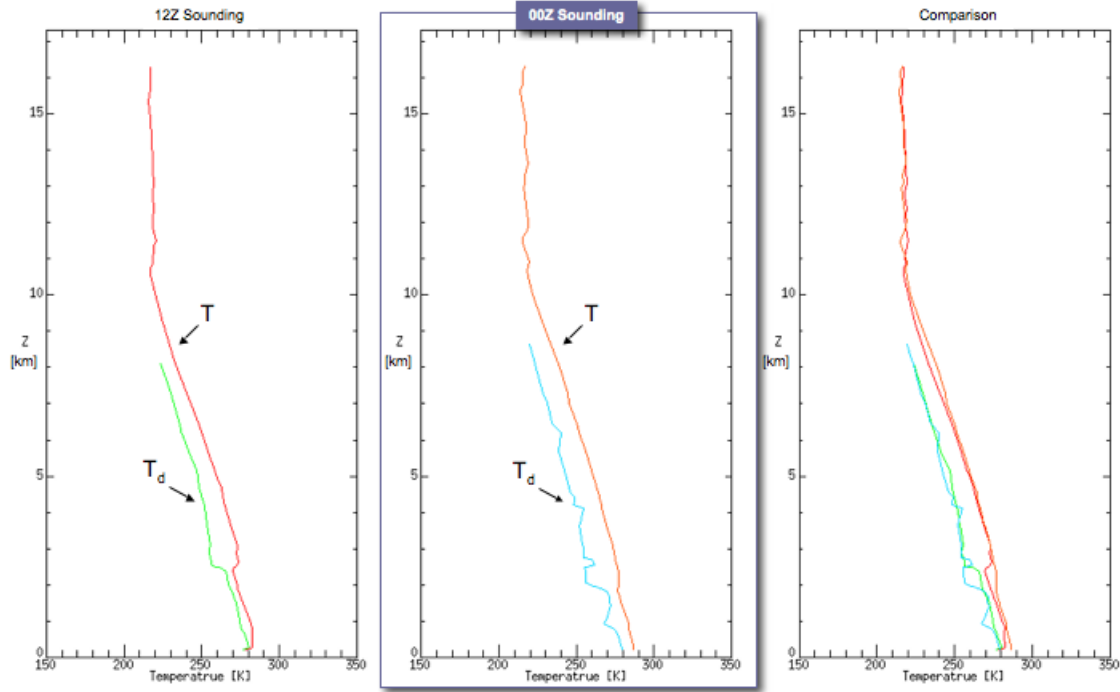


Figure 4.18: IDL tool developed to display and compare 12 UTC & 00 UTC radiosonde profiles. Note that the 12 UTC sounding is roughly saturated at the surface 00 UTC profile followed by a relatively moist layer capped ~ 2.5 km by a subsidence inversion. The 00 UTC sounding is less moist in comparison thus would be chosen to continue processing. The radiosonde profiles were observed from SSM on September 24, 1993.

4.18 illustrates morning and evening soundings from SSM on September 24, 1993. Note that the 12 UTC profile is roughly saturated at the surface followed by a relatively moist layer capped by a subsidence inversion at ~ 2.5 km. In contrast, the 00UTC profile [Figure 4.18] portrays less moisture, and was therefore chosen for further processing. Notice the dew point profile [Figure 4.18: green & blue lines] in each sounding have an approximate vertical extent of only roughly 8 km. As stated in Section 3.6.1, all soundings prior to 1993 did not report RH measurements below -40 °C, issued by the NWS because of the measurements known uncertainty. Methods to account for such absence of data will be discussed in Section 4.6.2. Lastly notice the plot [Figure 4.18 (right)] illustrating the comparison of the two soundings. Through simple visual inspection it is generally shown that as height (z) increases the difference between observations decreases, even with a

12 hour difference in observation time (note the atmospheric domain of this study is restricted to ideal atmospheric conditions for vicarious calibration, as discussed in Section 2.2). Consider another sounding comparison [Figure 4.19]. Illustrated are profiles which are more representative of modern radiosonde observations in reference to their vertical extent. Once the appropriate profile is determined for each day, the remaining structure

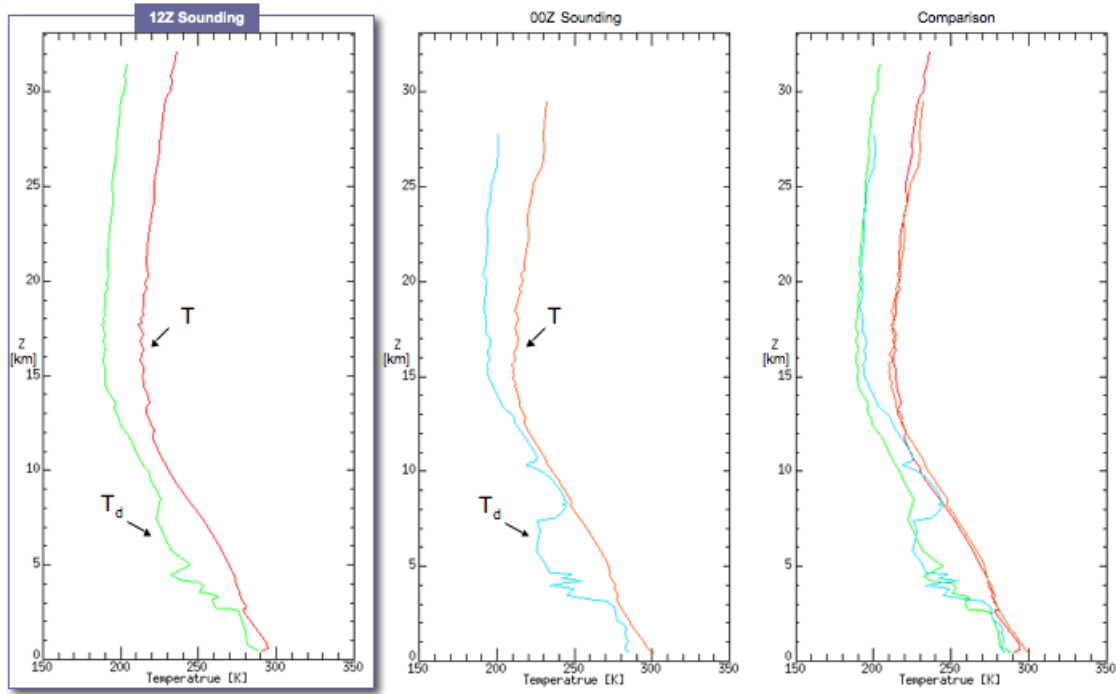


Figure 4.19: 12 UTC (right) & 00 UTC (left) radiosonde profiles from APX on July 20, 1998. The 12 UTC sounding has moist layers at the surface and ≈ 3 km. The 00 UTC profile portrays a roughly saturated layer with a depth of ≈ 5 km beginning at ≈ 8.5 km. The 12 UTC profile was chosen for further processing, however, the moist layer at ≈ 3 km was recognized and recorded.

of atmospheric column can be completed. The remaining steps of this process contain the surface interpolation and extrapolation, which includes joining a dew point temperature with buoy observations, as well as, accounting for the difference in altitude from the radiosonde profile and the water surface [Section 4.6.1]. The final step is to append and interpolate the upper atmospheric model to the observed data [Section 4.6.2].

4.6.1 Surface Correction

As shown above the atmospheric state variables (i.e. temperature (T), pressure (P_x), and dew point temperature (T_d),) are much more variant at the surface than that of the free atmosphere (i.e. above the boundary layer $\sim 1-2$ km). Recall that radiosonde observations are historically available typically only twice a day for a given location within the upper-air network. Surface observations are available hourly from both buoy platforms and near by surface stations. Thus, an atmospheric profile from a radiosonde observation can be adjusted by surface observations to account for any near surface modifications in the atmosphere at times different from sounding launch time (i.e. at the time of image acquisition). For the hours surrounding the time of image acquisition a surface interpolation is performed to interpolate the atmospheric variables of T , P_x and T_d to the time of image acquisition. The interpolated values are then extrapolated to the height of the boundary layer so that the generated atmospheric profile takes into account any near surface state modifications within the boundary layer [Figure 4.20], described in Schott (2007). Surface readings from radiosonde observations, taken over land, will generally be at an altitude higher than that of the desired water surface. Thus the extrapolation extends from the water surface to the height of the boundary layer. Note this approach assumes that the surface material type is uniform (i.e. uniform surface heat flux), so that the assumption to modify the profile to the height boundary layer holds true.

In cases where there is a sufficient discontinuity in surface type and surface heat flux (i.e. warm land to cold water) a similar correction to the above mentioned will be implemented using the IBL height as the point to extrapolate to [Figure 4.21]. Each day will be investigated for the presence of an IBL [Section 3.4.1.1] by use of Eq. 3.15 to calculate the IBL height h . Our implementation of h is as follows: land mixed layer values are taken from the 12z sounding. To adjust for surface warming, the lowest layer of the mixed-layer is replaced by surface observation temperature measurements averaged for the hours of 13 and 14 UTC (around 1 - 2 hours before image acquisition), as that is the air that is advected over the calibration site. The remaining needed data is obtained via buoy observations. Typical fetches for the proposed scenes are roughly 50 - 100 km depending on the prevailing wind direction. As recommended by Garratt and Ryan (1989), an $\alpha = 0.02$ was used. Understand that this calculation is used as a ballpark figure. In practice,

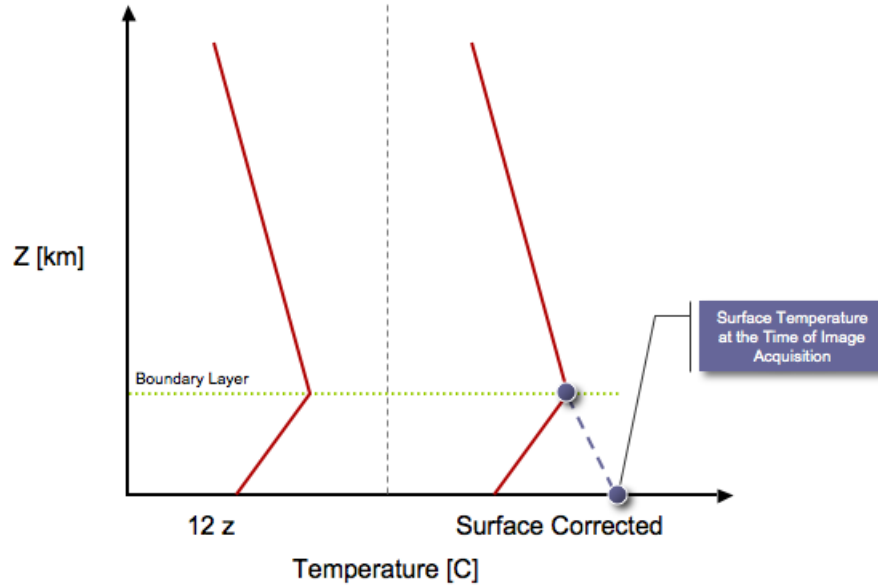


Figure 4.20: Schematic of the boundary layer surface correction described by Schott (2007). Original radiosonde profile (left) and surface corrected (right).

as described in Section 3.4.1.1, the predicted IBL height is valid to within 25-50% for x values of at least 5 - 300 km. Because field campaigns noted that this prediction is often an underestimate of the true IBL height, this approach used the maximum bound for the given fetch as the predicted IBL height. Typical values of the predicted IBL heights for the chosen sites should range from 30 m - 200 m, resulting in using heights ranging from 50 m - 300 m. Using the predicted IBL height, the nearest level in the chosen radiosonde sounding is then identified. This location is then used as the vertical extent of our surface extrapolation. Again, Figure 4.21 illustrates a schematic of the surface correction using the IBL as the vertical extent of the extrapolation. Note that the surface correction using the IBL height is typically shallower than the surface correction using the BL height.

Physically, this interpolation accounts for how the vertical profile observed over land will be modified as it is advected over the cooler water surface. Realize that if the water surface is warmer than that of the overlaid air-mass, the vertical extent of the surface interpolation process should be extended to the height of the boundary layer, as described in Section 3.4.1. In the event that the IBL height is not sufficient or non-existent the height calculation h returns the value "N/A". Figure 4.22 provides an example of such processing from a radiosonde at SSM on 17 May 1999 (site 1). Notice that a large surface inversion was created due to processing. This result makes physical sense if one considers

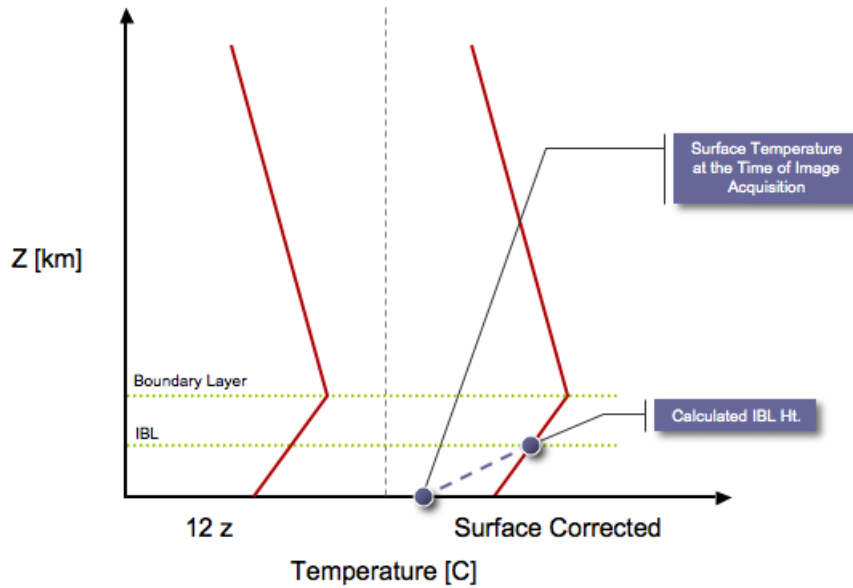


Figure 4.21: Schematic of the internal boundary layer surface correction. Original radiosonde profile (left) and surface corrected (right).

the lake temperature of 3°C and the warmer atmosphere overrunning it, resulting in a very stable and shallow IBL or marine boundary layer.

Through various case studies it appears the introduction of the IBL influences the resulting apparent temperature, on average, by roughly a tenth Kelvin; with the caveat of warm moist atmospheres demonstrating greater sensitivity (larger differences), compared to cool dry atmospheres, where differences were smaller and at times almost negligible [Appendix C]. A study was also performed to quantify the sensitivity of the proposed surface correction (i.e. IBL present and absent) compared to simply using the given radiosonde observations with the upper air modeled append. The study showed that the surface corrections are small in nature (typically ~ 0.1 K), however, significant in the recreation of the atmospheric column, as differences can exceed 1 K [Appendix D].

Recall the atmosphere directly over the calibration site is sampled hourly by NDBC moored buoys, providing temperature and pressure observations, however, dew point observations are typically not observed by NDBC moored buoys. This is a critical parameter because it represents a moisture metric in the most dense part of the atmosphere. To obtain a surface dew point temperature representative of that over the buoy location, at

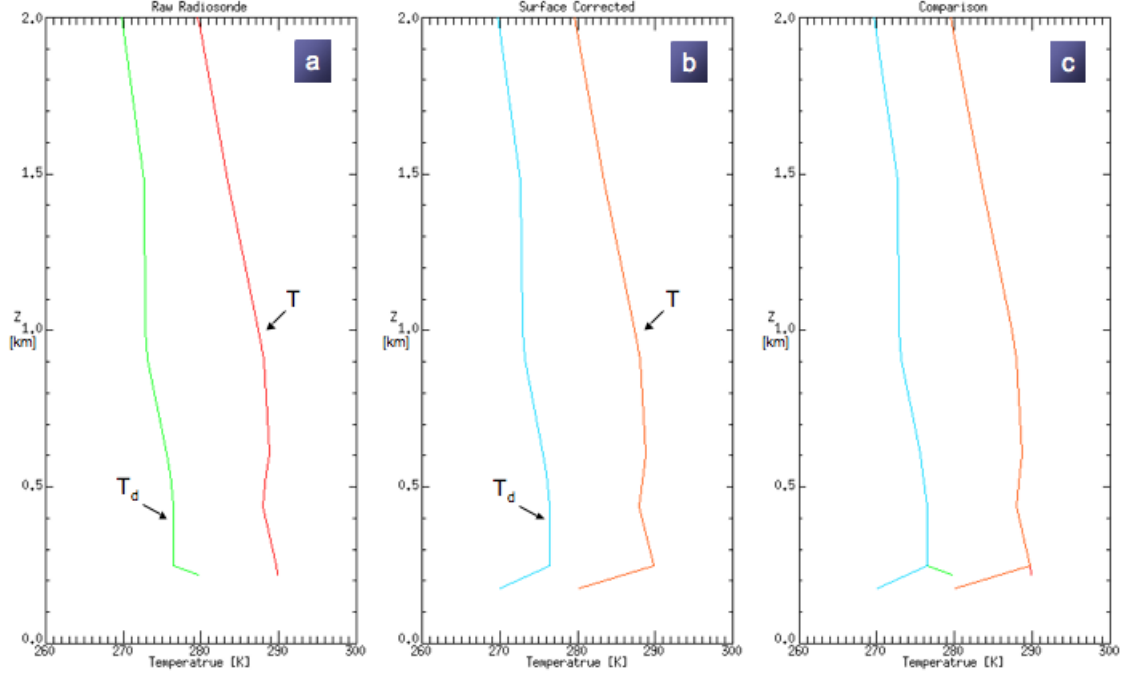


Figure 4.22: SSM 27 May 1990, 00z sounding: (a) Raw radiosonde observations. (b) Surface corrected profile, which represents the state of the surface atmosphere over the intended calibration location at the time of image acquisition. (c) Comparison plot.

the time of image capture, dew point measurements are obtained from the nearest surface hourly observation station. This dew point reading is typically merged with the accompanying buoy temperature and pressure observations. Due to image acquisition times generally occurring within the hour, the surface hourly data are interpolated using a linear interpolation scheme using the hour prior and post image capture. Realize that this method has the main limitation that the marine boundary layer (mid lake/open ocean) is often much cooler than that of the boundary layer over land, especially near noon LST. Resulting in the situation where the surface observation dew point observation is greater than that of the buoy dew point observation. To account for such an event the surface observation dew point depression is determined and applied to the buoy derived temperature to obtain a buoy surface dew point observation:

$$T_{d,buoy} = T_{buoy} - DD_{sf c obs} \quad [K] \quad (4.1)$$

Eq. 4.1 is used for the hours surrounding the time of image acquisition and interpolated

as previously mentioned.

This processing results in a radiosonde profile both spatially and temporally interpolated to account for the state of the surface atmospheric conditions at the time of image acquisition over the intended calibration location.

4.6.2 Upper-Air Interpolation & Processing

Two objectives are considered in regards to the proposed upper-air processing. To begin, an assumption is made that the upper atmosphere is static (i.e. from the vertical extent of the given sounding to 100 km). This is a reasonable assumption given our prior discussion [Section 3.4.3]. The MODTRAN supplied standard atmosphere: mid latitude summer profile will be used for the characterization of the "static" upper atmosphere [Figure 4.23]. Again only, the modeled profile's upper atmospheric data will be appended to each

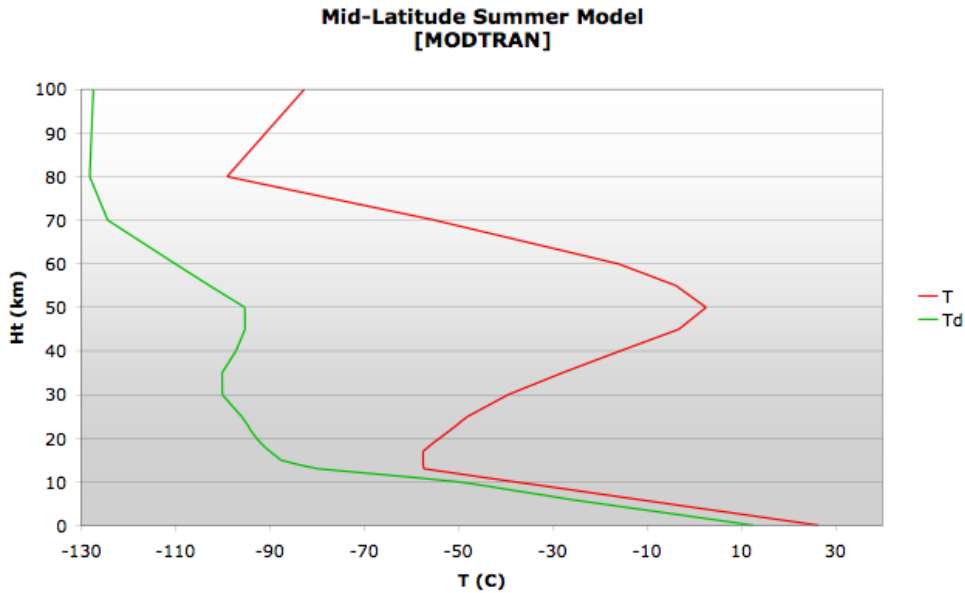


Figure 4.23: Illustrates one of MODTRANs standard atmospheres: Mid-Latitude Summer. radiosonde profile, resulting in a complete atmospheric column with the vertical extent of 100 km. Due to varying radiosonde observations the modeled data is rarely appended appropriately. For example, observe the 12 UTC radiosonde from APX on October 5, 1997 with MODTRANs mid latitude summer profile appended [Figure 4.24 (a)]. It is apparent through visual inspection that the temperature profile of the two profiles fit relatively well (which typically is observed). However, notice the modeled dew point profile and

the observed radiosonde dew point profile are not in agreement. To account for this issue the modeled dew point profile will be adjusted so that the two profiles adjoin smoothly [Figure 4.24 (b)]. Note this process typically involves adjustment of only a few layers and is common for radiosonde observations after 1994.

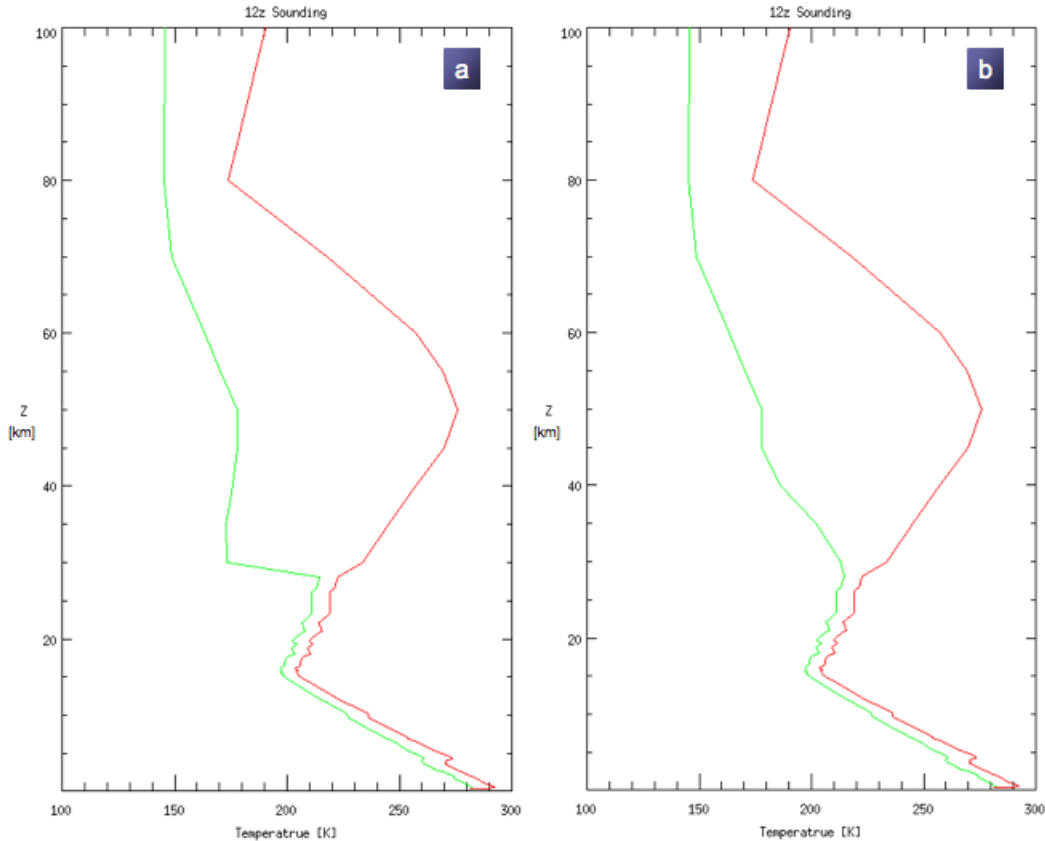


Figure 4.24: (a) 12 UTC radiosonde from APX October 5, 1997 (T - red & T_d - green), with MODTRANs mid latitude summer profile appended (T - orange & T_d - blue). Note the dew points from each profile are not in agreement, however, the temperature profiles are. (b) Resulting profile after processing the model dew point profile to be in agreement with the observed data.

For years prior to 1993 dew point measurements typically only reached a vertical extent of roughly 8-9 km. Thus, a new method is needed to adjoin the upper atmosphere, as well as interpolate missing observations from the mid latitude summer profile to a given atmospheric profile. Using IDL, a visualization tool was developed so that the user could plot both the given radiosonde profile and model profile to define the level at which to interpolate the too [Figure 4.25 (a)].

This processing takes the existing observed temperature radiosonde layers and inter-

polates the T_d profile from the last reporting altitude in the radiosonde profile, to a user defined altitude on the modeled T_d profile. In an effort to conserve existing information about the moisture content in the upper troposphere, the DD is found from the last reporting altitude observing both temperature and dew point. This DD is then conserved to the bottom of the tropopause (nominally 11 km). This assumption of a common upper tropospheric DD makes physical sense as the upper troposphere is relatively non-varying, within the restricted atmospheric domain of this study. More importantly, such processing results in little if any change in resulting apparent temperatures. Again stating, that warm moist atmospheres contribute the most to biases in sensor reaching radiance, thus as the altitude increases these affects are increasingly less important. With this said, the processing will continue to conserve the last reported DD as it makes reasonable physical sense, although not altering the final output, see Appendix E. Also c.f. Appendix H regarding the user work flow.

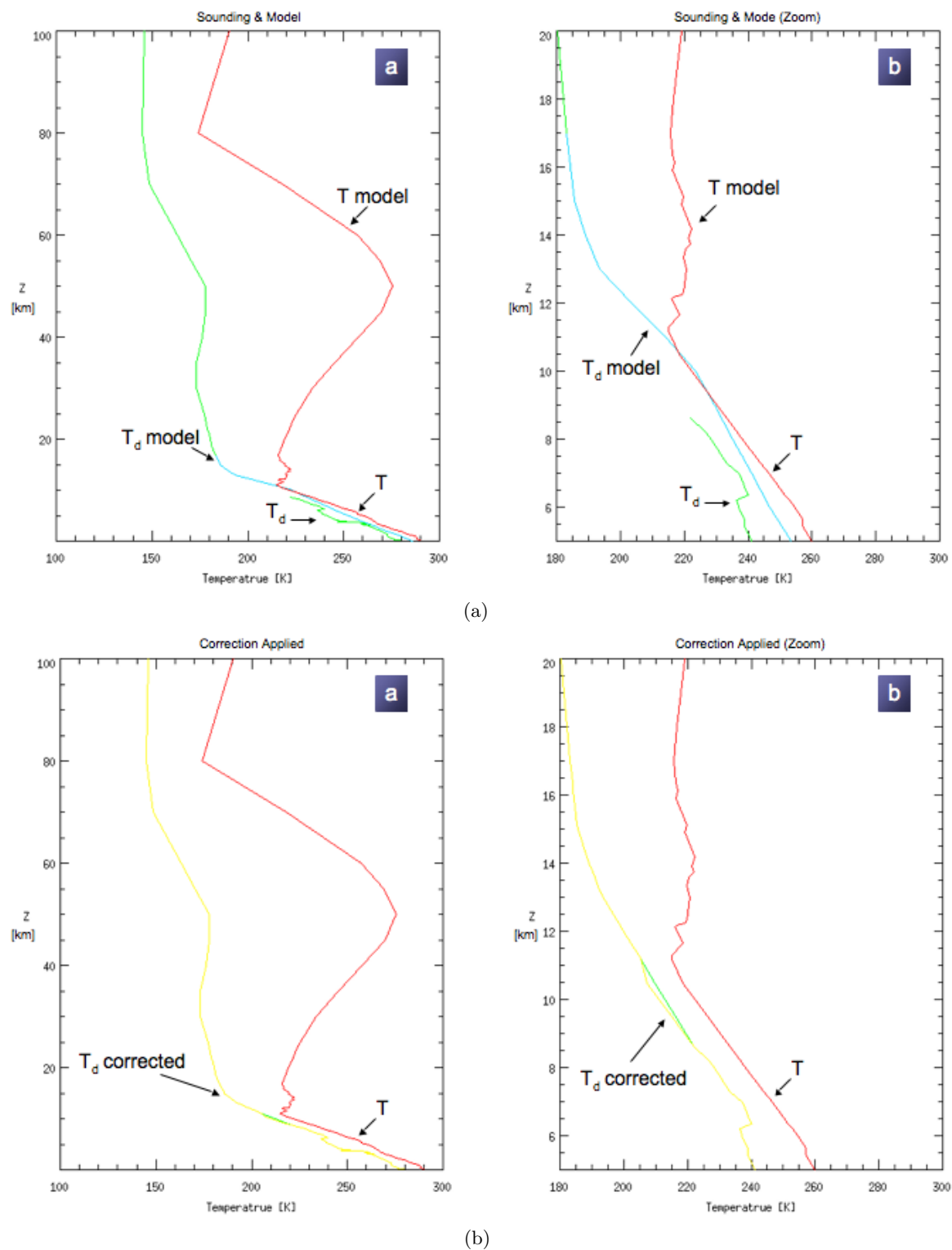


Figure 4.25: (a) SSM radiosonde May 27, 1990 - T (red) and T_d (green). MODTRAN mid latitude summer T_d profile (blue). (b) Final T_d profile.

4.7 Alternative Atmospheric Data Sources

The utility of atmospheric model data for vicarious calibration processes is investigated. The motivation is to allow for the confidence for future work to reach outside of the restrictions of the current NWS (or global) radiosonde network(s) and explore more exotic site locations. Discussed here are two different forms of atmospheric model data, which provide atmospheric profiles of temperature, pressure and moisture for a given location.

The first data source is intended for strictly historical studies and is termed Reanalysis. For example, NOAA has a data set referred to as the Reanalysis Project, and is a joint project between the National Centers for Environmental Prediction (NCEP) and the National Center for Atmospheric Research (NCAR). Note there are numerous reanalysis data sets, yet all are based on the principle of initializing a modern "trusted" atmospheric model with observed historic data. The simulation thus, begins at some point in history (nominally the 1950's for most data sets) and propagates forward at nominally 6 hr intervals. The output yields a gridded global assimilation, which fills in vast temporal and spatial data gaps about the earth. Thus providing information on atmospheric state variables in data sparse areas throughout history.

NOAA's Reanalysis data set spans the period from 1948 to present with a coarse grid-point spacing of 2° lat/lon and 28-60 vertical layers. Another data set is provided by the European Center for Medium range Weather Forecasting (ECMWF) forecast model [<http://dss.ucar.edu/pub/era40/>], which spans from 1957-2002, has 60 vertical layers and a grid-spacing of 125 km. This data is widely accepted, for example, Merchant et al. (1999) used the data set to validate temperature retrievals from the along-track scanning radiometer (ATSR) about various ocean locations.

The disadvantages of this type of data type is that it is large and cumbersome to work with, especially for the purposes in this study (i.e. obtain atmospheric profiles of T, Td and pressure). To acquire the needed data, the user must data mine about a given grid point of interest, to extract the desired state variables about each layer. Note if the desired location does not fall on a grid point an interpolation scheme must be implemented to acquire the appropriate data.

In terms of future and or current calibration efforts the BUFKIT data set is proposed.

BUFKIT is a forecast profile visualization and analysis tool kit developed by the staff at the National Weather Service (NWS) office in Buffalo and the Warning Decision Training Branch (WDTB) in Norman, OK [<http://www.wbuf.noaa.gov/bufkit/bufkit.html>]. The data offers hourly generated forecast soundings, via interpolation of traditional deterministic model output, over a given point on the earth's surface. In other words, for every hour a point forecast (for a given Lat./Lon.) of the atmospheric column is generated. The models are initialized four times daily: [00z, 06z, 12z, 18z] and provide the variables of interest: temperature, dew point, pressure and height. Unfortunately this data is not archived well, although, Penn State University (PSU), has an archive of data ranging roughly 2004 to present [<http://www.meteo.psu.edu/bufkit/>]. If one is interested in obtaining historic BUFKIT data the recommended option is to contact the local National Weather Service Office. Lastly, note that for every buoy location used in this effort, BUFKIT interpolation points are publicly and freely available [Figure 4.26] (points identified by the NWS and the NCEP).

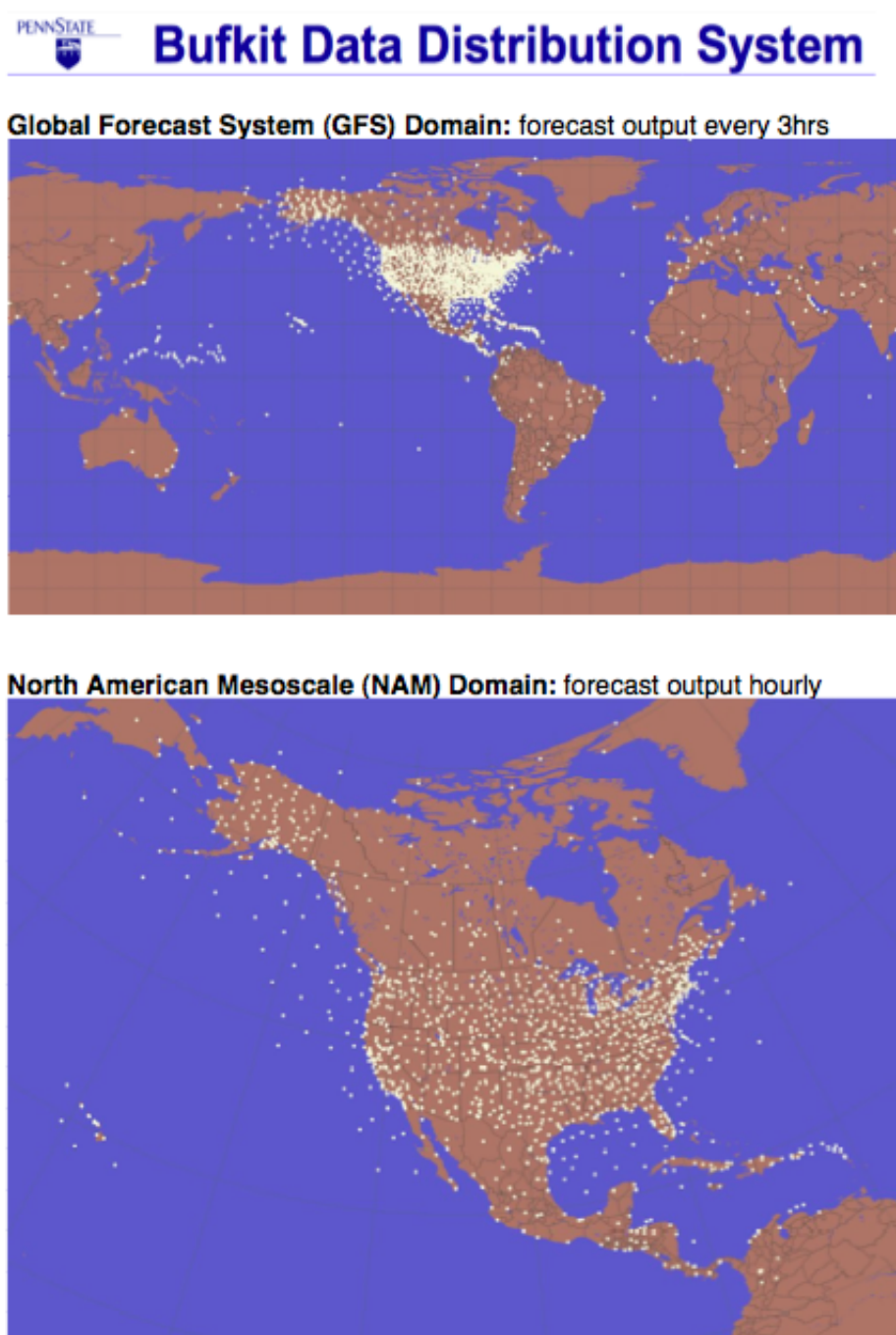


Figure 4.26: Illustrates the wide availability of data provided two model sources that can be used in this assimilation package.

4.8 Extracting Atmospheric Terms

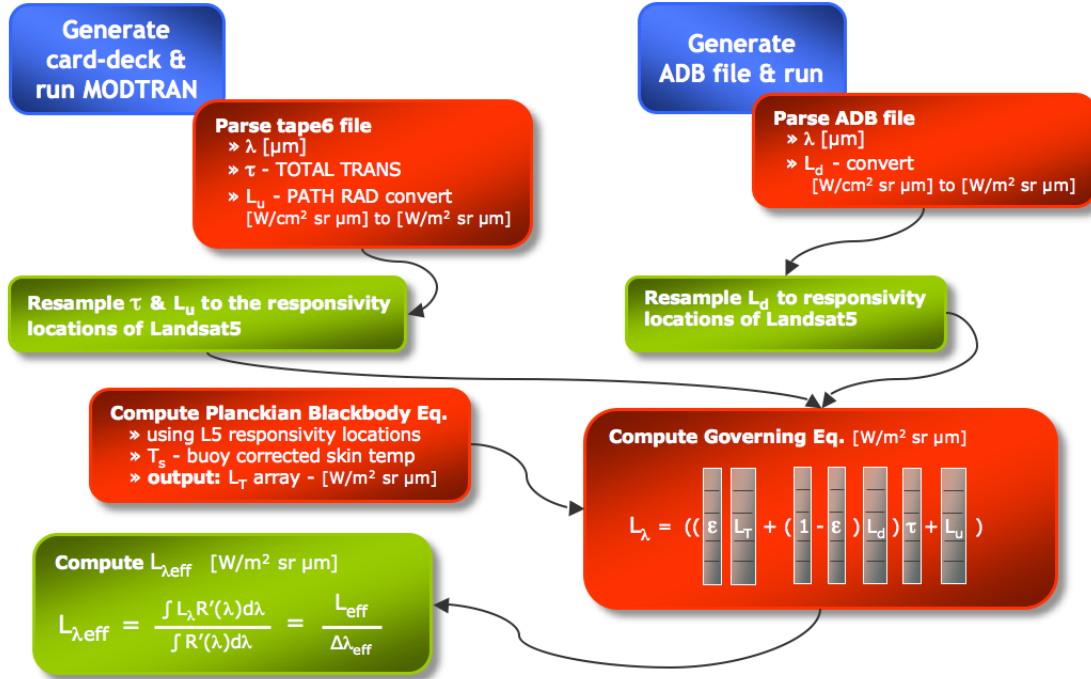


Figure 4.27: Computation of an effective radiance.

From the understanding of the use of MODTRAN [Section 3.5.3], solutions to upwelled radiance, downwelled radiance and atmospheric transmission are found for each day, over each individual calibration site. Using the methods described above [Sections 4.6.1 and 4.6.2], the assembled atmospheric column over each buoy is used as input to MODTRAN. (Appendix I illustrating the formatting needed to convert the derived column into the appropriate model format). Figure 4.27 illustrates the user workflow that was developed for the computation of a predicted at-sensor effective radiance [Eq. 3.14].

Data parsing is performed on the MODTRAN output "tape6" file. Extracted values of wavelength $[\mu\text{m}]$, transmission and path radiance (upwelled radiance) $[\frac{W}{\text{cm}^2 \text{sr} \mu\text{m}}]$ will be obtained from each run. MODTRAN in conjunction with DIRSIG is used to obtain downwelled radiance, as DIRSIG provides a spatial platform to compute the hemispherical integration [Eq. 3.26]. The output from DIRSIG provides an atmospheric database (ADB) file which is parsed to obtain the spectral downwelled radiance values $[\frac{W}{\text{cm}^2 \text{sr} \mu\text{m}}]$. Once the appropriate files have been parsed the units of both upwelled and downwelled radiance

are converted from $[\frac{W}{cm^2 sr \mu m}]$ to $[\frac{W}{m^2 sr \mu m}]$. All terms were computed with a fine spectral resolution, thus, it is necessary to resample each spectral term to the sensor responsivity locations defined by the Landsat 5 Band 6 responsivity file [Figure 3.5].

By obtaining a skin temperature T_s [Section 4.5], a surface leaving radiance vector can be found. This is accomplished using the Planck Equation [Eq. 3.1] and the known spectrally flat [Figure 2.4] emissivity of water, approximated to be $\epsilon = 0.986$. A radiance to temperature LUT was generated, as discussed [Section 2.5] and then used to obtain a T_s . The LUT is valid over a the temperature range of -3 to 35 °C, using a $\Delta T = .001$ K resulting in 36,000 element LUT. Note that the Plank Equation [Eq. 3.1] was solved independently for each temperature using the responsivity locations of Landsat 5 Band 6, thus a unique LUT is needed for each unique sensor. A predicted at-sensor effective radiance L_{eff} is then found [Eq. 3.14], which includes the peak normalized response of Landsat 5 Band 6 $[\frac{W}{m^2 sr \mu m}]$.

4.9 Obtain Image Derived Radiance

The next step in the proposed vicarious calibration process is to obtain an image derived radiance. This is obtained by extracting image ROI(s) about the known buoy location(s). To achieve a factor of three reduction in noise, a 3x3 averaged pixel ROI will be used [Figure 4.28]. TM band 6 has a ground spot distance (GSD) of 120 m x 120 m, therefore

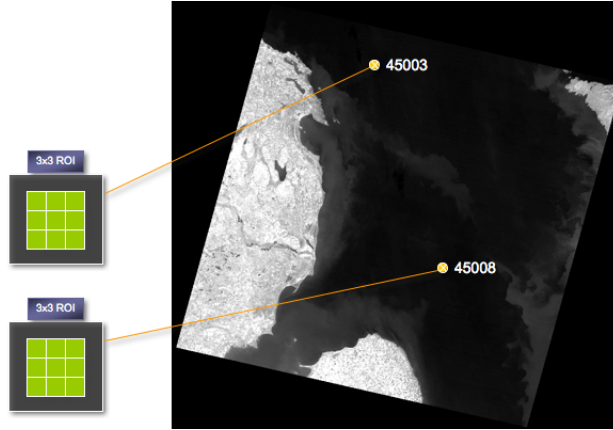


Figure 4.28: Illustration of obtaining the image derived radiance.

the area of the ROI is $129,600m^2$. To convert the area averaged digital count (DC) values

to radiometric values the following expression was used:

$$L = (DC_{avg} * gain) + bias \quad \left[\frac{W}{m^2 sr \mu m} \right] \quad (4.2)$$

where DC_{avg} is the area averaged DC values from the image, while the gain and bias values were taken from the image header file.

A comparison of the image derived radiance to the predicted at-sensor radiance, yields the final step in our processing. For clarity and consistency the following expression will be used throughout:

$$\Delta L = L_{image} - L_{predicted} \quad \left[\frac{W}{m^2 sr \mu m} \right] \quad (4.3)$$

where L_{image} is the image derived radiance and $L_{predicted}$ is the predicted at-sensor radiance, which intuitively means if ΔL is positive the sensor is reading hot (warm bias), likewise, if ΔL is negative the sensor is reading cold (cold bias). Using the radiance to temperature LUT mentioned in Section 4.8, the radiance values were converted to temperature then differenced in the order shown in Eq. 4.3, see Appendix H for user workflow.

4.10 Landsat 7 Process Validation Study

As discussed briefly in Section 3.1.2, the thermal band (Band 6) of the ETM+ instrument onboard the Landsat 7 satellite will be used in an effort to validate the proposed methodology against the known and trusted state of the Landsat 7 thermal band. In other words a calibration study will be conducted using the proposed methodology on Landsat 7 data. A calibration curve will be generated and compared to the results of both JPL's and RIT's vicarious calibration data, in an effort to develop confidence that the proposed methodology does not introduce artifacts into the calibration results and can be used confidently over the lifetime of Landsat 5. The study will use data from all calibration sites noted above.

4.11 Error Propagation: Process Error

Applying the general form of Eq. 2.17 on the governing equation [Eq. 3.14] an error analysis [Section 2.7] will be performed to deduce the confidence levels regarding the final calibration results; the following expression is used:

$$S_{L_{eff}} = \left[\left(\frac{\partial L_{eff}}{\partial \epsilon} S_\epsilon \right)^2 + \left(\frac{\partial L_{eff}}{\partial L_{BB}} S_{L_{BB}} \right)^2 + \left(\frac{\partial L_{eff}}{\partial L_d} S_{L_d} \right)^2 + \left(\frac{\partial L_{eff}}{\partial \tau} S_\tau \right)^2 + \left(\frac{\partial L_{eff}}{\partial L_u} S_{L_u} \right)^2 + 2\rho_{\tau, L_u} \frac{\partial L_{eff}}{\partial \tau} \frac{\partial L_{eff}}{\partial L_u} S_\tau S_{L_u} + 2\rho_{\tau, L_d} \frac{\partial L_{eff}}{\partial \tau} \frac{\partial L_{eff}}{\partial L_d} S_\tau S_{L_d} + 2\rho_{L_u, L_d} \frac{\partial L_{eff}}{\partial L_u} \frac{\partial L_{eff}}{\partial L_d} S_{L_u} S_{L_d} \right]^{\frac{1}{2}} \quad (4.4)$$

where:

$$\frac{\partial L_{eff}}{\partial \epsilon} = L_{BB} \tau - L_d \tau$$

$$\frac{\partial L_{eff}}{\partial L_{BB}} = \epsilon \tau$$

$$\frac{\partial L_{eff}}{\partial L_d} = \tau - \epsilon \tau$$

$$\frac{\partial L_{eff}}{\partial \tau} = \epsilon L_{BB} + L_d - \epsilon L_d$$

$$\frac{\partial L_{eff}}{\partial L_u} = 1$$

Table 4.2: Listing and declaration of error terms in Eq. 4.4.

Error Term	Value	Source
S_ϵ - emissivity	0.006	Average: Barsi (2000) & Konda et al. (1994)
$S_{L_{BB}}$ - target radiance	0.0473 [W/m ² srμm] or 0.358 K	(error prop. below)
S_τ - transmission		Case Dependent
S_{L_d} - downwelled rad.	[W/m ² srμm]	Case Dependent
S_{L_u} - upwelled rad.	[W/m ² srμm]	Case Dependent
ASSUMPTION: R' and the error in computing L_{BB} is assumed negligible		

Table 4.2 depicts each term's sensitivity in regards to the proposed process illustrating the estimated error associated with each term. All values have been defined by values taken from the literature, except error estimates for L_{BB} (essentially er-

ror associated with the bulk-to-surface ground truth temperature) and atmospheric variables (τ , L_u and L_d), in addition to the atmospheric correlated terms. Note that an average was used to obtain the reported error estimate on emissivity $\epsilon \pm 0.006$, derived from the findings of Konda et al. (1994) (± 0.004) and Barsi (2000) (± 0.008). For our purposes in this study, the error term $S_{L_{BB}}$ is strictly a function of the buoy derived predicted skin temperature. Note the error associated explicitly with the Planck equation will be assumed negligible, however, the temperature used to compute the Planck equation will be investigated. The NDBC guarantees bulk water temperature measurement accuracy of ± 1 K. This value takes the claim of an apparent situational dependence where the buoy hull structure may warm and scenarios of solar radiation reaching the submerged thermistor (note the NDBC's thermistors have an accuracy of 0.1 K), phone correspondence NDBC Rex Hervey. Given the characteristics of this study, for example, the near Noon image acquisition time for all images (i.e. high solar elevation), tends to reduce the thought of solar contamination yielding higher confidence on the observed values. It is proposed that the expected error of the NDBC bulk water temperature observations, for this study, are ± 0.3 K, roughly within the first standard deviation of the guaranteed value of ± 1 K.

4.11.1 Bulk to Skin Temperature Error Propagation Methodology

An error analysis is needed to determine the error associated in the prediction of the resulting bulk to skin temperature correction. For simplicity [Eq. 2.5] shown below:

$$T_s = T_z - az - d \quad (4.5)$$

will be used as the governing equation in this analysis. The bulk to skin temperature prediction error propagation analysis will be performed using [Eq. 4.6]:

$$S_{T_s} = \left[\left(\frac{\partial T_s}{\partial T_z} S_{T_z} \right)^2 + \left(\frac{\partial T_s}{\partial a} S_a \right)^2 + \left(\frac{\partial T_s}{\partial z} S_z \right)^2 + \left(\frac{\partial T_s}{\partial d} S_d \right)^2 \right]^{\frac{1}{2}} \quad (4.6)$$

Table 4.3: Listing and declaration of error terms in Eq. 4.6.

Error Term	Value	Source
S_{T_z} - water temperature at depth	0.3 K	as discussed above NDBC
S_a - thermal gradient	0.305 K/m	empirically derived
S_z - measurement depth	0.254 m	estimate
S_d - cool skin effect	0.07 K	Donlon et al. (2002)

Note that the error estimate of the gradient term (a) was derived using the guidance of the lead author of Zeng et al. (1999). Recall, the gradient term Eq. [2.6] restated:

$$a = 0.05 - \frac{0.6}{u_m} + 0.03 \ln(u_m) \quad (4.7)$$

a is a function of wind speed and valid provided $-1.1 < az < 0$ where z is the measurement depth. The study computed a using winds ranging from 0.1 to 13.5 m/s in 0.1 m/s increments. The values were then filtered by the valid range ($-1.1 < az < 0$) and the standard deviation of the resulting values was found. A standard deviation of 0.305 K/m was obtained and will be used as the error estimate for the gradient term a as it seems physically reasonable.

The final step in this process is to convert the final temperature error to radiance, so that it can be used in Eq. 4.4 in the term L_{BB} . Note the error in temperature was converted to an error in radiance using the LUT described in Section 2.5 in reference to a 300 K blackbody.

4.11.2 Atmospheric Error Propagation Methodology

Our attention is now brought to the error associated with the proposed atmospheric processes. Due to the complexity of the atmospheric terms, a statistical (i.e. Monte Carlo) approach will be used to deduce the error in τ , L_u and L_d . For the conditions we are working with (i.e. clear sky; fair weather) we will restrict our focus to 7 representative atmospheres. The range of profiles will span radiosonde observations, given our restricted domain, from a cold dry atmospheric column to a warm moist atmospheric column. Each profile was taken from soundings used in this calibration study. These profiles will be varied to account for possible atmospheric variability

regarding both instrument uncertainty, as well as, potential physically occurring atmospheric variability. The chosen profiles were selected from launch sites: SSM, APX, ACY, and WAL. Our focus is constrained to three main factors in regards to the above mentioned atmospheric processing [Section 4.6.1 and 4.6.2]: 1) **Surface:** buoy surface observation measurement uncertainty [Table 4.4] 2) **Boundary Layer:** IBL height uncertainty ($\pm 25\%$ of the predicted value) 3) **Upper-Air** radiosonde measurement uncertainty [Table 4.4].

Table 4.4: Declaration of specifications for atmospheric observations.

Buoy		Radiosonde	
Error Term	Value	Error Term	Value
Temperature	± 1 K or 0.3 K at 1 sigma	Temperature	± 0.3 K
Pressure Px	± 1 hPa or 0.3 hPa at 1 sigma	Pressure	± 2 hPa
Dew Point	± 1 K or 0.3 K at 1 sigma	Rel. Humidity	$\pm 2\%$
Source: NDBC		Source:	Elliott and Gaffen (1991)

Specifications for buoy observations were taken directly from the NDBC website: [http : //www.ndbc.noaa.gov/rsa.shtml](http://www.ndbc.noaa.gov/rsa.shtml). The values shown for radiosonde specifications were derived from a 1989 study of several models of radiosondes used in the United States in the 1980's Elliott and Gaffen (1991). Treating each of the seven profiles individually, surface measurements of temperature, dew point (when applicable) and pressure will be varied based on buoy derived surface observation measurement uncertainty [Table 4.4]. In cases where buoy derived dew point data is unavailable an error estimate of ± 3 K will be used to account for the potential error in the proposed interpolation scheme. Note that buoy derived dew point temperature data is available nominally after 2001 on NDBC moored buoys outside of the Great Lakes. All levels above the surface layer will be biased only by radiosonde instrument uncertainty [Table 4.4] to the vertical extent of the radiosonde profile. Note in order to apply the 2% relative humidity (RH) error estimate within the radiosonde observations, the values of dew point have to be converted to RH by use of Eq 4.8:

$$RH = \frac{e}{e_s} \times 100 \quad (4.8)$$

where e is the vapor pressure and e_s is the saturation vapor pressure. Provided a temperature and dew point temperature e and e_s can be found through the Hyland and Wexler (1983) equations:

$$\begin{aligned} \log e = & \frac{-0.58002206 \times 10^4}{T_d} + 0.1391499310^1 \\ & -0.4864023910^{-1} T_d \\ & +0.4176476810^{-4} T_d^2 \\ & -0.1445209310^{-7} T_d^3 \\ & +0.6545967310^1 \log(T_d) \end{aligned} \quad (4.9)$$

where T_d is in [K] and e in [Pa].

$$\begin{aligned} \log e_s = & \frac{-0.58002206 \times 10^4}{T} + 0.1391499310^1 \\ & -0.4864023910^{-1} T \\ & +0.4176476810^{-4} T^2 \\ & -0.1445209310^{-7} T^3 \\ & +0.6545967310^1 \log(T) \end{aligned} \quad (4.10)$$

where T is in [K] and e_s in [Pa]. Realize within the literature there are numerous vapor pressure and saturation vapor pressure equations. The Hyland and Wexler (1983) equations were chosen because they are widely accepted and most importantly used commercially by the company Vaisala, a radiosonde vender which is widely used by the NWS (US) and also popular around the globe.

Once converted to RH values, the reported sensor bias was applied and the values were converted back to dew point temperatures via Eq. 4.11:

$$T_d = \frac{243.5 \log\left(\frac{RH}{100}\right) + 17.67 \left(\frac{T}{243.5+T}\right)}{17.67 - \log\left(\frac{RH}{100}\right) + 17.67 \left(\frac{T}{243.5+T}\right)} \quad (4.11)$$

where T is in [C] and RH is the relative humidity in percent (%). Note Eq 4.11

calculates dew point temperature for a given T and RH according to World Meteorological Organization (WMO) standard procedure [Bolton (1980)]

In an effort to ensure the instrument error is applied in the most viable fashion the following approach is proposed. Radiosondes sample atmospheric temperature, relative humidity and pressure as a function of height. Therefore, in an attempt to characterize the amount of uncertainty introduced by this instrument it makes physical sense to vary all three parameters. Realize however, that atmospheric pressure is not a strong factor contributing to temperature error. For example, a small case study using three unique radiosonde profiles was conducted. Values of atmospheric pressure were independently biased both negatively and positively by measurement uncertainty for all radiosonde observation levels. Comparing the resulting temperature using original profile to each of the final temperature using the modified profiles, showed temperature differences of less than 0.005 K for all six cases (average difference = 0.002 K). However, for the sake of completeness the pressure modifications will be included in this study.

For each observation level in the radiosonde, the specified instrument uncertainty was applied using a Gaussian random noise generator [Figure 4.29] in an effort to account for all identified combinations of measurement uncertainty at each observation height. Note a different seed will be used for each case and variable. It was concluded that roughly 800 profiles were needed to achieve the desired distribution about each variable, therefore an overestimate of 1000 profiles will be generated for each case.

Profiles where the IBL is present results in a total of 3000 profiles, as a result of accounting for the \pm IBL height uncertainty. Figure 4.30 illustrates an example of the methodology discussed above; all profiles used in this study are shown in Appendix J.

The following provides a brief justification of the proposed methodology. Recall, surface measurements are observed hourly and interpolated to the nearest minute of the designated image acquisition time, thus confidence regarding these measurements are high. Above the surface layer, observations of atmospheric variables will

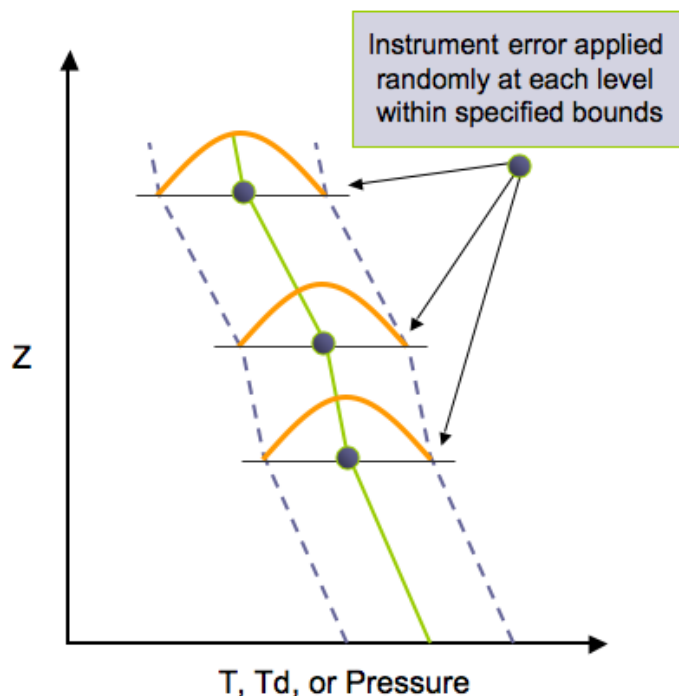


Figure 4.29: Schematic of atmospheric error propagation methodology. Note that temperature (T), dew point temperature (T_d) and pressure were all varied at each observation point in the radiosonde profile uniquely based upon the specified uncertainty in the measurement.

typically be representative of the desired atmospheric state because the atmosphere becomes considerably less varying as altitude increases (provided our restricted atmospheric domain), therefore, by solely using the sounding instrument specifications seems generally physically reasonable. Although, to resolve concerns of boundary layer and/or IBL modifications from the time of launch to the time of image capture, the IBL height is varied as well, in accordance to the above mentioned confidence in the height prediction. Note this modification is only valid on profiles where the IBL is present. For profiles where the IBL is not present the height of the BL is considered as truth, thus no further adjustments are applied.

All profiles were constructed in IDL and used as input to MODTRAN and DIRSIG to capture the atmospheric variability present in each of the constructed cases. For each profile an integrated value of τ , L_u and L_d was computed. The standard deviation of the integrated values (Landsat 5 Band 6 response applied) is

found to estimate the error introduced for each term in all 7 atmospheric cases.

The final task for this atmospheric error propagation study is to define the correlation values needed for Eq. 4.4. The atmospheric terms τ , L_u and L_d are correlated in nature and thus have been included in Eq. 4.4. To determine the correlation value between each variable, provided our restricted atmospheric domain, a study was conducted using a data set of 114 unique atmospheric profiles, chosen at "random", from assembled atmospheric profiles used in this calibration study. Again integrated values of τ , L_u and L_d were obtained and reported uniquely for each profile.

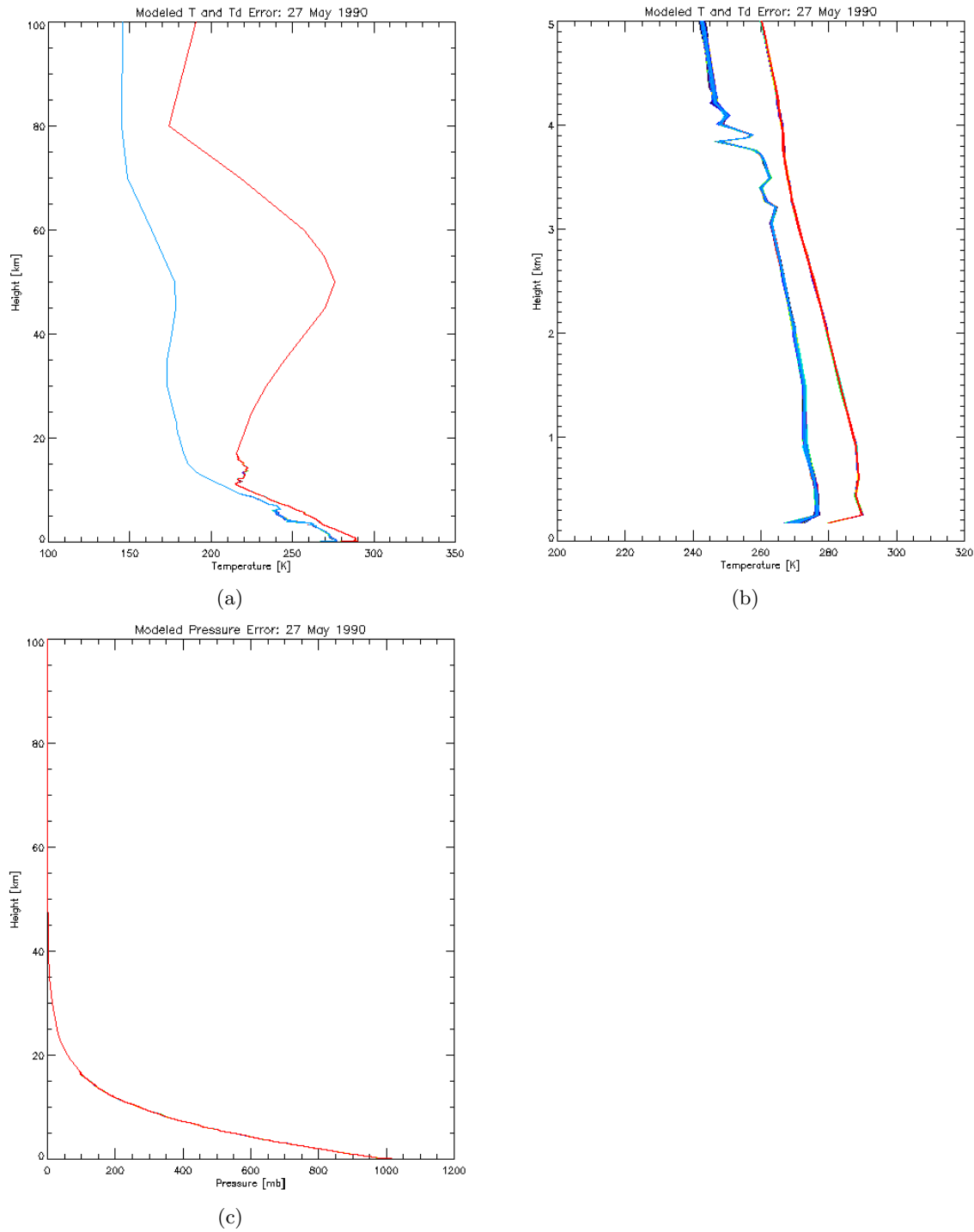


Figure 4.30: (a) SSM radiosonde May 27, 1990 varied according to values shown in Table 4.4. (b) Provides a closer view of the lower atmosphere. Note: surface level dew point (left) demonstrates the most variability. (c) Illustrates the modifications performed on the pressure observations.

4.12 Determination of Process Error

Provided the methodology developed in Section 4.11, the proposed vicarious calibration process error will be investigated and quantified to deduce the appropriate level of confidence encompassing each calibration point. Error propagation analysis will be presented in three parts. The first discusses the error involved in the determination of a predicted ground truth skin temperature using NDBC moored buoy bulk temperature observations, and the second discusses the atmospheric error propagation results. With all realized error sources assigned appropriate error estimates, the above mentioned error studies will be merged so that the total process error can be realized.

4.12.1 Ground Truth Process Error (T_b to T_s)

The error associated with the implemented Zeng et al. (1999) bulk to skin temperature model was found to be 0.358 K (or 0.0473 $[W/m^2 sr \mu m]$ in reference to a 300 K blackbody) assuming negligible error in the numerical computation of the Planck equation [Eq. 3.1]. This error metric was derived using the following inputs to Eq. 4.6: depth (z) = 0.6 m, as the majority of buoy platforms used in this study were 3m discus buoy's (i.e. $z = 0.6$ m); thermal gradient (a) = 0.305 K/m, provided by Eq. 2.6 using the reported average of all mean wind speeds used in this study (5.86 m/s); cool skin effect (d) = 0.17 K, which was used in all cases, reported by Donlon et al. (2002).

To explore the sensitivity of the reported error results and to understand where the weakest links are in the ground truth modeling process Figure 4.31 is offered. In this study low, moderate and strong wind speed cases were examined in terms of both the 3m and 12m discus buoy classes. Note the error estimate for each variable is shown in Table 4.5.

Input Parameters:		
Wind Speed	Variable Input:	Error Est.
1.5 m/s	a = -0.33784 K/m	0.305 K/m
5 m/s	a = -0.02172 K/m	0.305 K/m
10 m/s	a = 0.05908 K/m	0.305 K/m
	z = 0.6/1.5 m	0.254 m
	d = 0.17 K	0.07 K

(a)

Results:		
Wind Speed	$S(T_s)$: 3m Buoy (z=0.6 m)	$S(T_s)$: 12m Buoy Hull (z=1.5 m)
1.5 m/s	0.368 K	0.558 K
5 m/s	0.358 K	0.552 K
10 m/s	0.359 K	0.552 K

(b)

Figure 4.31: (a) Input values used to generate the $S(T_s)$ data shown (b) using Eq. 4.6. (b) Depicts the final error results for both a 3m buoy hull and 12m buoy hull.

The estimated error in the proposed modeling effort is within 0.4 K for all 3 m buoy hull ($z = 0.6$ m) cases, where as the 12 m buoy hull ($z = 1.5$ m) cases result in error larger in magnitude and within 0.6 K for all cases. Notice a large portion of the uncertainty arises due to the confidence levels of the NDBC reported bulk water temperature measurements. Although subtle, the data shown in Figure 4.31 is consistent with the methodology presented in Section 2.6, which noted: at low wind speeds the proposed model is more susceptible to error due to the complexity of the environment, where as at high wind speeds the environment is simplified and well characterized. A major finding in this study, which agrees with intuition, is that the magnitude of error in T_s is less for the 3 m class buoy's compared to the 12 m class buoy's. The likely reason is due to the fact that typically, as depth increases so does the T_b to T_s correction, which also increases the domain that the model is required to characterize.

A sensitivity analysis was then conducted on each term in Eq. 4.6, re-expressed in Eq. 4.12:

$$S_{T_s} = \left[\left(\frac{\partial T_s}{\partial T_z} S_{T_z} \right)^2 + \left(\frac{\partial T_s}{\partial a} S_a \right)^2 + \left(\frac{\partial T_s}{\partial z} S_z \right)^2 + \left(\frac{\partial T_s}{\partial d} S_d \right)^2 \right]^{\frac{1}{2}} \quad (4.12)$$

by modifying each term with a range of viable error values and reporting its impact

Table 4.5: Listing and declaration of error terms in Eq. 4.12.

Error Term	Value	Source
S_{T_z} - water temperature at depth	0.3 K	as discussed above NDBC
S_a - thermal gradient	0.305 K/m	empirically derived
S_z - measurement depth	0.254 m	estimate
S_d - cool skin effect	0.07 K	Donlon et al. (2002)

in terms of total error [Figure 4.32]. It was concluded that for the 3m class buoy's (i.e. $z = 0.6$ m) the most dominant and sensitive term was T_z (bulk temperature at depth z) [c.f. Figure 4.32 (a)] for all wind speeds; note for the sake of brevity only the 5 m/s wind speed case is shown. Also found to be moderately sensitive was the thermal gradient term a . Notice that the terms z and d were found to be rather insensitive, as Figures 4.32 (c-d) are relatively flat.

In contrast the 12m class buoy's ($z = 1.5$ m) illustrated a , the thermal gradient term, as the most dominant and sensitive term for all cases [Figure 4.32]. Compared to the above, it is apparent that the increased measurement depth is sufficient enough to drive these errors upward. Again this finding makes physical sense because the gradient term provides the model with the change in temperature with depth, thus any errors in the modeled thermal gradient impact contribute directly to towards the total error, even assuming all remain factors were negligible.

In conclusion we have shown the bulk temperature at depth T_z and thermal gradient a as the dominant terms for the 3m and 12m discus buoy classes, respectively. Realize that in the implemented Zeng et al. (1999) approach restrictions were placed on the valid range concerning each of the derived coefficients [2.6], thus this study illustrated that the concern of potential error at low wind speeds has for the most part been avoided. Again this study has concluded that for the average environmental conditions and measurement situations experienced in this study an expected error of 0.358 K (or 0.0473 $[W/m^2sr\mu m]$ in reference to a 300 K blackbody) was found for the bulk-to-surface water temperature model.

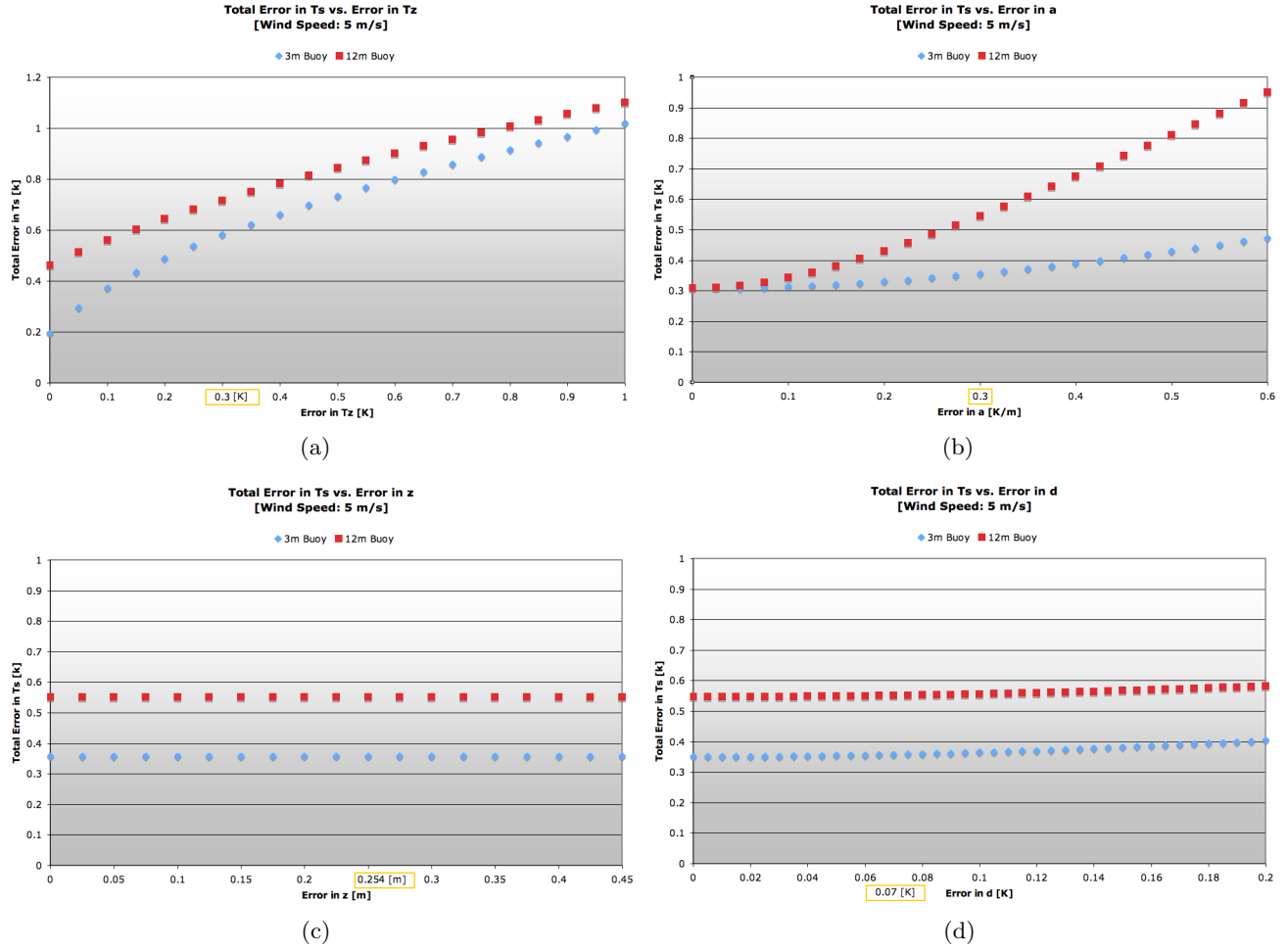


Figure 4.32: Sensitivity of each term in regards to the total process given a range of reasonable values, at a wind speed of 5 m/s for the 3m and 12m buoy classes. Note the orange box signifies the error estimate used: (a) Sensitivity in the bulk temperature measurement taken at depth T_z . (b) Sensitivity in the gradient a . (c) Sensitivity in depth z . (d) Sensitivity in the cool skin effect d .

4.12.2 Atmospheric Process Error

This study had two main objectives: 1) determine the error in the proposed atmospheric column generation methodology [Section 4.6]; 2) determine the correlation coefficients between: τ , L_u and L_d provided the restricted atmospheric domain of this study.

As discussed in Section 4.11.2, it was determined that the derived error values regarding our atmospheric processing would be derived via Monte Carlo methods, using the integrated values of τ , L_u and L_d over the bandpass of Landsat 5 Band 6. Results from the 7 profiles investigated are shown in Table 4.6; all profiles can be visualized in Appendix J. For clarity, the atmospheric cases shown in Table 4.6 generally increase in water vapor as one reads down the list. Also note that the case 06 July 1999 is to be considered as an extreme case for testing purpose (i.e. warm extremely moisture rich [Appendix J; Figure E.7])

Table 4.6: Atmospheric reconstruction error.

Date	Description	Station	IBL	Buoy T_d	$S(L_u)$	$S(L_d)$	$S(\tau)$
26Jan02	cold dry	WAL	-	x	0.002338	0.004037	0.0003705
28Apr03	cold dry	WAL	-	x	0.004035	0.009367	0.0005506
27May90	cool moist	SSM	$\pm 22m$	-	0.006762	0.01078	0.0009022
24Jun90	warm dry	SSM	$\pm 23m$	-	0.005505	0.009620	0.0007172
24Oct98	warm dry	APX	$\pm 58m$	-	0.01753	0.02895	0.002426
16Aug85	warm moist	WAL	$\pm 34m$	-	0.02433	0.04498	0.002783
06Jul99	warm moist	WAL	$\pm 12m$	-	0.02429	0.02772	0.002703

The major findings from the data presented in Table 4.6 are:

- All derived error estimates are small in magnitude.
- In agreement with intuition, the warm moist atmospheric profiles demonstrated larger error estimates, by an order of magnitude, compared to the cooler and drier atmospheric profiles examined in this study.

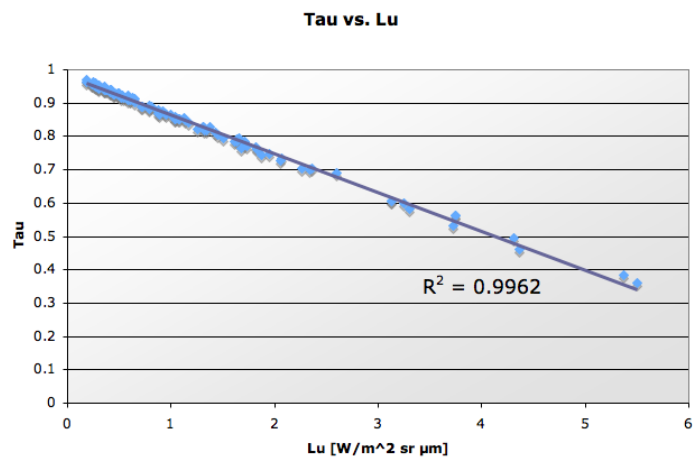
From a data set of 114 unique atmospheric profiles used in this study, correlations were found between each of the terms τ , L_u and L_d [Table 4.7]. All correlations were found to be high, which makes sense given the restricted domain of this study (i.e.

calibration quality atmospheric profiles). Figure 4.33 illustrates the data used to populate Table 4.7.

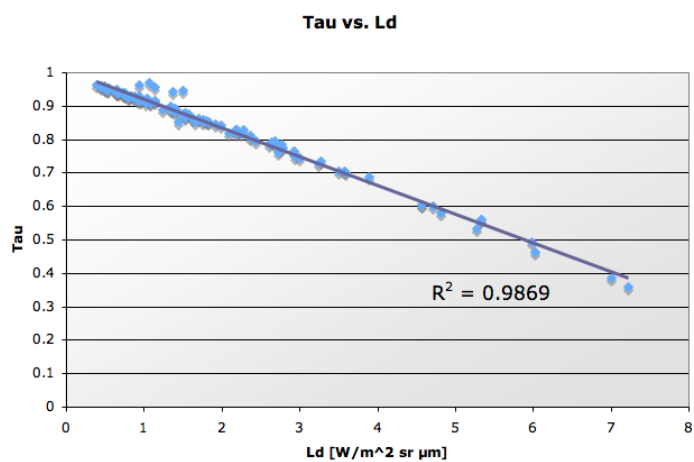
Table 4.7: Correlation values of τ , L_u and L_d derived from 114 unique atmospheric profiles.

ρ	Value
τ, L_u	-0.9981
τ, L_d	-0.9934
L_u, L_d	0.9925

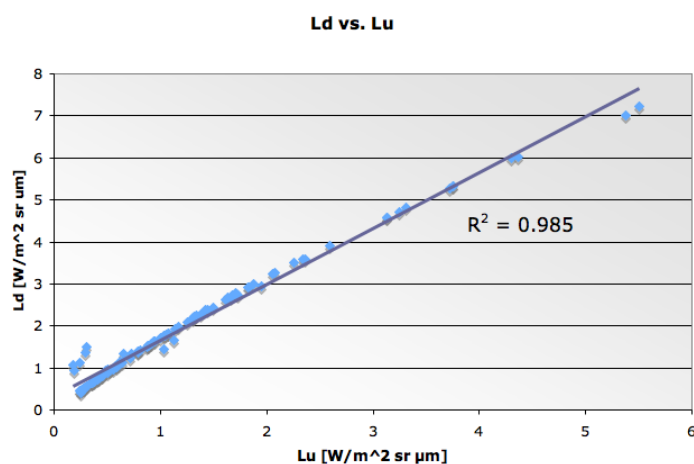
The results make physical sense: L_u and L_d increase as τ decreases and vice versa, as well as, L_u and L_d are positively correlated as both are driven by the same phenomenology.



(a)



(b)



(c)

Figure 4.33: Data derived from 114 unique atmospheric profiles used in the calibration campaign: (a) τ vs. L_u . (b) τ vs. L_d . (c) L_d vs. L_u .

4.12.3 Overall Process Error

In an effort to deduce the total error within the proposed methodology a final study was conducted on Eq. 4.4 described above. Results from the study are presented illustrating the overall process error sensitivity to both errors in the target temperature and errors in the atmospheric parameters. To portray this sensitivity, three target temperatures along with the atmospheric parameters and their uncertainties from seven unique atmospheric profiles were used as input to the error propagation's governing Eq. 4.4. Note this investigation includes the results of all prior error analyses. The result for each case is an error in effective radiance (S_{Leff}) converted to an apparent temperature [K] [Table 4.8]. Since the error in each case is dependent on both the target temperature and atmospheric parameters, each final error value is expressed as a temperature error at the sensor ($S_{Tat-sensor}$). This metric is shown in the last column of Table 4.8 and describes what a unit change in temperature on the ground results to in temperature error at the sensor for each atmospheric case expressed as:

$$S_{Tat-sensor} = \frac{\Delta T}{\Delta L_{eff}} S_{Leff} \quad (4.13)$$

where ΔT is a unit change in temperature (L_{BB}) in the governing Eq. 3.14 [$W/m^2 sr \mu m$], ΔL_{eff} is the change effective radiance [$W/m^2 sr \mu m$] provided the two temperatures used to calculate ΔT and S_{Leff} is the error in effective radiance [$W/m^2 sr \mu m$], given each case [Table 4.8]. For clarity it is restated that Table 4.8 includes all previous error propagation results and deduces the total process error given the range of possible atmospheric conditions witnessed in this study.

From Table 4.8 notice that the average temperature error at the sensor $S_{Tat-sensor}$ is 0.451 K, in reference to a 300 K blackbody for all cases. By taking the average of all cases which are physically reasonable for this calibration study an overall error estimate of 0.454 K was found. For example target temperatures of 300 K were not found in January for this study, thus were exclude.

Notice in Table 4.8 that for each atmospheric case, the error was found to increase with increasing target temperature. In addition, notice the peculiar result

Table 4.8: Error in the effective radiance (L_{eff}) at the sensor due to uncertainties in the entire proposed methodology. Note error is expressed in apparent temperature [K] and all other radiance values are in units of $[W/m^2 sr \mu m]$. Note all atmospheric error values used to populate this table are found in [Table 4.6], while all remaining error estimates are shown in [Table 4.2].

Atm.	T	ϵ	τ	S_τ	L_u	S_{L_u}	L_d	S_{L_d}	$S_{L_{eff}}$ [K]	$S_{T_{at-sensor}}$ [K]
26Jan02 (dry)	274	0.986	0.9401	0.0004	0.3725	0.0023	0.6693	0.004	0.407	0.439
	285								0.439	0.473
	300								0.494	0.533
28Apr03	274	0.986	0.9406	0.0006	0.4266	0.0040	0.7566	0.0094	0.405	0.436
	285								0.437	0.471
	300								0.492	0.530
27May90	274	0.986	0.8617	0.0009	0.9608	0.0068	1.6523	0.011	0.352	0.414
	285								0.378	0.445
	300								0.426	0.501
24Jun90	274	0.986	0.9057	0.0007	0.6665	0.0055	1.1687	0.0096	0.380	0.426
	285								0.410	0.459
	300								0.461	0.517
24Oct98	274	0.986	0.9068	0.0024	0.6574	0.0175	1.1453	0.029	0.382	0.427
	285								0.411	0.459
	300								0.464	0.519
16Aug85	274	0.986	0.7946	0.0029	2.056	0.0243	1.6611	0.045	0.313	0.400
	285								0.330	0.421
	300								0.368	0.469
06Jul99 (moist)	274	0.986	0.3846	0.0027	5.3754	0.0240	7.0086	0.028	0.149	0.391
	285								0.140	0.370
	300								0.142	0.374

illustrating that temperature errors are greater for the cooler and drier atmospheres compared to that of warm moist atmospheric cases. This result is counter intuitive, however, through investigation the following justification is offered. As the input values of L_u and L_d increase and the value of τ decreases (i.e. the state of the atmosphere increases in heat and moisture; note warm air can hold more moisture than cold air) the correlation term (ρ_{τ, L_u}), which has a negative sign, becomes increasingly more of a contributor; enough to pull down the overall error. For example, in the 28 April 2003 atmosphere [Appendix J Figure J.2] the correlation term (ρ_{τ, L_u}) is negligible, however, for the extreme moisture case [Appendix J; Figure J.7] the correlation term (ρ_{τ, L_u}) is found to be the most dominant term, thus extinguishing the bulk of the error in the overall process. With that said, this investigation has concluded that the proposed methodology exhibits larger error for cold dry atmospheric

profiles, opposed to that of warm moisture rich profiles.

To further develop our understanding of the sensitivity of the proposed vicarious calibration methodology, an investigation of the most dominant terms in regards to total error and sensitivity will be identified [Figures 4.34 & 4.34, Figures 4.36 & 4.37; for the nominal spring and early summer case (lower moisture content) and mid to late summer case (increased moisture content), respectively]. Beginning with the spring - early summer case, it was found that at low temperatures (below ~ 285 K) the target temperature term (L_{BB}) was found to be the most dominant contributor to total error followed by the emissivity term (ϵ). As temperature increased however, the magnitude of the L_{BB} term remained constant and was eventually overtaken by the emissivity term at 300 K becoming the largest contributor to total error. At all temperatures for these atmospheric cases the emissivity term was found to be the most sensitive [Figure 4.34]. This result makes physical sense because for this type of atmosphere (i.e. low overall water vapor concentration) the transmission term requires large errors to have a strong impact on the total error, where any error in emissivity results directly towards the total error.

Similar to the results found for the spring - early summer atmospheric case, the most dominant term in the mid to late summer atmospheric case was the L_{BB} term for all target temperatures. Note however, as the target temperature increased as did the contribution of the correlation term (ρ_{τ, L_u}), which nearly overtook the dominance of the L_{BB} term, in terms of magnitude contributing towards total error, at the target temperature of 300 K. Which again verified, that as the target temperature increased, in moderate to high moisture content atmospheric profiles (i.e. as a general rule of thumb: $\tau < \sim 90$, and more importantly $L_u \geq \sim 1.0$ [$W/m^2 sr \mu m$]), as did the (negative signed) term (ρ_{τ, L_u}), which lead to an overall reduction in total error. The most sensitive term in this case was found again to be the emissivity term ϵ [Figure 4.36], however, it should be stated that τ and L_u are also sensitive terms for this case [Figure 4.37]. For example, a 1% change in transmission results in a rough 0.755 K fluctuation in total error [Figure 4.37]. In addition, notice similar to the previous case the downwelled radiance term L_d was found to be extremely

insensitive, which is the result of high target emissivity (i.e. ϵ of water 0.986).

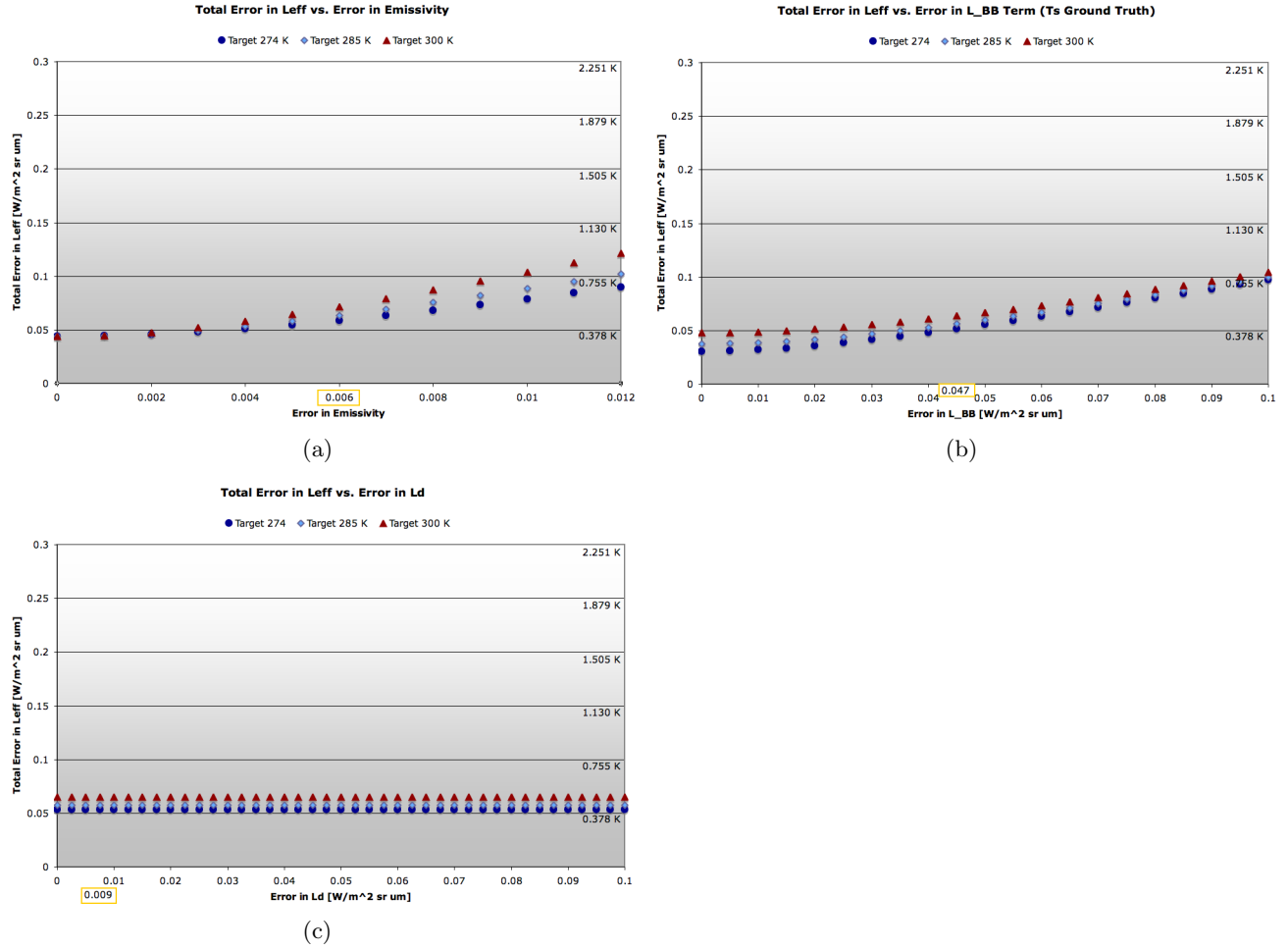


Figure 4.34: Sensitivity of each term in regards to total error: Spring Atmosphere (a) Sensitivity in the ϵ . (b) Sensitivity in L_{BB} . (c) Sensitivity in L_d .

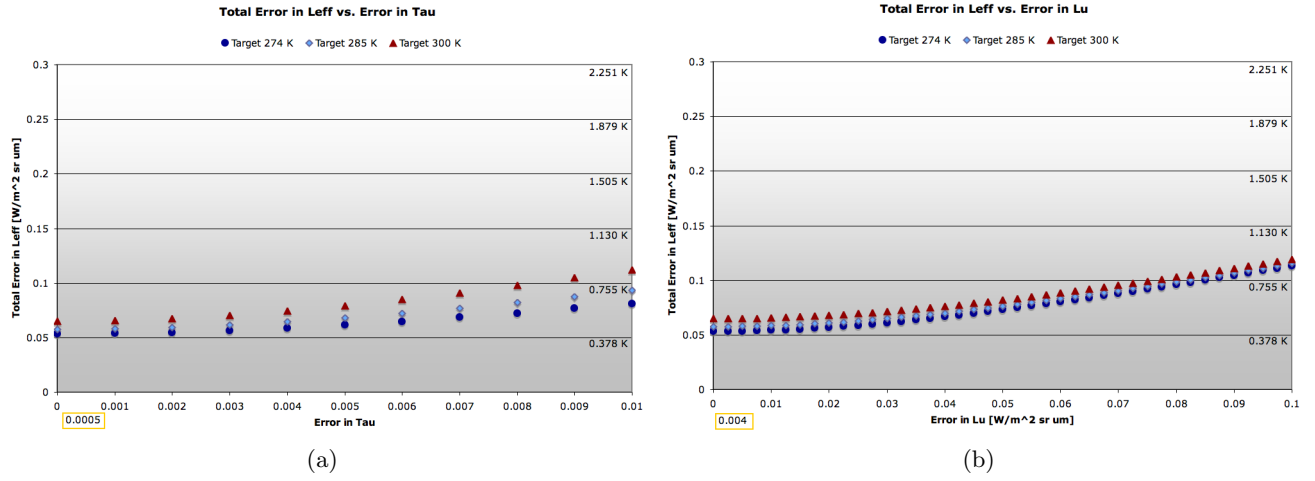


Figure 4.35: Sensitivity of each term in regards to total error: Spring Atmosphere (a) Sensitivity in the τ . (b) Sensitivity in L_u .

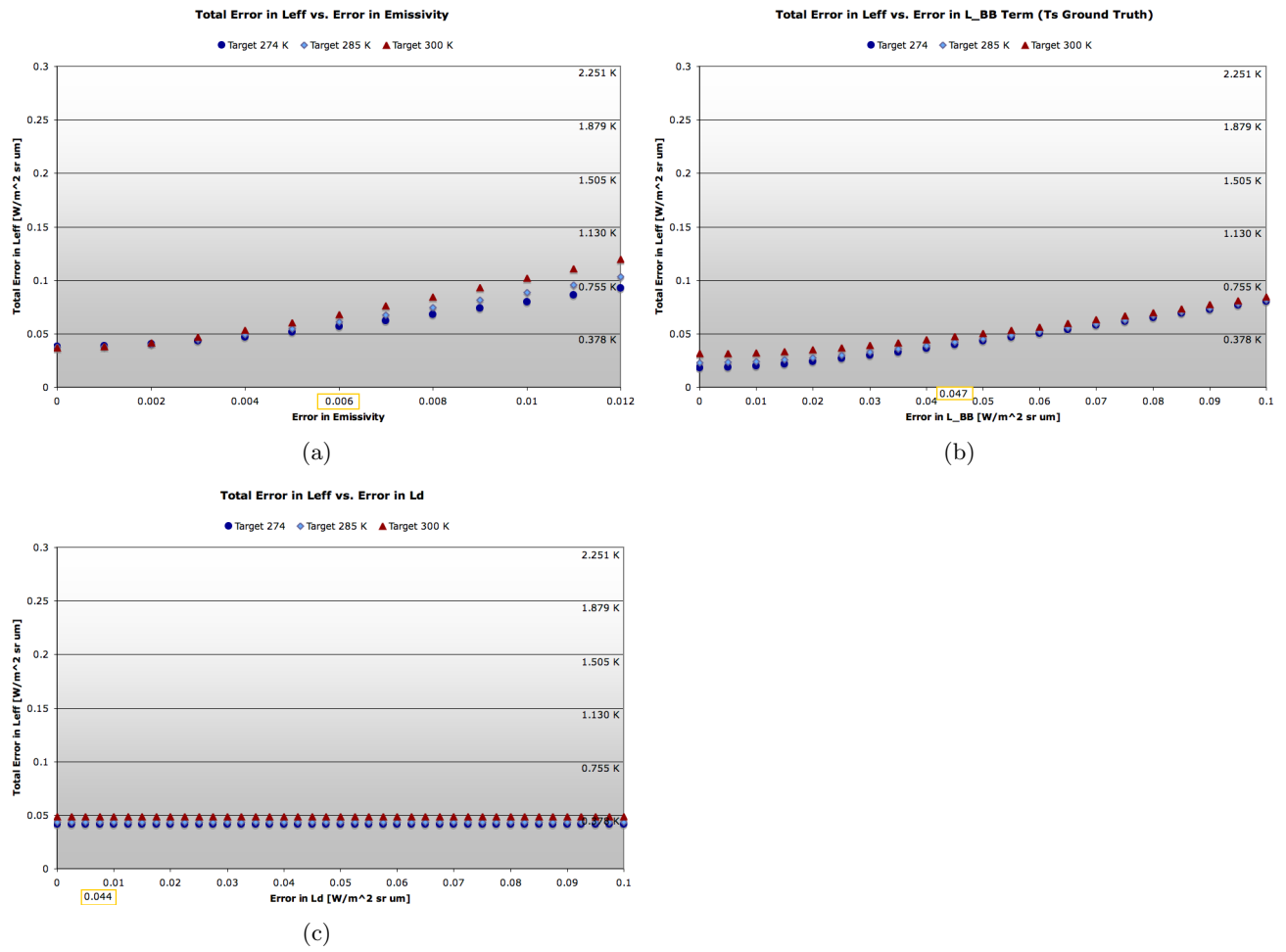


Figure 4.36: Sensitivity of each term in regards to total error: Summer Atmosphere (a) Sensitivity in the ϵ . (b) Sensitivity in L_{BB} . (c) Sensitivity in L_d .

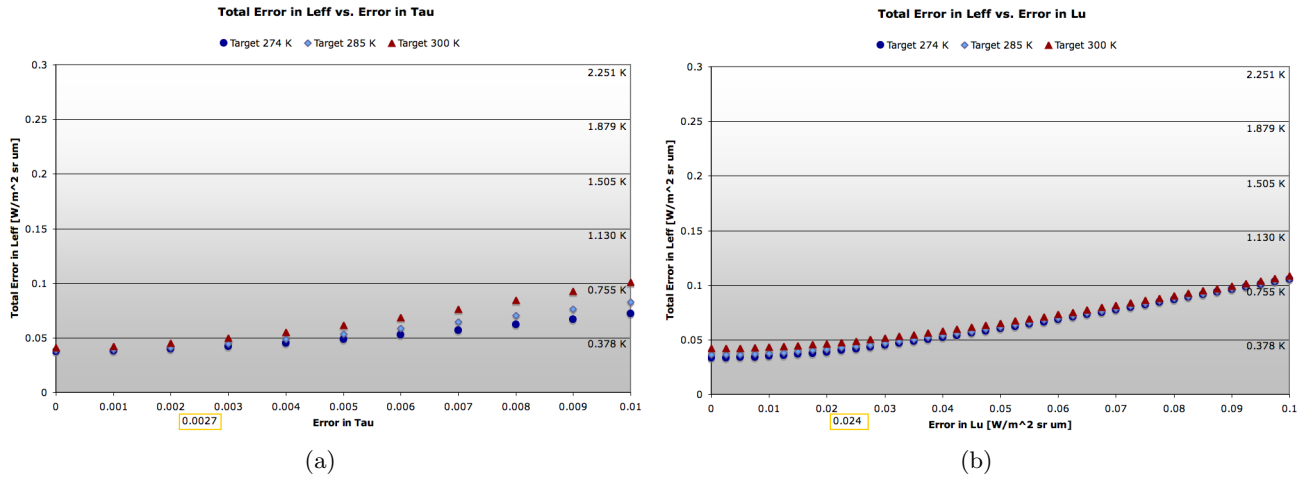


Figure 4.37: Sensitivity of each term in regards to total error: Summer Atmosphere (a) Sensitivity in the τ . (b) Sensitivity in L_u .

Summary:

- The proposed methodology was found to have an expected error of ± 0.454 K.
- Total error was found to be larger in magnitude for cold dry atmospheric profiles compared to warm moisture rich profiles, due to the effects of the (negative signed) correlation term (ρ_{τ, L_u}) .
- Overall the target temperature term (L_{BB}) was found to be the most dominant, where the emissivity term ϵ was found to most dominant at high target temperatures (i.e. 300 K) except for warm moist atmospheres where the term (L_{BB}) dominates.
- Overall the most sensitive term was found to be the emissivity term ϵ , which was eventually overtaken by the transmission term τ in the presence of warm and highly moisture rich atmospheric profiles.

4.13 Validation of Approach

It is critical to this work that the proposed approach is rigorously validated, so that a high level of confidence can be established in the application of the approach and its use propagated back in time. In this section comparisons studies are presented using both Landsat 7 and Landsat 5 data sets. This section is intended to validate the approach, as well as quantify the error in the proposed methodology compared to the traditional method (i.e. ground truth via contact thermistors opposed to using buoy derived ground truth) [Section 4.13.3].

4.13.1 Landsat 7 Comparison Study

Verification analysis will begin by a comparison of calibration results obtained using the proposed methodology on the Landsat 7 ETM+ thermal band and comparing the results to the existing calibration record, established using the traditional methods. As mentioned previously, the Landsat 7 ETM+ is ideal for verification purposes in this study, as it is a trusted and well calibrated sensor. The study resulted in 32 calibration points using data from all proposed calibration sites, over the period of 2000 - 2007. Results from the study are shown in Figure 4.38. Through simple visual inspection [Figure 4.38] the two data sets appear to be consistent. To further validate that the previous calibration effort is not significantly different from the proposed methodology an F-test, testing if both the slope and intercept of the two regression lines [Figure 4.38] was performed. At the 99% C.I. the two trend lines (traditional methodology and proposed buoy methodology) were found to be not statistically different. Additionally the temperature bias from the two datasets was found to be not statistically different at the 99% C.I. using a two sampled t-test. Note the same study was performed on RIT previous data only and results were found to be consistent with the above mentioned.

The findings from this study are two fold: 1) we have shown that the proposed methodology provides consistent, and not statistically different, results against a composition of prior work from two independent sources (i.e. JPL and RIT); based

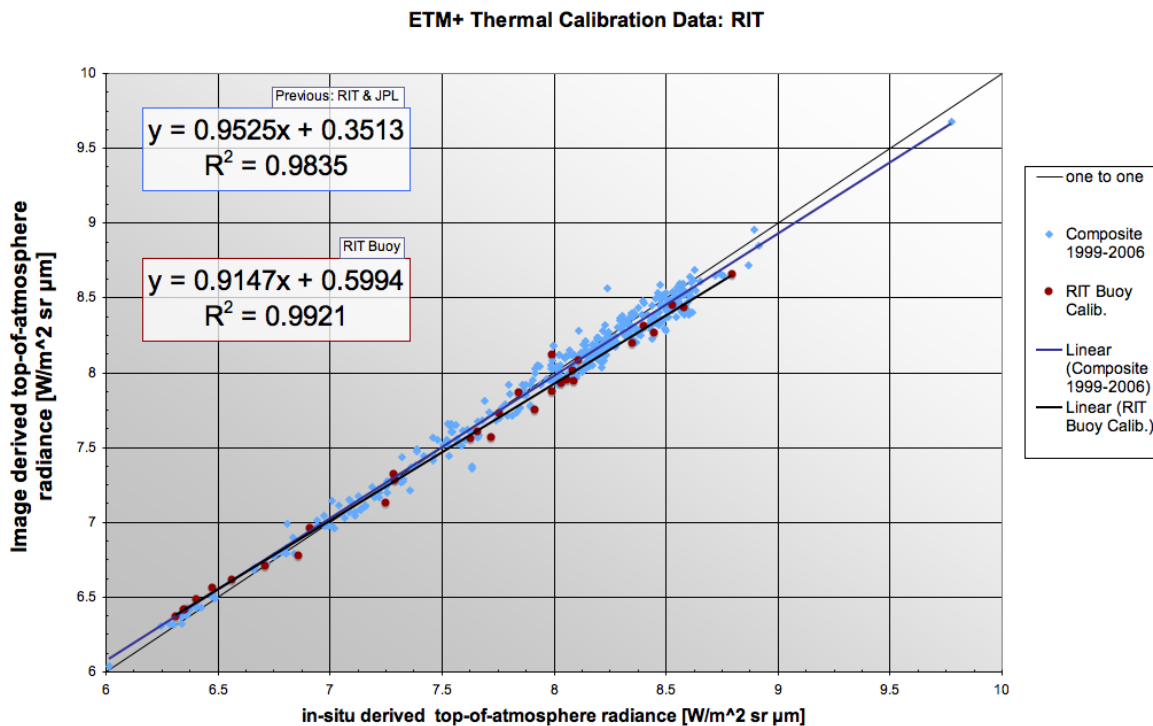


Figure 4.38: Derived calibration curve from the proposed methodology (red), compared to the previous vicarious calibration results from JPL and RIT.

on a study using a stable, well calibrated and trusted instrument; 2) a high level of confidence is established on the utility of this methodology in the construction of the historical calibration record of the Landsat 5 TM thermal band.

4.13.2 Landsat 5 Comparison Study

Results from this calibration campaign are now plotted against the previous Landsat 5 calibration results of JPL and RIT; note the previous efforts have a limited data range (i.e. 1999 to 2007) [Figure 4.39]. Also note that all data sets illustrated in this section are data presented with the NASA 1999+ correction applied (cold biased corrected). Through inspection of Figure 4.39 and Figure 4.40 it was concluded that both the proposed methodology and previous studies are visually consistent with one another. To verify this claim quantitatively two hypothesis tests were performed. Realize that only data post 1999 was used for all tests. Investigated first was if both the slope and intercept of the two regression lines [Figure 4.40] are significantly

different using an F-test. The second, tested if the bias temperatures from the two data sets were statistically different via a two sampled t-test. Results found that the slope and intercept of the two regression lines to be not statistically different at the 99% C.I., however, found that the bias temperatures are statistically different at the 99% C.I.. Through further analysis the absolute bias temperature data was averaged for all data post 1999 in both methods. Results showed the difference from the new methodology compared to the traditional methodology was 0.105 K [Table 4.9]. Note the same measure was applied to all NASA JPL data post 1999, which resulted in an absolute average difference compared to the proposed method of 0.251 K. Recall, as previously mentioned the JPL utilizes ideal calibration conditions (i.e. calibration site: Lake Tahoe, offers reduced atmospheric effects and ground truth is obtained from a buoy mounted radiometer) thus it makes sense the JPL data provides less error [Table 4.9]. In conclusion the new methodology demonstrates consistent results, at the few tenths Kelvin level, compared to the results of previous Landsat 5 calibration campaigns.

Table 4.9: Absolute average bias temperature difference for 1999+ data from: proposed methodology (RIT buoy), RIT traditional approach, & JPL.

Source	Number of Calibration Points	Absolute Average [K]	Difference from RIT Buoy [K]
RIT Buoy	88	0.752	0.0
RIT Traditional	207	0.647	0.105
JPL	77	0.501	0.251

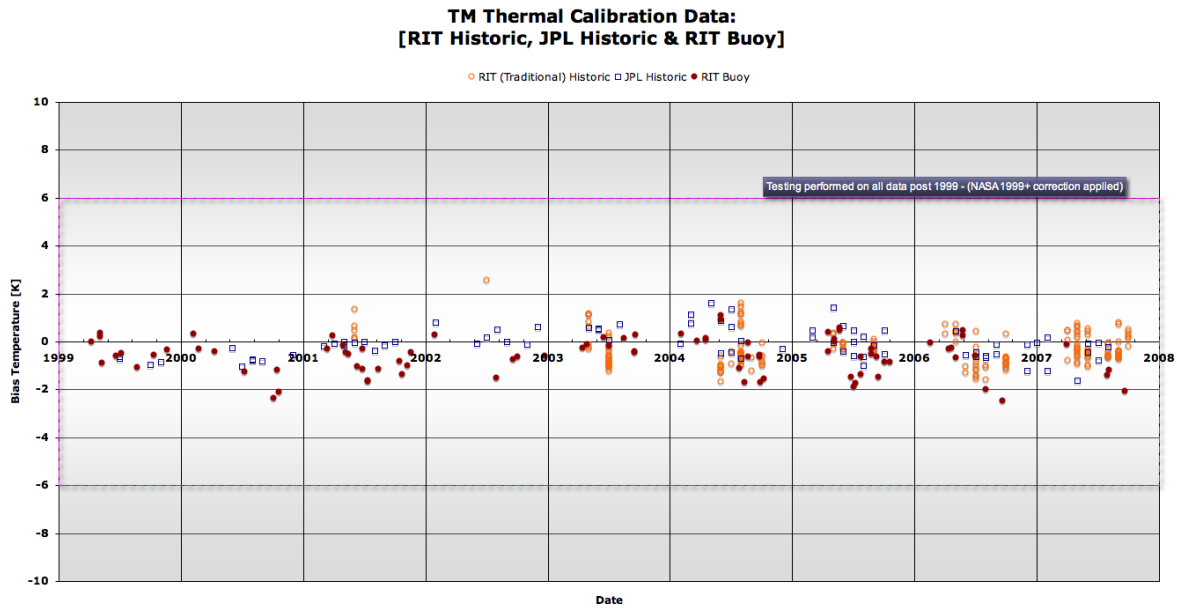


Figure 4.39: Derived calibration curve from the proposed methodology compared to the previous vicarious calibration results from JPL and RIT, temperature bias versus time.

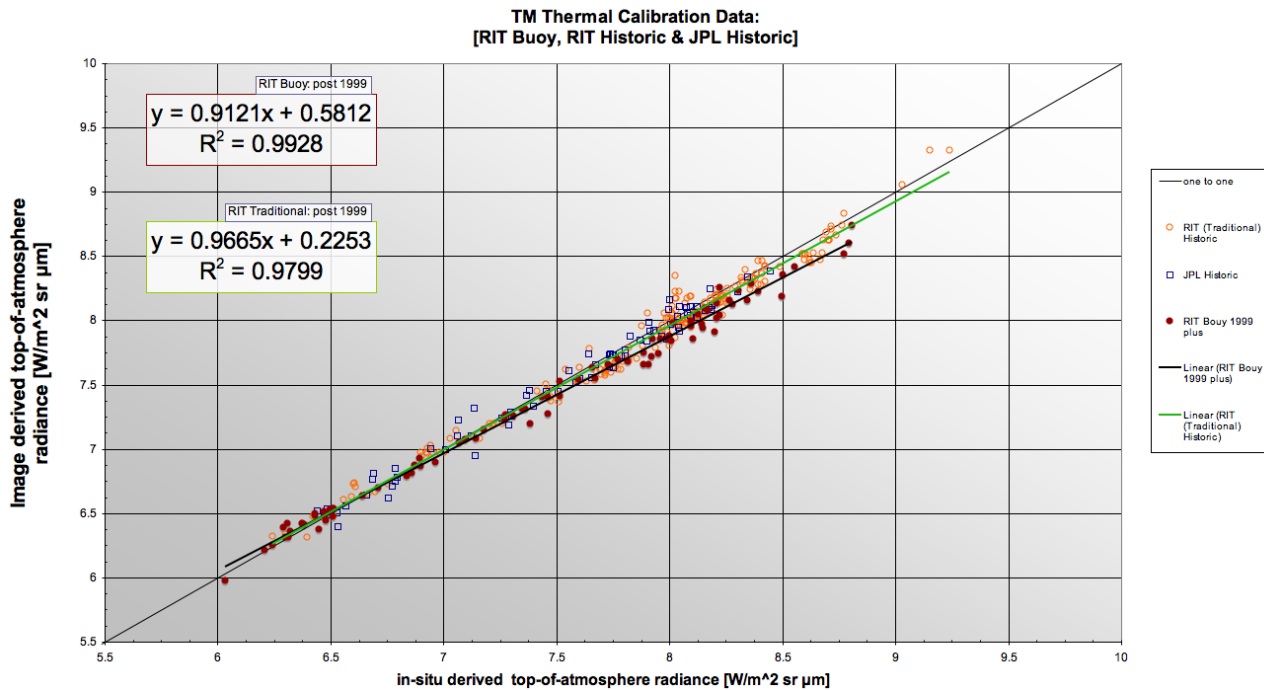


Figure 4.40: Derived calibration curve from the proposed methodology compared to the previous vicarious calibration results from JPL and RIT, radiance domain.

4.13.3 Proposed Methodology vs. Traditional Methodology

In an effort to quantify the difference in process error between the proposed methodology and traditional methodology (i.e. ground truth collected via contact thermistors) an error prorogation analysis was performed regarding the traditional method. Recall, the proposed method relies on buoy derived measurements, which are fed into a model to predict the required ground truth observations. The traditional approach utilizes contact thermistors, which are deployed on the water's surface at the time of, or as close as possible, to satellite overpass to acquire ground truth measurements. Note the only difference between the two approaches is the method in which ground truth measurements are obtained. The expression with which the error propagation analysis was conducted on is shown in Eq. 4.14; note the equation is stated in terms of band effective values.

$$S_{L_{eff}} = \left[\left(\frac{\partial L_{eff}}{\partial \epsilon} S_{\epsilon} \right)^2 + \left(\frac{\partial L_{eff}}{\partial L_{BB}} S_{L_{BB}} \right)^2 + \left(\frac{\partial L_{eff}}{\partial L_d} S_{L_d} \right)^2 + \left(\frac{\partial L_{eff}}{\partial \tau} S_{\tau} \right)^2 + \left(\frac{\partial L_{eff}}{\partial L_u} S_{L_u} \right)^2 + 2\rho_{\tau, L_u} \frac{\partial L_{eff}}{\partial \tau} \frac{\partial L_{eff}}{\partial L_u} S_{\tau} S_{L_u} + 2\rho_{\tau, L_d} \frac{\partial L_{eff}}{\partial \tau} \frac{\partial L_{eff}}{\partial L_d} S_{\tau} S_{L_d} + 2\rho_{L_u, L_d} \frac{\partial L_{eff}}{\partial L_u} \frac{\partial L_{eff}}{\partial L_d} S_{L_u} S_{L_d} \right]^{\frac{1}{2}} \quad (4.14)$$

where:

$$\frac{\partial L_{eff}}{\partial \epsilon} = L_{BB} \tau - L_d \tau$$

$$\frac{\partial L_{eff}}{\partial L_{BB}} = \epsilon \tau$$

$$\frac{\partial L_{eff}}{\partial L_d} = \tau - \epsilon \tau$$

$$\frac{\partial L_{eff}}{\partial \tau} = \epsilon L_{BB} + L_d - \epsilon L_d$$

$$\frac{\partial L_{eff}}{\partial L_u} = 1$$

The study compared the two methods using the respective error metrics and input values for all considered error propagation profiles [Appendix J]. Results from the study are shown in Table 4.11. The traditional approach was found to be on

Table 4.10: Listing and declaration of error terms in Eq. 4.4.

Error Term	Value	Source
S_ϵ - emissivity	0.006	Average: Barsi (2000) & Konda et al. (1994)
$S_{L_{BB}}$ - target radiance	0.2 K or 0.0265 $[W/m^2 sr \mu m]$	Zeng et al. (1999)
S_τ - transmission		case dependent
S_{L_d} - downwelled rad.	$[W/m^2 sr \mu m]$	case dependent
S_{L_u} - upwelled rad.	$[W/m^2 sr \mu m]$	case dependent
ASSUMPTION: R' and the error in computing L_{BB} is assumed negligible		

average 0.112 K less than the proposed methodology [Table 4.12]. This conclusion is encouraging because it suggests that the difference between the two methods is essentially within the sensor noise of the instrument. Recall in Section 4.13.2 the historic RIT Landsat 5 calibration data, calibrated with the traditional approach was found to be statistically different from the proposed method, as well as ~ 0.1 K different when comparing the average absolute bias temperatures. Thus, the above error propagation results further verify the previous findings that the two methods are only approximately 0.1 K different, with the traditional method exhibiting less error.

Table 4.11: Data from the comparison error propagation study, comparing the proposed method to the traditional method. Reported is the error in the effective radiance (L_{eff}) at the sensor and the error in temperature at the sensor provided a unit change in target temperature due to uncertainties in the entire proposed methodology. Note error is expressed in apparent temperature [K].

Date	Target Temperature	New	Method	Traditional	Method
		$S_{L_{eff}}$	$S_{Tat-sensor}$	$S_{L_{eff}}$	$S_{Tat-sensor}$
26Jan02 (dry)	274	0.407	0.439	0.236	0.324
	285	0.439	0.473	0.288	0.369
	300				
28Apr03	274	0.405	0.436	0.232	0.321
	285	0.437	0.471	0.284	0.366
	300				
27May90	274				
	285	0.378	0.445	0.225	0.332
	300	0.426	0.501	0.298	0.404
24Jun90	274				
	285	0.410	0.459	0.257	0.350
	300	0.461	0.517	0.333	0.424
24Oct98	274				
	285	0.411	0.459	0.258	0.351
	300	0.464	0.519	0.336	0.426
16Aug85	274				
	285	0.330	0.421	0.174	0.299
	300	0.368	0.469	0.238	0.364
06Jul99 (moist)	274				
	285	0.140	0.370	0.036	0.221
	300	0.142	0.374	0.042	0.229

Table 4.12: Error comparison: proposed method vs. traditional method

	Proposed Method	Traditional Method
Average:	0.454 K	0.341 K
Average Difference: 0.112 K		

Chapter 5

Results

5.1 Preprocessing of the Calibration Data

A total of 168 Landsat 5 scenes have been processed, which resulted in 214 calibration points spanning the years of 1984 to 2007 [Figure 5.1].

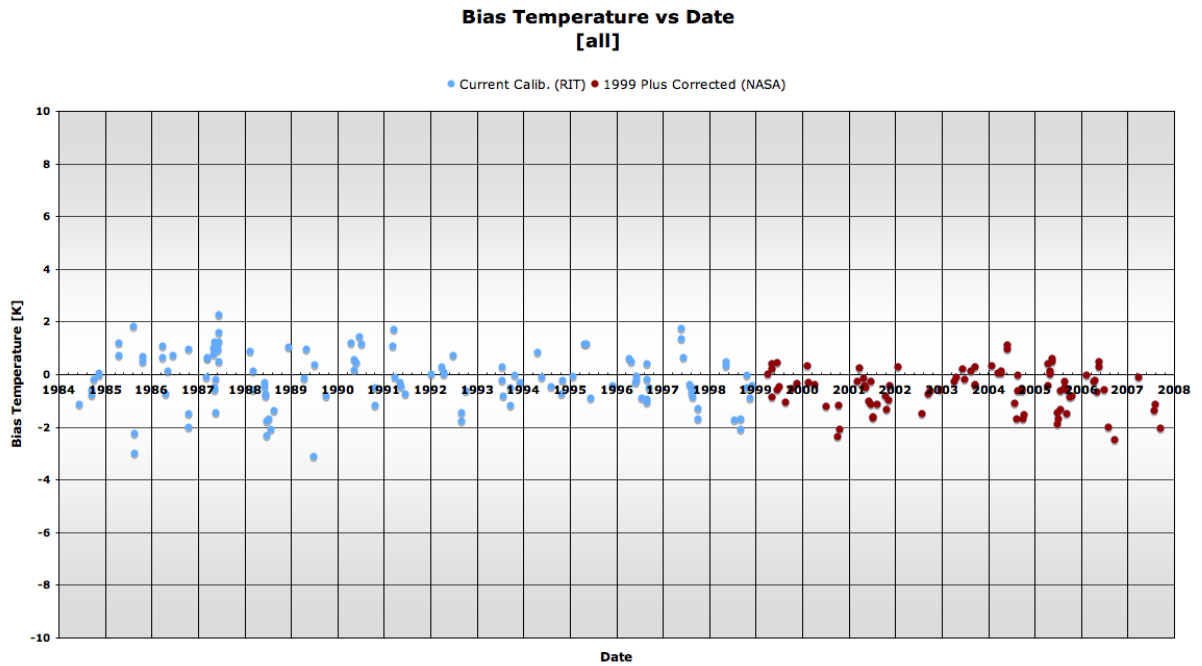


Figure 5.1: Temperature bias observed over time. Note if the sensor was perfectly calibrated and/or there were no fluctuations or uncertainties in current processing the resulting points would all lie on the 0 K bias line.

All data displayed in red [Figure 5.1] signify data that have been corrected as per the 2001 NASA applied correction [Section 2.1]. Meaning we can not directly compare the data plotted in red (corrected) to the data plotted in blue (raw) at this point, due to the NASA applied cold bias correction [Figure 5.1]. Thus the 2001 NASA correction must be removed from the data set prior to analyses of the Landsat 5 thermal instrument over time.

Before analysis is performed, the data will be preprocessed by the suggested filters (i.e. radiosonde dew point depression (DD) less than 3 K, large T_s corrections, highly variant surface thermal gradients and volcanic contamination correction). Figure 5.2 illustrates points that have failed to pass the constructed filters of: $DD < 3K$ for any layer within the observed radiosonde profile and scenes where the buoy location was over a sharp thermal gradient. As a result of the two filters, 16 points or roughly 8% of the data have been removed from the data set. Most of these filtered points were added to the data set in the early stages of this work, thus were included before the filter selection was decided upon. Therefore many scenes not reported, were preprocessed and excluded prior to any processing because they failed a given filter criteria (i.e. predominately radiosonde observations with $DD < 3 K$).

As discussed in Section 2.4, the impact of major volcanic eruptions on temperature retrieval missions is widely known. Through a study shown in Appendix B, the corrections shown in Table 5.1 were applied to the data set. Figure 5.3 illus-

Table 5.1: Volcanic correction summary.

Year	MODTRAN ID and Correction	Avg. Corr.	Pts
1984	4 high volcanic (volc.) profile and aged volc. extinction	0.1440 K	6
-	-		
1991	2 moderate volc. profile and fresh volc. extinction	0	0
1992	4 high volc. profile and aged volc. extinction	0.0943 K	6
1993	7 high volc. profile and background stratospheric extinction	0.1102 K	5
1994	7 high volc. profile and background stratospheric extinction	0.1060 K	5
1995	6 moderate volc. profile and background stratospheric extinction	0.0260 K	5

trates the data with the above mentioned corrections applied (27 points or roughly 13% of the data have been influenced by this correction). Note the applied volcanic contamination corrections are all small ($\sim 0.1 K$).

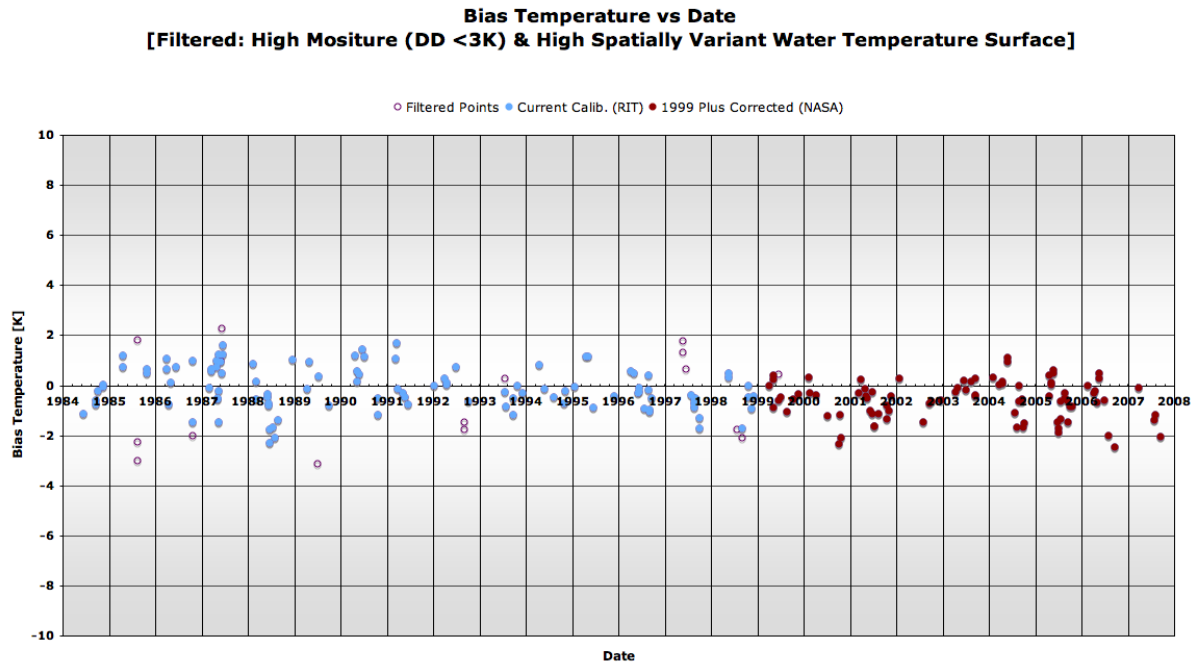


Figure 5.2: Dew point depression less than 3 K and highly spatially variant water temperature surfaces have been filtered (maroon) out of the existing data set.

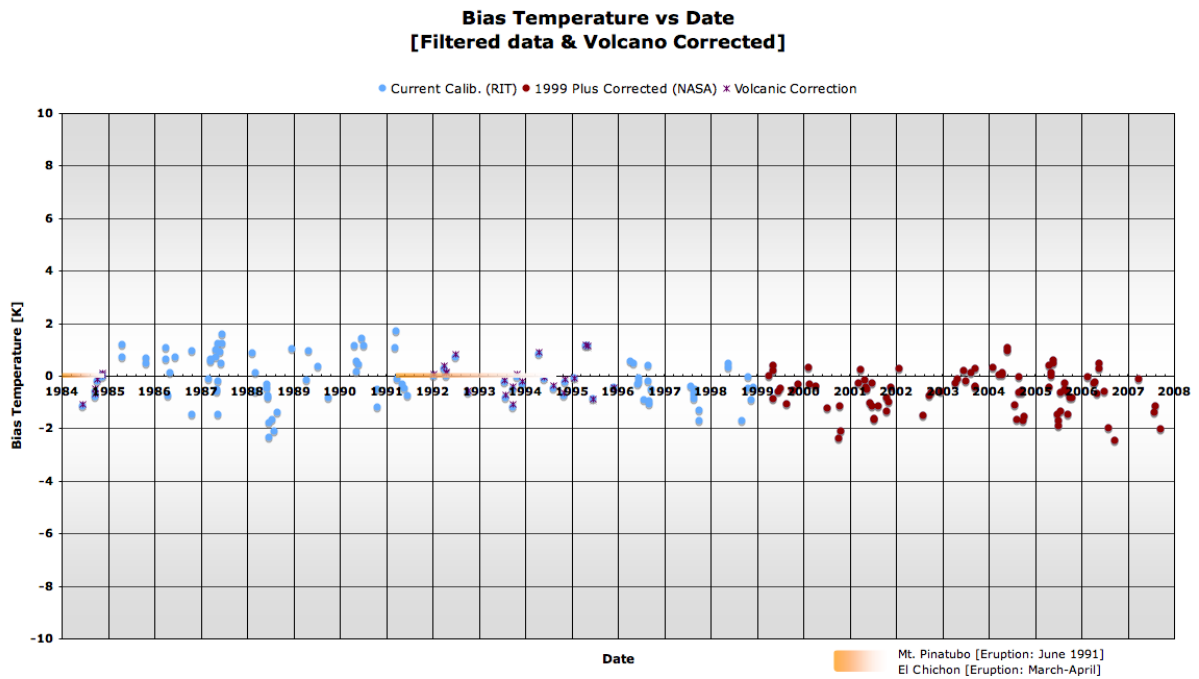


Figure 5.3: Illustrates the filtered data along with the data that has been corrected for volcanic contamination (maroon).

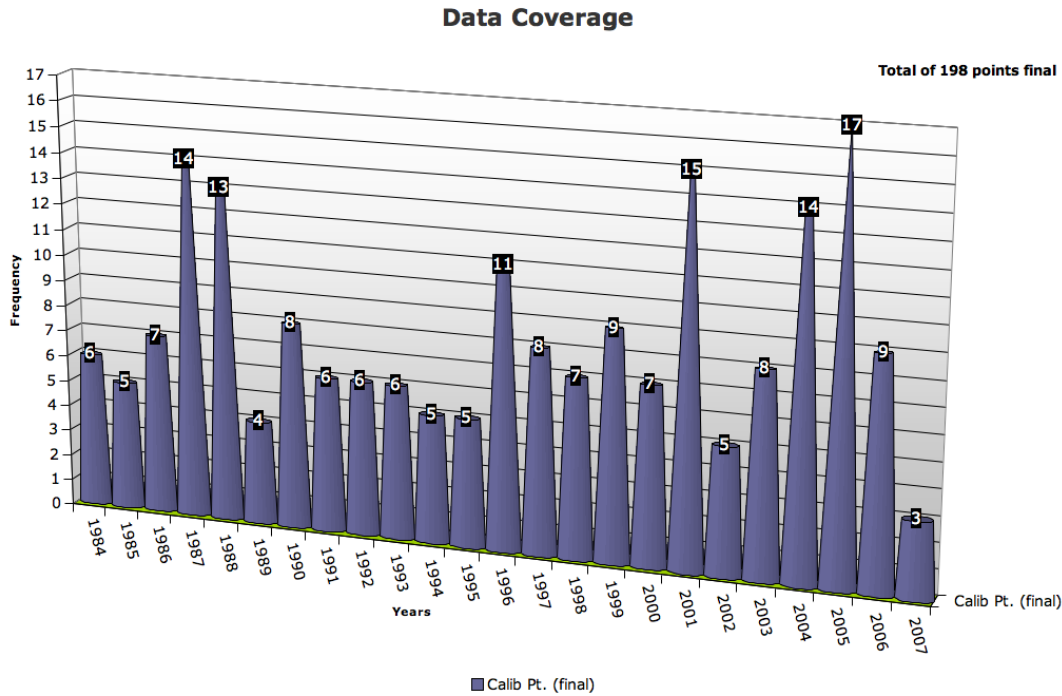


Figure 5.4: Histogram displaying the data coverage (filtered data) for all data to be used towards the final calibration results.

Figure 5.4 depicts a histogram illustrating the data coverage of the filtered data set consisting of 198 calibration points; which will be referred to as the final data set from this point forward. Note that each year has at least three calibration points resulting in a median of seven points per year.

The result of all filters [Figures 5.2 & 5.3] yields the final data set [Figure 5.5]. Note the data illustrated in Figure 5.5 is the same data as Figure 5.3, with an addition six month moving average shown. The plotted moving average provides a simple way to smooth and visualize the data to assist in the identification of discernible patterns. Through visual inspection of Figure 5.5 (*c.f.* moving average), notice a visible seasonal oscillation. This pattern suggests that the first half of the year, typically low target temperatures (average of all target temperatures January - June: 280.84 K), is slightly warm biased where the later half of the year, typically higher target temperatures (average of all target temperatures July - December: 289.79 K), is slightly cold biased. It is important to identify that the seasonal oscillation is evident throughout the entire data set [Figure 5.5], with the exception of the first few years after launch.

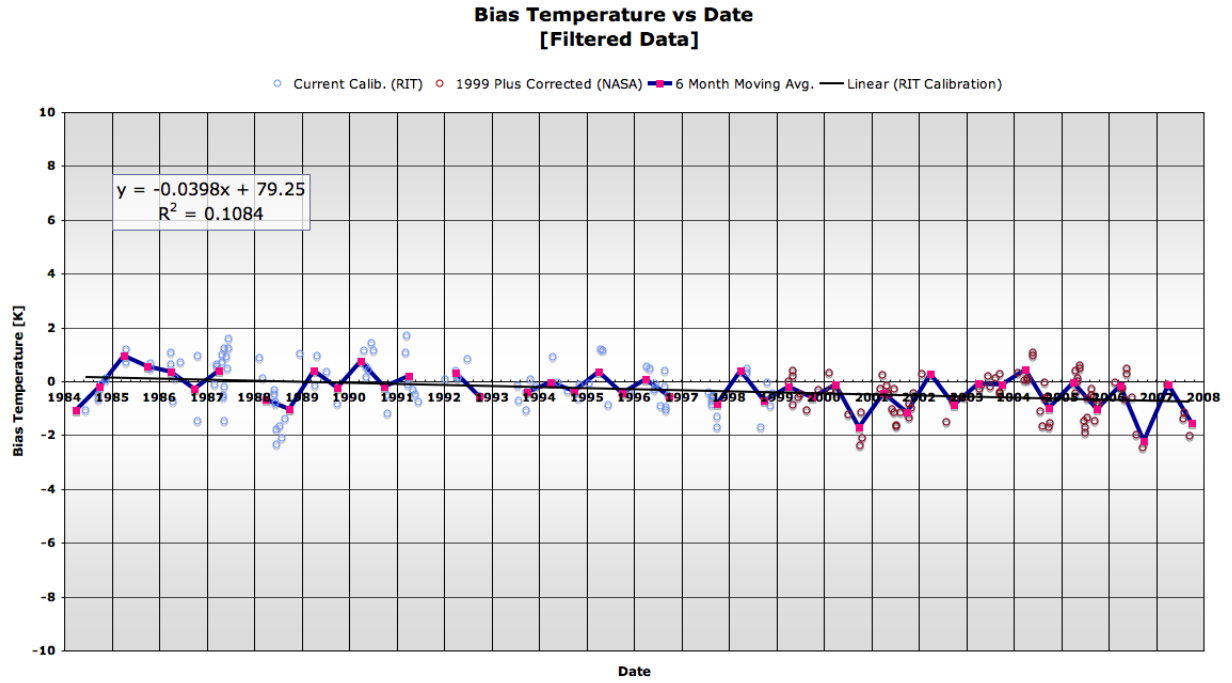


Figure 5.5: Illustrates all filtered data. Note it is this data that will be used for the final calibration analysis.

To aid in the investigation of the apparent seasonal oscillation the data are visualized in the radiance domain, plotting the predicted at-sensor radiance versus image derived radiance for each scene [Figure 5.6 and 5.7 (all data and filtered data, respectively)]

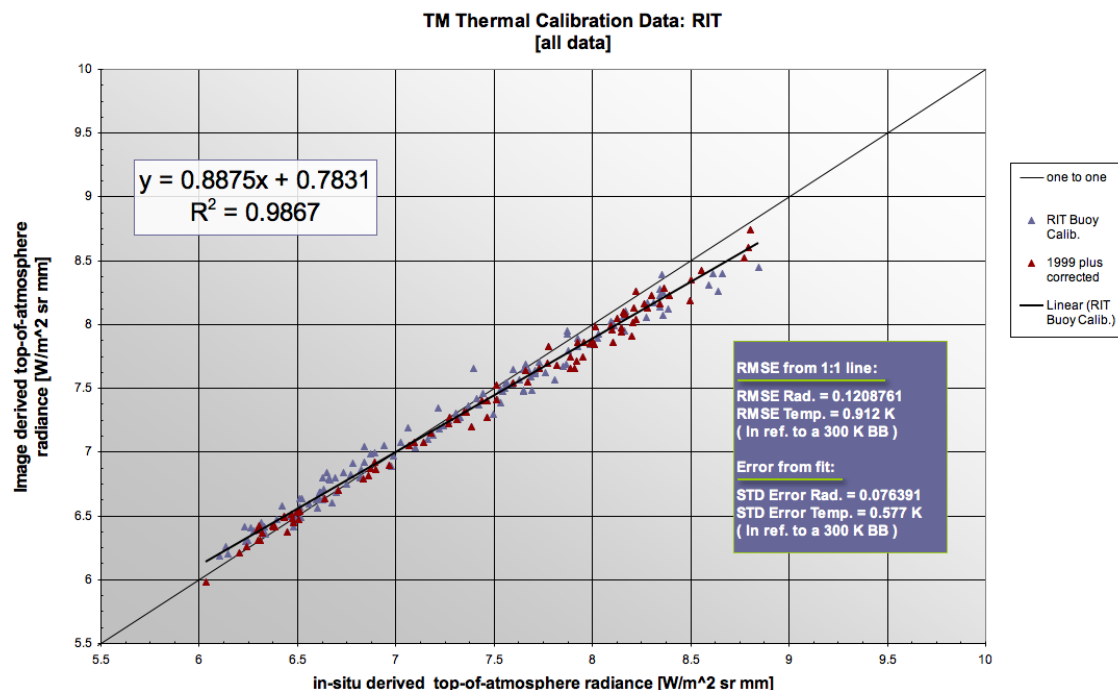


Figure 5.6: Predicted at-sensor radiance vs. image derived radiance for all data. Observe the lower radiances appear to be influenced by an apparent warm bias, where higher radiance values appear to be indicative of a cold bias.

Through analysis of Figure 5.7 it is evident that the sensor has a gain issue. Recall, Figure 5.5 illustrated that a seasonal oscillation is evident overtime, illustrating that lower temperature targets (first 6 months of the year) were positively biased, and that higher temperature targets (last 6 months of the year) were negatively biased. Through inspection of Figures 5.6 & 5.7 (all and filtered data, respectively) it is clear that low radiance targets portray a slight warm bias and higher radiance targets demonstrate a cold bias. This conclusion again is not only consistent with the above mentioned seasonal oscillation observed in [Figure 5.5], but also provides adequate evidence that the sensor has difficulty characterizing the gain. Note in Figures 5.6 & 5.7 the 1999+ NASA corrected values (i.e. cold bias corrected) have been highlighted.

Examining the root mean square error (RMSE) for all data (i.e. raw "unfiltered" data) is 0.912 K, where the filtered data set yields a RMSE of 0.813 K, both with respect to the 1:1 line. The standard error (STD) for the resulting regression line was found to be 0.577 K and 0.514 K for the unfiltered and filtered data respec-

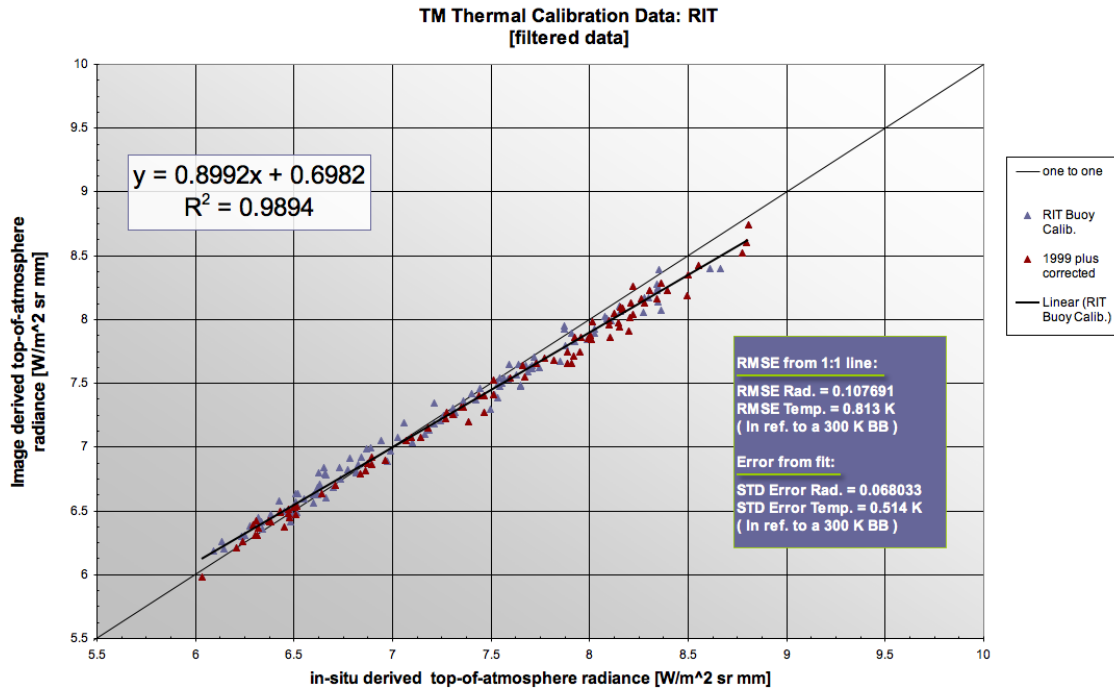


Figure 5.7: Predicted at-sensor radiance vs. image derived radiance: filtered data. Note there appears to be a gain issue with lower radiances portraying an apparent warm bias, where higher radiance values appear to be indicative of a cold bias.

tively. Emphasis must be placed on the fact that from an "overall perspective" the instrument has fluctuated only minimally, roughly within ± 1 K, over the lifetime of the instrument.

Important (filtered and 1999 NASA applied correction data set):

- The state of the instrument has roughly fluctuated within a minimal bound of approximately ± 2 K for all calibration data over the lifetime of the instrument.
- Results are consistent with previous vicarious calibration efforts, demonstrating a warm bias in the mid 1980's followed by a cold bias around the year 2000.
- An apparent gain issue is evident: low radiance targets portray a slight warm bias where higher radiance targets demonstrate a cold bias.
- It is clear the Landsat 5 TM thermal band has fluctuated slightly over time.

All analysis performed here contributing to the final calibration results will focus solely on the unbiased data [Figure 5.8]. That is to say, all data post April 1, 1999 will be uncorrected by subtracting the applied cold bias correction of $+0.092 [W/m^2 sr \mu m]$.

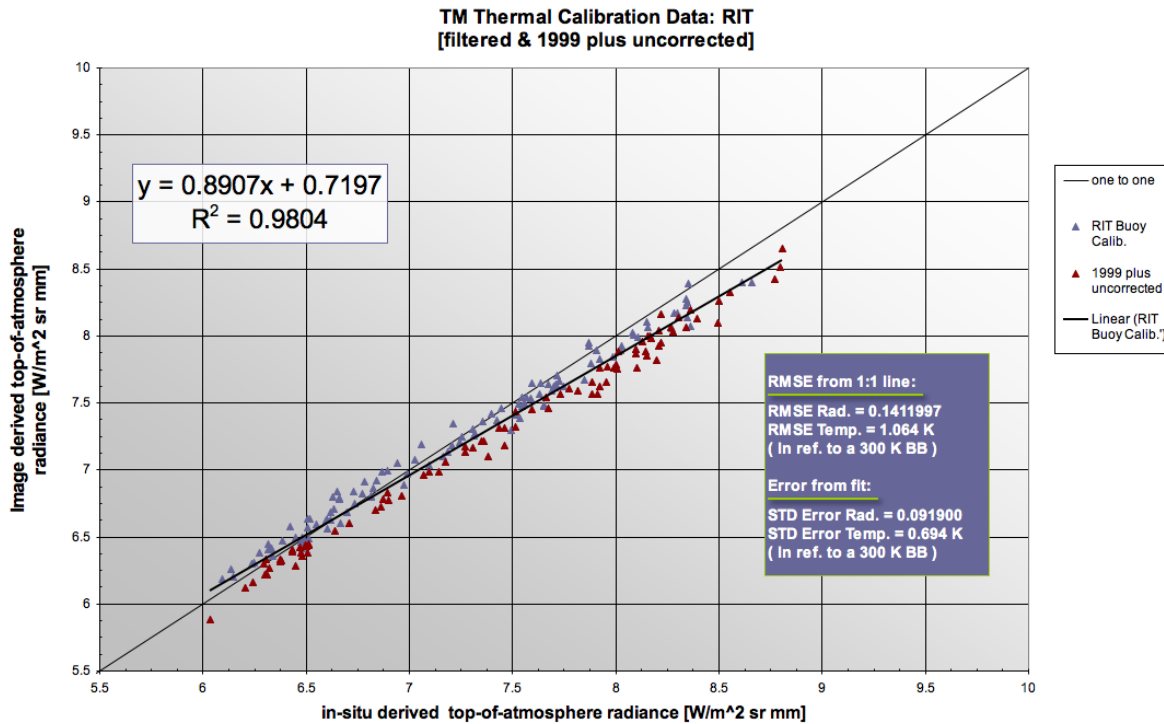


Figure 5.8: Predicted at-sensor radiance vs. image derived radiance: filtered and 1999 plus uncorrected data. Note the graph depicts evidence of a gain issue (cold bias) higher radiance values.

Recall the data set which included the 1999+ NASA correction [Figure 5.7] suggested that there is a slight warm bias at low radiances and a slight cold bias at high radiances. Notice however, after the 1999+ correction is removed [Figure 5.8], all data post 1999 illustrate a dominant cold bias, which is also apparent in Figure 5.9. Realize that the cold influence is more pronounced at higher radiances, although still noticeable at low radiances [Figure 5.8]. This result presents an interesting finding which may suggest that a time dependent gain correction is needed. In preparation of such a correction, Figure 5.10 is offered to illustrate trend lines for data both pre- and post-1999; realize this is the same data as illustrated in Figure 5.8. Through visual inspection of Figure 5.10 it is clear that the two trend lines appear

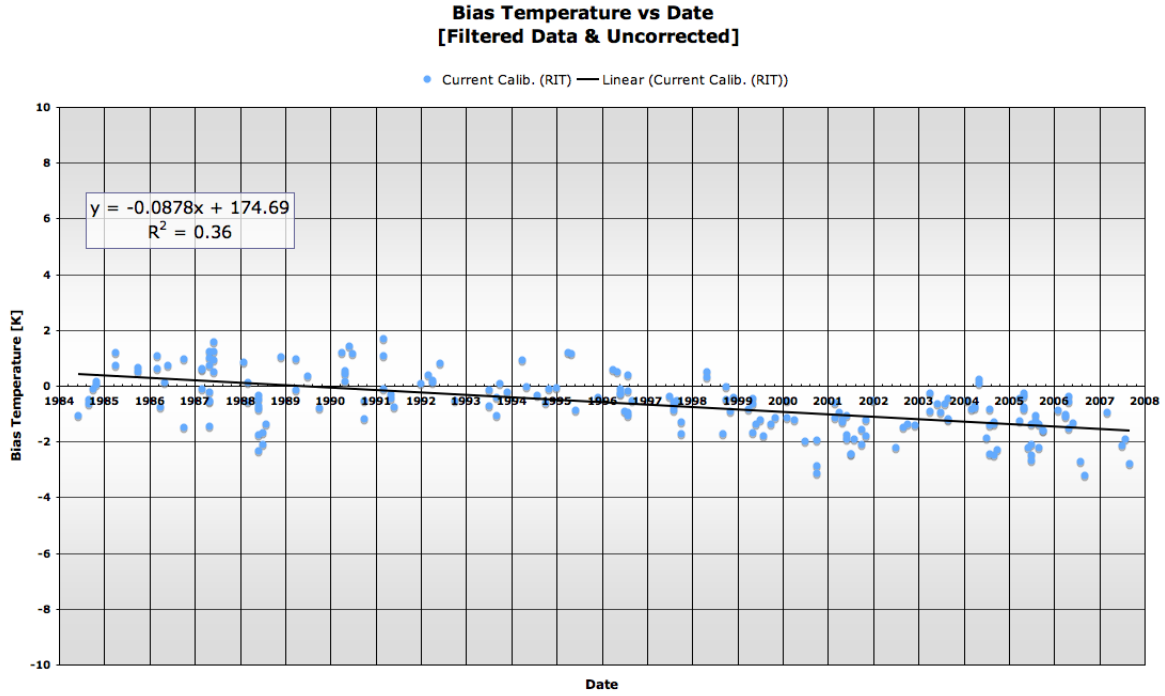


Figure 5.9: Temperature bias vs time: filtered and uncorrected data.

to be noticeably different although were found to be not statistically different at the 99% C.I., using an F-test, testing if both the slope and intercept of the two regression lines were significantly different. To perform this hypothesis test dummy variables were utilized according to the methods found in Weisberg (1985). Additionally the temperature bias from the two datasets were tested and found to be significantly different at the 99% C.I. using a two sampled t-test. Through further investigation it was found that the absolute average temperature bias was 0.7 K and 1.39 K for data prior to and post 1999, respectively; resulting in a absolute difference of 0.686 K.

For clarity, all hypothesis tests presented in this work have been checked for normality (based on the D'Agostino & Pearson omnibus normality test), as well as checked that the variances were not statistically different (for two sampled tests) so that the results of the t-test could be trusted. Recognize for the sake of brevity, it is implied that if a t-test was used, all prior tests did not fail (i.e. normality and variance check).

Figure 5.9 suggests that a temperature bias exists over time, suggesting that the

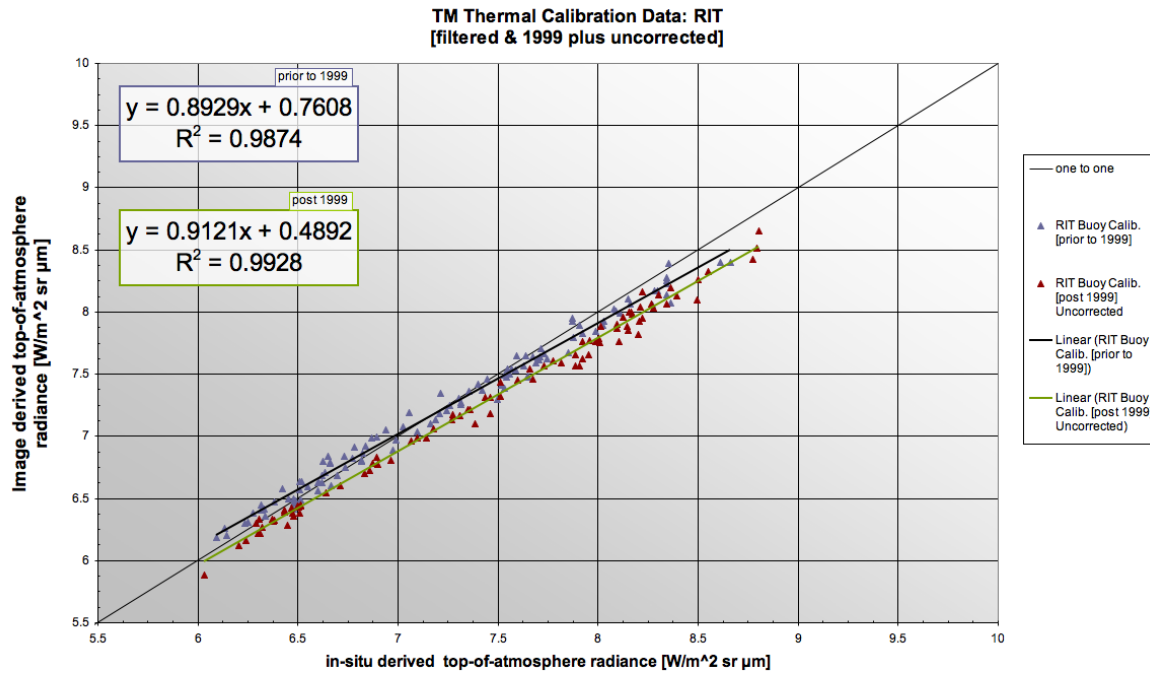


Figure 5.10: Temperature bias vs time: filtered and uncorrected data; shown are trendlines for data pre and post 1999.

sensor had a warm bias from roughly 1984 to 1990 and is cold biased thereafter. Notice that this result is consistent with the previous calibration efforts.

Through visual inspection of Figure 5.10 notice that the two trendlines are relatively equal in slope, although offset by differing intercepts. This suggests the gain of the instrument (i.e. slope of the data [Figure 5.10]) is not correct but constant over time, where as the bias post 1999 is found to shift by a constant [Figure 5.10]. Simply stated the data suggest the gain of the instrument has consistently been off and that the bias has shifted by a relative constant for all data post 1999.

For completeness and to reemphasize the point that the data suggests a bias exists between low and high radiances Figure 5.11 is offered. Note the data post 1999 illustrates a dominant cold bias. Again notice that the seasonal oscillation in the data suggests that the instrument demonstrates a clear gain issue. In an effort to validate that the data set warrants calibration corrections, two test were conducted. The first performed test was a two tailed t-test on the uncorrected data using the difference between image derived radiance and in-situ derived radiance to

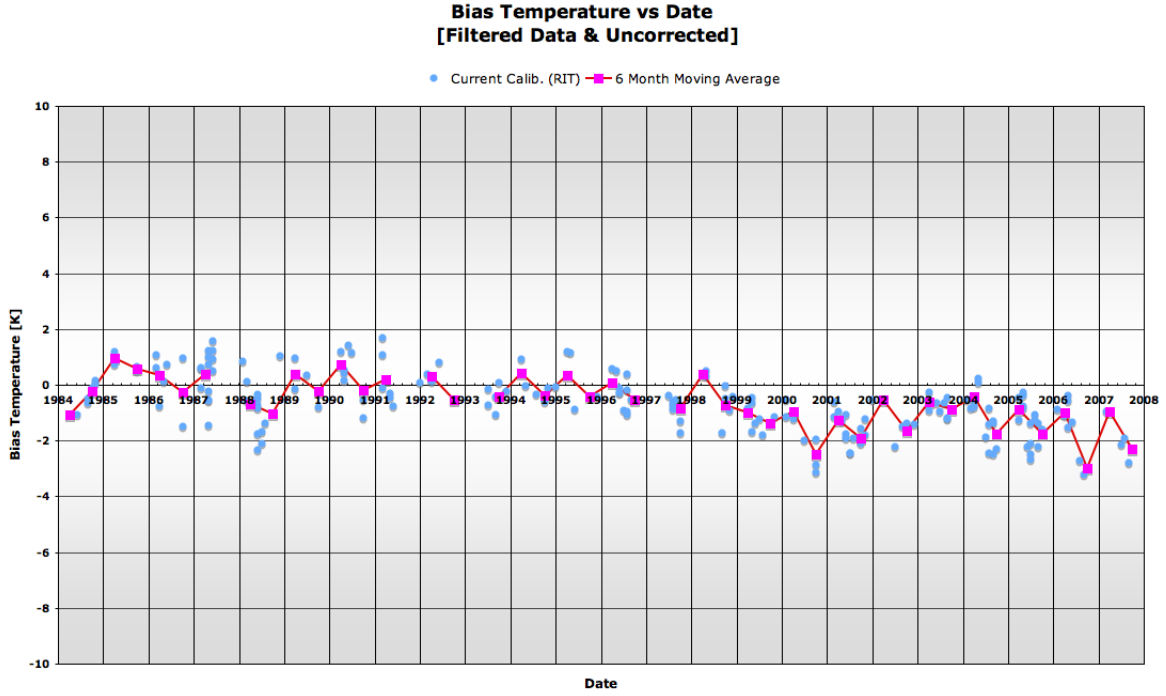


Figure 5.11: Temperature bias vs time: 6 month moving average on the filtered and uncorrected data.

investigate if the data are statistically different from 0.0 [$W/m^2 sr \mu m$] (i.e. the 1:1 line [Figure 5.8]). The uncorrected data set was found to be statistically different from 0 K using a confidence interval (C.I.) of 99%. A second test was performed to determine if the absolute value of the bias temperature data was statistically greater than the $NE\Delta T$ of the instrument, note the upper bound of the reported $NE\Delta T$ (0.3 K) was used; [Section 3.1.1]. The test showed the absolute value of the bias temperature was statistically greater than 0.3 K using a C.I. of 99%. The two tests noted above illustrate that the uncorrected data are significantly different from the 1:1 line, as well as statistically greater than the $NE\Delta T$ of the sensor. This conclusion verifies the calibration record of the instrument warrants further investigation (i.e. the sensor is out of calibration and corrections are needed).

Important conclusions from Figures 5.8 to 5.11:

- Results are consistent with previous vicarious calibration efforts, demonstrating a warm bias in the mid 1980's followed by a cold bias around the year 2000.
- If the data investigated are treated as one sample (i.e. pre and post 1999 together), the data suggest that the instrument has a pronounced gain issue (or cold bias at radiance's above roughly $6.6 [W/m^2 sr \mu m]$).
- If the data investigated are treated as two samples (i.e. pre and post 1999), the data suggest that the instrument prior to 1999 has both a warm bias at low radiances and cold bias at higher radiances, where as the data post 1999 is dominated by a cold bias.
- For all filtered & uncorrected calibration data, results confirm that the instrument has fluctuated slightly over the lifetime of the instrument:
RMSE = 1.064 K.

From this point forward all results will be derived from the uncorrected data shown in Figures 5.8 to 5.11. In the remaining stages of this work an investigation will take place in an effort to determine the most appropriate correction to be applied to the historical calibration record of the Landsat 5 TM thermal band. In the conclusion of this work a recommendation will be presented, verified and put forward regarding the method to permanently correct the historical calibration record of the Landsat 5 TM Band 6.

5.2 Calibration Results: Proposed Corrections

This section will propose seven unique calibration correction approaches. Each approach will be discussed and summarized independently. For clarity a global correction implies a single correction is applied to the entire data set.

5.2.1 Linear (Global: Slope & Intercept) Correction

To establish an impartial view of the calibration data over time, a linear correction will first be applied. The correction is straightforward, and is applied so that the instrument characterizes all radiance levels equally from a gain and bias perspective,

which allows for the further examination of a true sensor bias over time. The linear regression or best fit line [Figure 5.8] (note: strong correlation $R^2=0.9791$) was used to find the difference from the true 1:1 line. Thus, the regression model was given scene derived (ground truth predicted) values to predict the best fit line, which was then differenced with the 1:1 line. The resulting differences were then applied to the image derived radiance to yield [Figure 5.12] the gain corrected values.

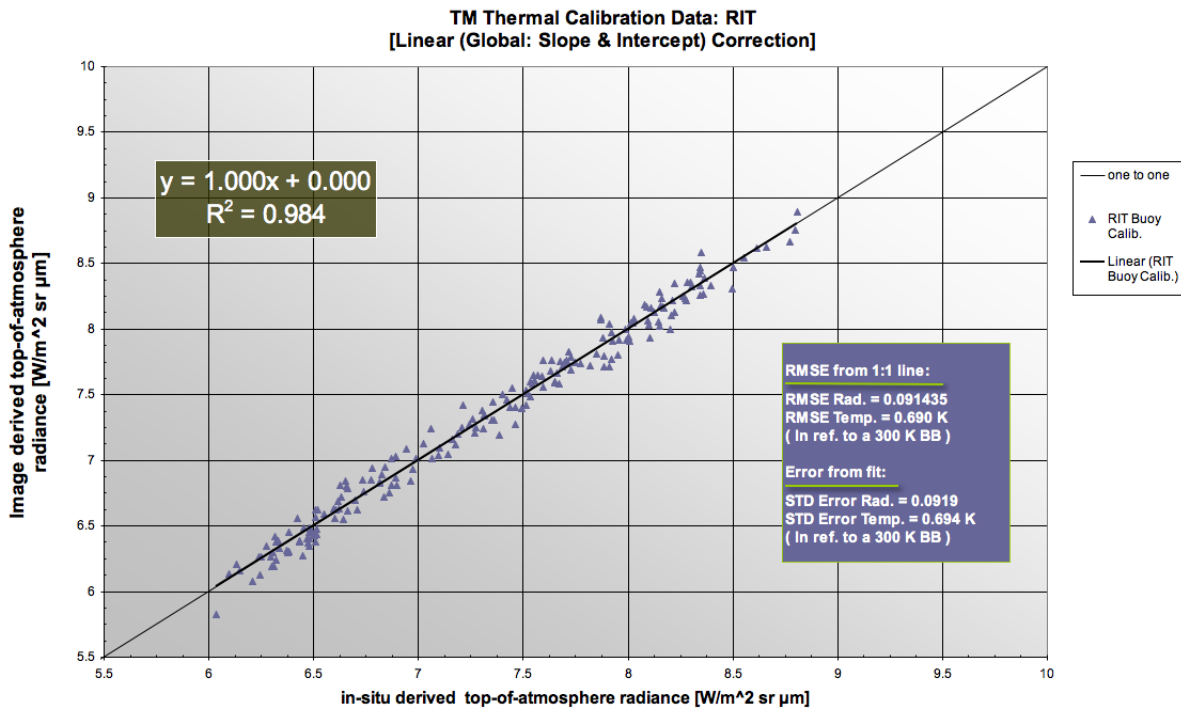


Figure 5.12: Predicted at-sensor radiance vs. image derived radiance: linear (global: slope & intercept) correction.

The data demonstrates a RMSE of 0.69 K contributing to a 0.374 K reduction in RMSE compared to that of the original uncorrected data (RMSE of 1.064 K) [Figure 5.8]. Through visual inspection of Figure 5.12, the gain correction appears to have performed well, note the standard error of the fitted line was 0.694 K and the resulting slope and intercept are effectively 1.0 and 0.0, respectively. To further verify this correction, a t-test was performed to investigate if the corrected values were statistically different from the 1:1 line (i.e. are the bias radiances different from 0.0 $[W/m^2 sr \mu m]$). At the 99% C.I. the data was found to be not significantly

different from the 1:1 line.

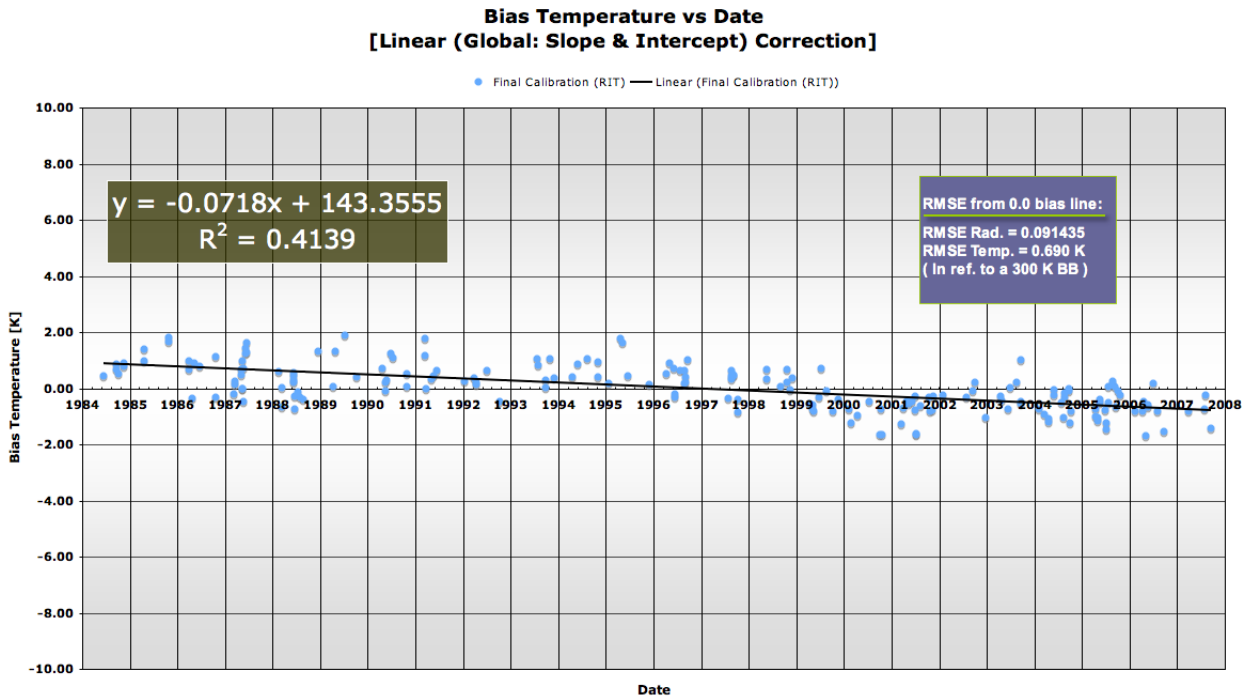


Figure 5.13: Applied linear (global: slope & intercept) correction plotted as a function of time.

The linear (global: slope & intercept) corrected values are now plotted as a function of time [Figure 5.13]. The data suggests that after correcting for the gain fluctuation a temperature bias exists over time in the instrument. The period from 1984 through roughly 1998 are for the most part positively biased around 1 K. In contrast, from the period of roughly 1999 to 2007 the data appears to be dominated by more of a cold bias within or around -1 K. Observe that the reported slope of the trend line (-0.0718 K/year) [Figure 5.27] results in a total change in bias temperature of -1.723 K over the 24 year span the satellite has been in orbit, alluding to the fact that further corrections (i.e. bias related corrections) may need to be applied to this data set. Interesting to note is that from 1999 to 2007 a rough sinusoidal behavior may be present in the data set. Through visual inspection, this "oscillation" has an apparent period of roughly 5 years. Although the cause of such behavior is unknown at this time, it should be flagged as an interesting finding.

Summary:

- Linear (global: slope & intercept) correction: RMSE of 0.69 K.
- Reduction in RMSE compared to the filtered & uncorrected data: 0.374 K.
- The correction exposed a temperature bias exists over time, which amounts to a total change over time of -1.732 K (warm bias to a cold bias [Figure 5.27]).
- The corrected data demonstrate a visible fluctuation in bias temperature over time, thus further corrections are needed.

5.2.2 Linear (Dual: Slope & Intercept) Correction

From the equations shown in Figure 5.10, a linear (dual: slope & intercept) correction was applied to the dataset. Meaning all data prior to 1999 were corrected separately from all data post 1999 (using the same method as in Section 5.2.1) by the appropriate regression equations (note: strong correlations $R^2=0.9874$ & $R^2=0.9928$, pre and post 1999 data; respectively); results are shown in Figure 5.14. The linear (dual: slope & intercept) correction demonstrates a RMSE of 0.488 K, which contributes to a 0.576 K reduction in RMSE compared to that of the original uncorrected data.

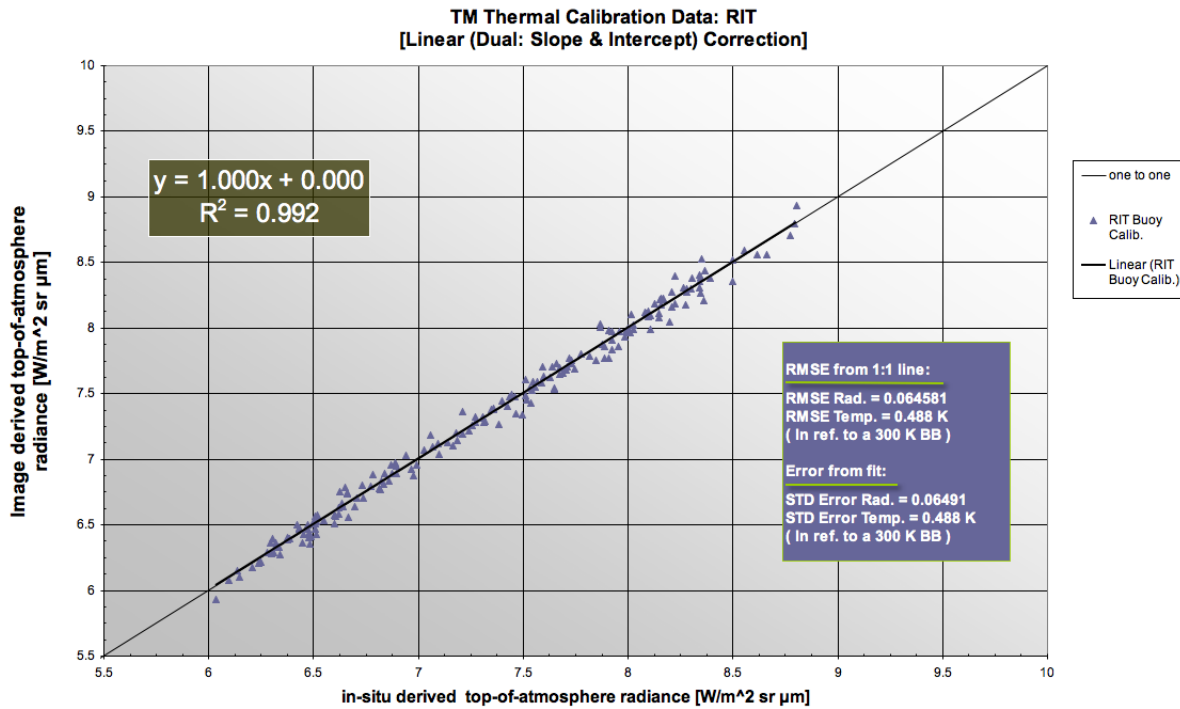


Figure 5.14: Predicted at-sensor radiance vs. image derived radiance: linear (dual: slope & intercept) correction.

Figure 5.15 illustrates the linear (dual: slope & intercept) correction compared to the linear (global: slope & intercept) correction. Notice the bulk of the differences occur at low radiances, where the linear (dual: slope & intercept) correction is superior. The linear (dual: slope & intercept) corrected values are plotted as a function of time [Figure 5.16]. Notice the correction has performed well and results in a very small bias ~ 0.1 K over the duration of the study [Figure 5.16]; observe the

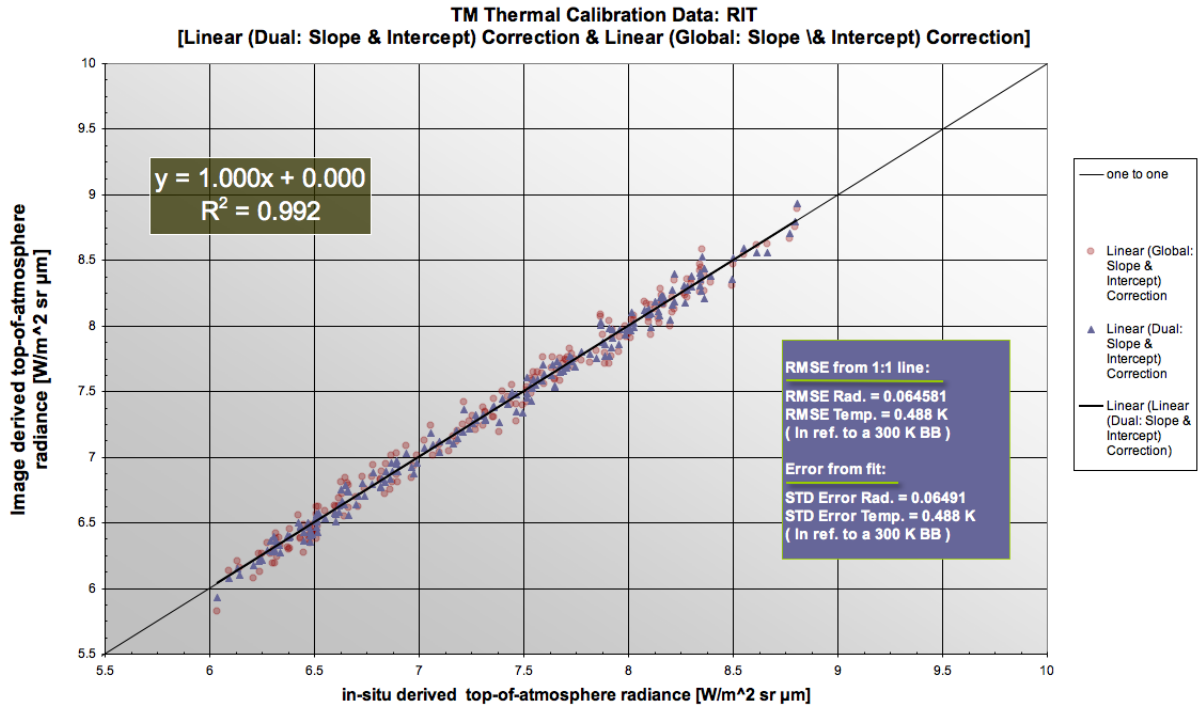


Figure 5.15: Predicted at-sensor radiance vs. image derived radiance: linear (dual: slope & intercept) correction (purple) plotted with the Linear (global: slope & intercept) correction (red). Notice the bulk of the differences are at low radiances.

best-fit line has a slope of -0.0044 K/year. Also, it should be realized that 0.1 K is within the sensor noise, thus the linear (dual: slope & intercept) correction may be sufficient as an independent correction. A test was conducted evaluating if the bias data was statistically different for the zero bias line. Results found the slight bias was not statistically different from zero biased line at the 99% C.I. via a two tailed t-test.

Plotting a 6 month moving average of the corrected data as a function of time [Figure 5.17] reveals that the correction has eliminated the the seasonal variation shown in Figure 5.11. However, notice that a cyclical trend that decreases in both magnitude and period with time is discernible. To aid in the investigation of the apparent fluctuation, a 6 month and 2 year running average is shown [Figure 5.18]. Through visual inspection [Figure 5.18] a slight two to three year oscillation which varies within approximately $\pm 0.5K$ is clearly noticeable in the data set.

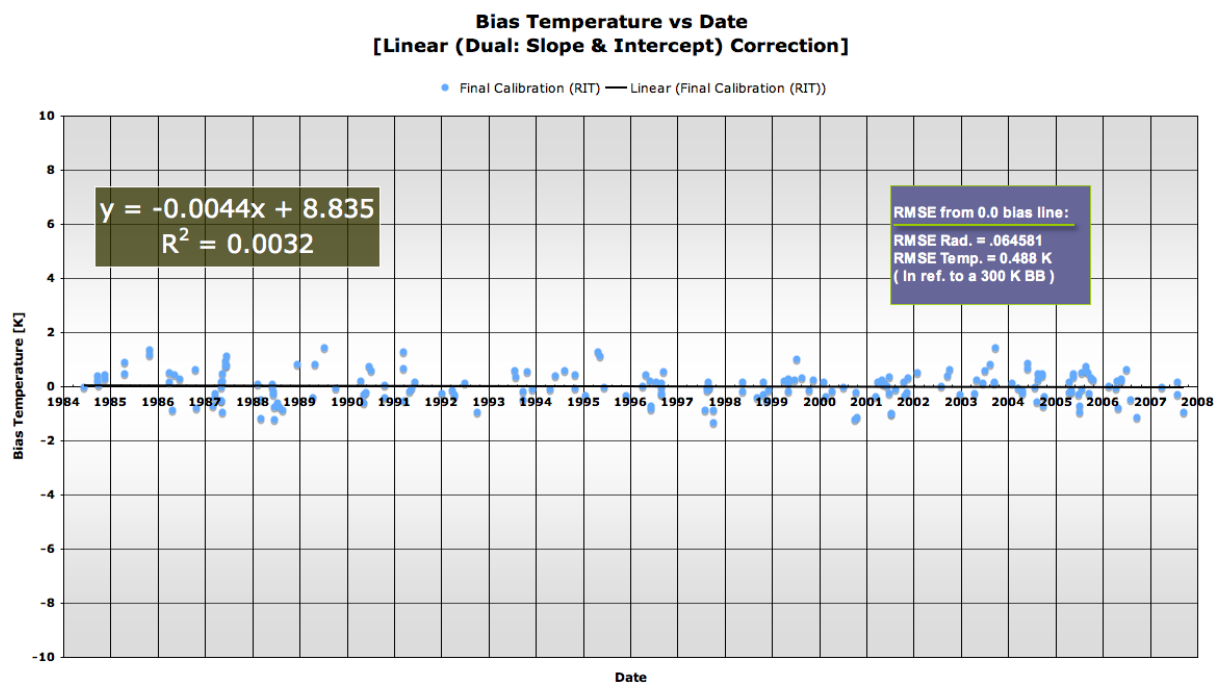


Figure 5.16: Applied linear (dual: slope & intercept) correction plotted as a function of time.

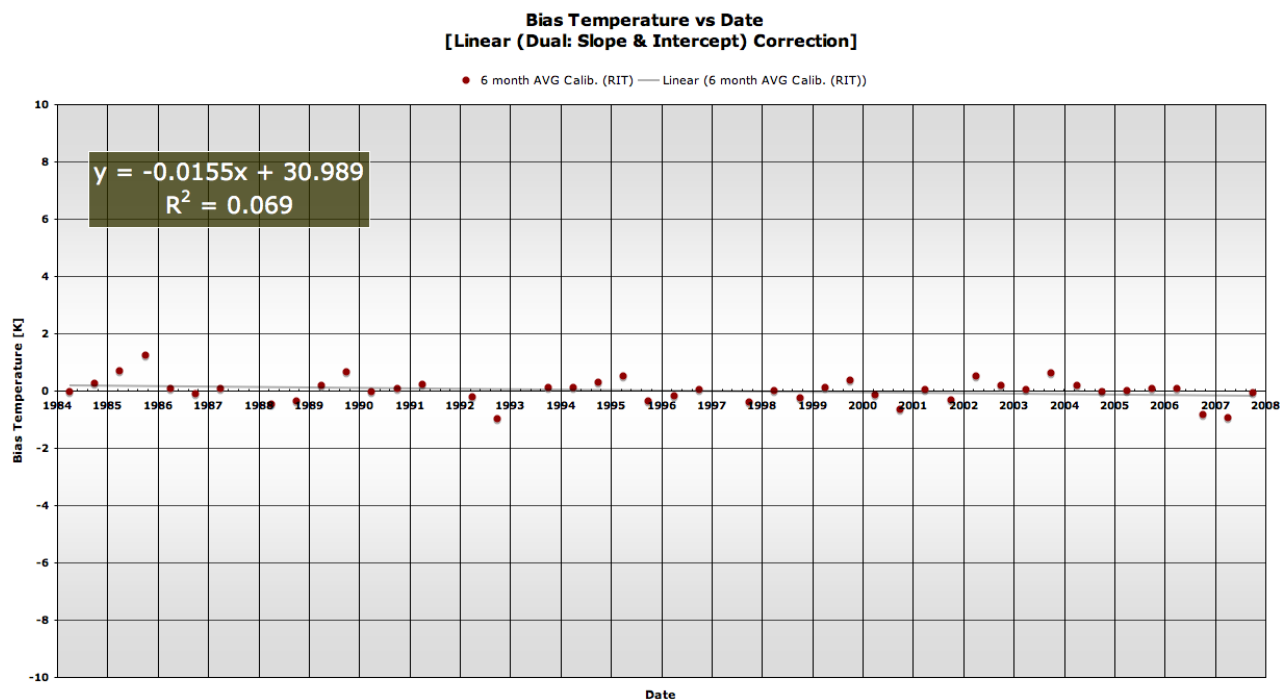


Figure 5.17: Illustrates a 6 month moving average applied to the linear (dual: slope & intercept) corrected data plotted as a function of time.

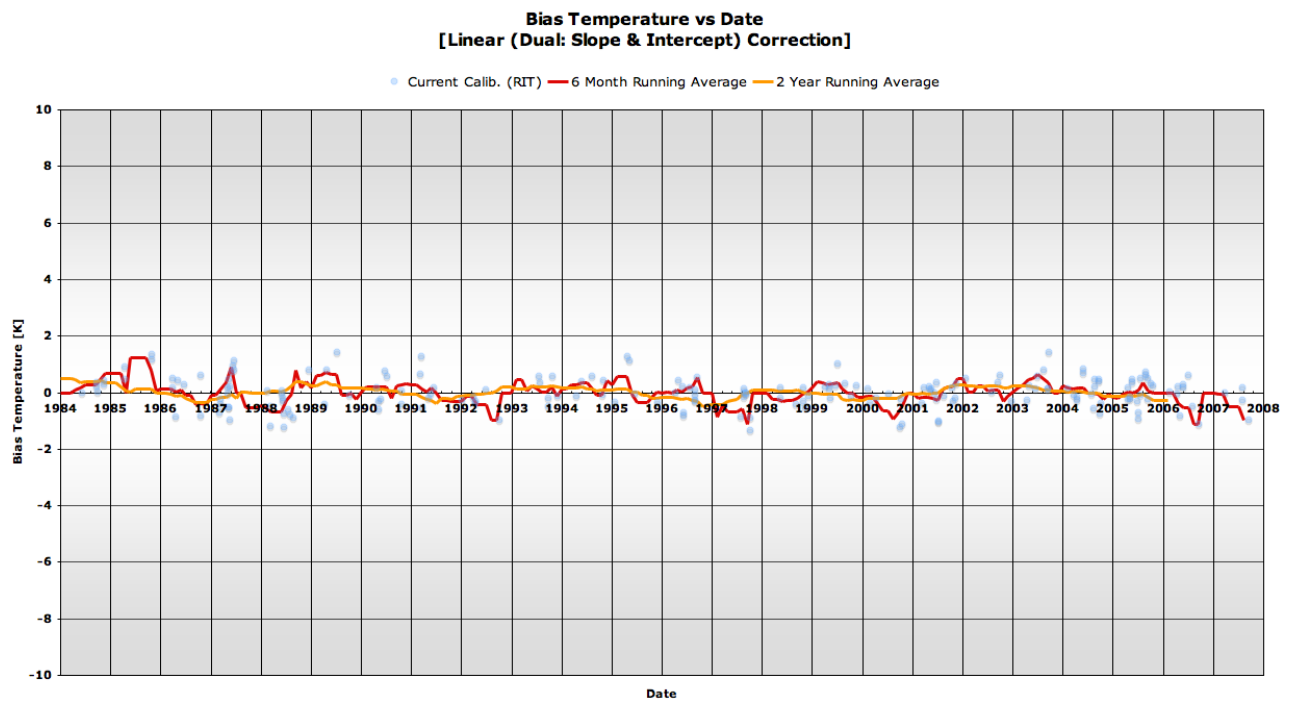


Figure 5.18: Illustrates a 6 month and 2 year running average applied to the linear (dual: slope & intercept) corrected data plotted as a function of time.

Summary:

- Linear (dual: slope & intercept) correction out performed the Linear (global: slope & intercept) correction.
- Linear (dual: slope & intercept) correction: RMSE of 0.488 K.
- Reduction in RMSE compared to the filtered & uncorrected data: 0.576 K.
- The linear (dual: slope & intercept) correction demonstrates a bias over time that is not statistically different from zero, although a rough 2 year cyclical fluctuation in the bias over time is evident [Figure 5.17 & 5.18]
- The correction illustrated a slight temperature bias over time amounting to a total change of -0.1 K (warm bias to a cold bias [Figure 5.16]) over the lifetime of the instrument.
- Total change in bias over the time domain of the study is within sensor noise.

5.2.3 Linear (Global Slope & Dual Intercept) Correction

Recall the equations shown in Figure 5.10, which represent the regression lines for the data prior to and post 1999. Through inspection of Figure 5.10 notice that the slope of the two lines are similar and differ by a clear bias. As previously mentioned, the bias was found to be significantly different between the two data sets, however, the slope and intercept were tested and found to be not statistically different. Provided the information that the slopes of the two lines are similar, a weighted average will be taken between the two slopes, to obtain a global slope correction (weighted average slope = 0.901418589). The bias correction for the two data sets (i.e. data prior to and post 1999) will be treated differently as they were found to be significantly different. Thus all data prior to and post 1999 were corrected uniquely. The intercept correction was found by taking the regression line of the appropriate class, solving for the intercept (i.e. fixed slope) for all values of x (in-situ derived radiance) and averaging the results. This method was applied to both data sets resulting in intercepts of $b_1 = 0.698989001$ and $b_2 = 0.568537821$ (prior to and post 1999, respectively). The correction consists of a single slope correction with two unique time dependent intercept values. The correction resulted in a RMSE of 0.491 K [Figure 5.19], contributing to a 0.573 K reduction in RMSE compared to that of the original uncorrected data. Figures 5.19 and 5.20 demonstrate that the correction performed well, both removing the gain issue and significantly reducing the bias in the sensor over time. Notice from Figure 5.20 a slight temperature bias is shown over time, amounting to a total change of -0.12 K over the 24 year period (warm bias to a cold bias), although realize this level of bias change is within sensor noise.

A test was conducted evaluating if the bias data was statistically different for the zero bias line. Results found the bias temperatures were not statistically different from zero biased line at the 99% C.I. via a two tailed t-test.

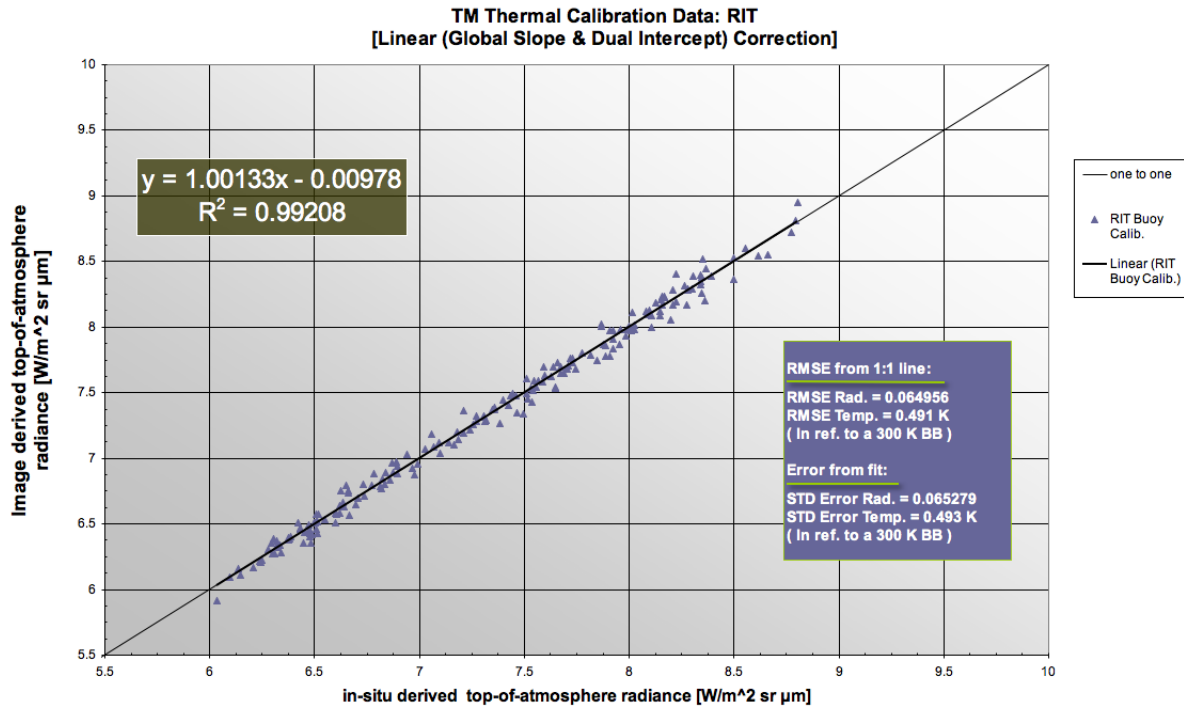


Figure 5.19: Predicted at-sensor radiance vs. image derived radiance: linear (global slope & dual intercept) correction.

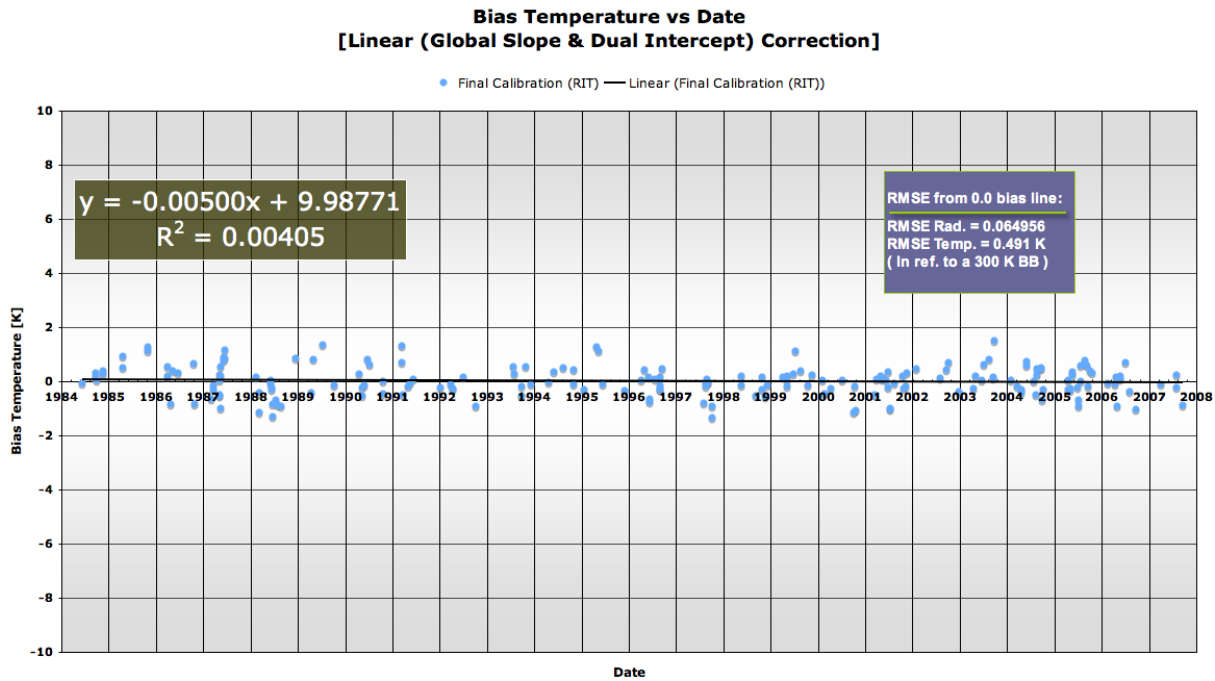


Figure 5.20: Applied linear (global slope & dual intercept) correction plotted as a function of time.

Summary:

- Linear (global slope & dual intercept) correction: RMSE of 0.491 K.
- Reduction in RMSE compared to the filtered & uncorrected data: 0.576 K.
- The correction successfully removed the gain issue and bias over time.

5.2.4 Global Bias Correction

For the moment any gain related artifacts will be ignored and focus will be brought solely on a global bias correction. Recall from Figure 5.9 that an apparent temperature bias exists over time in the instrument. Where from 1984 through roughly 1990 the data are for the most part positively biased around 0.5 K, conversely from roughly 1990 to 2007 the data appears to be increasingly dominated by a cold bias which approaches -2 K.

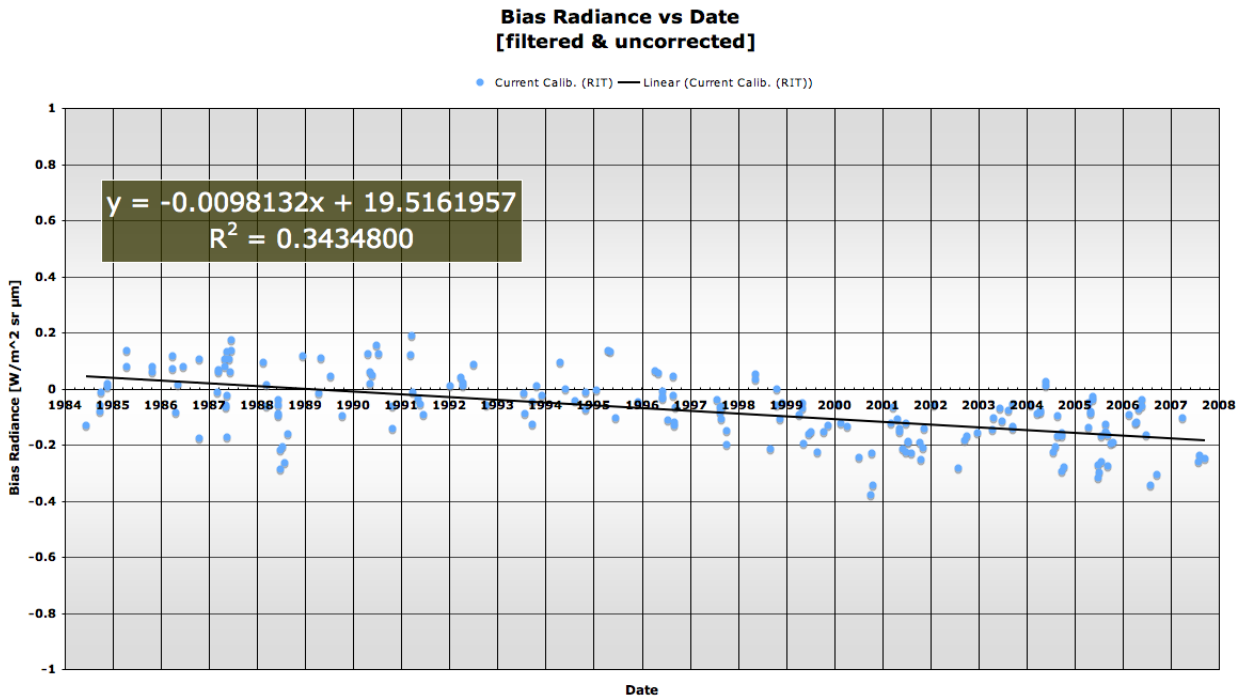


Figure 5.21: Bias radiance vs time: bias radiance (filtered and uncorrected data).

To apply the global bias correction, the equation of the best fit line over time [Figure 5.21] was used to find the difference from the 1:1 line so that a correction could be obtained to remove the sensor bias from the data set (i.e. the differences from the predicted line to the 0.0 bias line were applied to the image derived radiances). Applying the bias correction over time, the data demonstrates a RMSE of 0.736 K, in reference to a 300 K blackbody, contributing to a 0.328 K reduction in RMSE, compared to that of the uncorrected data. Figure 5.22 depicts the global

bias corrected data as a function of time, where as Figure 5.23 displays the global bias corrected results in the radiance domain.

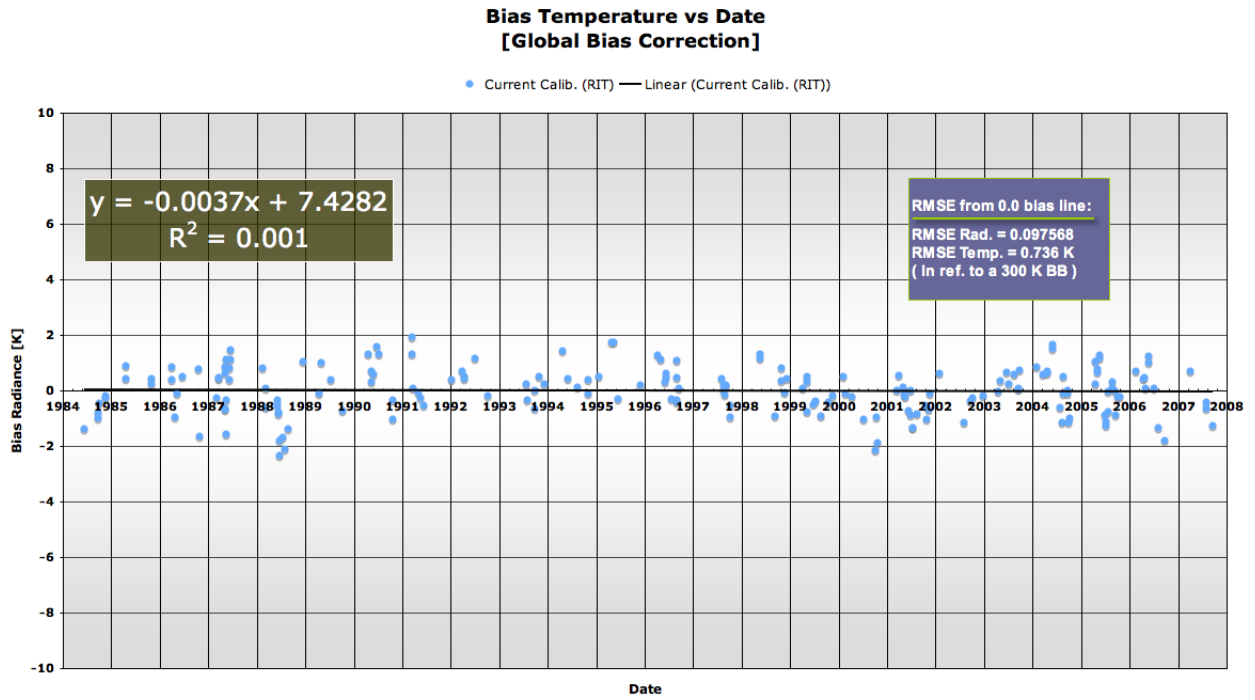


Figure 5.22: Temperature bias vs time: global bias correction.

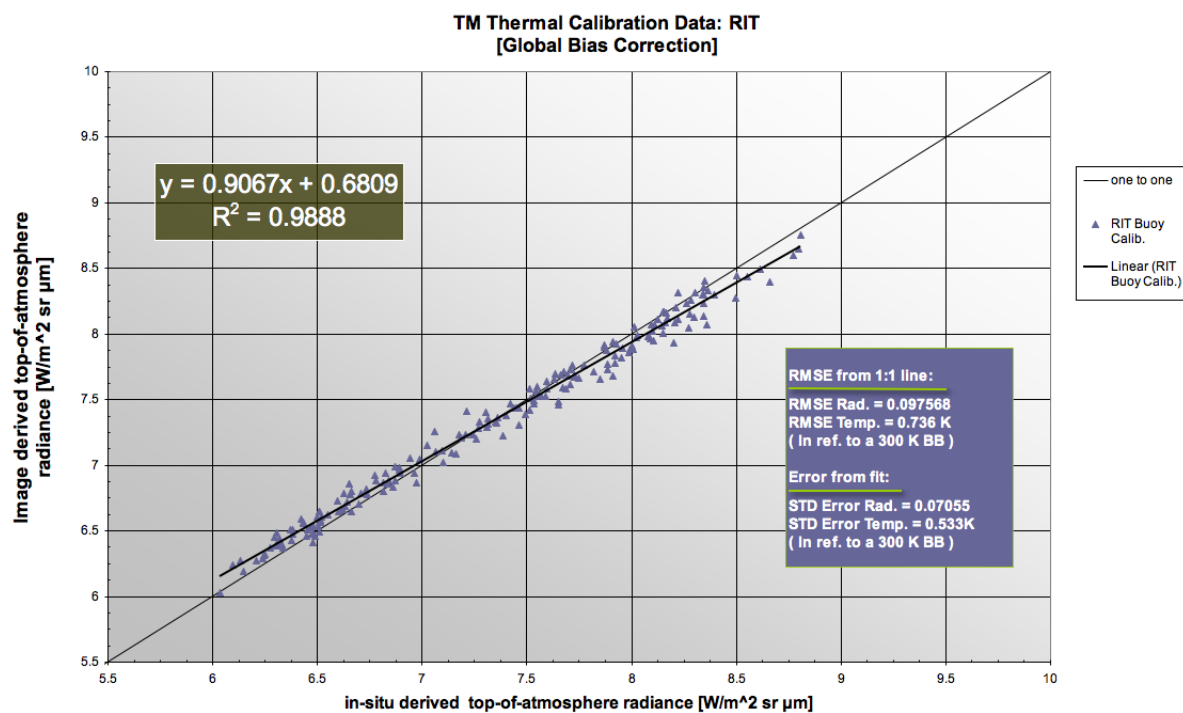


Figure 5.23: Predicted at-sensor radiance vs. image derived radiance: global bias correction.

From Figure 5.22 the global bias correction is shown to have performed well (bias radiance was found to be not statistically different from 0 [$W/m^2sr\mu m$] at the 99% C.I.), however, analysis of Figure 5.23 illustrates that with the biased removed, the sensor still exhibits difficulty in the gain.

Summary:

- Global bias correction: RMSE of 0.736 K.
- Reduction in RMSE compared to the filtered & uncorrected data: 0.328 K.
- The Global bias correction successfully removed the bias over time, however, unveiled that with the biased removed, the sensor still exhibits difficulty in the gain [Figure 5.23].

5.2.5 Time Dependent Bias Correction

A time dependent bias correction will now be applied to the data set. Again all data prior to 1999 will be treated as one class, while all data post 1999 will be treated as a second class; the regression equations used for this correction are shown in Figure 5.24. Equivalent to previous corrections, the distance from the best fit line to the zero bias line was found and then subtracted from the image derived radiance from the filtered and uncorrected data set [Figure 5.8]. The time dependent bias correction resulted in a RMSE of 0.711 K, which provided a 0.353 K reduction in RMSE compared to the filtered and uncorrected data set. Through visual inspection of Figure 5.25 the time dependent bias correction is shown to be successful in removing the overall slope of the data. However, again realize that by applying only the bias correction, the data clearly illustrates the need for an additional gain correction [Figure 5.26]. One notable finding from this correction was that the standard error (STD), between the correction applied (time dependent bias correction) image derived radiance and the scene derived radiance (truth), [Figure 5.26] was 0.493 K meaning the regression line had a relatively good fit.

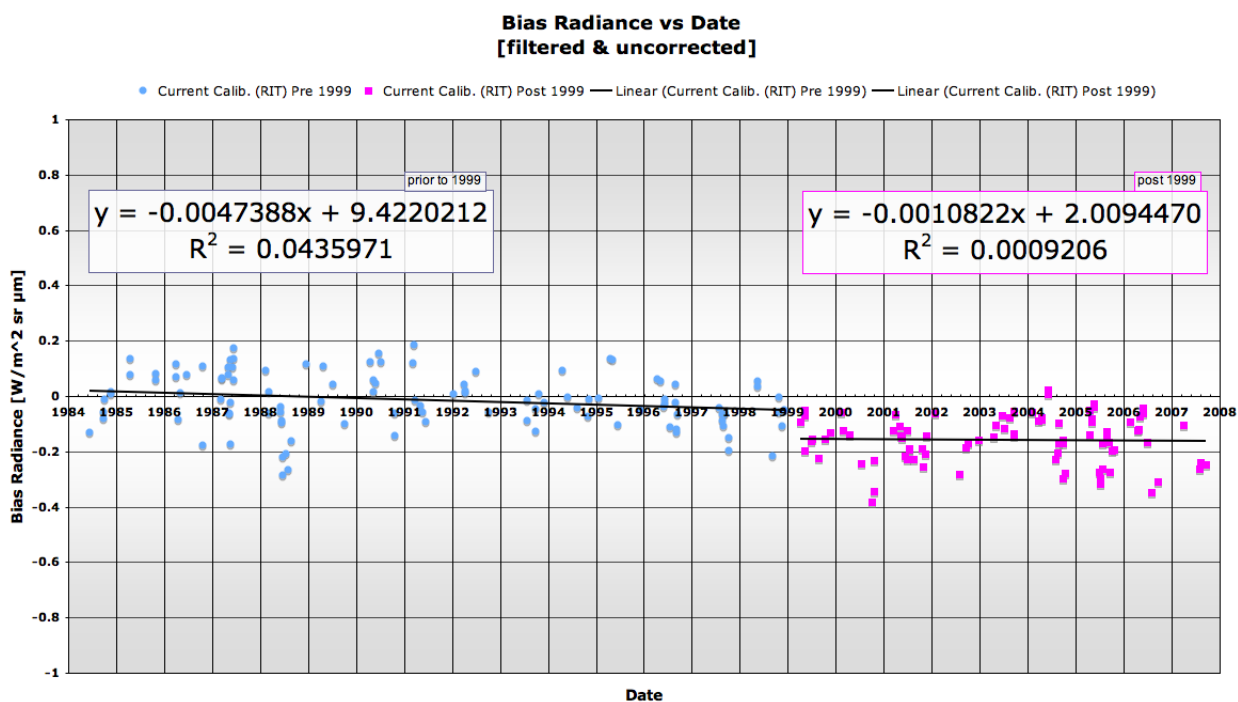


Figure 5.24: Bias radiance vs. time: filtered and uncorrected data; shown are trendlines for data pre and post 1999.

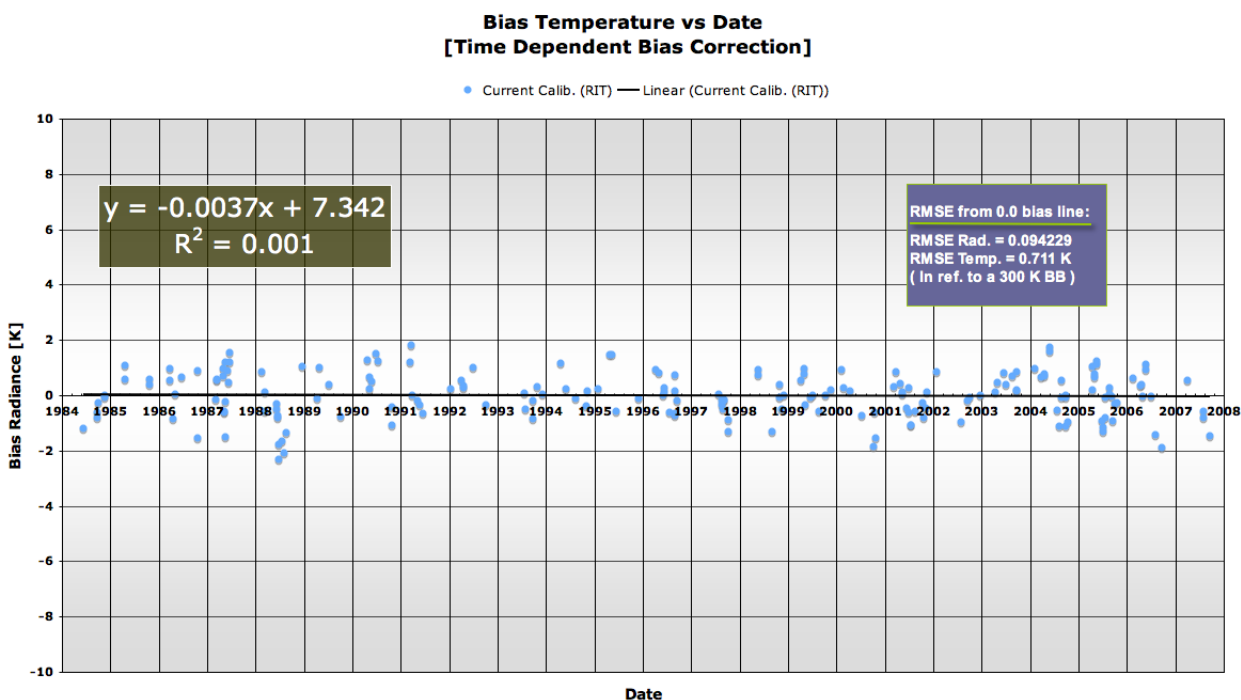


Figure 5.25: Temperature bias vs time: time dependent bias corrected values.

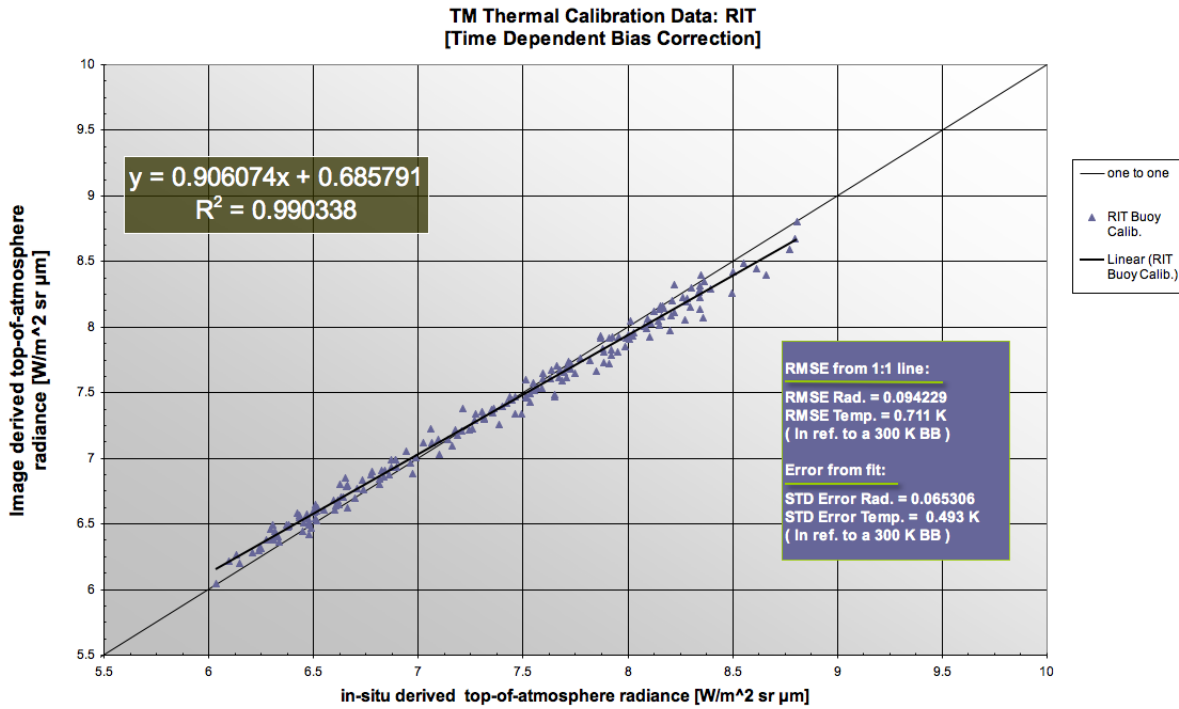


Figure 5.26: Predicted at-sensor radiance vs. image derived radiance: time dependent bias correction.

Summary:

- Time dependent bias correction: RMSE of 0.711 K.
- Reduction in RMSE compared to the filtered & uncorrected data: 0.353 K.
- Time dependent bias correction had a small standard error 0.493 K.
- The time dependent bias correction successfully removed the bias over time, however, the sensor still exhibits difficulty in the gain [Figure 5.23].

5.2.6 Dual: Linear (Global: Slope & Intercept) & Global Bias Correction

Proposed is a dual correction that first applies the linear (global: slope & intercept) correction [Figure 5.27 (linear (global: slope & intercept) corrected data plotted as a function of time)] and then corrects for the sensor bias over time. The dual correction is motivated by the fact that after correcting for the fluctuation in gain, a noticeable temperature bias is shown to exist over time in the instrument. The period from 1984 through roughly 1998 are for the most part positively biased around 1 K, in contrast, from the period of roughly 1999 to 2007 the data appear to be dominated by a cold bias within or around -1 K [Figure 5.27].

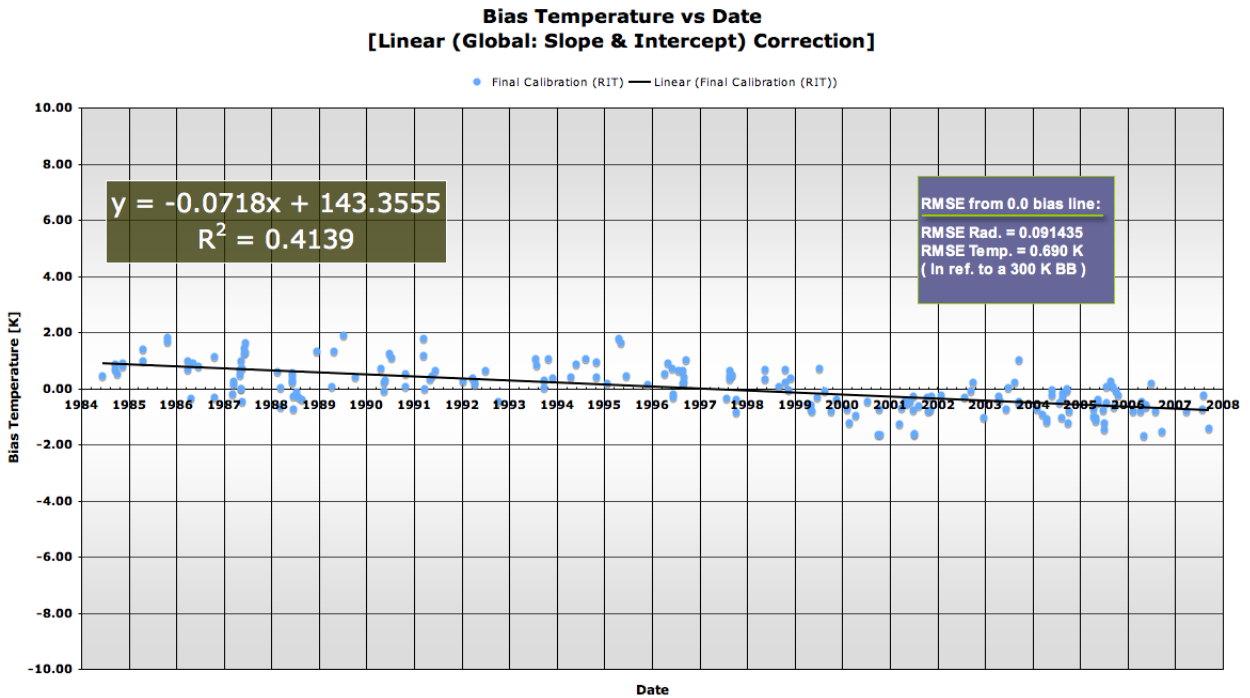


Figure 5.27: Temperature bias vs time: linear (global: slope & intercept) corrected values.

To address the bias over time, a methodology similar to the above mentioned process was used. Using the equation of the best fit line [Figure 5.28 (bias radiance data)] a predicted line was differenced with the zero bias line to yield a correction value that is applied to the image derived radiance. Applying the global bias cor-

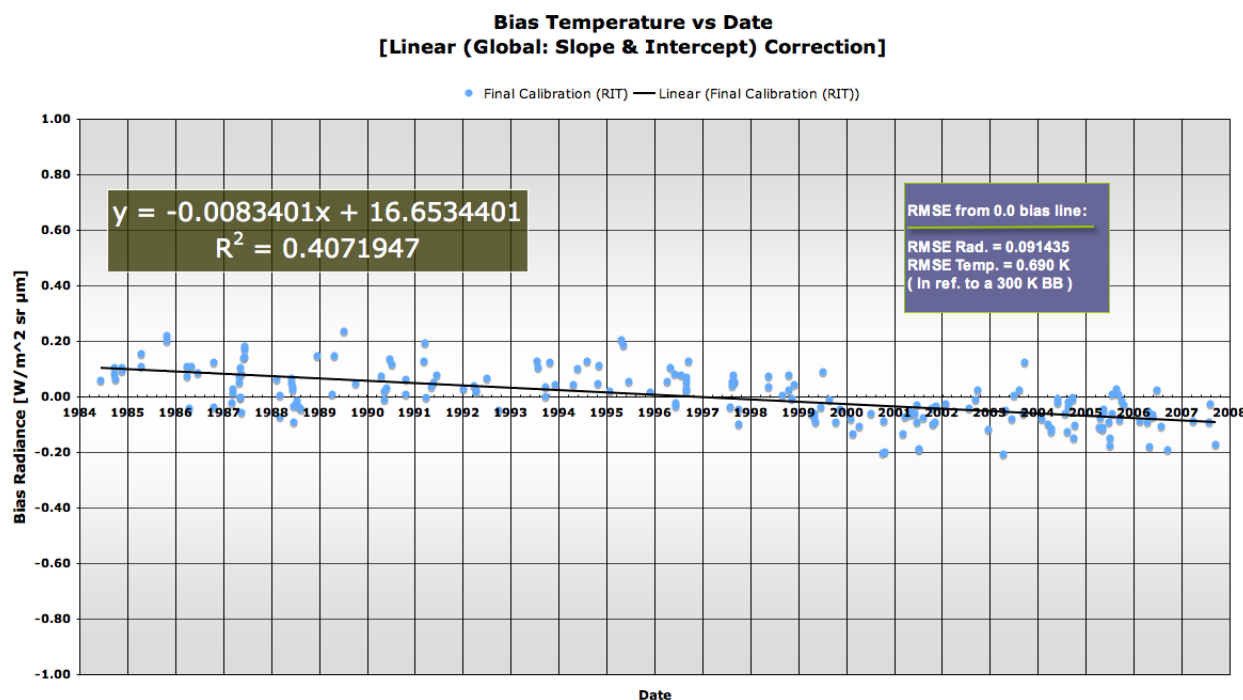


Figure 5.28: Radiance bias vs time: linear (global: slope & intercept) corrected values.

rection to the globally gain corrected data demonstrated a RMSE of 0.532 K, in reference to a 300 K blackbody, contributing to an additional 0.158 K reduction in RMSE, compared to that of the global gain corrected data [Figure 5.12]. Figure 5.29 displays the gain and bias corrected results in the radiance domain, where as Figure 5.30 depicts the gain and bias corrected data as a function of time.

Notice from Figure 5.29 that the resulting regression equation has a slope that is slightly greater than 1 and an intercept different from 0. Also notice from the data plotted as a function of time [Figure 5.30] the slope of the regression line is approximately 0, illustrating that the bias correction was successful. It is clear, that although the applied bias correction [Figure 5.30] has eliminated the overall slope of the data set, the linear model is not sufficient in removing residual fluctuations about the best fit line in the calibration curve.

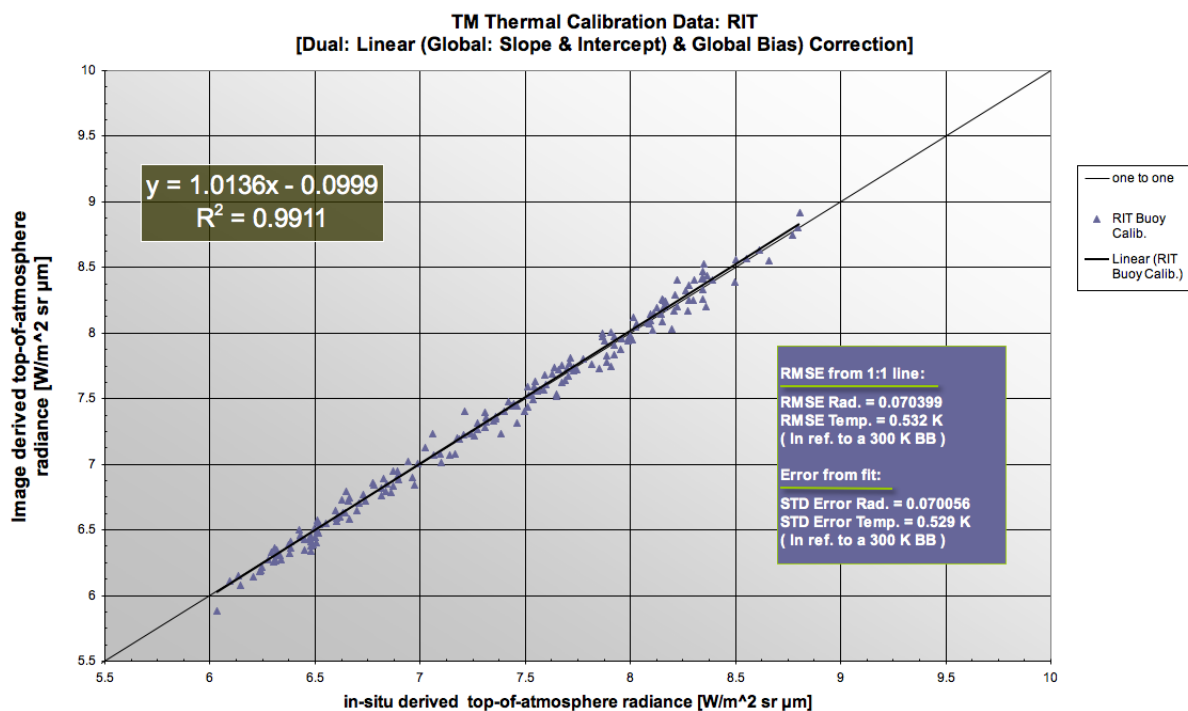


Figure 5.29: Predicted at-sensor radiance vs. image derived radiance: linear (global: slope & intercept) & global bias correction.

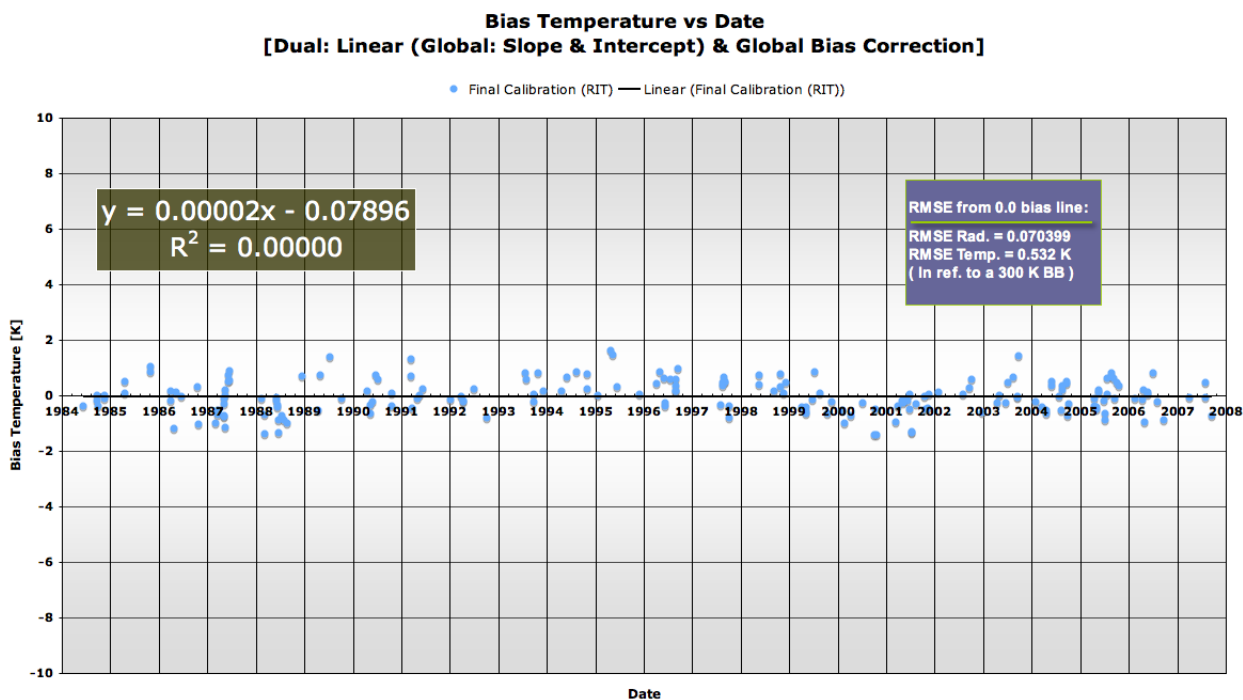


Figure 5.30: Temperature bias vs time: linear (global: slope & intercept) & global bias corrected values.

Summary:

- Dual: linear (global: slope & intercept) & global bias correction: RMSE of 0.532 K.
- Reduction in RMSE compared to the filtered & uncorrected data: 0.532 K.
- Dual correction successfully addressed the gain and bias over time, however, was out performed by the linear (Dual: slope & intercept) correction and the linear (global slope & dual intercept) correction.

5.2.7 Dual: Time Dependent Bias & Linear (Global: Slope & Intercept) Correction

This is another dual correction which first applies the time dependent bias correction [Figure 5.25] and then applies a linear (global: slope & intercept) correction using the regression equation shown in Figure 5.26. The dual correction is motivated by the small STD error reported after the time dependent bias correction was applied (STD error = 0.493 K), as well as observing that a linear (global: slope & intercept) correction was needed through investigation of Figure 5.26. The correction was applied to the time dependent bias data, found by differencing the best fit line [Figure 5.26] with the 1:1 line. The dual correction provided a RMSE of 0.493 K, with a STD error of 0.493 K. Figure 5.31 illustrates the results in the radiance domain, where Figure 5.32 portrays the bias temperature over time. Note after the correction was applied the data resulted in a slight bias overtime [Figure 5.32].

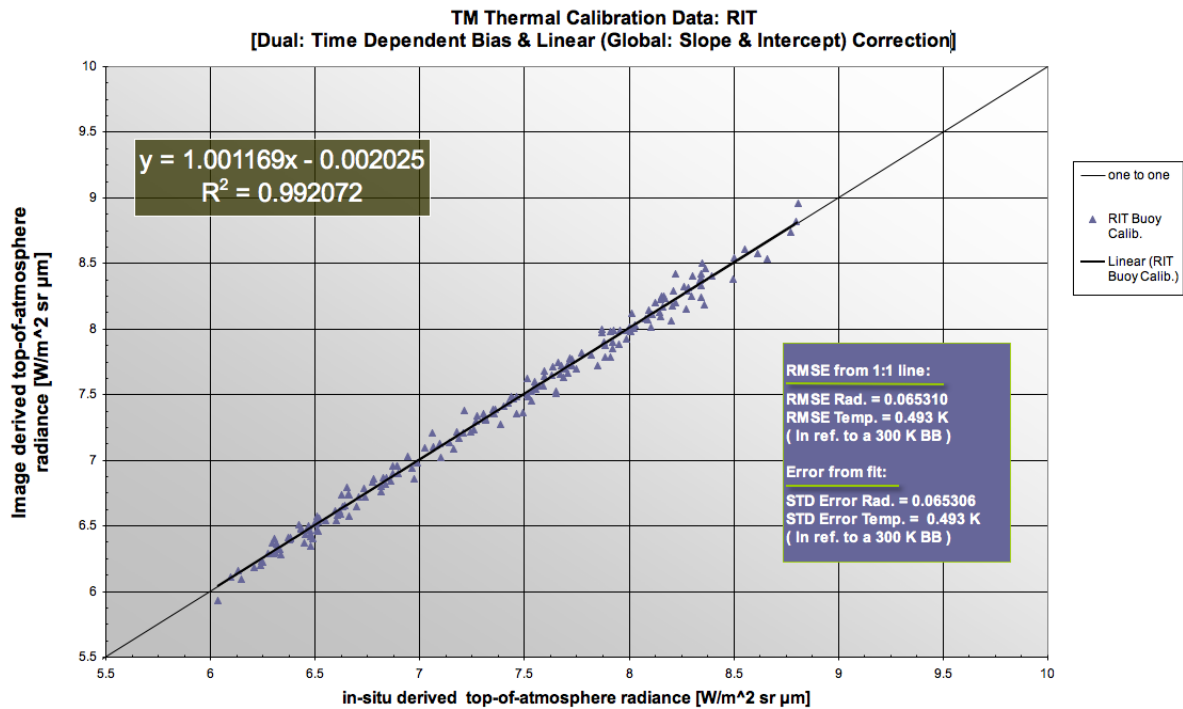


Figure 5.31: Predicted at-sensor radiance vs. image derived radiance: time dependent bias and linear (global: slope & intercept) corrected.

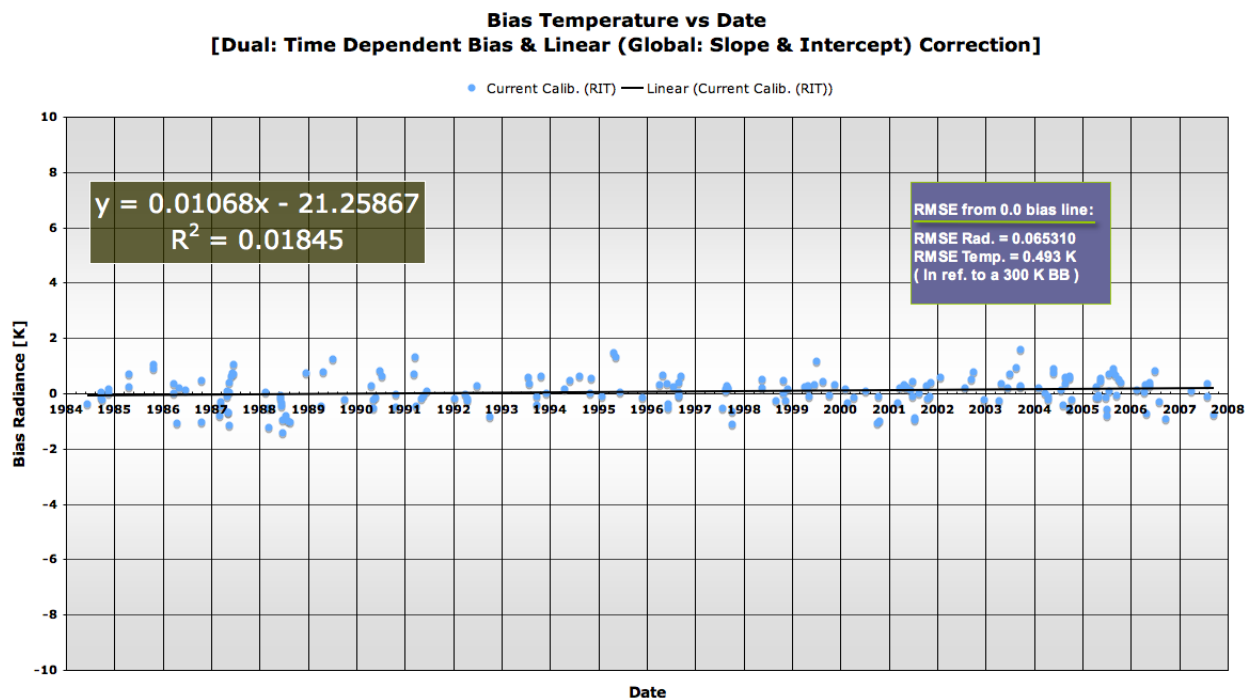


Figure 5.32: Temperature bias vs time: time dependent bias and linear (global: slope & intercept) correction corrected values.

Summary:

- Dual: (time dependent bias & linear (global: slope & intercept) correction: RMSE of 0.493 K.
- Reduction in RMSE compared to the filtered & uncorrected data: 0.571 K.
- Dual: (time dependent bias & linear (global: slope & intercept) correction addressed the sensor gain and bias issues, however, needed an ongoing time dependent correction to do so. Note after correction, the data resulted in a slight bias overtime.

5.2.8 Conclusions: Summary of the Proposed Corrections

First and foremost it is imperative to stress the point that with no corrections applied to the instrument, a RMSE of 1.064 K was found. Meaning that the Landsat 5 TM thermal band (Band 6), originally planned for a 3 year mission, has fluctuated only slightly (~ 1 K) over the 24+ years in orbit. With that said, realize that the needed calibration corrections are small in nature, however, significant. A summary of all of the proposed corrections is shown in Table 5.2. Note the RMSE in temperature for each correction is reported, recall RMSE was derived from the differences between the image derived radiance (satellite observed) and the scene derived radiance (truth). The standard error is also reported to illustrate how well the data fit to the resulting regression line after the correction was applied. Lastly, reported is each of the corrections final RMSE in temperature compared to the RMSE in temperature of the filtered and uncorrected data (i.e. how much did the given correction contribute towards the reduction of error.) All reported temperatures are in reference to a blackbody at 300 K.

Table 5.2: Summary of the proposed calibration corrections.

Proposed Correction	RMSE [K]	Standard Error [K]	Difference Compared to No Correction [K]
No Correction	1.064	0.694	x
NASA 1999+ Correction (only)	0.813	0.514	0.251
Linear (Global: Slope & Intercept) Correction	0.690	0.694	0.374
Linear (Dual: Slope & Intercept) Correction	0.488	0.488	0.576
Linear (Global Slope & Dual Intercept) Correction	0.491	0.493	0.573
Global Bias Correction	0.736	0.533	0.328
Time Dependent Bias Correction	0.711	0.493	0.353
Dual: Linear (Global: Slope & Intercept) & Global Bias Correction	0.532	0.529	0.532
Dual: Time Dependent Bias & Linear (Global: Slope & Intercept) Correction	0.493	0.493	0.571

Table 5.2 illustrates that the linear (dual: slope & intercept) correction, applied to the two time periods, trumps all alternative corrections resulting in a RMSE

and STD error equal to 0.488 K. Although also notice, the linear (global slope & dual intercept) correction and the dual: time dependent bias & linear (global: slope & intercept) correction also performed well. The linear (dual: slope & intercept) correction is believed to be the most appropriate and physically justified correction proposed. As discussed in Section 5.1, there was ample proof that a gain issue was present in the data set due to the identified seasonal oscillation in the bias temperature data over time [Figure 5.11]. Where on average lower temperature targets (first 6 months of the year) were positively biased, and on average higher temperature targets (last 6 months of the year) were negatively biased. This result was further verified through analysis of Figure 5.8 (image derived radiance against the in-situ derived radiance: filtered and uncorrected data) illustrating that low radiance targets portray a slight warm bias and higher radiance targets demonstrate a cold bias. This conclusion reiterates that sufficient evidence supporting the claim that a seasonal oscillation is present in the data set due to a gain issue in the instrument.

Discussion will now focus on the verification of why the linear (dual: slope & intercept) correction was superior. Recall, the data set which included the 1999+ NASA correction [Figure 5.7] suggested that there is a slight warm bias at low radiances and a slight cold bias at high radiances. However, it was discovered that after the 1999+ correction was removed [Figure 5.8], all data post 1999 illustrated a dominant cold bias, which was also apparent in Figure 5.9. It is suspected that an event occurring to the sensor (or spacecraft) either before or during the year 1999 caused a significant change in the sensor's performance. To validate this claim, a two sampled t-test was performed testing if the biased data prior to 1999 was statistically different from the biased data post 1999. Results found that the bias temperatures prior to 1999 were statistically different from the data post 1999 at the 99% C.I.. This result is further verified through visual inspection of Figure 5.11. In conclusion, given these results it makes physical sense that the linear (dual: slope & intercept) correction out performed the global corrections.

It must be stated, that with the linear (dual: slope & intercept) correction applied

there still remains an approximate 0.1 K bias in the calibration curve over the span of 24 years. An additional global bias correction was applied to the linear (dual: slope & intercept) corrected values resulting in a 0.001 K reduction in RMSE. Therefore, at this time it is not recommended that the linear (dual: slope & intercept) corrected values warrant any further corrections, as the amount of residual bias is within sensor noise. With that said, the bias of the instrument may need to be continually monitored in the future. To validate that the correction performed well and that the resulting error is random in nature Figure 5.33 is offered to show that the data looks approximately normally distributed.

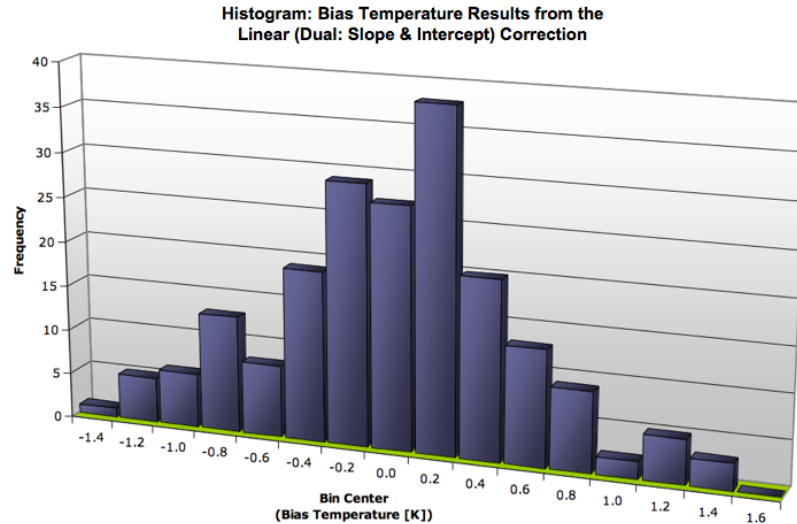


Figure 5.33: Histogram of the bias temperature from the linear (dual: slope & intercept) correction.

Additionally note that the alternative corrections shown in Table 5.2 were proposed to further justify that the sensor was truly influenced by a gain related issue and not a bias or more complicated cross between the two. Although the time dependent bias correction independently provided a RMSE of 0.711 K, it demonstrated a STD error of 0.493 K. Thus, after the Linear (Global: Slope & Intercept) correction was applied an RMSE of 0.493 K resulted [Table 5.2] . Clearly, the linear (dual: slope & intercept) correction is a more convenient and justified conclusion opposed to the alternative dual correction. Note the comparison of the linear (dual: slope & intercept) correction and linear (global slope & dual intercept) correction is not as straightforward, as both are easily justified corrections. The recommendation

of the linear (dual: slope & intercept) correction was made because it provides the lowest RMSE of 0.488 K and best fit to the model equations standard error of 0.488 K. However, note this correction is very similar to the linear (global slope & dual intercept) correction providing comparable results (RMSE = 0.491 K & STD error = 0.493 K).

5.2.9 Recommendation

Although numerous corrections were presented in Table 5.2 only the linear (dual: slope & intercept) correction and the linear (global slope & dual intercept) correction are to be considered as viable final corrections. Understand that this work was intended to develop and justify possible calibration corrections to be presented to NASA, from which a final decision regarding the most appropriate correction given all data (including the previous efforts of RIT & JPL) will be made. Again, this vicarious calibration campaign recommends the linear (dual: slope & intercept) correction be applied to all Landsat 5 TM data [Table 5.3]. Note, however, the linear (global slope & dual intercept) correction is also a justified approach, thus is presented as a potential option [Table 5.3].

From Section 4.12.3, recall that the proposed methodology was found to have an expected error of ± 0.454 K. This conclusion was verified through inspection of the final calibration results, which had a RMSE = 0.488 K and demonstrates that both the final calibration results and the expected error of the proposed methodology are consistent. This makes physical sense because the proposed correction has removed all but random errors, thus the residual error in the final calibration data is on the order of the uncertainty in the process.

Important:

- The expected error for the entire process was found to be ± 0.454 K, which is consistent with the derived RMSE of the final calibration results of 0.488 K. This finding further validates the results presented in this vicarious calibration campaign.

Table 5.3: Proposed calibration equations. Note observed radiance is in units $[W/m^2 sr \mu m]$.

Linear (Dual: Slope & Intercept) Correction	
Data prior to 1999:	
Corrected Value =	$\frac{Observed\ Radiance - Intercept}{Slope} = \frac{Observed\ Radiance - 0.7607601}{0.8928897}$
Data post 1999:	
Corrected Value =	$\frac{Observed\ Radiance - Intercept}{Slope} = \frac{Observed\ Radiance - 0.4892183}{0.9120797}$
Linear (Global Slope & Dual Intercept) Correction	
Data prior to 1999:	
Corrected Value =	$\frac{Observed\ Radiance - Intercept}{Slope} = \frac{Observed\ Radiance - 0.901418589}{0.698989001}$
Data post 1999:	
Corrected Value =	$\frac{Observed\ Radiance - Intercept}{Slope} = \frac{Observed\ Radiance - 0.901418589}{0.568537821}$

5.2.10 Reverse Engineering Case

This section is offered to investigate the error in temperature retrieval (i.e. the reverse engineering case) provided the final calibration results of this campaign. This methodology entails using the imagery from the now calibrated sensor to deduce the surface leaving radiance by backing out (i.e. compensating) for the atmospheric effects to the sensor reaching radiance. The governing equation for the reverse engineering case is found by solving Eq. 3.14, re-illustrated in Eq. 5.1 (note: expressed are the band effective terms) for the surface leaving radiance L_{BB} expressed in Eq. 5.2.

$$L_{eff} = (\epsilon L_{BB} + (1 - \epsilon)L_d)\tau + L_u \quad (5.1)$$

$$L_{BB} = \frac{L_{eff} - L_u}{\epsilon\tau} - \frac{(1 - \epsilon)L_d}{\epsilon} \quad (5.2)$$

Applying the general form of Eq. 2.17 on the governing equation [Eq. 5.2] an

error propagation [Section 2.7] is performed, the general equation is expressed as:

$$S_{L_{BB}} = \left[\left(\frac{\partial L_{BB}}{\partial L_{eff}} S_{L_{eff}} \right)^2 + \left(\frac{\partial L_{BB}}{\partial \epsilon} S_{\epsilon} \right)^2 + \left(\frac{\partial L_{BB}}{\partial \tau} S_{\tau} \right)^2 + \left(\frac{\partial L_{BB}}{\partial L_d} S_{L_d} \right)^2 + \left(\frac{\partial L_{BB}}{\partial L_u} S_{L_u} \right)^2 + 2\rho_{\tau, L_u} \frac{\partial L_{BB}}{\partial \tau} \frac{\partial L_{BB}}{\partial L_u} S_{\tau} S_{L_u} + 2\rho_{\tau, L_d} \frac{\partial L_{BB}}{\partial \tau} \frac{\partial L_{BB}}{\partial L_d} S_{\tau} S_{L_d} + 2\rho_{L_u, L_d} \frac{\partial L_{BB}}{\partial L_u} \frac{\partial L_{BB}}{\partial L_d} S_{L_u} S_{L_d} \right]^{\frac{1}{2}} \quad (5.3)$$

where:

$$\begin{aligned} \frac{\partial L_{BB}}{\partial L_{eff}} &= \frac{1}{\epsilon \tau} \\ \frac{\partial L_{BB}}{\partial \epsilon} &= \frac{L_u - L_{eff}}{\epsilon^2 \tau} + \frac{L_d}{\epsilon^2} \\ \frac{\partial L_{BB}}{\partial \tau} &= \frac{L_u - L_{eff}}{\epsilon \tau^2} \\ \frac{\partial L_{BB}}{\partial L_d} &= \frac{-1}{\epsilon} + 1 \\ \frac{\partial L_{BB}}{\partial L_u} &= \frac{-1}{\epsilon \tau} \end{aligned}$$

Table 5.4: Listing and declaration of error terms in Eq. 5.3.

Error Term	Value	Source (our use only)
$S_{L_{eff}}$ - image derived radiance	0.488 K or 0.064581 $[W/m^2 sr \mu m]$	final calibration results
S_{ϵ} - emissivity	0.006	Barsi (2000)
S_{τ} - transmission		case dependent
S_{L_d} - downwelled rad.	$[W/m^2 sr \mu m]$	case dependent
S_{L_u} - upwelled rad.	$[W/m^2 sr \mu m]$	case dependent

Realize the error estimates shown in Table 5.4 are the exact same values used in the forward engineering case, with the exception of the term L_{eff} which was assigned the final calibration results found in this study. Results are shown in Figure 5.34.

Results show the reverse engineering case (i.e. traditional remote single band temperature retrieval process) demonstrates an average of ~ 0.6 K (0.638 K) resulting from the selected profiles, excluding the most extreme case 06 July 1999. Results found that for the extreme case (06 July 1999) an error of 1.136 K can be expected. It should be stated that the most dominant and sensitive term was the term L_{eff} , followed by transmission and upwelled radiance. Again the final correction resulted

Temperature Retrival	Radiance	Temperature
Date: 26Jan02	[W/m ² sr μ m]	[K]
275	0.077581764	0.586
285	0.081421524	0.615
300		
Date: 28Apr03		
275	0.07715332	0.583
285	0.08091535	0.611
300		
Date: 27May90		
275		
285	0.08413171	0.635
300	0.090689293	0.685
Date: 24Jun90		
275		
285	0.08207306	0.620
300	0.08880058	0.670
Date: 24Oct98		
275		
285	0.082073179	0.620
300	0.088994664	0.672
Date: 16Aug85		
275		
285	0.087329914	0.659
300	0.092862818	0.701
Date: 06Jul99		
275		
285	0.172710518	1.301
300	0.171654212	1.293

Figure 5.34: Data from the reverse engineering error propagation study.

in a of RMSE = 0.488 K or 0.0646 $[W/m^2 sr \mu m]$ and was used in this study.

5.2.11 Summary

In this section it was established that the final calibration correction (Linear (Dual: Slope & Intercept) Correction) resulted in a RMSE of 0.488 K, is consistent with the derived process error of 0.454 K or 0.060 $[W/m^2 sr \mu m]$ in reference to a 300 K black-body. Thus with confidence it is concluded that the proposed methodology results in an average process error of ~ 0.454 K. Lastly the reverse engineering case was investigated and found to provide surface temperatures, using the proposed atmospheric assimilation scheme and calibration results of roughly 0.6 K for typical atmospheric cases and up to approximately 1 K in extreme (moisture rich) atmospheric cases.

5.3 Summary Statistics

The historical calibration of Landsat 5 TM Band 6 was performed over a temperature range of 273.16 - 298.49 K (0.014 - 25.34°C). Figure 5.35 illustrates a histogram of the ground truth temperatures used to build the final calibration curve. This

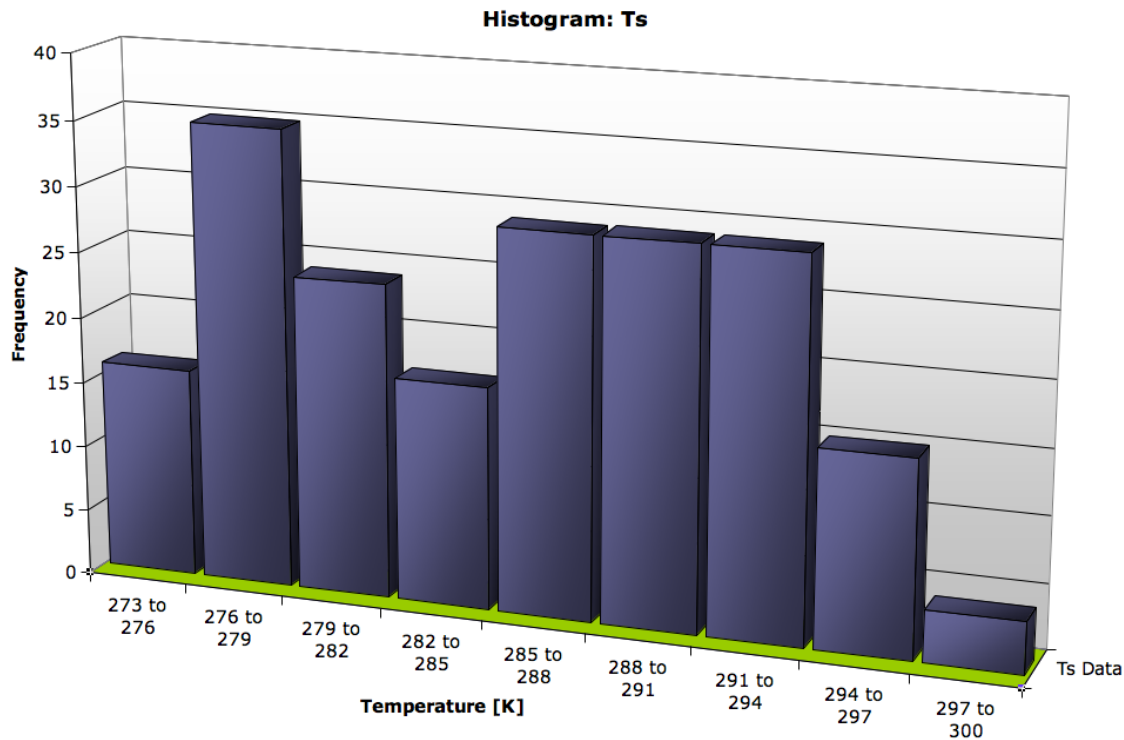


Figure 5.35: Illustrates a histogram of the ground truth T_s used in the final calibration results.

data depicts that the study has characterized temperatures at and below roughly 296 K well, however, is somewhat limited at higher temperatures. Due to the spatial limitations of this study (i.e. availability of historic quality controlled buoy observations coinciding synonymously with accessible atmospheric data) high temperature targets are difficult to acquire. For example, Schott (1979) illustrated that cooling water discharges from power plants can provide high water target temperatures, although it is clear that this source of data is impractical for this methodology due to the limitations of the environmental data sources used. Note from our discussion in Section 2.2, water targets are typically used to validate temperatures from roughly

0 °C to 30 °C. With that said, the reported calibration results nearly span the expected range given the target used. A brief survey was again conducted investigating the potential of alternative site locations, for example in the Gulf of Mexico and the east coast of Florida (Cape Canaveral). The survey verified that temperatures in both regions peak at a temperature of roughly 30°C, thus the inclusion of such sites does not promise any large gains in terms of the final results. In addition, one has to consider that the alternative locations are within the tropics (i.e. water vapor rich), thus posing the potential for higher atmospheric correction errors.

Figure 5.36 depicts a histogram of the corrections applied to the T_b measurement's to acquire the desired ground truth T_s . The majority of the corrections were less than 0.2 K. Realize the bulk of the larger corrections are based on the observations from the 12m class buoy's (i.e. $z = 1.5\text{m}$). To ensure that artifacts have not been introduced into the calibration record due to large bulk-to-surface temperature corrections a filter of 0.5 K was applied to the absolute values of the temperature corrections. Meaning that no bulk-to-surface temperature correction was larger than $|0.5K|$. All days which failed to pass the filter (18 points in total, $\sim 9\%$ of the data set) were removed from the calibration curve. The study found that the difference in RMSE for the reduced T_s filtered data set and original data set was negligible (0.002 K), in addition the change in slope and intercept of the data plotted as image derived radiance against in-situ derived radiance was also found to be negligible as well ($\Delta\text{slope} = 0.0003$ and $\Delta\text{intercept} = 0.0015$). In conclusion these findings allow for increased or assured confidence that the magnitude of the previous bulk-to-surface temperature filter was appropriately chosen. Recall, the applied temperature filter rejected all corrections greater than 1 K for the 3 m buoy hull type and 2 K for all 12 m buoy hull types.

Table 5.5: Summary statistics of ground truth data from the final calibration results.

Average T_s Correction	0.095 K
Average Absolute T_s Correction	0.216 K

From Table 5.5 it is concluded that on average the applied correction is within

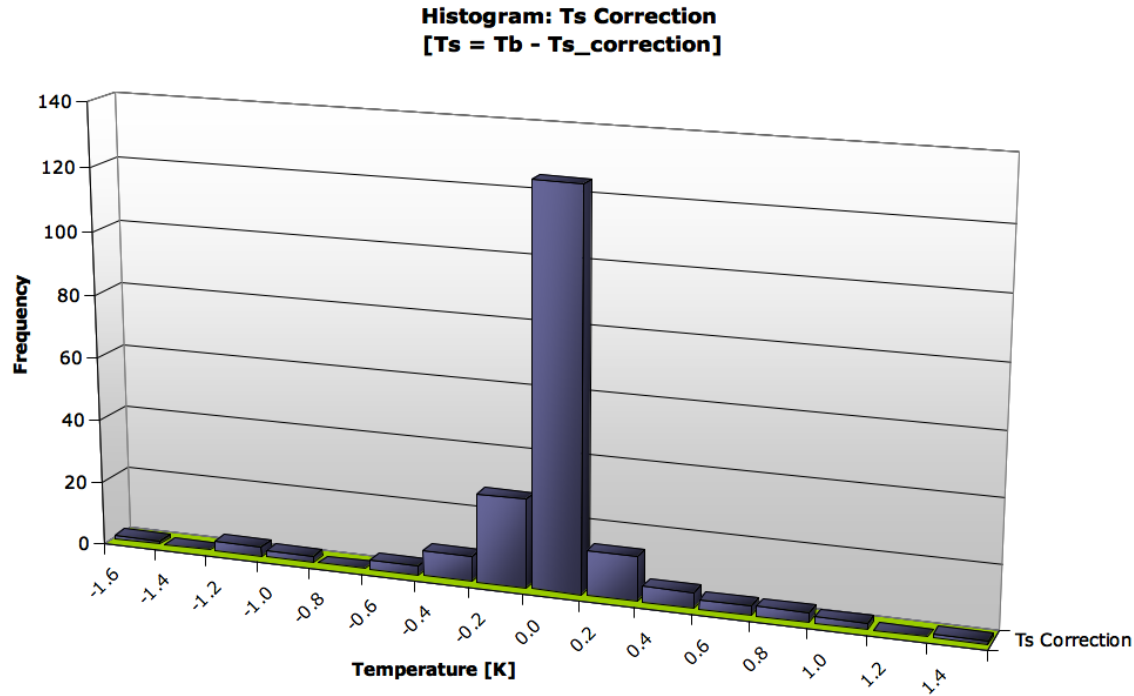


Figure 5.36: Illustrates the corrections applied to the T_b measurements to acquire the ground truth T_s . Note all data is based on the final calibration results.

0.1 K. It also should be stated the average wind speed was 5.86 m/s, as noted previously. Another notable statistic is that the Donlon et al. (2002) correction (0.17 K) for high average wind speeds (nominally greater than 10 m/s) was used for approximately 22% of the final calibration results. The reported wind speed statistics, provide strong evidence that the proposed Zeng et al. (1999) model can be adequately applied to any of the sites mentioned in this study, as the fetches are both large (i.e. ocean like) and sufficiently windy to validate the proposed model. Figure 5.37 illustrates each sites contribution to the final calibration results. It is clear that the Site 4 (Delmarva Peninsula) provided the bulk of the final calibration data. The reason being the ocean buoy platforms are deployed year round, as opposed to only during the warm season in the Great Lakes. Thus, we took advantage of the promise of higher potential scene availability from the ocean site. Notice also that Site 1 (Lake Huron) contributed heavily to the final calibration results.

Figures 5.38 and 5.39 are presented to demonstrate the temperatures provided

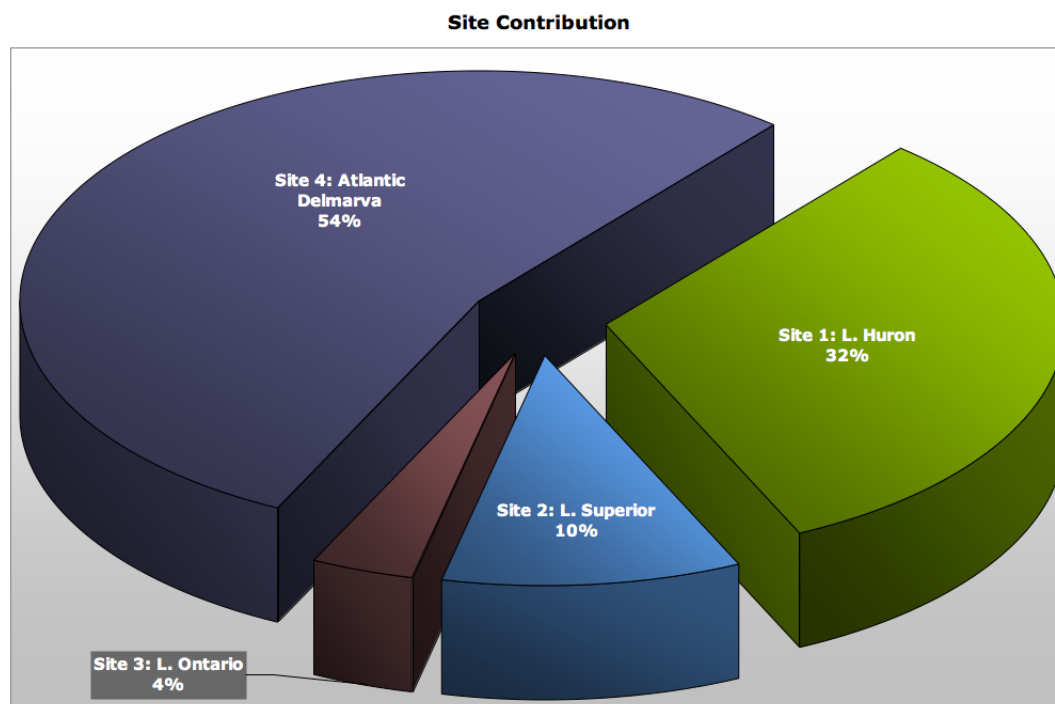
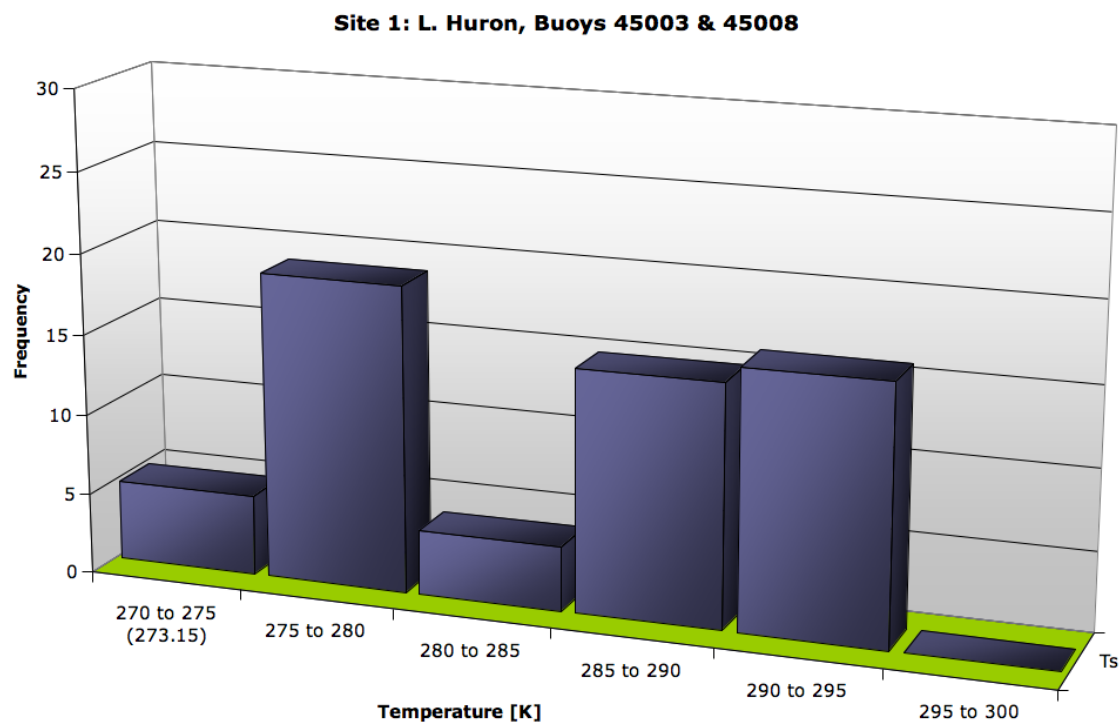
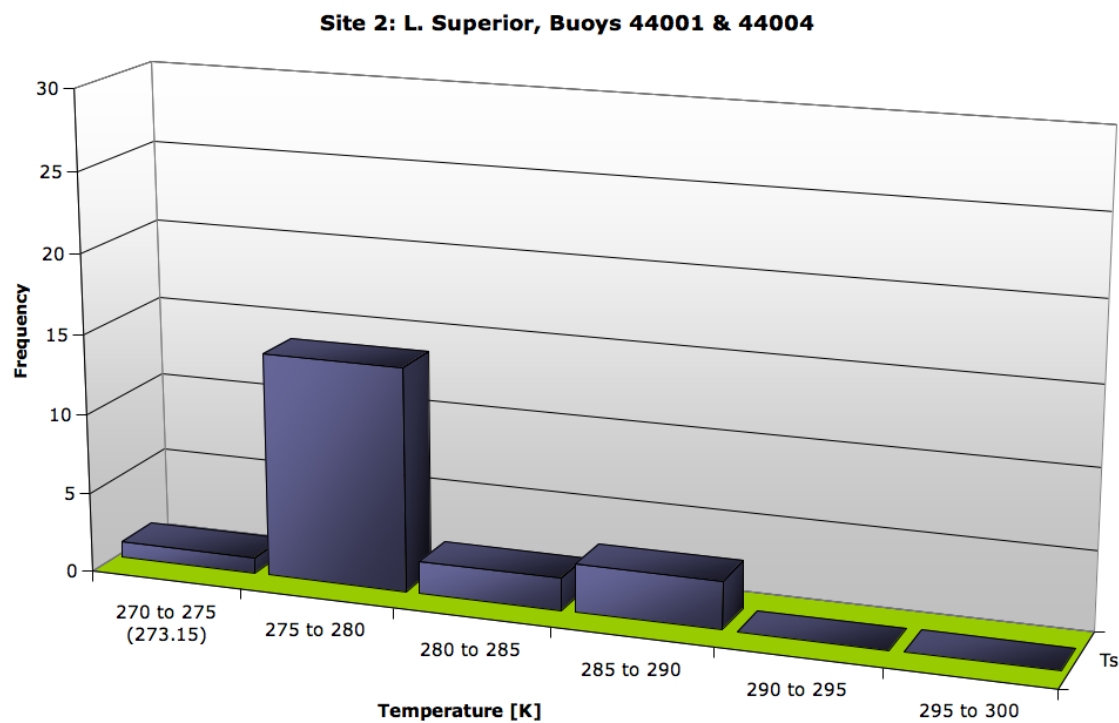


Figure 5.37: Illustrates the contribution of each site, in regards to the obtained ground truth T_s based on the final calibration results.

from each calibration site. As discussed Lake Huron provides a range of both low (273.15 - 280 K) and "high" (285 - 295 K) target temperatures [Figure 5.38 (a)], however, note that for all Great Lake sites no target temperatures were found above 295 K [Figure 5.38 and 5.39 (a)]. Site 2 (Lake Superior) as expected, due to the size of the lake, provided mainly low target temperatures. Figure 5.39 (a) illustrates the Lake Ontario (Site 3) data set, which is limited in numbers because the buoy archive began in 2002. Though limited, this data was important as it provided a direct comparison to results performed previously by RIT, discussed above. Lastly, Figure 5.39 (b) illustrates site 4 (Delmarva Peninsula) data. Notice that this location (Site 4) provided a wide range of target temperatures (275 K - 300 K), which consist of the majority of the high target temperature cases in this study. Also note, however, that this location did not offer any target temperatures below 275 K.

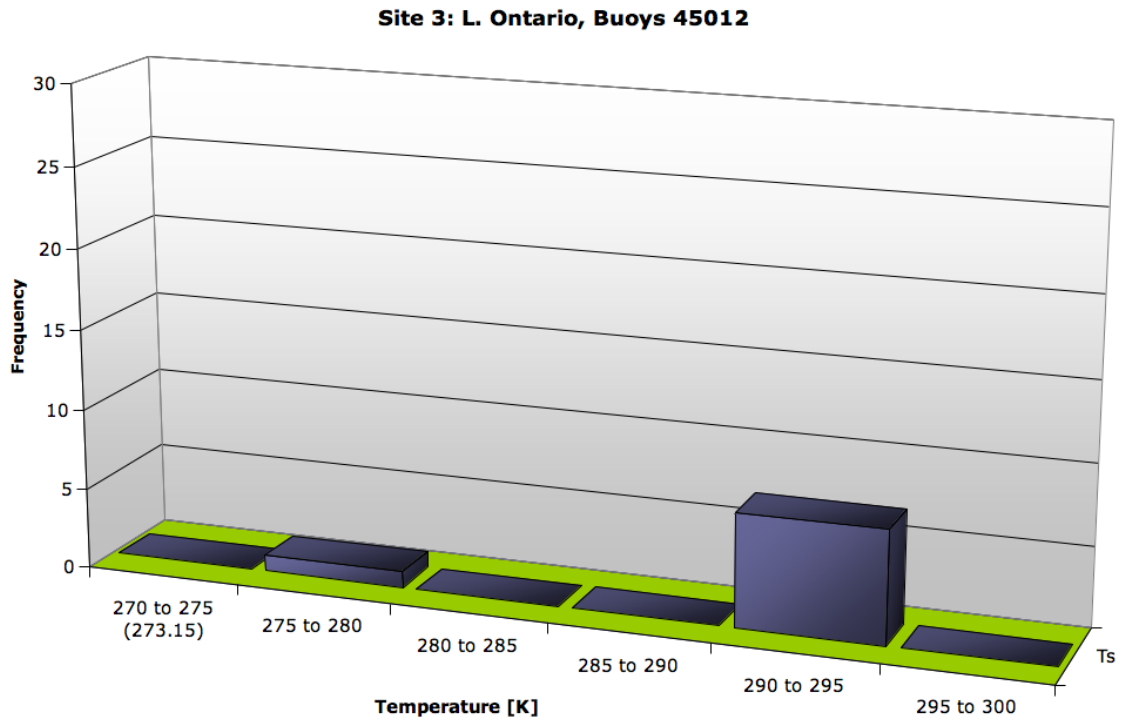


(a)

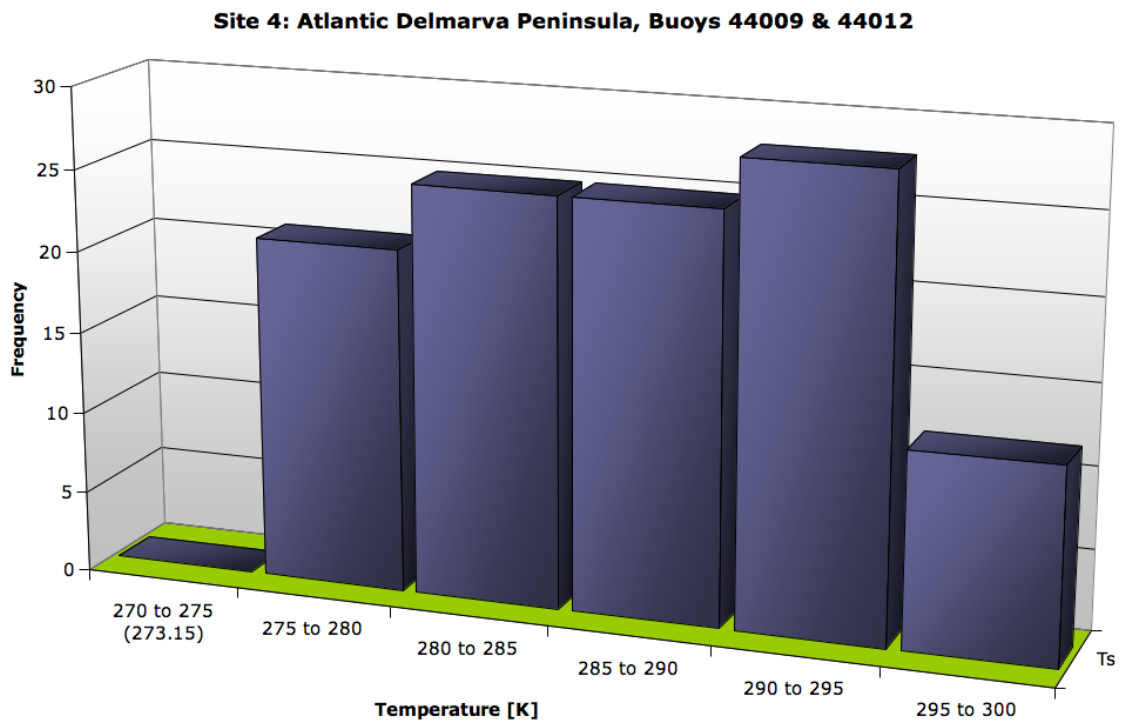


(b)

Figure 5.38: Site specific ground truth temperatures: (a) Site 1: Lake Huron. (b) Site 1: Lake Superior.



(a)



(b)

Figure 5.39: Site specific ground truth temperatures: (a) Site 3: Lake Ontario. (b) Site 4: Delmarva Peninsula.

5.4 Recommendations and Summary

This investigation has developed and characterized the historical calibration record of the Landsat 5 TM thermal band. The implemented vicarious calibration approach took advantage of the NDBC's long-standing moored buoy fleet to acquire the ground truth measurements needed throughout the lifetime of Landsat 5. Through fusion of environmental data sources (i.e. buoy, surface and radiosonde observations) the atmospheric column over each target (i.e. buoy location) was recreated and used as input into MODTRAN to yield a predicted at-sensor radiance. The predicted at-sensor radiance was defined as truth, so that a comparison could be made with the actual observed satellite radiance to investigate the state of the instrument.

This effort also characterized all defined process errors involved in the generation of the calibration curve. Through analysis of an error propagation study the proposed methodology was shown to have an expected error of ± 0.454 K. This conclusion was verified through inspection of the final calibration results, which had a $\text{RMSE} = 0.488$ K and demonstrates that both the final calibration results and the expected error of the proposed methodology are essentially equal. This result makes physical sense because the proposed correction has removed all but random errors, thus the residual error in the final calibration data is on the order of the uncertainty in the process.

It is important to note that through both error propagation analysis and straight comparison, results further verify the findings that the traditional and proposed methods are only approximately 0.1 K different, with the traditional method exhibiting less error. This conclusion is encouraging as it suggests that the difference between the two methods is essentially within the sensor noise of the instrument.

Through an error propagation investigation of the reverse engineering case, which included the final calibration results of this work, it was concluded that on average the sensor is able to retrieve surface temperatures with an accuracy of ~ 0.6 K (for typical atmospheric conditions) and for extremely warm and moist atmospheric conditions an accuracy of ~ 1.0 K can be expected.

Suggestions for future work: Site 1 (Lake Huron) remains the optimal site location as it provides two buoys locations within a given scene. It is the best site in terms of environmental data, and has unique physical characteristics which are favorable for calibration studies (i.e. offers contrasting target temperatures due to the Lake Huron's bathymetry and ideal atmospheric characteristics as the location is within the heart of the Great Lakes). The one caveat to this location is that buoy observed maximum temperatures rarely exceed 22°C, thus an ocean site (site 4) should also be considered. Realize this methodology is not limited to the suggested calibration sites, but may be implemented anywhere about the globe provided the appropriate environmental data is accessible (i.e. 24 hr buoy observed wind speed and bulk temperature data, in addition to atmospheric profile data close to the time of image capture. In other words, the user could define as many locations as deemed necessary to fulfill the optimal data requirements. Note that for the four sites used in this study a median of 7 pts a year was found with a maximum of 17 pts. Understand that an important goal of this study was to validate the proposed methodology, thus it was somewhat discouraged to use a large number of sites in an effort to reduce the number of variable factors. However, with the methodology now validated, it is emphasized that all global locations which satisfy the data requirements of the proposed methodology can be used.

In most practical cases the user domain is limited by the NDBC moored buoy fleet, which has deployed platforms in the coastal and offshore waters from the western Atlantic to the Pacific Ocean around Hawaii, and from the Bering Sea to the South Pacific [NDBC]. Through a brief investigation, future sites may include sites in the northwest: near Kodiak, Alaska [Figure 5.40 (a); buoy ID 46077 & 46080]; the northeast: near Gray, MI, Chatham, MA and Upton, NY [Figure 5.40 (b); buoy ID's 44007, 44018 and 44017, respectively]; the west: Quillayute, OR and Vandenberg, CA [Figure 5.40 (c); buoy ID's 46087 and 46001, respectively]; and the southeast: near Charleston, SC, Newport, NC, Jacksonville, FL and Slidell Muni, LA [Figure 5.40 (d); buoy ID's 41004, 41025, 41008 and 42007, respectively]. Note locations on the west coast, especially in the southwest should be cautioned due to

the common presence of the marine layer (i.e. low level clouds). It is emphasized that in addition to the necessary data requirements to satisfy the proposed methodology, accurate knowledge of both the buoy platform, as well as buoy location is needed.

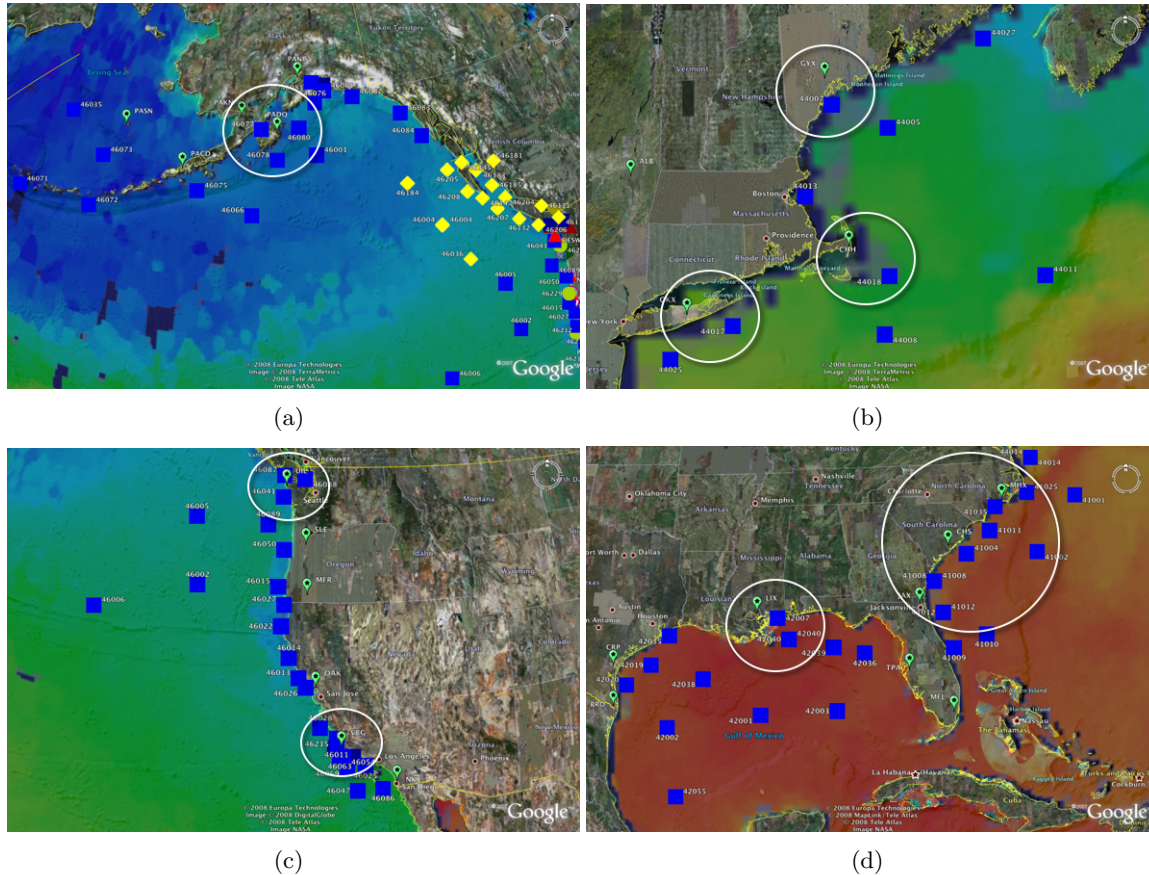


Figure 5.40: Potential calibration sites for future work: (a) Northwest (b) Northeast. (c) West. (d) Southeast. Note the blue squares depict moored buoy locations, where the green stars illustrate radiosonde locations.

Recommendation: Results indicate the Landsat 5 TM thermal band, originally planned for a 3 year mission, has fluctuated only slightly (~ 1 K) over the 24+ years in orbit. The calibration curve developed in this study is consistent with previous results from campaigns performed in 1985 and post 1999. The data indicated that the sensor exhibited a clear gain issue (i.e. over estimates low radiance targets and under estimates high radiance targets) found to be approximately consistent over time. Additionally, an event occurring either prior to or during 1999 caused a discernible fluctuation in sensor performance (i.e. dominant cold bias) for all data

post 1999. It is the recommendation of this vicarious calibration campaign that a linear (dual: slope & intercept) correction be applied to the Landsat 5 data archive. As a result of the correction, the Landsat 5 TM Band 6 is absolutely radiometrically calibrated to within ± 0.488 K, in reference to a 300 K blackbody, verified through an extensive error propagation analysis. Clearly the results of this work should be combined with the previous efforts of RIT and JPL to deduce a final calibration record and correction, as all mentioned calibration data are consistent and trusted.

The proposed methodology was verified by a comparison study to the traditional approach (i.e. non buoy derived ground truth) using the closely monitored and trusted Landsat 7 data calibrated using the traditional approach. The comparison found the two methods were not statistically different, which offered the confidence that this methodology could be applied successfully over the domain of this study. This comparison not only validates the calibration record of Landsat 5 TM Band 6, but also demonstrates the utility of the method in future efforts.

This work has demonstrated that a successful historical vicarious calibration campaign can be conducted using exclusively free and easily accessible data. It has been established that the proposed methodology can be implemented to achieve a high level of radiometric integrity, which includes both historic and future efforts, in the calibration of remote thermal infrared systems.

Appendix A

Landsat Program Overview

Table A.1: Landsat program overview: Landsat 1 to Landsat 7 Lillesand et al. (2004)

Satellite	Launched	Decommissioned	RBV Bands	MSS Bands	TM Bands	Orbit
Landsat 1	July 23, 1972	January 6, 1978	1-3 (simultaneous images)	4-7	None	18 days/900 km
Landsat 2	January 22, 1975	February 25, 1982	1-3 (simultaneous images)	4-7	None	18 days/900 km
Landsat 3	March 5, 1978	March 31, 1983	A-D (1 band side-by-side images)	4-8 ^a	None	18 days/900 km
Landsat 4	July 16, 1982 ^b	June 15, 2001	None	1-4	1-7	16 days/705 km
Landsat 5	March 1, 1984	—	None	1-4	1-7	16 days/705 km
Landsat 6	October 5, 1993	Failure upon launch	None	None plus pan band (ETM)	1-7	16 days/705 km
Landsat 7	April 15, 1999	—	None	None plus pan band (ETM+)	1-7	16 days/705 km

^aBand 8 (10.4-12.6 μm) failed shortly after launch^bTM data transmission failed in August 1993

Appendix B

Volcanic Contamination Correction Study

IVULCN	
[2]	moderate volcanic profile and aged volcanic extinction
[3]	high volcanic profile and fresh volcanic extinction
[4]	high volcanic profile and aged volcanic extinction
[5]	moderate volcanic profile and fresh volcanic extinction
[6]	moderate volcanic profile and background stratospheric extinction
[7]	high volcanic profile and background stratospheric extinction
[8]	extreme volcanic profile and fresh volcanic extinction

(a)

5-Sep-92	IVULCN	Temp Bias [K] with Volcanic Correction	Difference [K]: T Bias No Volc. Cor. - T Bias with Volc. Cor.	Original T Bias [K]
Buoy 45003	[2]	2	-0.177	1.923
	[3]	0.78	1.043	
	[4]	1.927	-0.104	
	[5]	1.666	0.157	
	[6]	1.999	-0.176	
	[7]	1.92	-0.097	
	[8]	-1.436	3.259	

5-Sep-92	IVULCN	Temp Bias [K] with Volcanic Correction	Difference [K]: T Bias No Volc. Cor. - T Bias with Volc. Cor.	Original T Bias [K]
Buoy 45008	[2]	1.375	0.025	1.4
	[3]	0.12	1.28	
	[4]	1.294	0.106	
	[5]	1.027	0.373	
	[6]	1.375	0.025	
	[7]	1.29	0.11	
	[8]	-2.15	3.55	

22-Jul-93	IVULCN	Temp Bias [K] with Volcanic Correction	Difference [K]: T Bias No Volc. Cor. - T Bias with Volc. Cor.	Original T Bias [K]
Buoy 45003	[2]	-1.442	0.027	-1.415
	[3]	-2.724	1.309	
	[4]	-1.524	0.109	
	[5]	-1.79	0.375	
	[6]	-1.442	0.027	
	[7]	-1.525	0.11	

22-Jul-93	IVULCN	Temp Bias [K] with Volcanic Correction	Difference [K]: T Bias No Volc. Cor. - T Bias with Volc. Cor.	Original T Bias [K]
Buoy 45008	[2]	0.005	0.026	0.032
	[3]	-1.278	1.31	
	[4]	-0.076	0.108	
	[5]	-0.344	0.376	
	[6]	0.005	0.026	
	[7]	-0.081	0.113	

(b)

24-Sep-93	IVULCN	Temp Bias [K] with Volcanic Correction	Difference [K]: T Bias No Volc. Cor. - T Bias with Volc. Cor.	Original T Bias [K]
Buoy 45003	[2]	0.596	0.024	0.62
	[3]	-0.601	1.221	
	[4]	0.519	0.101	
	[5]	0.26	0.36	
	[6]	0.596	0.024	
	[7]	0.517	0.103	

24-Sep-93	IVULCN	Temp Bias [K] with Volcanic Correction	Difference [K]: T Bias No Volc. Cor. - T Bias with Volc. Cor.	Original T Bias [K]
Buoy 45008	[2]	0.899	0.024	0.923
	[3]	-0.349	1.272	
	[4]	0.819	0.104	
	[5]	0.549	0.374	
	[6]	0.898	0.025	
	[7]	0.817	0.106	

20-Apr-94	IVULCN	Temp Bias [K] with Volcanic Correction	Difference [K]: T Bias No Volc. Cor. - T Bias with Volc. Cor.	Original T Bias [K]
Buoy 45003	[2]	-0.898	0.019	-0.879
	[3]	0	0	
	[4]	-0.847	-0.032	
	[5]	-0.637	-0.242	
	[6]	-0.899	0.02	
	[7]	-0.846	-0.033	

(c)

Figure B.1: Volcanic correction study: (a) MODTRAN IVULCN description (b-c) Case Study Data.

This study investigated the sensitivity of the MODTRAN IVULCN parameter described in Figure B.1 (a). The study tested four different scenes from the Lake Huron calibration site (Site 1), which amounted to 7 unique cases. The sensitivity analysis was performed by comparing the temperature bias obtained from the original atmospheric profile compared to the volcanic (IVULCN) modified profile. The study found that the IVULCN parameter introduced larger changes for fresh volcanic settings and relatively small changes to aged volcanic conditions, when compared to the original profiles. Notice differences can exceed 3 K in extreme cases, although for all practical conditions relevant in this study ($IVULCN = 2, 4, 6$ or 7), all corrections result in an approximate change to the total temperature bias of ~ 0.1 K.

Appendix C

Internal Boundary Layer Study

This study investigated the sensitivity of the internal boundary layer (IBL) correction compared to the traditional surface correction on atmospheric conditions where the IBL was present. Specifically, this effort was conducted to quantify the sensitivity in MODTRAN through a comparison of the two methodologies. In total 9 profiles were investigated using atmospheric profiles from all calibration sites. Each chosen profile was independently modified by the proposed surface correction [Section 4.6.1] 1) using the traditional method: height of the boundary layer as the height of the surface correction; 2) using the IBL height as the height of the surface correction. Recall, the IBL correction accounts for a boundary layer within the boundary layer (BL) which entails using a shallower height than the BL. Reported is the difference in terms of overall temperature bias, provided through utilizing the entire proposed process.

The major finding in this study was that the difference between the two methods is typically small $\sim 0.1K$ (specifically, 0.077 K). However, note the difference between methods can approach ~ 0.2 K in situations where there is a shallow IBL present within a deep BL [Figure C.1 - C.3]; realize that sensitivity is enhanced for warm moist profiles [Figures C.4 & C.5]. Meaning a smaller difference in methods concerning a warm moist atmospheric profile could potentially result in a larger change than the same modifications in a cool dry atmospheric profile (ex. comparison of Figures C.4 & C.5 to Figure C.6). Through investigation, it is clear that

the introduction of the IBL correction does not typically introduce large differences compared to the traditional methodology, however, differences can be more considerable in the presence of a warm moist atmosphere. In general, results indicate that the IBL correction introduces an ~ 0.1 K difference in temperature compared to the traditional boundary layer correction [Table C.1].

Table C.1: Results from the IBL surface correction study.

Date	Radiosonde Location	Temperature Bias BL Correction [K]	Temperature Bias IBL Correction [K]	$ \Delta T_{BL-IBL} $ [K]
27 May 90	APX	0.573	0.428	0.145
10 Jun 84	ACY	-1.028	-1.163	0.135
17 Jun 86	APX	0.784	0.717	0.067
16 Aug 85	ACY	-3.122	-2.997	0.125
06 Jul 99	WAL	-0.399	-0.486	0.087
24 Aug 05	APX	-0.562	-0.512	0.05
26 Jun 01	APX	-0.224	-0.284	0.06
02 Jul 03	APX	-0.2	0.194	0.006
28 Jun 88	ACY	0.083	0.064	0.019

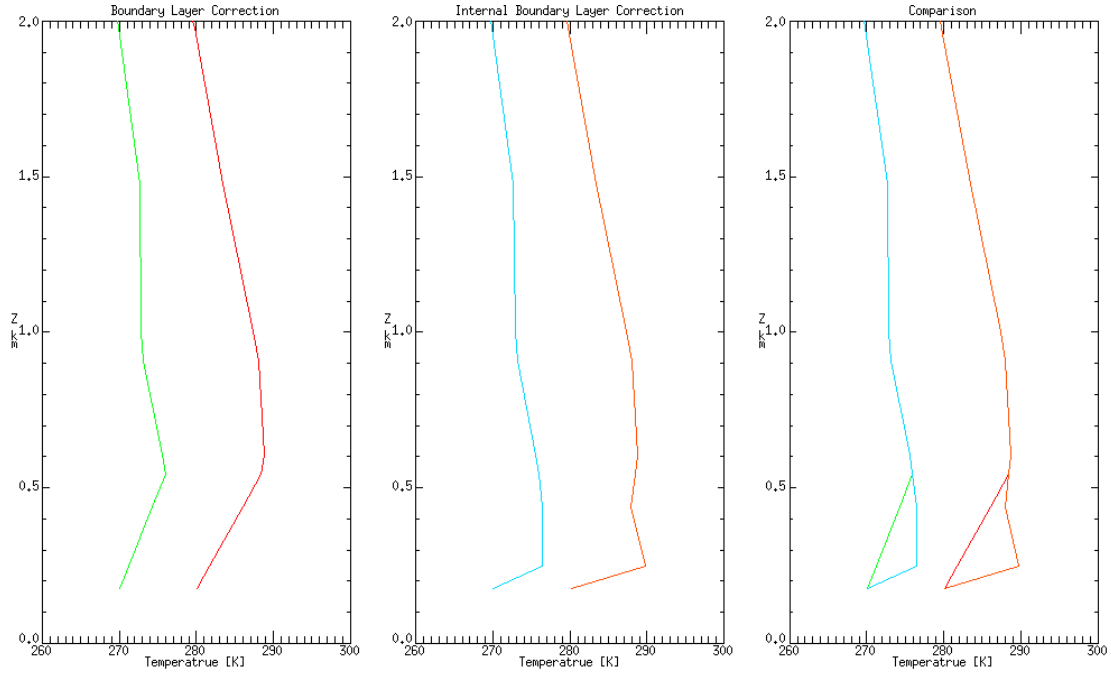


Figure C.1: Radiosonde observations from APX on 27 May, 1990.

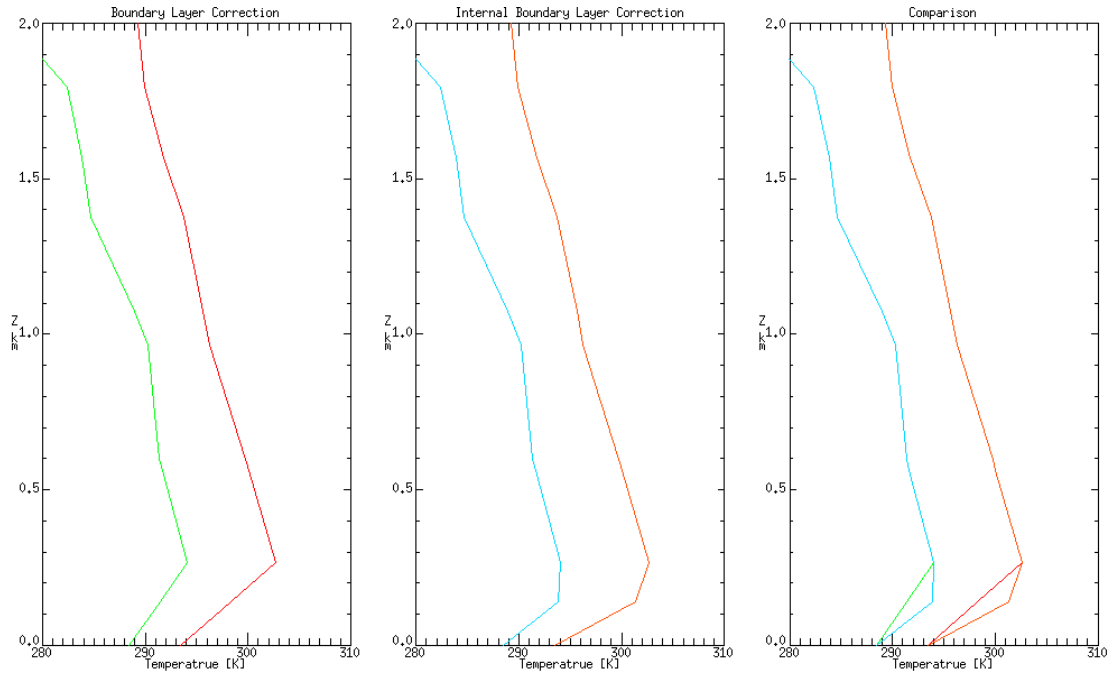


Figure C.2: Radiosonde observations from ACY on 10 June, 1984.

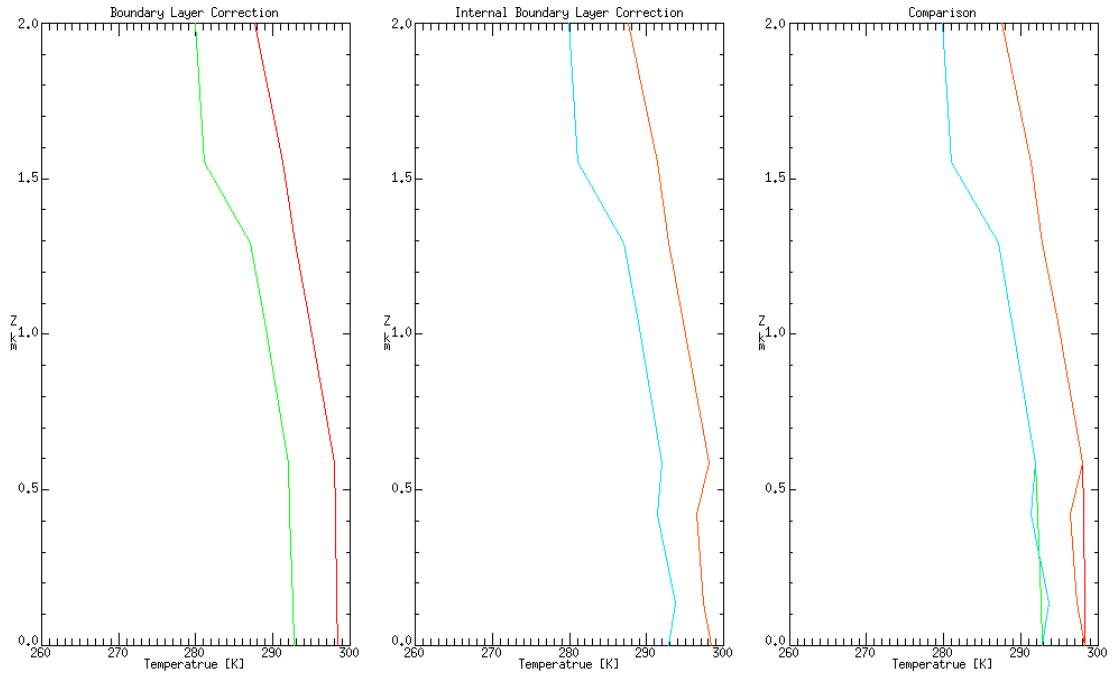


Figure C.3: Radiosonde observations from ACY on 16 August, 1985.

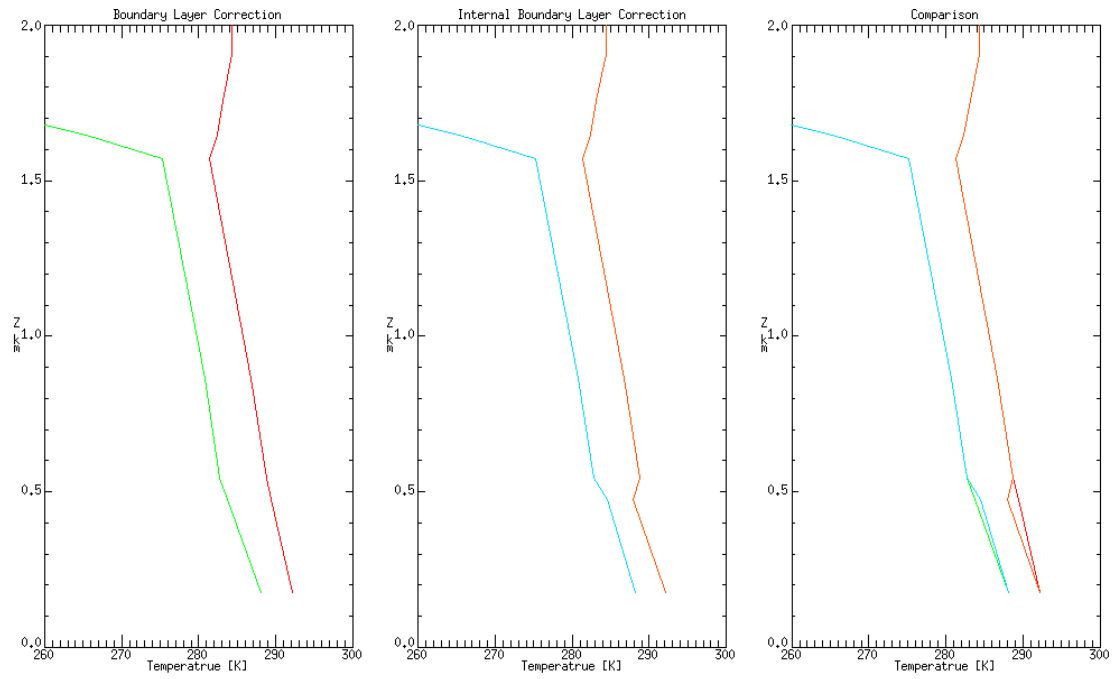


Figure C.4: Radiosonde observations from APX on 24 August, 2005.

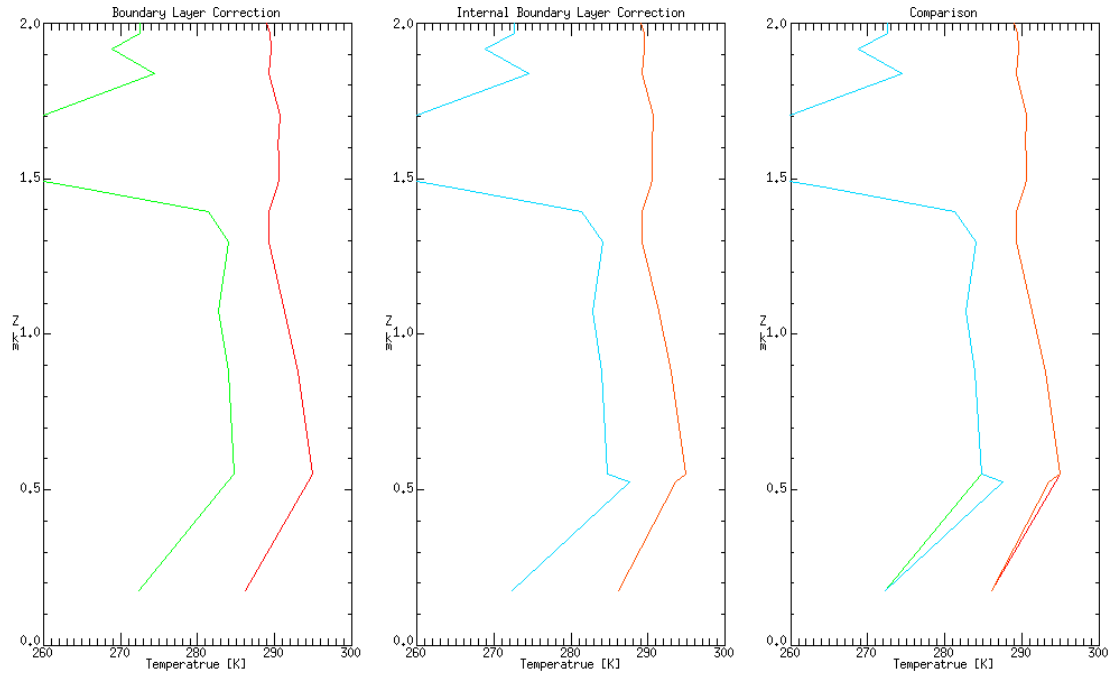


Figure C.5: Radiosonde observations from APX on 26 June, 2001.

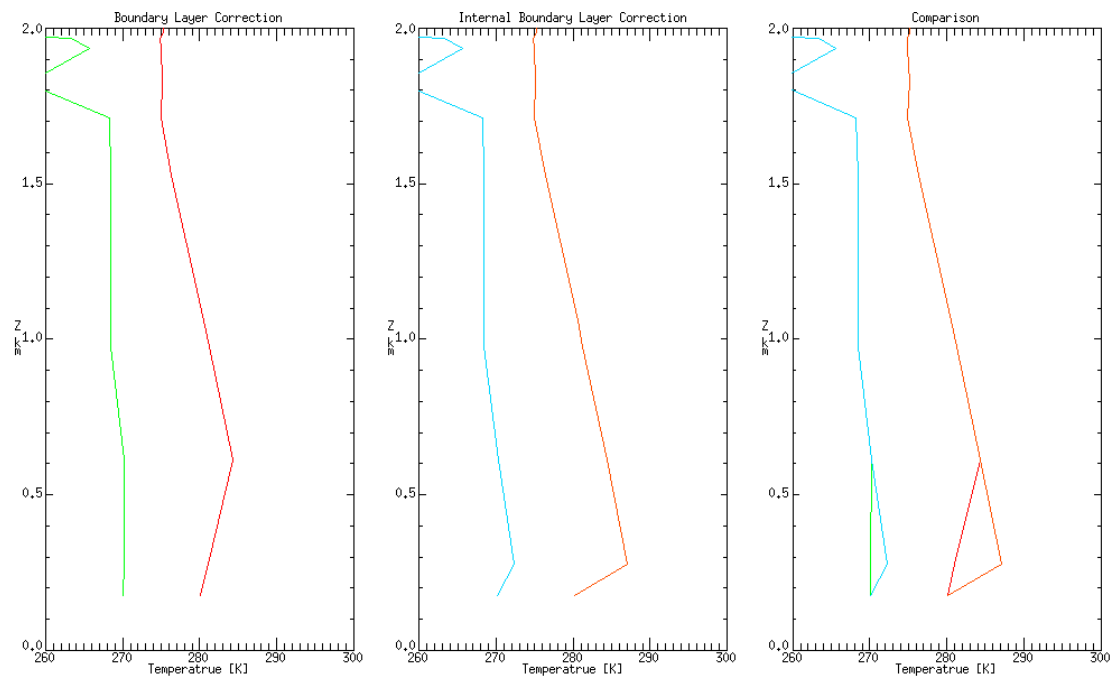


Figure C.6: Radiosonde observations from APX on 17 June, 1986.

Appendix D

Surface Correction Study

This study is focused on quantifying the proposed surface correction by comparison with profiles which have no surface correction applied (i.e. raw radiosonde observations integrated with the proposed upper-air correction to yield a 0-100 km profile). Recall the surface correction is proposed to account for both spatial and temporal phenomena correcting for the fact that radiosonde observations are taken at some time and place different from the desired location. A total of 37 profiles were used in this study. Each profile was surface corrected by the proposed methodology, and then ran through the complete process, which resulted in a temperature bias. Similarly, the 37 profiles were assembled using only the radiosonde observations (i.e. no surface correction applied) and the same process was performed to yield a temperature bias for each profile. Note that the ground altitude was adjusted differently for the two cases, where the water level was used in the applied surface correction case and the elevation of the radiosonde launch site was used for the non-surface corrected radiosonde profiles.

Results demonstrate that the surface correction proposed in this effort is small in magnitude compared to that of the original radiosonde observed surface values [Figure D.2].

Date	Location	No Surface Correction (Raw Radiosonde Surface Data) [K]	Surface Corrected [K]	Difference: No Correction - Surface Corrected [K]	Absolute difference [K]
September 22, 2004	huron	-0.419	-0.552	0.133	0.133
September 22, 2004	huron	-0.542	-0.641	0.099	0.099
August 21, 2004	huron	0.031	-0.035	0.066	0.066
August 21, 2004	huron	-0.636	-0.639	0.003	0.003
August 31, 1996	huron	-0.975	-1.080	0.105	0.105
August 31, 1996	huron	-0.838	-0.968	0.130	0.130
July 23, 2005	huron	-0.612	-0.627	0.015	0.015
July 23, 2005	huron	-1.372	-1.358	-0.014	0.014
July 20, 1998	huron	-1.818	-1.748	-0.070	0.070
May 23, 2006	huron	0.530	0.478	0.052	0.052
May 23, 2006	huron	0.306	0.273	0.033	0.033
March 16, 1987	huron	0.207	0.625	-0.418	0.418
March 16, 1987	huron	1.097	0.575	0.522	0.522
May 4, 1999	huron	0.415	0.212	0.203	0.203
May 4, 1999	huron	0.174	0.383	-0.209	0.209
May 3, 1987	huron	0.698	0.732	-0.034	0.034
May 3, 1987	huron	0.675	0.991	-0.316	0.316
June 4, 1987	huron	0.974	0.971	0.003	0.003
June 4, 1987	huron	0.835	0.927	-0.092	0.092
April 13, 1992	delmarva	0.117	0.084	0.033	0.033
April 13, 1992	delmarva	-0.004	0.007	-0.011	0.011
March 28, 1986	delmarva	1.052	1.055	-0.003	0.003
March 28, 1986	delmarva	0.610	0.626	-0.016	0.016
August 23, 1999	delmarva	-1.085	-1.059	-0.026	0.026
May 9, 1987	delmarva	-0.625	-0.581	-0.044	0.044
May 9, 1987	delmarva	-0.570	-0.529	-0.041	0.041
September 21, 1984	delmarva	-0.574	-0.602	0.028	0.028
September 21, 1984	delmarva	-0.703	-0.786	0.083	0.083
July 10, 1989	delmarva	-0.688	0.343	-1.031	1.031
July 6, 1999	delmarva	-0.551	-0.486	-0.065	0.065
February 15, 2006	delmarva	0.002	-0.020	0.022	0.022
June 2, 1996	delmarva	-0.283	-0.312	0.029	0.029
June 14, 1991	delmarva	-0.606	-0.767	0.161	0.161
June 16, 1987	superior	1.419	1.586	-0.167	0.167
June 16, 1987	superior	0.874	1.218	-0.344	0.344
May 29, 2004	superior	0.968	0.935	0.033	0.033
May 29, 2004	superior	1.128	1.091	0.037	0.037

Figure D.1: Depicts the results from the surface and non-surface corrected data sets.

Figure D.2 depicts a box plot of the absolute difference between the surface corrected and non-surface corrected data sets. Notice that average difference is ~ 0.1 K and that for the investigated profiles a minimum and maximum absolute difference of 0.003 K and 1.031 K respectively, was found. At first glance the results appear

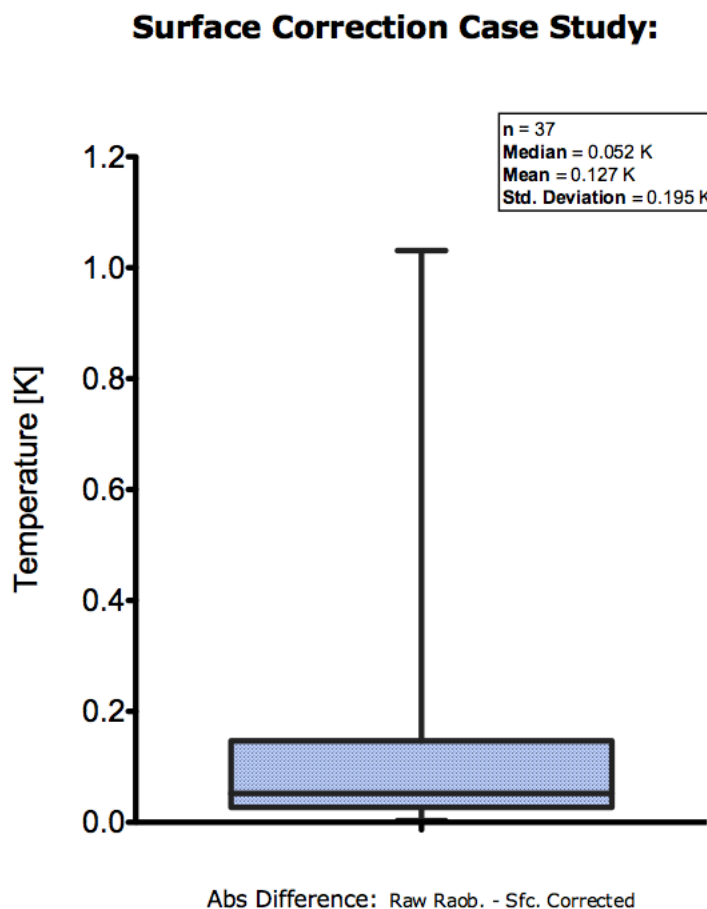


Figure D.2: Depicts a box plot of the absolute difference between the surface and non-surface corrected data sets.

somewhat counter intuitive as the expected difference was thought to be larger. However, the findings can be justified through the following explanation. Recall, a general assumption was made that the atmosphere was approximately uniform and non-varying about the scene. To allow for this assumption to approximate truth, each scene used in this calibration campaign was rigorously pre-processed both visually and quantitatively (i.e. cloud and dewpoint depression screened, respectively). With that said, it makes physical sense that the differences were found to be small

in magnitude between the raw radiosonde and the assembled column, as the scene locations were chosen for their ideal atmospheric characterization locations (given the restrictions of the data networks). Also note, due to the influence of the IBL, the majority of the corrections are restricted to a single layer modification compared to the raw radiosonde observations. Meaning a bulk of the corrections are small in nature, thus relative differences in each profile are small (corrected and not corrected). Lastly, the data with no correction applied, shown in Figure D.1 was substituted into the final calibration results to test whether the surface correction accounted for a change in bias temperature of the resulting calibration curve. Results from the study showed the RMSE to increase by a negligible margin (0.005 K). This study has verified that the surface correction is small in nature (typically ~ 0.1 K), however, significant in the recreation of the atmospheric column, as differences can exceed 1 K. Shown below is a subset of examples, which helps the reader understand the magnitude of change introduced by the surface correction.

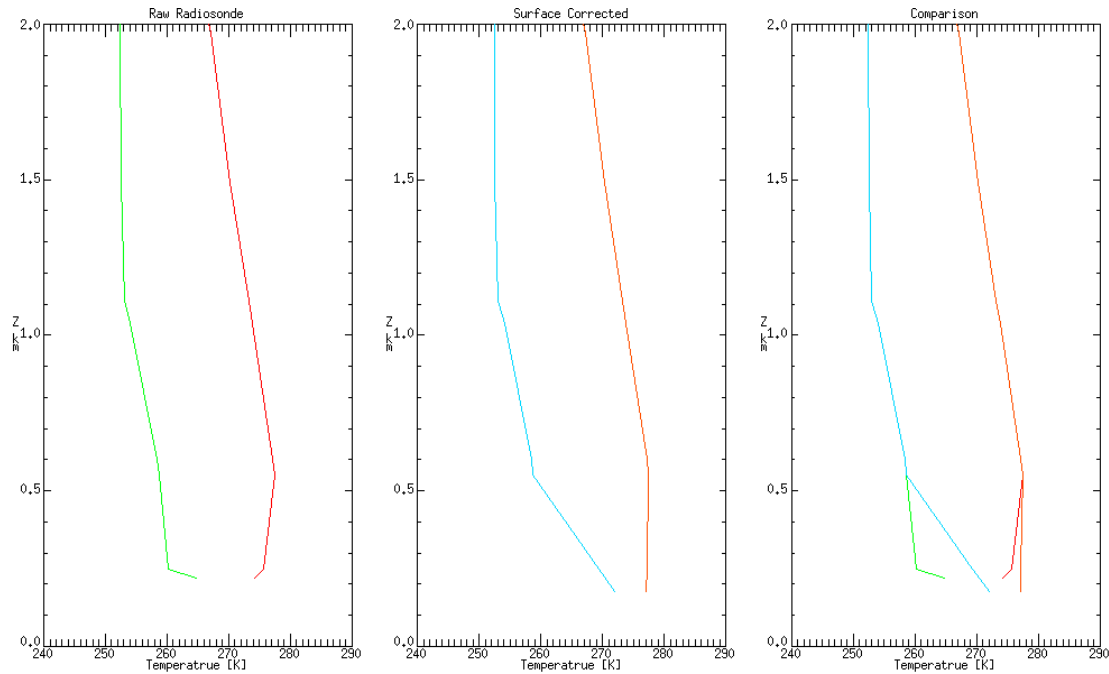


Figure D.3: Depicts the comparison of surface corrected data and the surface values from the radiosonde launched at 12z from APX on 03 May, 1987.

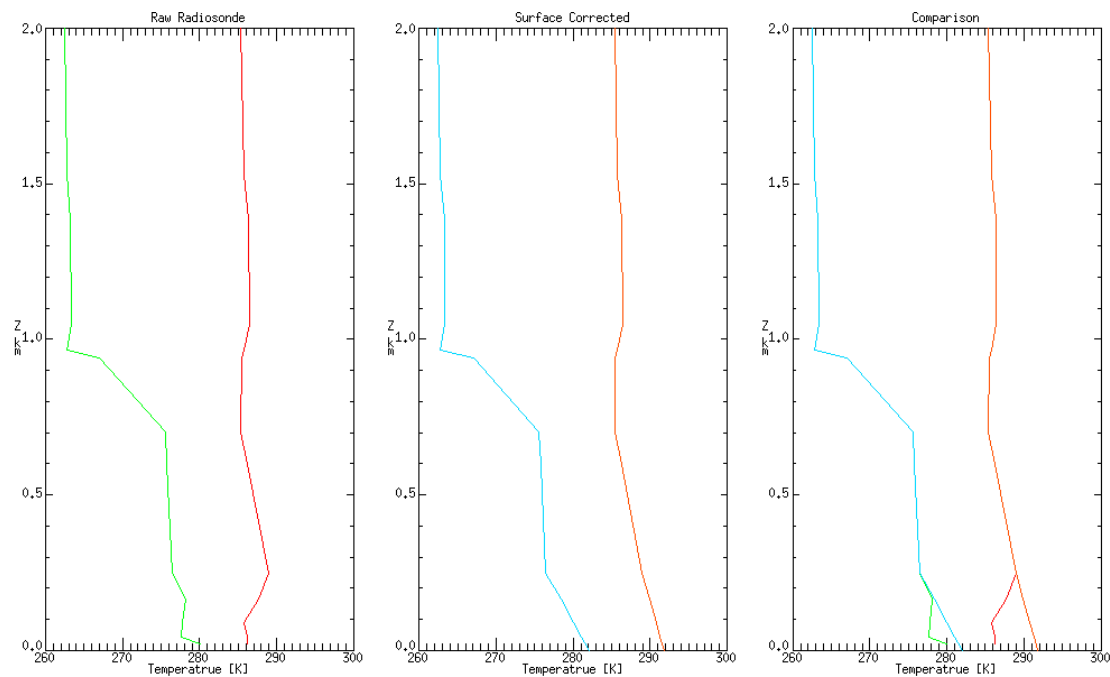


Figure D.4: Depicts the comparison of surface corrected data and the surface values from the radiosonde launched at 12z from ACY on 14 June, 1991.

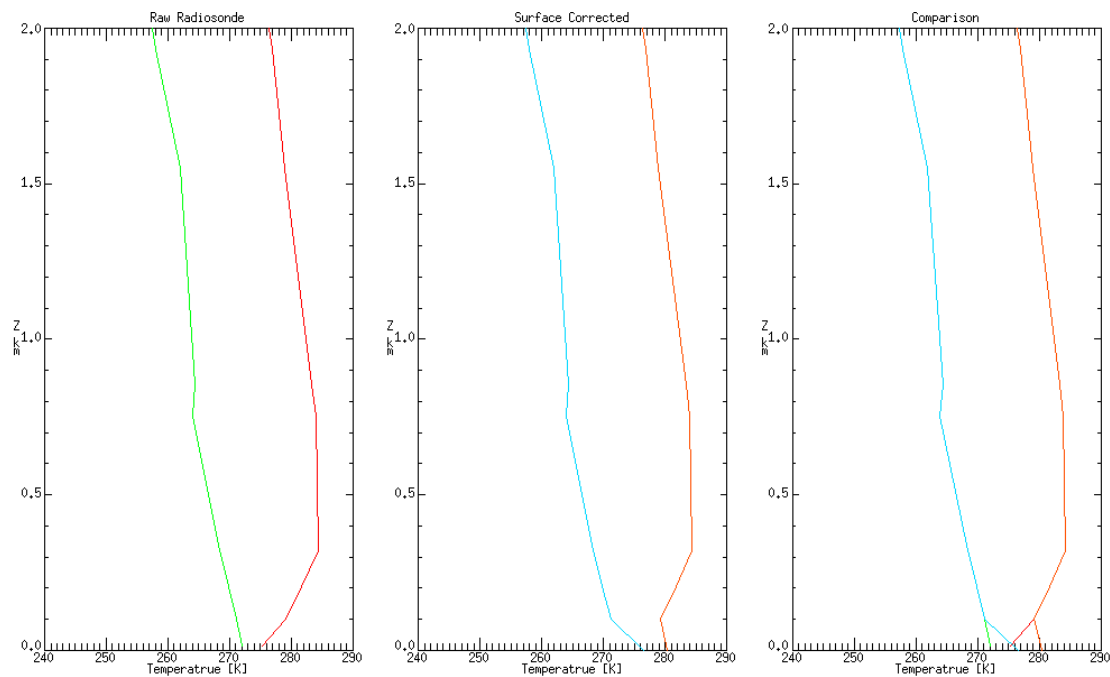


Figure D.5: Depicts the comparison of surface corrected data and the surface values from the radiosonde launched at 12z from WAL on 14 February, 2006.

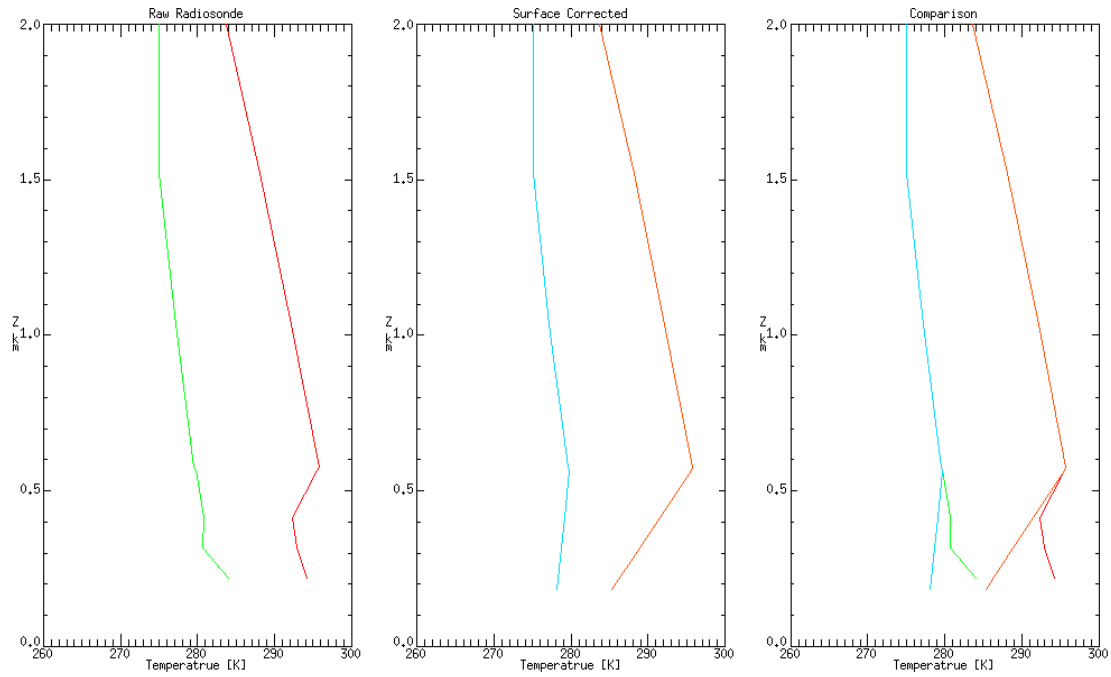


Figure D.6: Depicts the comparison of surface corrected data and the surface values from the radiosonde launched at 12z from SSM on 16 June, 1987.

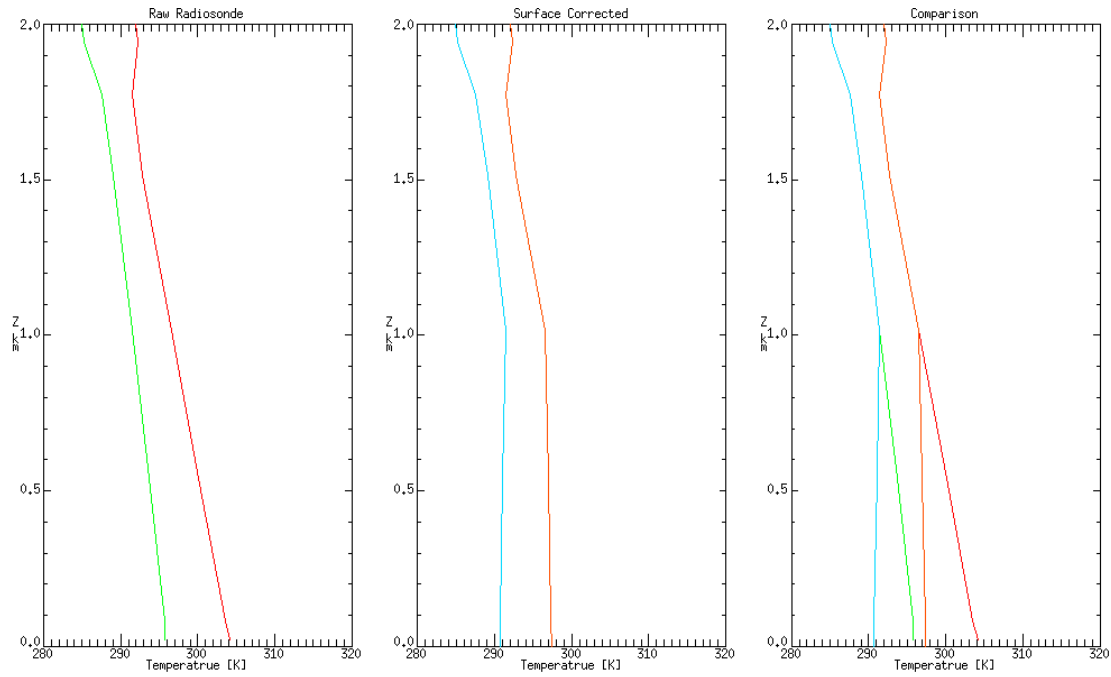


Figure D.7: Depicts the comparison of surface corrected data and the surface values from the radiosonde launched at 00z from ACY on 10 July, 1989.

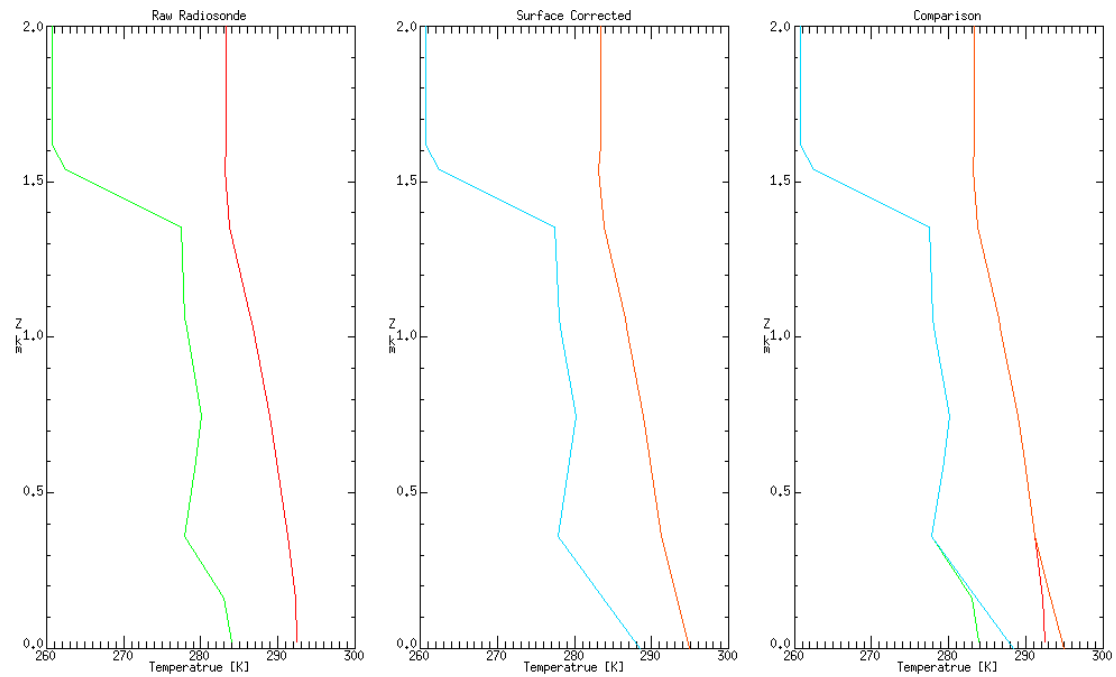


Figure D.8: Depicts the comparison of surface corrected data and the surface values from the radiosonde launched at 00z from ACY on 21 September, 1984.

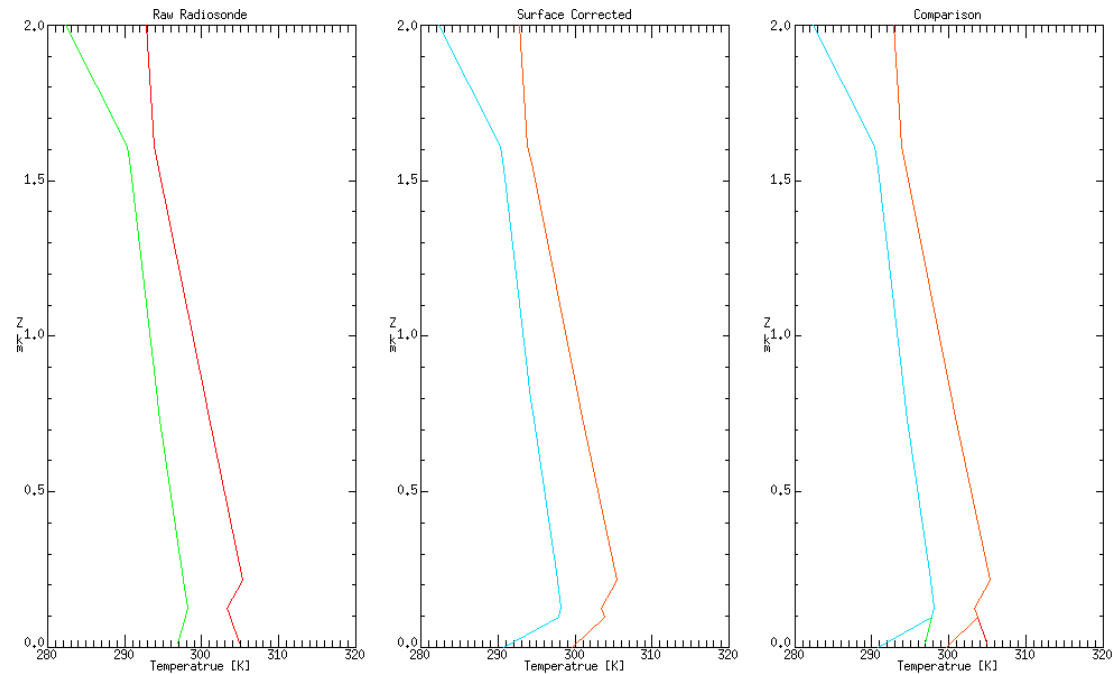


Figure D.9: Depicts the comparison of surface corrected data and the surface values from the radiosonde launched at 12z from WAL on 06 July, 1999.

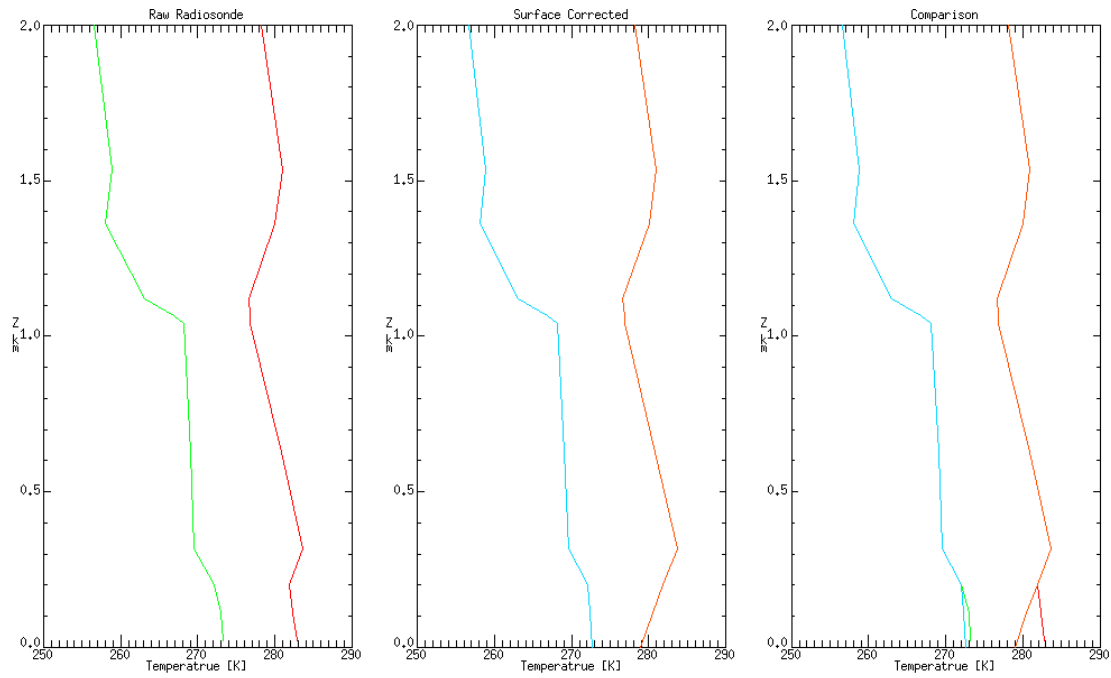


Figure D.10: Depicts the comparison of surface corrected data and the surface values from the radiosonde launched at 00z from ACY on 28 March, 1986.

Appendix E

Upper Air Study

This study was developed to investigate the sensitivity of the upper atmosphere in terms of the retrieved temperature bias given the proposed methodology. Simply stated the study is motivated by the need to identify the error introduced by the difficulty in accounting for the upper atmosphere, as well as determining at what height do the profiles of temperature and dew point become critical (i.e. errors introduced above sensor noise ~ 0.1 K).

Seven atmospheric profiles were used in this study [Section 4.12.2]. The profiles were each individually processed in MODTRAN. For each profile, the entire reconstructed atmospheric profile (i.e. surface correction and upper-air correction applied; 0 - 100 km) was input into MODTRAN and an initial temperature bias was found. Next the number of layers in the input profile was reduced (i.e. vertical extent of the profile was reduced) and the process was repeated. The focus was to reduce the vertical extent of the atmospheric column from 100 km down to a level where errors were found to be comparable to sensor noise (i.e. 0.1 K). The rate at which layers were reduced was not fixed, but followed a general rule of roughly 5 - 20 km above 10 km (i.e. including and above the stratosphere) and approximately 1 km below 10 km (i.e. in the troposphere). Note the resulting temperature bias for each reduced profile was compared against the temperature bias found from using the entire 0-100 km profile.

Through inspection of Figures E.1 - E.7 and raw data Figure E.8, it was found

that as the vertical extent of the input profile decreased the difference in absolute temperature bias compared to the full column increased. Meaning that the removal of atmospheric layers in the upper atmosphere is less sensitive than the removal of layers extending down into the mid and lower atmosphere, which makes physical sense. The upper atmosphere, which included all layers above 10 km was found to be highly insensitive with an average absolute difference of 0.008 K for all cases. Specifically, the average absolute difference at approximately 10 and 20 km was 0.01 and 0.02 K, respectively. The average height provide the fixed radiosonde observations where the difference approximately exceeded 0.1 K was 4.47 km. Note that the (4.47 km) result is not a good measure, as the data suggests a strong dependence on the amount of moisture present in each atmospheric profile [Figures E.1 - E.7]. Warm moist profiles (note surface temperatures near or above 300 K) [Figure E.6 & E.7] demonstrated a critical height of roughly 7 km. The more typical profiles [Figures E.5 - E.3 and E.1] illustrated a critical height of approximately 4.35 km, and the driest of cases [Figure E.2] illustrates a critical height of roughly 2 km. Results illustrate that warm moist atmospheres are more sensitive than cooler and less moist atmospheric profiles.

In each profile [Figures E.1 - E.7] notice that the vertical extent of the radiosonde observations have been highlighted. If the MODTRAN input profiles included data only to the vertical extent of the radiosonde profile a temperature difference of only 0.006 K results for all tested cases. Realize, if the vertical extent exceeded 30 km [Figure E.1, E.2, E.5 & E.6], which spanned all cases in this study (i.e. warm moist - cool dry), using only layers up to the vertical extent of the radiosonde observations a temperature difference of only 0.001 K was found. Most importantly, this study demonstrated that uncertainties due to the recreation of the upper atmospheric column (i.e. beyond the vertical extent of the radiosonde observations), translates into potential errors that are essential negligible.

Summary:

- The upper atmosphere is shown to be less sensitive than the lower atmosphere.
- Warm moist atmospheres are more sensitive than cool dry atmospheres.
- Warm moist calibration quality profiles demonstrate an approximate critical height of ~ 7 km.
- Typical calibration quality profiles exhibit a critical height of ~ 4.35 km.
- Dry calibration quality profiles can exhibit a critical height of ~ 2 km.
- If the vertical extent of the radiosonde reaches approximately 30 km, then by using only these layers and comparing to the results of the entire profile a temperature difference of 0.001 K was found.

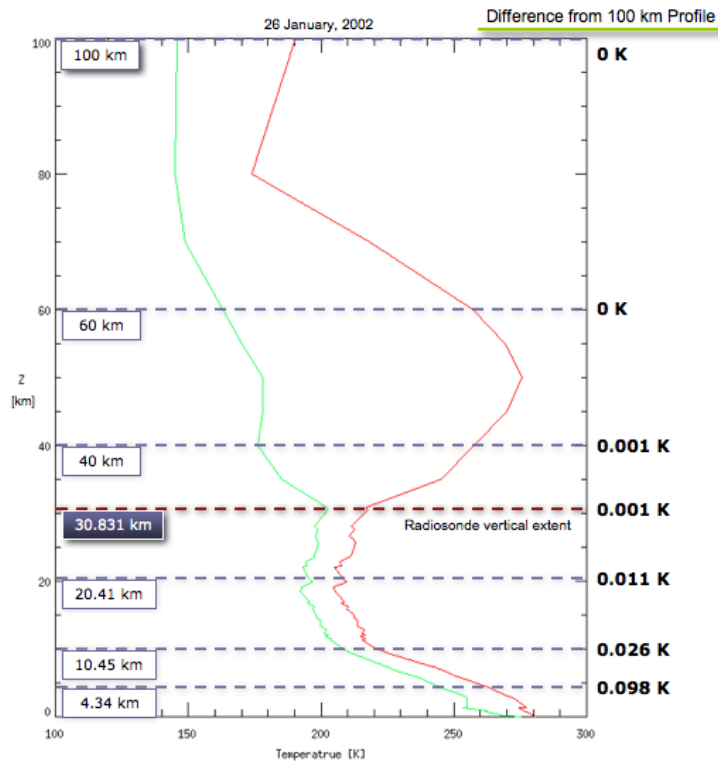


Figure E.1: Radiosonde observations from WAL at 12z on 26 Jan 02.

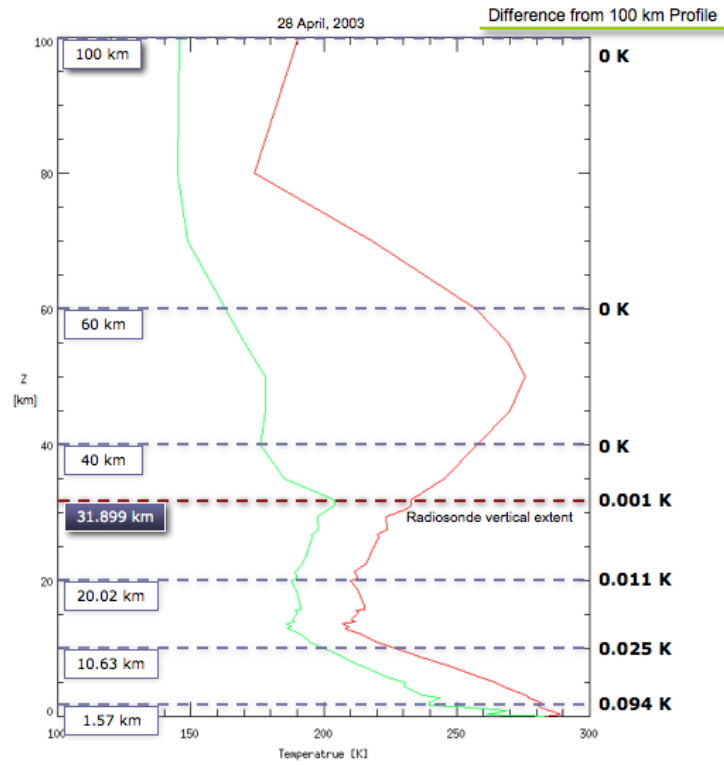


Figure E.2: Radiosonde observations from WAL at 12z on 28 Apr 03.

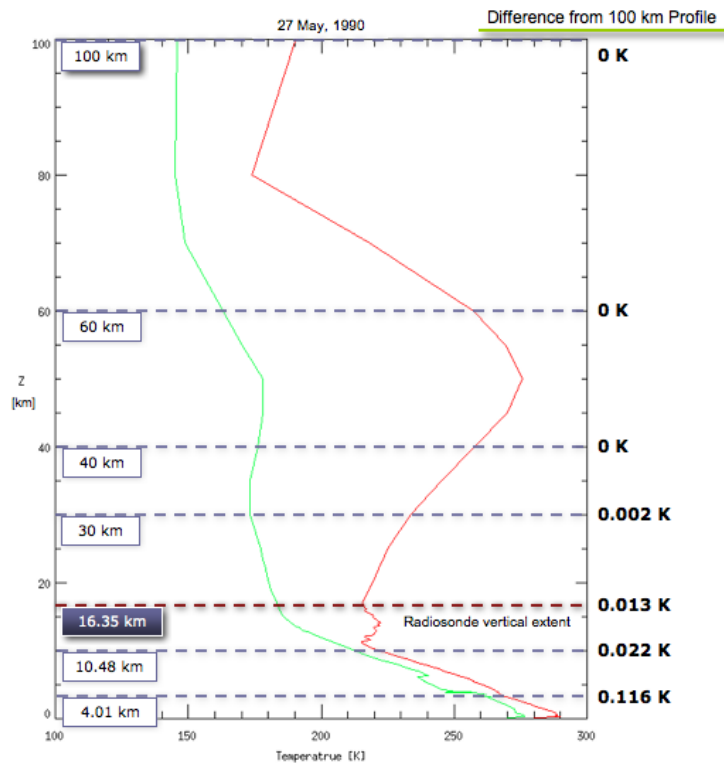


Figure E.3: Radiosonde observations from SSM at 00z on 27 May 90.

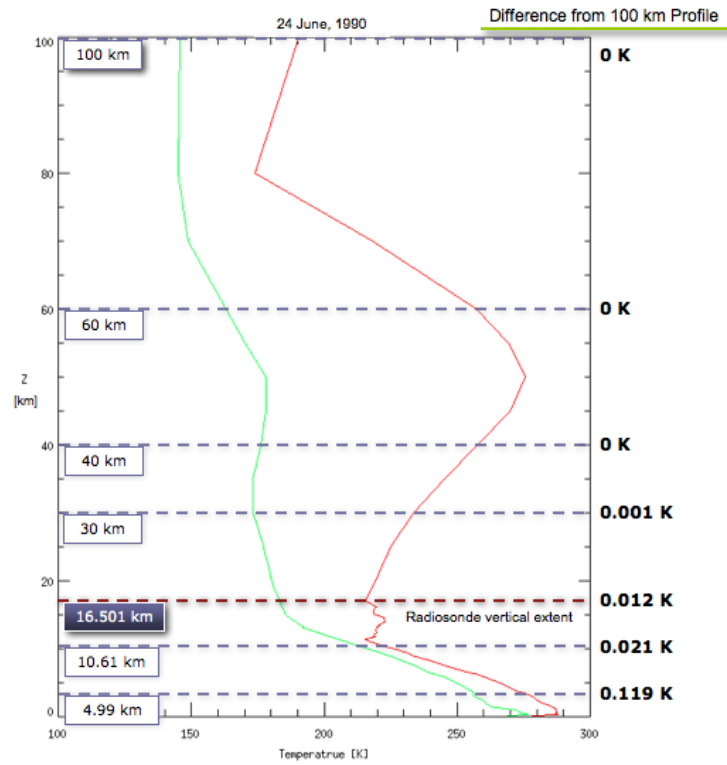


Figure E.4: Radiosonde observations from SSM at 00z on 24 Jun 90.

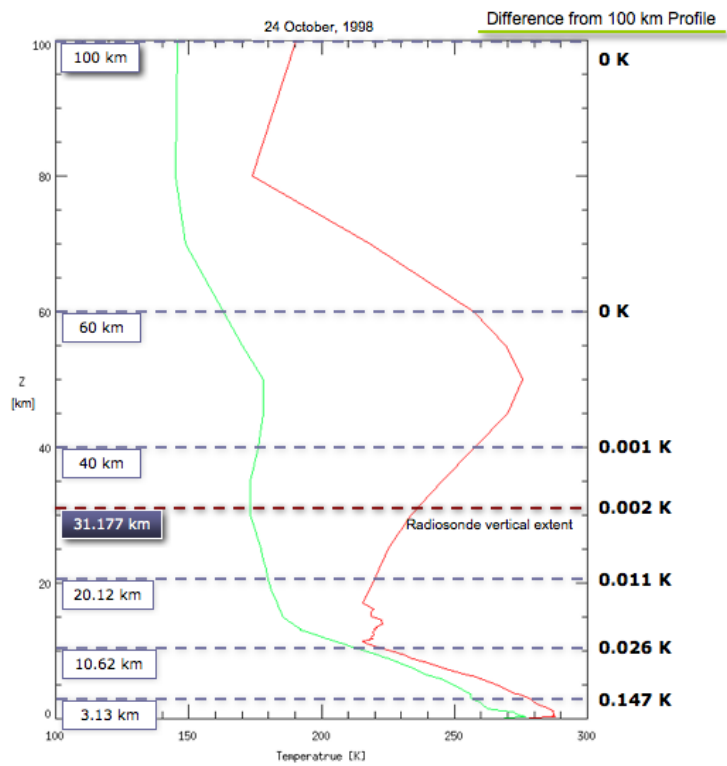


Figure E.5: Radiosonde observations from APX at 12z on 24 Oct 98.

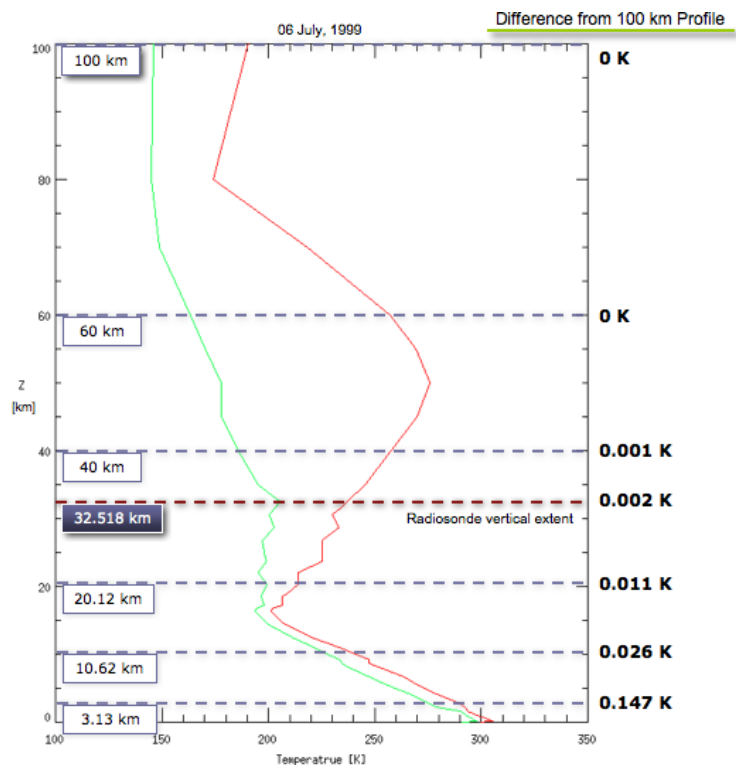


Figure E.6: Radiosonde observations from WAL at 00z on 06 Jul 99.

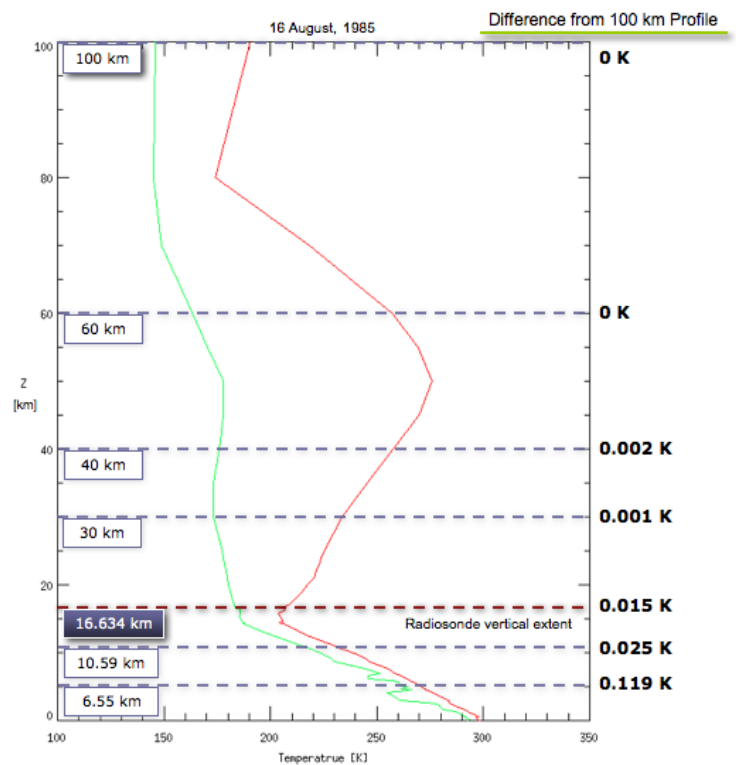


Figure E.7: Radiosonde observations from WAL at 12z on 16 Aug 85.

16-Aug-85				6-Jul-99				24-Oct-98			
Vertical Extent [km]	Number of layers	Temperature Bias [K]	Difference from 100 km	Vertical Extent [km]	Number of layers	Temperature Bias [K]	Difference from 100 km	Vertical Extent [km]	Number of layers	Temperature Bias [K]	Difference from 100 km
100	62	-2.997	0	100	51	-0.486	0	100	75	-0.03	0
60	59	-2.997	0	60	48	-0.486	0	60	72	-0.03	0
40	55	-2.995	0.002	40	44	-0.486	0	40	68	-0.031	0.001
30	53	-2.996	0.001	32.518	42	-0.487	0.001	31.177	66	-0.032	0.002
20	47	-3.008	0.011	30.604	40	-0.487	0.001	28.482	63	-0.033	0.003
18	45	-3.01	0.013	28.716	39	-0.488	0.002	24.959	59	-0.035	0.005
16.634	43	-3.012	0.015	24.254	36	-0.492	0.006	20.118	52	-0.041	0.011
14	39	-3.014	0.017	20.238	32	-0.498	0.012	15.098	38	-0.049	0.019
12.408	35	-3.018	0.021	16.26	26	-0.503	0.017	12.041	30	-0.053	0.023
10.593	33	-3.022	0.025	10.976	21	-0.511	0.025	10.621	28	-0.056	0.026
9.678	32	-3.031	0.034	9.243	19	-0.53	0.044	9.414	26	-0.058	0.028
8.719	30	-3.037	0.04	8.39	17	-0.54	0.054	8.203	25	-0.065	0.035
7.589	28	-3.066	0.069	6.717	15	-0.602	0.116	7.414	23	-0.07	0.04
6.548	25	-3.149	0.152	5.914	14	-0.668	0.182	6.205	21	-0.081	0.051
5.297	21	-3.353	0.356	5.028	13	-0.806	0.32	5.332	19	-0.099	0.069
								4.565	16	-0.116	0.086
								3.133	13	-0.177	0.147
								2.191	13	-0.198	0.168

24-Jun-90				27-May-90				28-Apr-03			
Vertical Extent [km]	Number of layers	Temperature Bias [K]	Difference from 100 km	Vertical Extent [km]	Number of layers	Temperature Bias [K]	Difference from 100 km	Vertical Extent [km]	Number of layers	Temperature Bias [K]	Difference from 100 km
100	73	1.414	0	100	81	0.428	0	100	58	-0.108	0
60	70	1.414	0	60	78	0.428	0	60	55	-0.108	0
40	66	1.414	0	40	74	0.428	0	40	51	-0.108	0
30	64	1.413	0.001	30	72	0.426	0.002	31.899	49	-0.109	0.001
20	58	1.406	0.008	20	68	0.419	0.009	20.023	37	-0.119	0.011
16.501	54	1.402	0.012	16.35	62	0.415	0.013	15.364	31	-0.126	0.018
14.535	48	1.4	0.014	12.188	48	0.409	0.019	10.63	20	-0.133	0.025
12.585	39	1.397	0.017	10.478	42	0.406	0.022	9.42	19	-0.135	0.027
10.606	29	1.393	0.021	9.285	41	0.403	0.025	7.528	17	-0.143	0.035
9.399	28	1.39	0.024	8.048	38	0.393	0.035	5.74	15	-0.155	0.047
8.343	24	1.38	0.034	6.958	36	0.381	0.047	4.963	14	-0.162	0.054
7.391	23	1.367	0.047	5.905	32	0.355	0.073	3.105	12	-0.187	0.079
6.295	21	1.344	0.07	4.938	29	0.335	0.093	2.014	10	-0.2	0.092
4.994	19	1.295	0.119	4.005	24	0.312	0.116	1.574	9	-0.202	0.094
3.741	17	1.232	0.182								

26-Jan-02			
Vertical Extent [km]	Number of layers	Temperature Bias [K]	Difference from 100 km
100	62	0.278	0
60	59	0.278	0
40	55	0.277	0.001
30.831	53	0.277	0.001
20.41	41	0.267	0.011
15.13	32	0.26	0.018
10.45	21	0.252	0.026
9.27	19	0.25	0.028
7.29	17	0.238	0.04
6.001	15	0.224	0.054
4.341	13	0.18	0.098

Figure E.8: Seven atmospheric profile data used in the upper-air sensitivity analysis. Note the green highlighted cell symbolize the vertical extent of the radiosonde profile and that temperature differences are reported as absolute temperature differences.

Appendix F

MODTRAN Standard Atmosphere's

Shown below are the MODTRAN standard atmospheric profiles of Mid-Latitude Summer, Mid-Latitude Winter and Tropical. Profiles obtained via parsing the MODTRAN output file Tape 6.

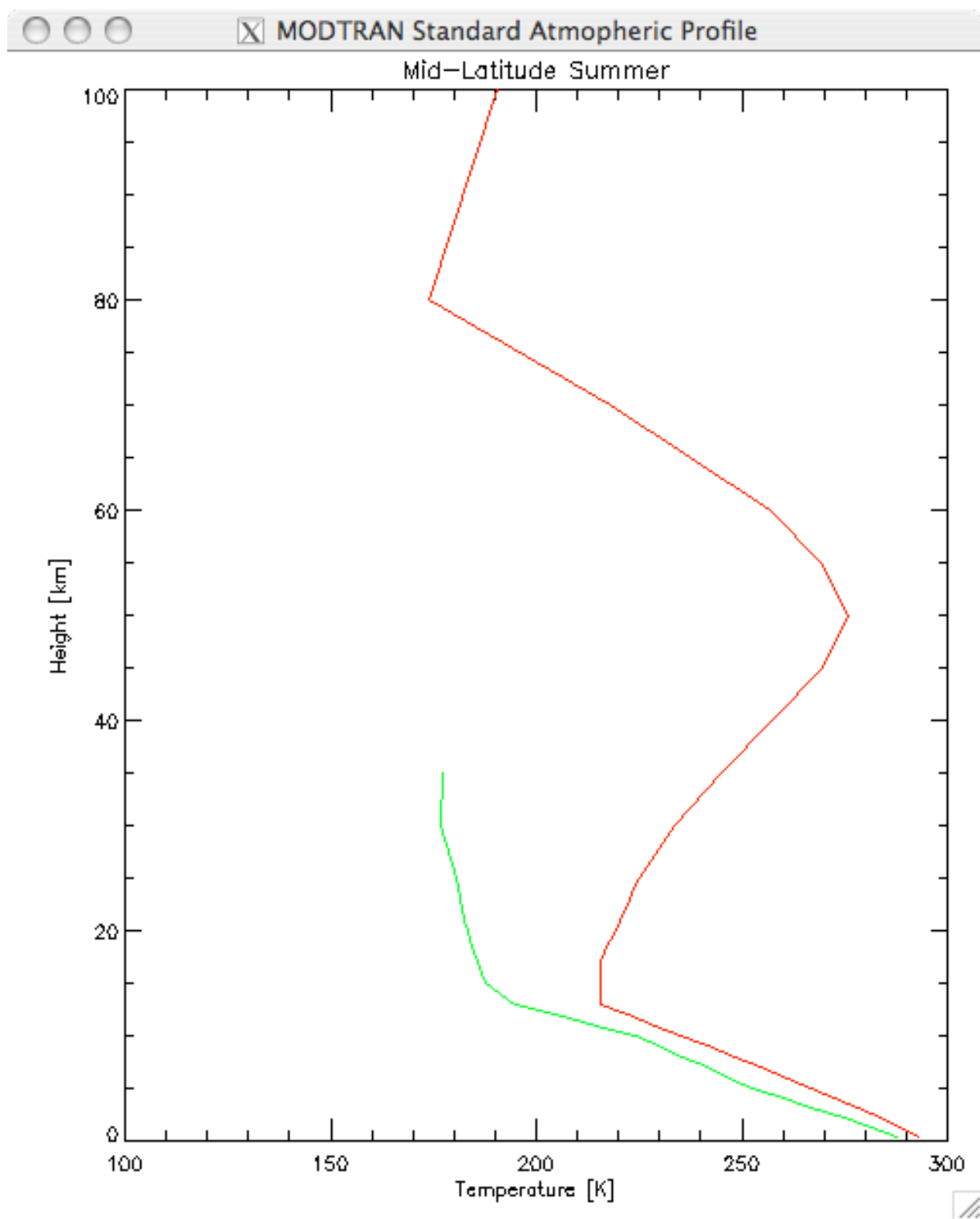


Figure F.1: MODTRAN Standard Atmosphere: Mid-Latitude Summer.

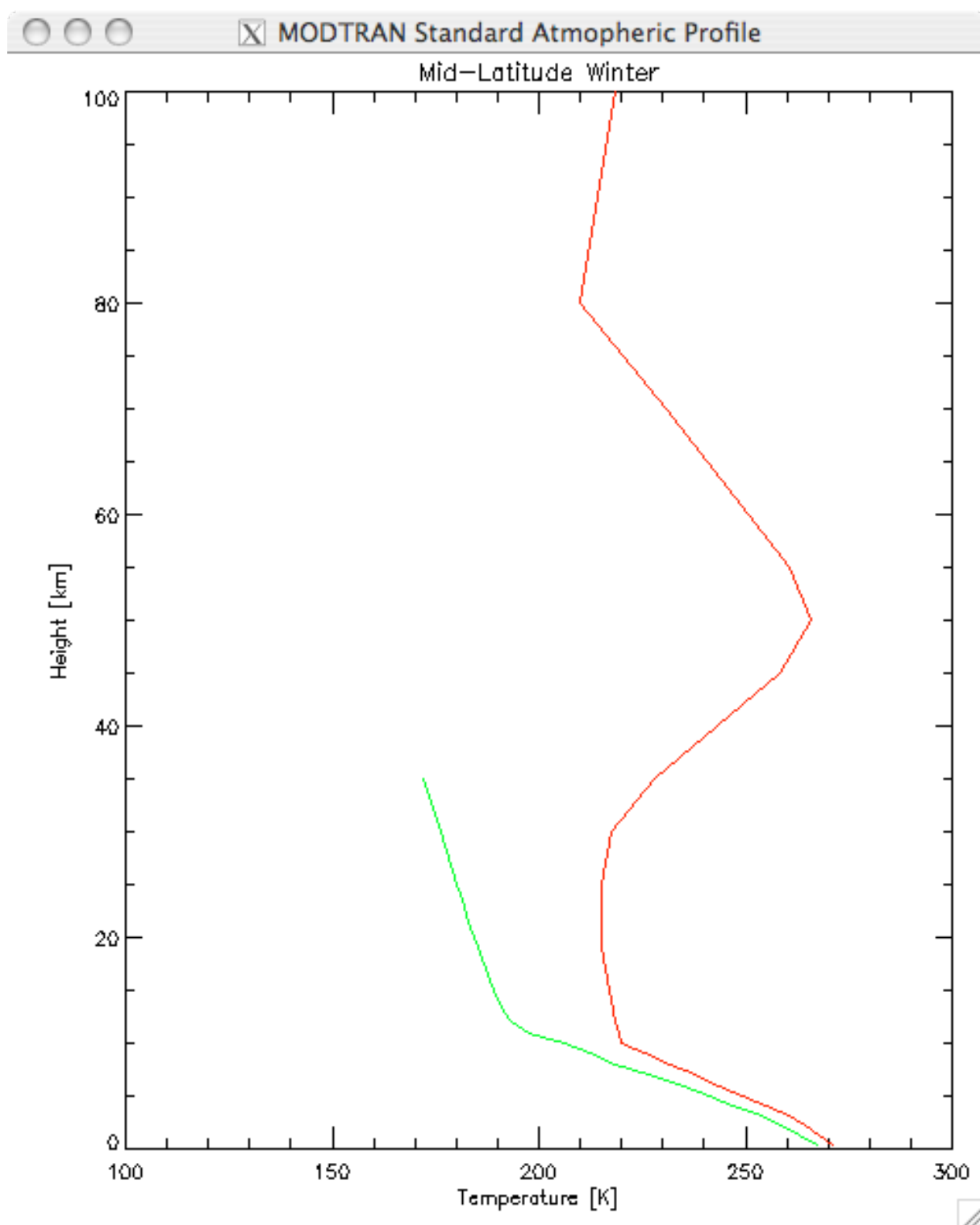


Figure F.2: MODTRAN Standard Atmosphere: Mid-Latitude Winter.

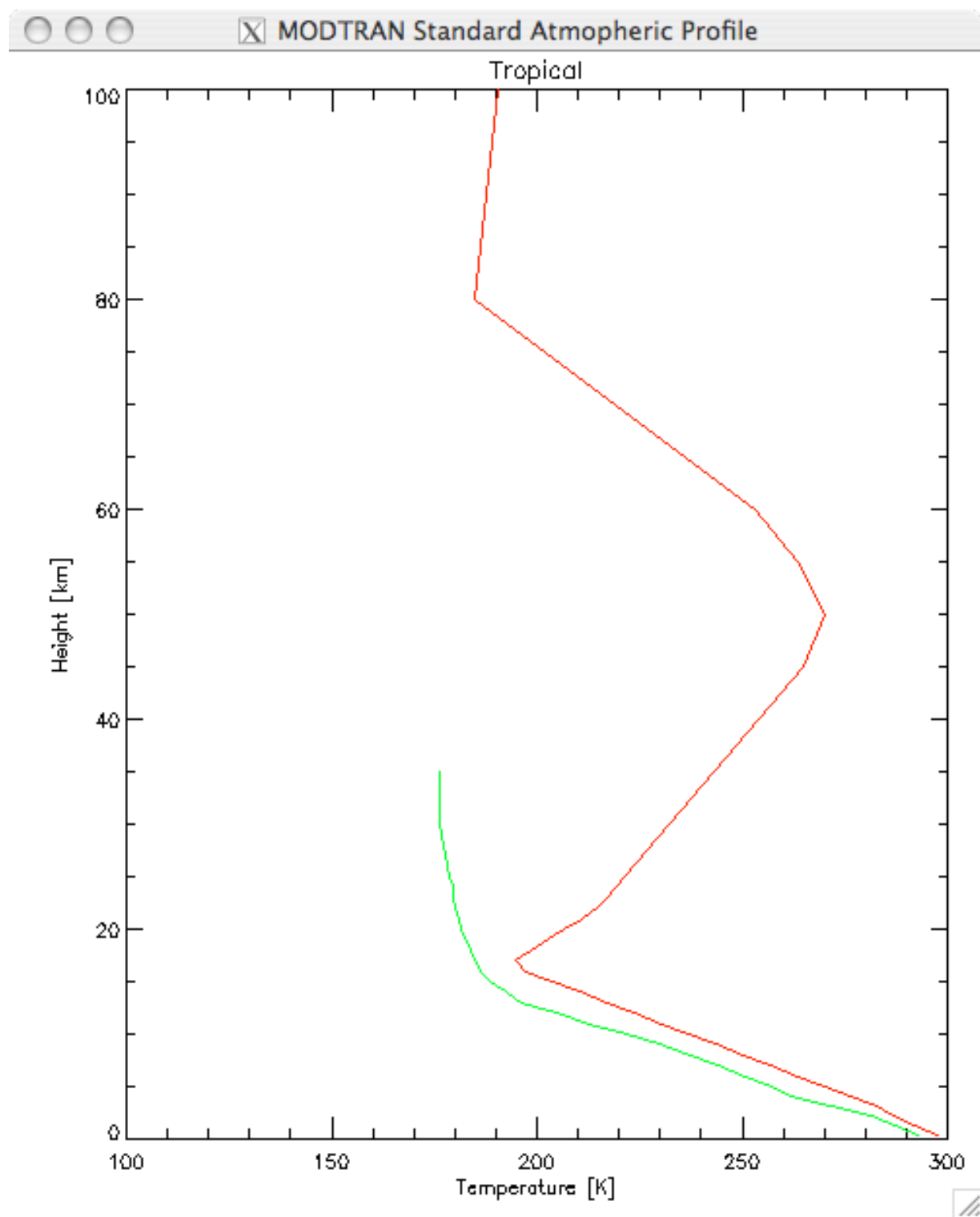


Figure F.3: MODTRAN Standard Atmosphere: Tropical.

Appendix G

Buoy Hull Type and Location History

Depicted below are the buoy locations and payloads used throughout the history of this study. Buoy ID 45012 is not listed as it has remained at the same location and used the same type of payload over its history (3m VEEP, 43.6 N/77.4 W). Note data was obtained via:

http://www.ndbc.noaa.gov/data_availability/data_avail.php

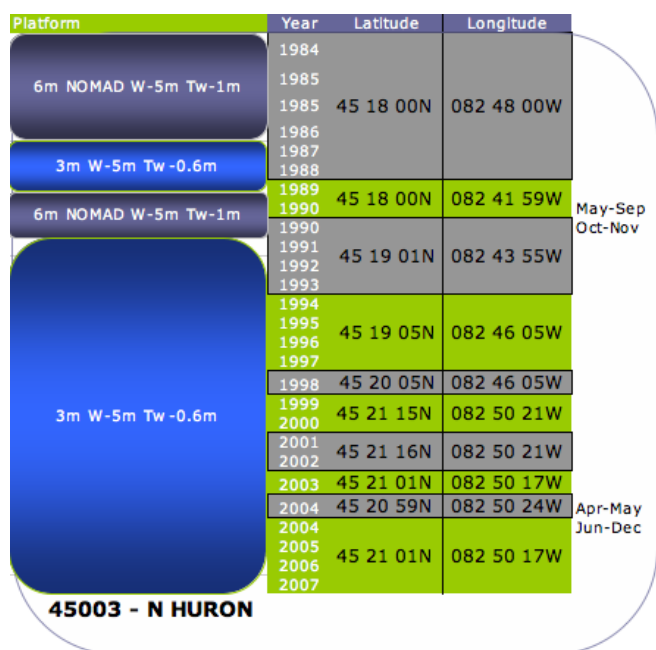


Figure G.1: Buoy location and payload history buoy ID 45003.

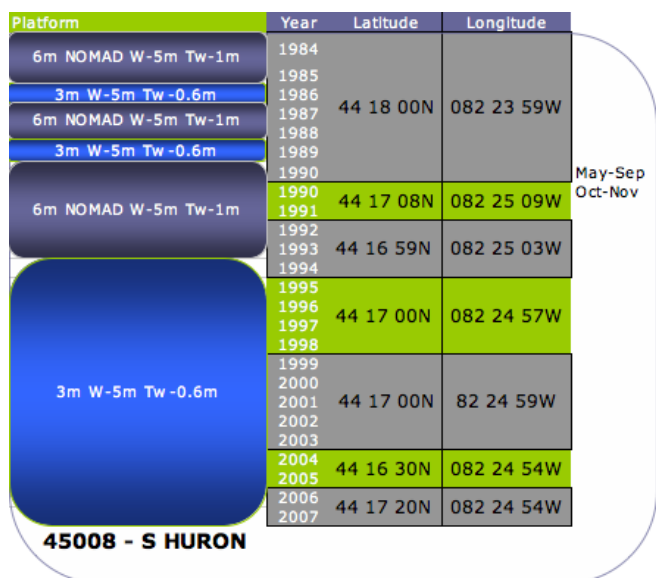


Figure G.2: Buoy location and payload history buoy ID 45008.

Platform	Year	Latitude	Longitude	
6m NOMAD W-5m Tw-1m	1984	48 00 00N	087 36 00W	
12m DACT W-10m Tw-1.5m	1985			
	1986	48 00 00N	087 41 59W	
12m GSBP W-10m Tw-1.5m	1987			
	1988			
	1988	47 36 00N	087 06 00W	Jan-Feb
	1989	48 00 00N	087 41 59W	
	1990			
	1990	48 02 01N	087 42 03W	Apr-Sep
	1991			Oct-Dec
	1992			
	1993	48 02 53N	087 45 59W	
	1994			
	1995			
	1996			
3m VEEP W-5m Tw-0.6m	1997			
	1998			
	1999	48 03 49N	087 46 40W	
	2000			
	2001			
	2002			
	2003			
	2004	48 04 19N	087 46 35W	
	2005			
	2006	48 03 49N	087 46 37W	
	2007			

45001 - MID SUPERIOR

Figure G.3: Buoy location and payload history buoy ID 44001.

Platform	Year	Latitude	Longitude	
6m NOMAD W-5m Tw-1m	1984	47 11 59N	086 30 00W	
	1985			
	1986			
	1987	47 36 00N	086 30 00W	
	1988			
	1989			
	1989			Apr-Sep
	1990	47 30 00N	086 30 00W	Oct-Dec
12m GSBP W-10m Tw-1.5m	1990			Apr-Sep
	1991			Oct-Dec
	1992	47 31 00N	086 30 00W	
	1993			
3m VEEP W-5m Tw-0.6m	1993			Apr-Jul
	1994			Aug-Dec
	1995	47 32 45N	086 32 03W	
	1996			
	1997			
	1998			
	1999	47 33 52N	086 33 06W	
	2000			
	2001			
	2002			
	2003			
	2004			
	2005	47 34 19N	086 32 59W	
	2006			
	2007			
	2007	47 33 20N	086 32 10W	Oct-Dec

45004 - E SUPERIOR

Figure G.4: Buoy location and payload history buoy ID 44004.

Platform	Year	Latitude	Longitude		
LNB - 12m hull Tw = 1.5 Wind = 10m	1984	38 30 00N	074 36 00W	Jan-Sep Oct-Dec May Jun-Dec	
	1985				
	1985				
	1986				
	1987				
	1988				
	1989				
	1990				
	1990	38 27 00N	074 42 00W		
	1991				
1992					
1993					
3m DACT	1993	38 27 49N	074 42 07W		
	1994				
	1995				
	1996				
	1997				
	1998				
	1999				
	2000				
	2001				
	2002				
	2003				
	2004				
	2004				
	2005				
	2006				
2007					
2008					

44009 - DELAWARE BAY

Platform	Year	Latitude	Longitude		
LNB - 12m hull Tw = 1.5 Wind = 10m	1984	38 48 00N	074 36 00W	Sep Oct-Dec	
	1985				
	1986				
	1987				
	1988				
	1989				
	1990				
	1990	38 47 24N	074 34 48W		
	1991				
	1992				

44012 - FIVE FATHOM

Figure G.5: Buoy location and payload history buoy ID 44009 & 44012.

Appendix H

User Workflow

1) Image Derived Radiance

- Image acquisition time from the image header file.
- Investigate image and extract ROI(s) [3x3].
- DC to radiance conversion Eq. 4.2: Image Derived Radiance [$W/m^2sr\mu m$].

2) Buoy Derived T_s

- Acquire 24 hr buoy derived wind speed and T_b data [Section 4.2].
- Run Zeng et al. (1999) model [Section 2.6]: ground truth T_s .

3) Atmospheric Column Generation and Modeling

- Acquire radiosonde, surface and buoy data [Section 4.2].
- Assemble the interpolated atmospheric profile [Section 4.6].
- Generate scene specific MODTRAN tape 5 card deck.
- Run MODTRAN to acquire τ and L_u .
- Run MODTRAN plus DIRSIG to acquire L_d .
- Compute the predicted scene radiance [Figure 4.8] $L_{predicted}$ [$W/m^2sr\mu m$].

4) Calibration Metric

- Compare: Image Derived Radiance and Predicted Scene Radiance [$W/m^2sr\mu m$].

Appendix I

MODTRAN Formatting

Number of Input Layers	T	7	2	2	0	0	0	0	0	0	0	1	1	1	293.054	0.00
	f	0f	0	0.00000								0.000				
Volcanic Input	1	1	0	0	0	0	23.000	0.000	0.000	0.000	0.000	0.000	0.000	0.000	0.177	
	53	0	0	0Jun0799	INTERP											
Ground Altitude [km]	0.177	1.022E+02	2.929E+02	2.843E+02	0.000E+00	0.000E+00	0.000E+00	0.000E+00	0.000E+00	0.000E+00	0.000E+00	0.000E+00	0.000E+00	0.000E+00	0.000E+00	0.000E+00
	0.466	9.660E+01	2.945E+02	2.835E+02	0.000E+00	0.000E+00	0.000E+00	0.000E+00	0.000E+00	0.000E+00	0.000E+00	0.000E+00	0.000E+00	0.000E+00	0.000E+00	0.000E+00
Sensor Altitude [km]	1.560	8.500E+01	2.860E+02	2.750E+02	0.000E+00	0.000E+00	0.000E+00	0.000E+00	0.000E+00	0.000E+00	0.000E+00	0.000E+00	0.000E+00	0.000E+00	0.000E+00	0.000E+00
	2.422	7.660E+01	2.820E+02	2.650E+02	0.000E+00	0.000E+00	0.000E+00	0.000E+00	0.000E+00	0.000E+00	0.000E+00	0.000E+00	0.000E+00	0.000E+00	0.000E+00	0.000E+00
Lat., Lon.	3.543	6.680E+01	2.741E+02	2.661E+02	0.000E+00	0.000E+00	0.000E+00	0.000E+00	0.000E+00	0.000E+00	0.000E+00	0.000E+00	0.000E+00	0.000E+00	0.000E+00	0.000E+00
	4.086	6.240E+01	2.720E+02	2.551E+02	0.000E+00	0.000E+00	0.000E+00	0.000E+00	0.000E+00	0.000E+00	0.000E+00	0.000E+00	0.000E+00	0.000E+00	0.000E+00	0.000E+00
Bandpass [μm]	5.830	5.000E+01	2.620E+02	2.431E+02	0.000E+00	0.000E+00	0.000E+00	0.000E+00	0.000E+00	0.000E+00	0.000E+00	0.000E+00	0.000E+00	0.000E+00	0.000E+00	0.000E+00
	6.763	4.420E+01	2.560E+02	2.271E+02	0.000E+00	0.000E+00	0.000E+00	0.000E+00	0.000E+00	0.000E+00	0.000E+00	0.000E+00	0.000E+00	0.000E+00	0.000E+00	0.000E+00
DOY	7.500	4.000E+01	2.506E+02	2.286E+02	0.000E+00	0.000E+00	0.000E+00	0.000E+00	0.000E+00	0.000E+00	0.000E+00	0.000E+00	0.000E+00	0.000E+00	0.000E+00	0.000E+00
	9.008	3.240E+01	2.394E+02	2.194E+02	0.000E+00	0.000E+00	0.000E+00	0.000E+00	0.000E+00	0.000E+00	0.000E+00	0.000E+00	0.000E+00	0.000E+00	0.000E+00	0.000E+00
Target Temperature [K]	10.020	2.800E+01	2.312E+02	2.252E+02	0.000E+00	0.000E+00	0.000E+00	0.000E+00	0.000E+00	0.000E+00	0.000E+00	0.000E+00	0.000E+00	0.000E+00	0.000E+00	0.000E+00
	11.729	2.160E+01	2.189E+02	2.129E+02	0.000E+00	0.000E+00	0.000E+00	0.000E+00	0.000E+00	0.000E+00	0.000E+00	0.000E+00	0.000E+00	0.000E+00	0.000E+00	0.000E+00
Ground Altitude [km]	12.220	2.000E+01	2.162E+02	2.092E+02	0.000E+00	0.000E+00	0.000E+00	0.000E+00	0.000E+00	0.000E+00	0.000E+00	0.000E+00	0.000E+00	0.000E+00	0.000E+00	0.000E+00
	13.023	1.760E+01	2.164E+02	2.054E+02	0.000E+00	0.000E+00	0.000E+00	0.000E+00	0.000E+00	0.000E+00	0.000E+00	0.000E+00	0.000E+00	0.000E+00	0.000E+00	0.000E+00
Sensor Altitude [km]	14.030	1.500E+01	2.142E+02	1.992E+02	0.000E+00	0.000E+00	0.000E+00	0.000E+00	0.000E+00	0.000E+00	0.000E+00	0.000E+00	0.000E+00	0.000E+00	0.000E+00	0.000E+00
	15.010	1.280E+01	2.089E+02	1.939E+02	0.000E+00	0.000E+00	0.000E+00	0.000E+00	0.000E+00	0.000E+00	0.000E+00	0.000E+00	0.000E+00	0.000E+00	0.000E+00	0.000E+00
Lat., Lon.	16.714	9.720E+00	2.101E+02	1.931E+02	0.000E+00	0.000E+00	0.000E+00	0.000E+00	0.000E+00	0.000E+00	0.000E+00	0.000E+00	0.000E+00	0.000E+00	0.000E+00	0.000E+00
	17.698	8.290E+00	2.136E+02	1.946E+02	0.000E+00	0.000E+00	0.000E+00	0.000E+00	0.000E+00	0.000E+00	0.000E+00	0.000E+00	0.000E+00	0.000E+00	0.000E+00	0.000E+00
Bandpass [μm]	18.750	7.000E+00	2.129E+02	1.939E+02	0.000E+00	0.000E+00	0.000E+00	0.000E+00	0.000E+00	0.000E+00	0.000E+00	0.000E+00	0.000E+00	0.000E+00	0.000E+00	0.000E+00
	20.870	5.000E+00	2.159E+02	1.949E+02	0.000E+00	0.000E+00	0.000E+00	0.000E+00	0.000E+00	0.000E+00	0.000E+00	0.000E+00	0.000E+00	0.000E+00	0.000E+00	0.000E+00
DOY	24.130	3.000E+00	2.222E+02	1.982E+02	0.000E+00	0.000E+00	0.000E+00	0.000E+00	0.000E+00	0.000E+00	0.000E+00	0.000E+00	0.000E+00	0.000E+00	0.000E+00	0.000E+00
	30.161	1.200E+00	2.309E+02	2.059E+02	0.000E+00	0.000E+00	0.000E+00	0.000E+00	0.000E+00	0.000E+00	0.000E+00	0.000E+00	0.000E+00	0.000E+00	0.000E+00	0.000E+00
Target Temperature [K]	40.000	3.330E-01	2.575E+02	1.760E+02	0.000E+00	0.000E+00	0.000E+00	0.000E+00	0.000E+00	0.000E+00	0.000E+00	0.000E+00	0.000E+00	0.000E+00	0.000E+00	0.000E+00
	50.000	9.510E-02	2.757E+02	1.779E+02	0.000E+00	0.000E+00	0.000E+00	0.000E+00	0.000E+00	0.000E+00	0.000E+00	0.000E+00	0.000E+00	0.000E+00	0.000E+00	0.000E+00
Ground Altitude [km]	60.000	2.720E-02	2.571E+02	1.631E+02	0.000E+00	0.000E+00	0.000E+00	0.000E+00	0.000E+00	0.000E+00	0.000E+00	0.000E+00	0.000E+00	0.000E+00	0.000E+00	0.000E+00
	70.000	6.700E-03	2.181E+02	1.488E+02	0.000E+00	0.000E+00	0.000E+00	0.000E+00	0.000E+00	0.000E+00	0.000E+00	0.000E+00	0.000E+00	0.000E+00	0.000E+00	0.000E+00
Sensor Altitude [km]	80.000	1.200E-03	1.741E+02	1.450E+02	0.000E+00	0.000E+00	0.000E+00	0.000E+00	0.000E+00	0.000E+00	0.000E+00	0.000E+00	0.000E+00	0.000E+00	0.000E+00	0.000E+00
	100.000	1.000E-06	1.905E+02	1.457E+02	0.000E+00	0.000E+00	0.000E+00	0.000E+00	0.000E+00	0.000E+00	0.000E+00	0.000E+00	0.000E+00	0.000E+00	0.000E+00	0.000E+00
Lat., Lon.	100.000	0.177	180.000	0.000	0.000	0.000	0.000	0.000	0.000	0.000	0.000	0.000	0.000	0.000	0.000	0.000
	1	2	252	0												
Bandpass [μm]	44.290	82.420	0.000	0.000	15.350	0.000	0.000	0.000	0.000	0.000	0.000	0.000	0.000	0.000	0.000	0.000
	10.000	12.900	0.100	0.100RM	M	A										
DOY	0															

Figure I.1: Depicts a MODTRAN tape 5 cardeck. Note inputs of particular importance are highlighted (c.f. MODTRAN (1998) for details).

Appendix J

Error Propagation: Atmospheric Profiles

Shown are the 7 modified atmospheric profiles selected for the atmospheric error propagation study [Section 4.11]. For each profile the pressure, temperature, and dew point temperature modifications are shown, note 1000 unique profiles were used for each case. Also illustrated are the Landsat 5 TM Band 6 effective values of: L_u , L_d and τ for each of the original reconstructed (i.e. surface and upper-air corrections applied) profiles; provided to give the reader insight into what the particular profile looked like, as well as to understand the resulting values of the atmospheric terms given the atmospheric profile.

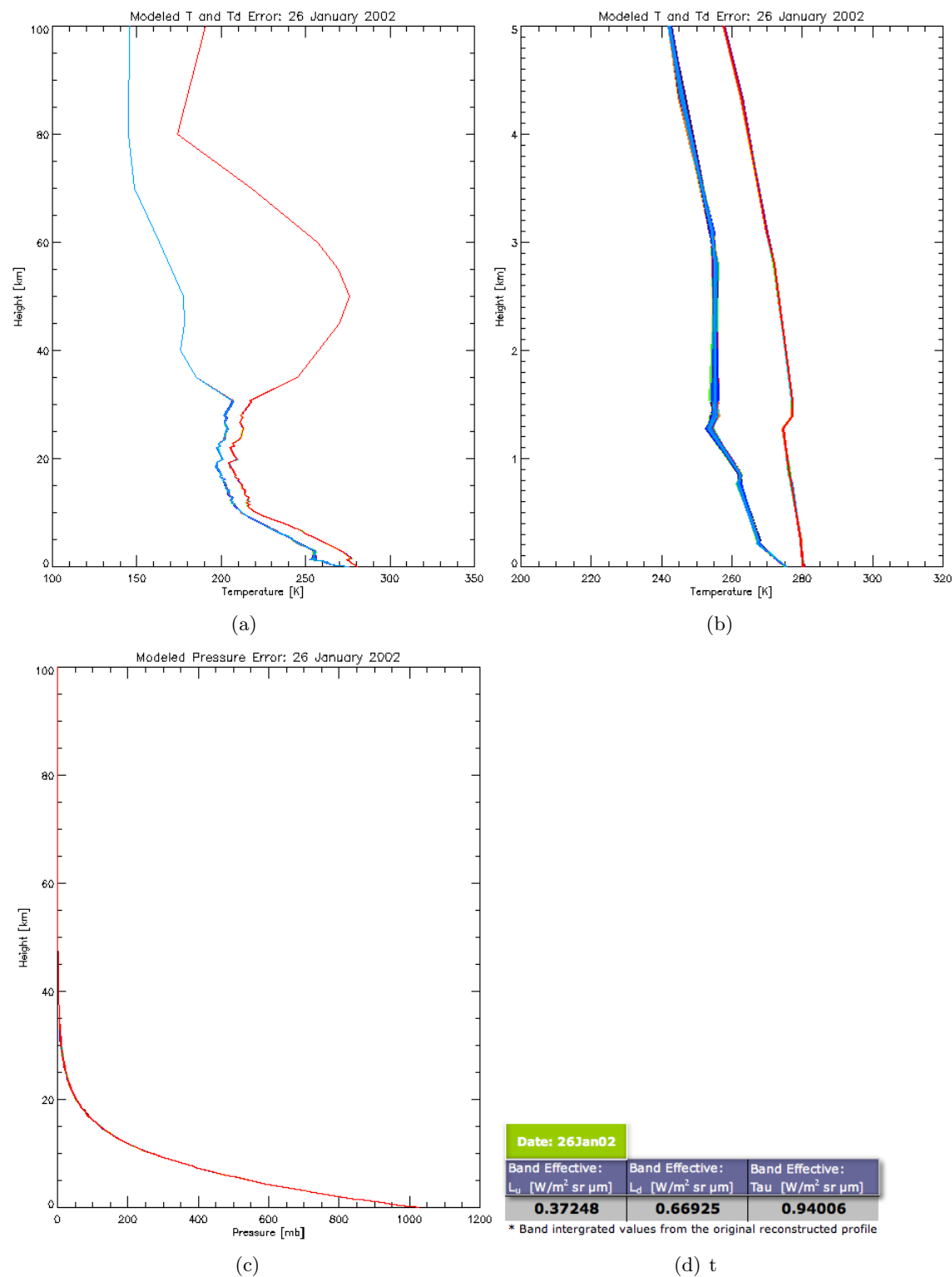


Figure J.1: Modified radiosonde profiles (1000) from WAL at 12z 26Jan02: (cold dry) (a) Temperature and dew point profiles. (b) Zoom: Temperature and dew point profiles. (c) Pressure profiles.

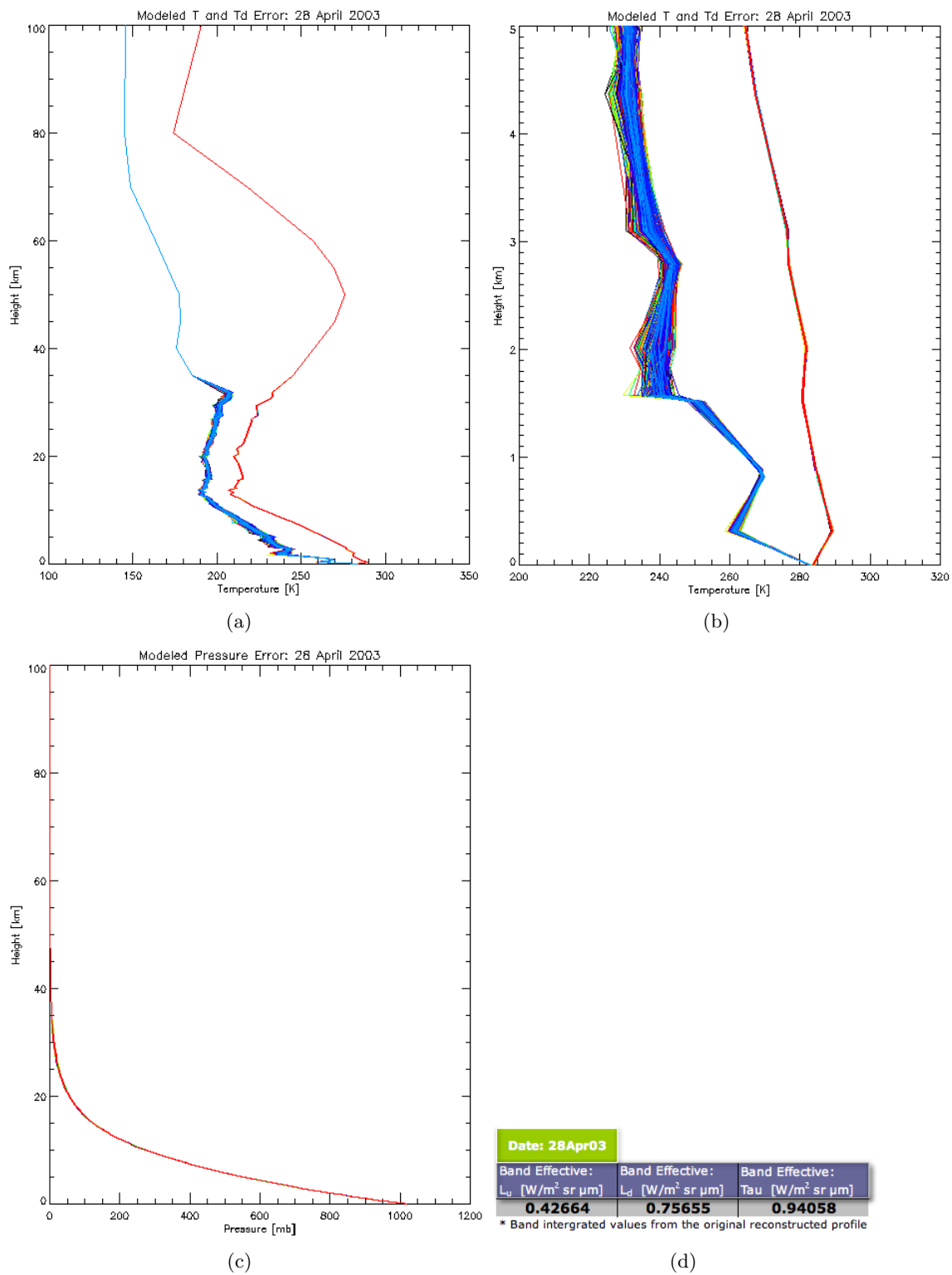


Figure J.2: Modified radiosonde profiles (1000) from WAL at 12z on 28April03: (cold dry)
(a) Temperature and dew point profiles. (b) Zoom: Temperature and dew point profiles.
(c) Pressure profiles.

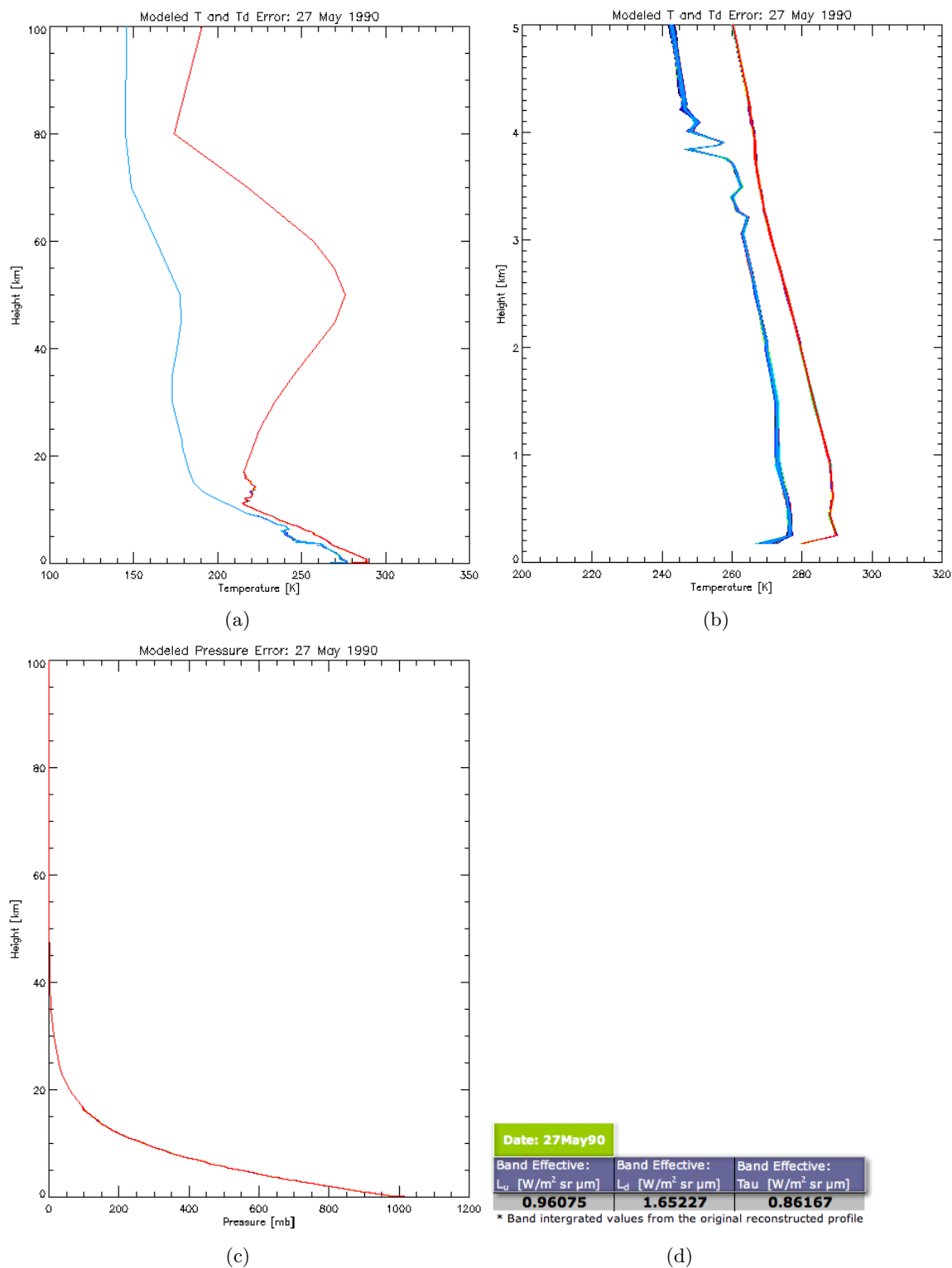


Figure J.3: Modified radiosonde profiles (1000) from SSM at 00z on 27 May 90: (Cool Moist) (a) Temperature and dew point profile. (b) Zoom: Temperature and dew point profile. (c) Pressure profile.

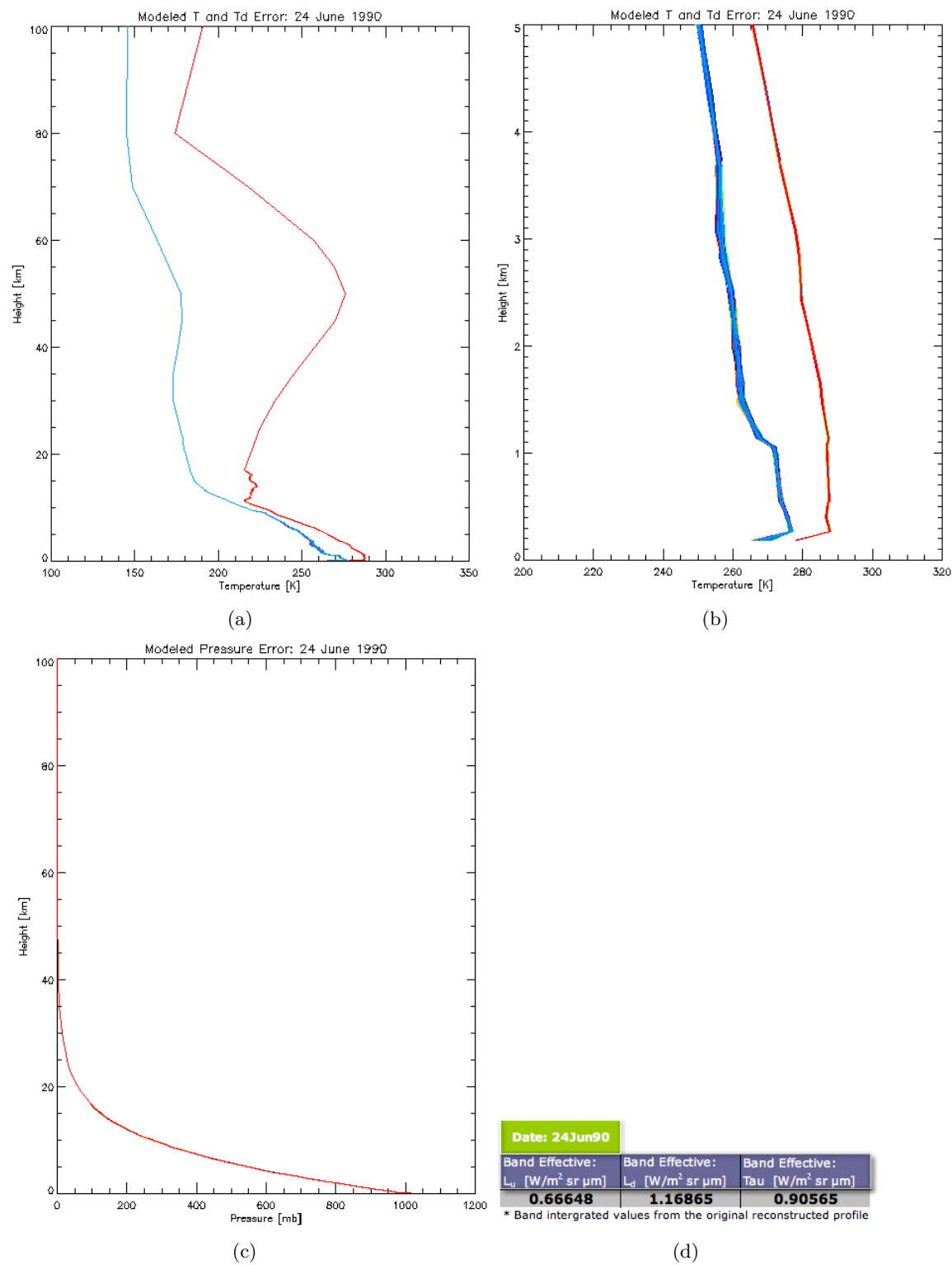


Figure J.4: Modified radiosonde profiles (1000) from SSM at 00z on 24 Jun 90: (Warm Dry) (a) Temperature and dew point profile. (b) Zoom: Temperature and dew point profile. (c) Pressure profile.

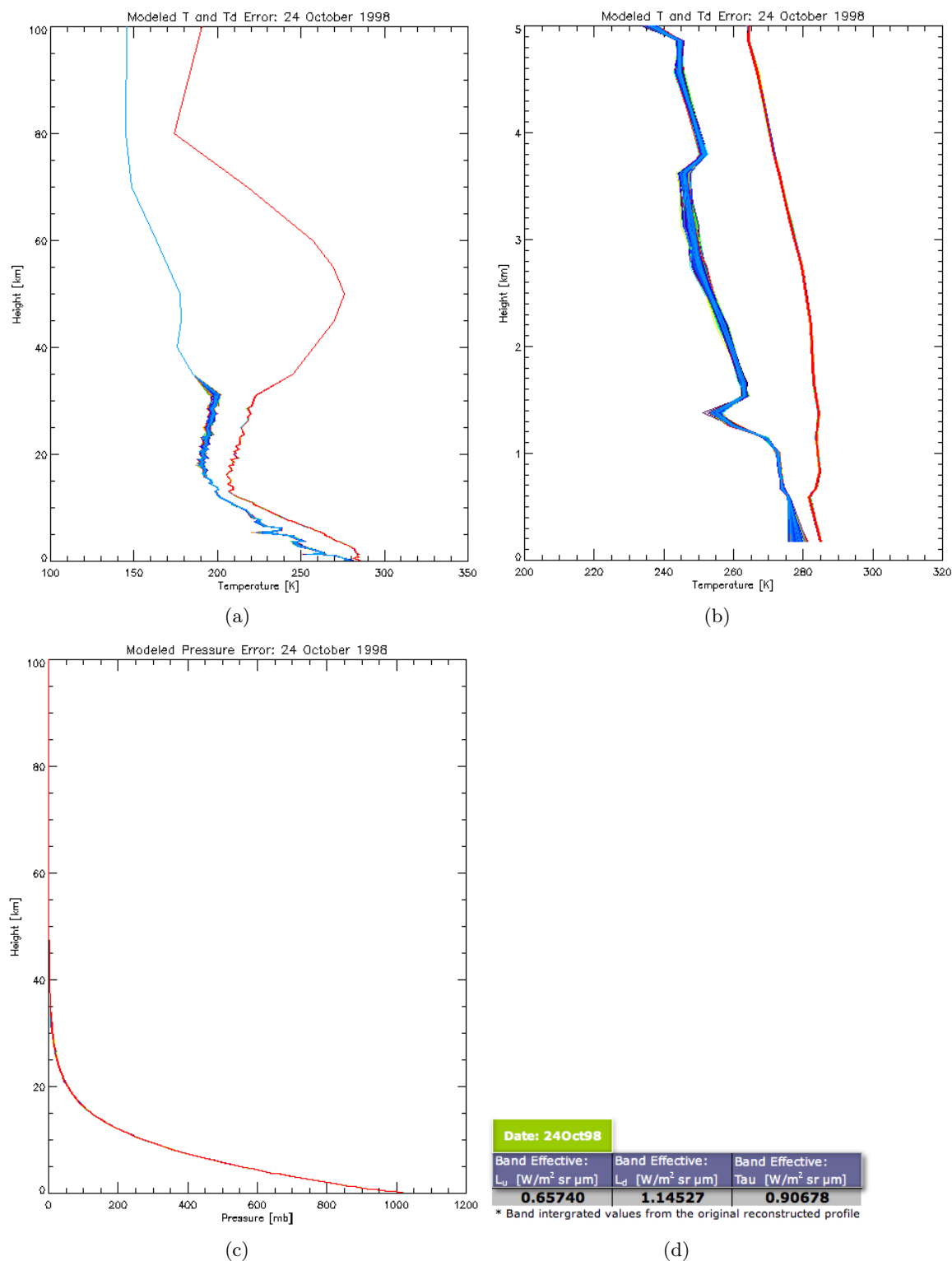


Figure J.5: Modified radiosonde profiles (1000) from APX at 12z on 24 Oct 98: (Warm Dry) (a) Temperature and dew point profile. (b) Zoom: Temperature and dew point profile. (c) Pressure profile.

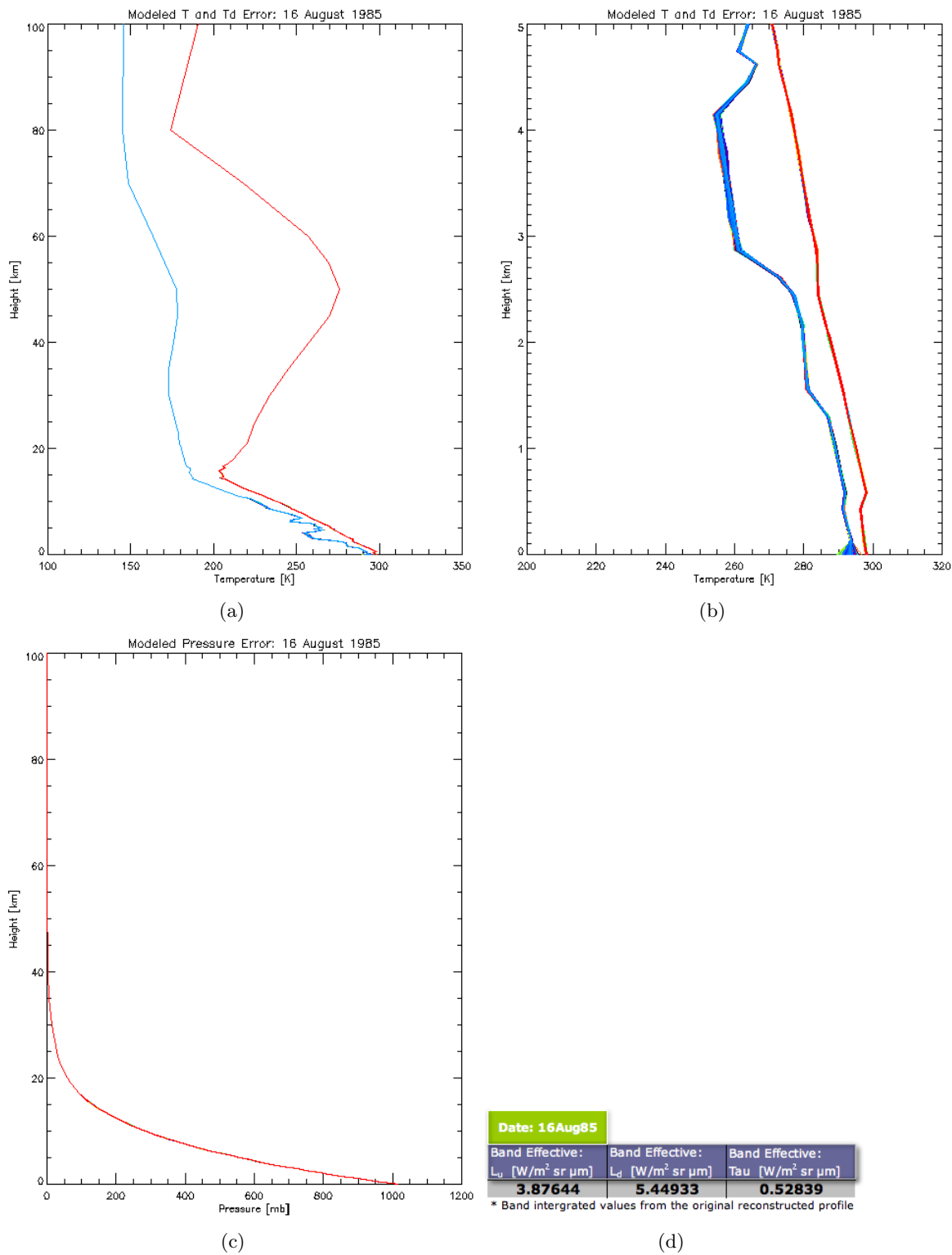


Figure J.6: Modified radiosonde profiles (1000) from WAL at 12z on 16 Aug 85: (Warm Moist) (a) Temperature and dew point profile. (b) Zoom: Temperature and dew point profile. (c) Pressure profile.

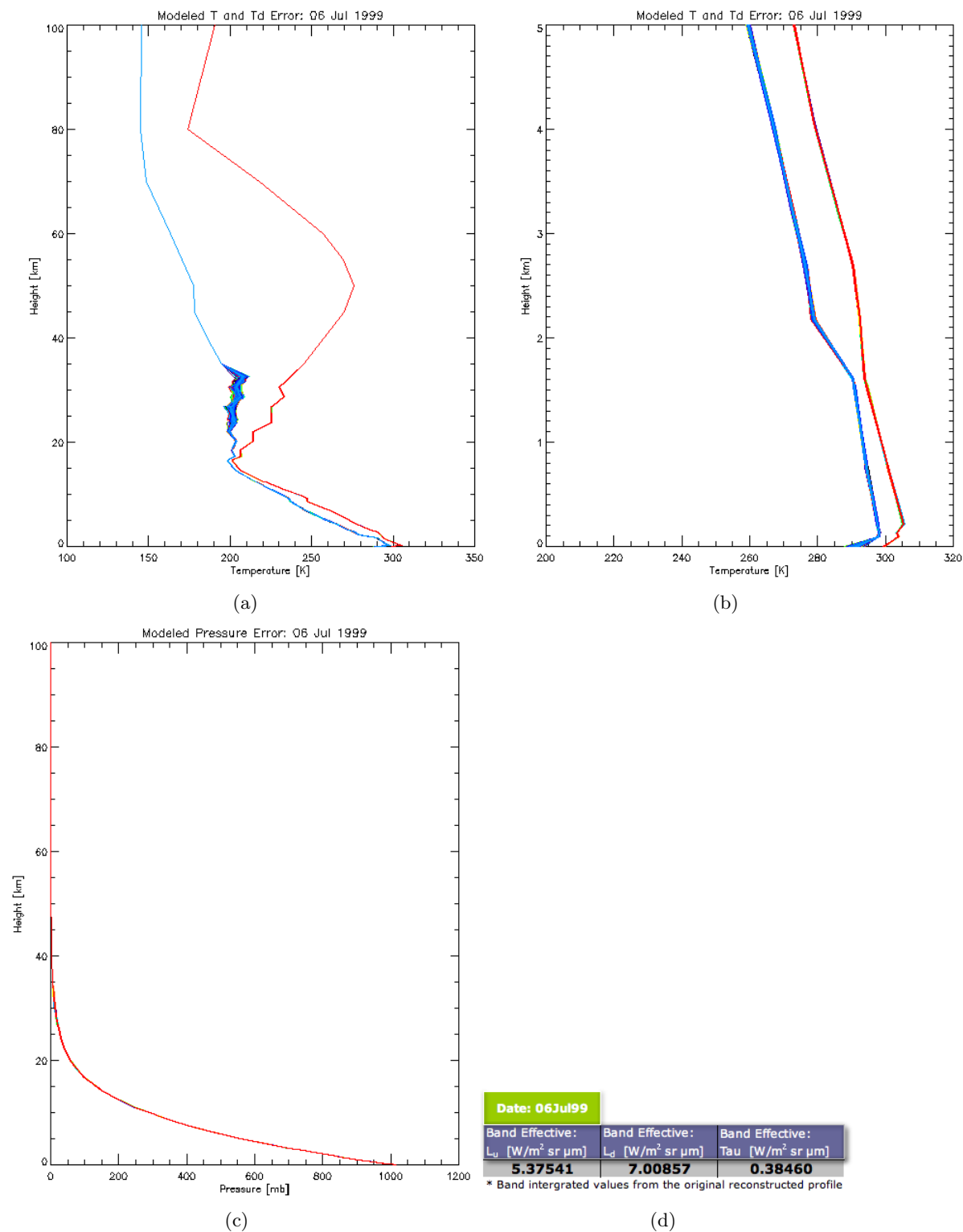


Figure J.7: Modified radiosonde profiles (1000) from WAL at 00z on 06 Jul 99: (Warm Moist) (a) Temperature and dew point profile. (b) Zoom: Temperature and dew point profile. (c) Pressure profile.

Bibliography

AMS. *American Meteorological Society Glossary*, April 15, 2008 .

W. M. Angevine, J. E. Hare, C. W. Fairall, D. E. Wolfe, R. J. Hill, W. A. Brewer, and A. B. White. Structure and formation of the highly stable marine boundary layer over the Gulf of Maine. In *Journal of Geophysical Research*, volume 111, 2006.

W. L. Barnes and J. C. Price. Calibration of a satellite infrared radiometer. In *Applied Optics*, volume 19, pages 2153–2161, 1 July 1980.

R. G. Barry and R. J. Chorley. *Atmosphere, weather & climate*. Methuen & Co Ltd, London EC4P 4EE, third edition, 1977.

J. Barsi. *MISI and Landsat ETM plus: Thermal Calibration and Atmospheric Correction*. Rochester Institute of Technology, Rochester, NY, 2000.

J. Barsi, J. Schott, F. Palluconi, D. Helder, S. Hook, B. Markham, and G. Chander. Landsat TM and ETM+ thermal band calibration. In *Can. J. Remote Sensing*, volume 29, pages 141–153, 2003.

J. A. Barsi, S. J. Hook, J. R. Schott, N. G. Raqueno, and B. L. Markham. Landsat-5 thematic mapper thermal band calibration update. In *IEEE Geoscience and Remote Sensing Letters*, volume 4, pages 552–555, October 2007.

L. A. Bartolucci, M. Chang, P. E. Anuta, and M. R. Graves. Atmospheric effects on Landsat TM thermal IR data. In *IEEE Transactions on Geoscience and Remote Sensing*, volume 26, pages 171–176. IEEE, March 1988.

- F. Becker. The impact of spectral emissivity on the measurement of land surface temperature from a satellite. In *Int. J. Remote Sensing*, volume 8, pages 1509–1522, 1987.
- A. Berk, G. P. Anderson, L. S. Bernstein, P. K. Acharya, H. Dothe, M. W. Matthew, S. M. Adler-Golden, J. J. H. Chetwynd, S. C. Richtsmeier, B. Pukall, C. L. Allred, L. S. Jeong, and M. L. Hoke. Modtran4 radiative transfer modeling for atmospheric correction. In *Optical Spectroscopic Techniques and Instrumentation for Atmospheric and Space Research III*, pages 348–353, Denver, Colorado, 1999. SPIE Vol. 3756.
- D. Bolton. The computation of equivalent potential temperature. In *Monthly Weather Review*, volume 108, pages 1047–1053, 1980.
- A. P. Cracknell. *The Advanced Very High Resolution Radiometer*. Taylor & Francis, Bristol, PA, 1997.
- G. T. Csanady. Equilibrium theory of the planetary boundary layer with an inversion lid. In *Boundary Layer Meteorology*, volume 6, pages 63–79, 1974.
- K. P. Czajkowski, S. N. Goward, and H. Ouaidrari. Impact of AVHRR filter functions on surface temperature estimation from the split window approach. In *Int. J. Remote Sensing*, volume 19, pages 2007–2012, 1998.
- P. Dash, F. M. Gottsche, F. S. Olesen, and H. Fischer. Land surface temperature and emissivity estimation from passive sensor data: theory and practice - current trends. In *International Journal of Remote Sensing*, volume 23, pages 2563–2594, 2002.
- C. J. Donlon, P. J. Minnett, C. Gentemann, T. J. Nightingale, I. J. Barton, B. Ward, and M. J. Murray. Toward improved validation of satellite sea surface skin temperature measurements for climate research. In *Journal of Climate*, volume 15, pages 353–369. AMS, February 15 2002.

- W. P. Elliott and D. Gaffen. On the utility of radiosonde humidity archives for climate studies. In *Bulletin American Meteorological Society*, volume 72, pages 1507–1520, October 1991.
- W. J. Emery, D. Baldwin, P. Schlussel, and R. Reynolds. Accuracy of in situ sea surface temperatures used to calibrate infrared satellite measurements. In *Journal of Geophysical Research*, volume 106, pages 2387–2405, February 15 2001.
- C. W. Fairall, E. F. Bradley, J. S. Godfrey, G. A. Wick, and J. B. Edson. Cool-skin and warm-layer effects on sea surface temperature. In *Journal of Geophysical Research*, volume 101, pages 1295–1308, January 15 1996.
- J. R. Garratt and B. F. Ryan. The structure of the stably stratified internal boundary layer in offshore flow over the sea. In *Boundary Layer Meteorology*, volume 47, pages 17–40, 1989.
- M. B. Gbah, S. J. Jacobs, G. A. Meadows, and A. Braktovich. Circulation and turbulent exchange characteristics during the thermal bar in Lake Ontario. In *Journal of Geophysical Research*, volume 103, pages 12807–12821, 1998.
- R. P. Gupta. *Remote Sensing Geology*. Springer, Heidelberg, Germany, second edition, 2003.
- A. R. Harris, S. J. Brown, and I. M. Mason. The effect of windspeed on sea surface temperature retrieval from space. In *GEOPHYSICAL RESEARCH LETTERS*, volume 21, page 17151718. AGU, 1994.
- L. A. Horrocks, B. Candy, T. J. Nightingale, R. W. Saunders, A. O’Carroll, and A. R. Harris. Parameterizations of the ocean skin effect and implications for satellite-based measurements of sea-surface temperature. In *Journal of Geophysical Research*, volume 108, March 15 2003.
- H. G. Houghton. *Physical Meteorology*. The MIT Press, Cambridge, MA and London, England, 1985.

- S. A. Hsu. On the growth of a thermally modified boundary layer by advection of warm air over a cooler sea. In *Journal of Geophysical Research*, volume 88, pages 771–774, 1983.
- R. W. Hyland and A. Wexler. Formulations for the thermodynamic properties of the saturated phases of H₂O from 173.15k to 473.15k. In *ASHRAE Trans*, volume 89, pages 500–519, 1983.
- L. E. Keiner and X.-H. Yan. Empirical orthogonal function analysis of sea surface temperature patterns in delaware bay. In *IEEE Transactions on Geoscience and Remote Sensing*, volume 35, pages 1299–1306, September 1997.
- M. Konda, N. Imasato, K. Nishi, and T. Toda. Measurement of the sea surface emissivity. In *Journal of Oceanography*, volume 50, pages 17 – 30, 1994.
- A. Kumar, P. J. Minnett, G. Podesta, and R. H. Evans. Error characteristics of the atmospheric correction algorithms used in retrieval of sea surface temperatures from infrared satellite measurements: Global and regional aspects. In *Journal of the Atmospheric Sciences*, volume 60, pages 575–585, February 1 2003.
- X. Li, W. Pichel, E. Maturi, P. Clemente-Colon, and J. Sapper. Deriving the operational nonlinear mulichannel sea surface temperature algorithm coefficients for NOAA-15 AVHRR/3. In *Int. J. Remote Sensing*, volume 22, pages 699–704, 2001.
- T. M. Lillesand, R. W. Kiefer, and J. W. Chipman. *Remote Sensing and Image Interpretation*. John Wiley & Sons, Inc., New York, NY, fifth edition, 2004.
- C. J. Merchant, A. R. Harris, M. J. Murray, and A. M. Zavody. Toward the elimination of bias in satellite retrievals of sea surface temperature 1) theory, modeling, and interalgorithm comparison. volume 104, pages 565–578. *J. Geophys. Res.*, 1999.
- L. M. Miloshevich, H. Vomel, A. Paukkunen, A. J. Heymsfield, and S. J. Oltmans. Characterization and correction of relative humidity measurements from Vaisala

- RS80-A radisondes at cold temperatures. In *Journal of Atmospheric and Oceanic Technology*, pages 135–156, February 2001.
- MODTRAN. *MODTRAN User's Manual*. Air Force Research Laboratory, Hanscom AFB, MA, versions 3.7 and 4.0 edition, 1998.
- M. Montanaro, C. Salvaggio, S. D. Brown, D. W. Messinger, and A. J. Garrett. Apparent temperature dependence on localized atmospheric water vapor. In *SPIE*, 2008.
- NWS. *National Weather Service radiosonde fact-sheet*, March 2, 2008 .
- J. F. Price, R. A. Weller, and R. Pinkel. Diurnal cycling: Observations and models of the upper ocean responses to diurnal heating, cooling, and wind mixing. In *International Journal of Remote Sensing*, volume 19, pages 2105–2117, 1998.
- Y. R. Rao, M. G., and G. C. Muhr. Circulation and turbulent exchange characteristics during the thermal bar in Lake Ontario. In *Limnology and Oceanography*, volume 49, pages 2190–2200, 2004.
- R. W. Reynolds. Impact of Mount Pinatubo aerosols on satellite-derived sea surface temperatures. In *Journal of Climate*, volume 6, pages 768–774, April 1993.
- G. K. Rodgers. Field investigation of the thermal bar in Lake Ontario: Precision temperature measurements. In *Proceedings of the 14th Conference Great Lake Resources*, pages 618–624, 1971.
- R. J. Ross and W. P. Elliott. Tropospheric water vapor climatology and trends over North America: 1973-93. In *Journal of Climate*, volume 9, pages 3561–3574, December 1996.
- R. Ryan, M. Pagnutti, V. Zanoni, G. Harrington, D. Howell, and R. Stewart. Methods for LWIR radiometric calibration and characterization. Technical Report Commission I, Working Group I/2, Remote Sensing Directorate, Lockheed Martin Space Operations - Stennis Programs and NASA Earth Science Applications Directorate.

- P. Schluessel, W. J. Emery, H. Grassl, and T. Mammen. On the bulk-skin temperature difference and its impact on satellite remote sensing of sea surface temperature. In *Journal of Geophysical Research*, volume 95, pages 341–356, August 15 1990.
- D. J. R. Schott and N. Raqueno. NASA research 2006 final report: Landsat radiometric calibration: Towards a 20 year record of calibrated thematic mapper class data. Nasa research 2006 final report, Rochester Institute of Technology, 2006.
- J. R. Schott. *Remote Sensing: The Image Chain Approach*. Oxford University Press, New York, NY, second edition, 2007.
- J. R. Schott. Temperature measurements of cooling water discharged from power plants. In *Photogrammetric Engineering and Remote Sensing*, volume 45, pages 753–761, 1979.
- J. R. Schott and E. W. Schimminger. Data use investigations for applications explore mission a (heat capacity mapping mission). In *Calspan Report No. 6175-M-1*, number NASA Accession No. E81-10079, 1981.
- J. R. Schott and W. Volchok. Thematic mapper thermal infrared calibration. In *Photogrammetric Engineering and Remote Sensing*, volume 51, September 1985.
- J. R. Schott, W. J. Volchok, and J. D. Biegel. Radiometric analysis of the longwave infrared channel of the thematic mapper on Landsat 4 and 5. Technical report, 1986.
- J. R. Schott, S. D. Brown, R. V. Raqueño, H. N. Gross, and G. Robinson. An advanced synthetic image generation model and its application to multi/hyperspectral algorithm development. In *Canadian Journal of Remote Sensing*, volume 25, pages 99–111, 1999.
- D. J. Schwab, G. A. Leshkevich, and G. C. Muhr. Automated mapping of surface water temperature in the Great Lakes. In *J. Great Lakes Res.*, volume 25, pages 468–481, 1999.

- P. N. Slater, S. F. Biggar, K. J. Thome, D. I. Gellman, and P. R. Spyak. Vicarious radiometric calibration of EOS sensors. In *Journal of Atmospheric and Oceanic Technology*, volume 13, pages 349–359, April 1996.
- A.-S. Smedman, H. Bergstrom, and B. Grisogono. Evolution of stable internal boundary layers over a cold sea. In *Journal of Geophysical Research*, volume 102, pages 1091–1099, January 15 1997.
- F. Sospedra, V. Caselles, and E. Valor. Effective wavenumber for thermal infrared bands - application to Landsat-TM. In *J. Geophys. Res. of Remote*, volume 91, pages 8411–8427, 1986.
- L. L. Stowe, R. M. Carey, and P. P. Pellegrino. Monitoring the Mt. Pinatubo aerosol layer with NOAA/11 AVHRR data. In *Geophysical Research Letters*, volume 19, pages 159–162, January 24 1992.
- R. B. Stull. *An Introduction to Boundary Layer Meteorology*. Kluwer Academic Publishers Inc., Norwell, MA, 1988.
- H. Tonooka, F. D. Palluconi, S. J. Hook, and T. Matsunaga. Vicarious Calibration of ASTER Thermal Infrared Bands. In *IEEE Transactions on Geoscience and Remote Sensing*, page 2733. 2746, IEEE, December 2005.
- USGS. *USGS: Landsat Project Facts*, March 4, 2008 .
- E. Villa-Aleman, A. J. Garrett, R. J. Kurzeja, B. L. O. Steen, and M. M. Perdergast. Thermal Targets for Satellite Calibration. Technical Report WSRC-MS-2000-00921, Department of Energy (DOE).
- J. M. Wallace and P. V. Hobbs. *Atmospheric Science An Introductory Survey*. Academic Press, New York, 1977.
- C. Walton, W. Pichel, J. Sapper, and D. May. The development and operational application of nonlinear algorithms for the measurement of sea surface temperatures with the NOAA polar-orbiting environmental satellites. In *Journal of Geophysical Research*, volume 103, pages 999–1028, 1998.

- Z. Wan and J. Dozier. Land-surface temperature measurement from space: Physical principles and inverse modeling. In *Transactions on Geoscience and Remote Sensing*, volume 27, pages 268–278. IEEE, May 1989.
- Z. Wan, Y. Zhang, X. Ma, M. D. King, J. S. Myers, and X. Li. Vicarious calibration of the moderate-resolution imaging spectroradiometer airborne simulator thermal-infrared channels. In *Applied Optics*, volume 38, pages 6294–6306, 20 October 1999.
- M. Watanabe, Y. Iwasaka, T. Shibata, M. Hayashi, M. Fujiwara, and R. Neuber. The evolution of Pinatubo aerosols in the arctic stratosphere during 1994-2000. In *Atmospheric Research*, volume 69, pages 199–215, 2004.
- S. Weisberg. *Applied Linear Regression*. John Wiley & Sons, New York, second edition, 1985.
- X. Zeng, M. Zhao, R. E. Dickinson, and Y. He. A multiyear hourly sea surface skin temperature data set derived from the TOGA TAO bulk temperature and wind speed over the tropical Pacific. In *Journal of Geophysical Research*, volume 104, pages 1525–1536, January 15 1999.